SAPIENZA
UNIVERSITÀ DI ROMA

Constraints on Neutrino Physics in light of recent Cosmological Data

Scuola di Dottorato in Scienze Astronomiche, Chimiche, Fisiche e Matematiche, Vito Volterra

Dottorato di Ricerca in Astronomia – XXV Ciclo

Candidate

Maria Archidiacono

ID number 698803

Thesis Advisor

Prof. Alessandro Melchiorri

PhD Coordinator

Prof. Roberto Capuzzo Dolcetta

A thesis submitted in partial fulfillment of the requirements
for the degree of Doctor of Philosophy in Astronomy

November 2012

Thesis defended on 21st January 2013
in front of a Board of Examiners composed by:

F. Ricci, PO, Sapienza, Roma
S. Capozziello, PO, Univ. di Napoli Federico II
F. La Franca, PA, Univ. di Roma 3
O. Straniero, Dirigente di ricerca, INAF, Oss. di Teramo
M. Castellani, Ricercatore Astronomo, INAF, Oss. di Roma

Constraints on Neutrino Physics in light of recent Cosmological Data
Ph.D. thesis. Sapienza – University of Rome

This thesis has been typeset by LaTeX and the Sapthesis class.

Author's email: maria.archidiacono@gmail.com

$o\tilde{\imath}\delta\alpha$ $\acute{o}\tau\iota$ $ou\chi$ $o\tilde{\imath}\delta\alpha$

Contents

Introduzione

La connessione tra osservazioni cosmologiche e fisica del neutrino rappresenta uno dei piu' interessanti e fecondi argomenti della fisica delle astroparticelle.

Esperimenti terrestri hanno dimostrato che i neutrini oscillano e quindi hanno massa. Tuttavia gli esperimenti sulle oscillazioni non possono misurare il valore assoluto di tale massa, ma solo la differenza dei quadrati delle masse. In particolare gli esperimenti sulle oscillazioni dei neutrini atmosferici forniscono solo il modulo della differenza dei quadrati delle masse tra il secondo e il terzo autostato di massa. Non conoscendo il segno di questa misura, esistono due possibili gerarchie delle masse dei neutrini: quella normale e quella invertita. Le due differenze dei quadrati delle masse misurate implicano in ogni caso l'esistenza di almeno due neutrini dotati di massa.

A differenza degli esperimenti sulle oscillazioni, la cosmologia misura la somma delle masse dei neutrini e, attualmente, e' l'unica strada alternativa agli esperimenti sul decadimento beta, e supera questi ultimi in accuratezza. Tutto cio' e' possibile perche' la presenza dei neutrini lascia un segno attraverso il free-streaming nei dati cosmologici: lo spettro di potenza delle anisotropie della radiazione di fondo cosmico a microonde (Cosmic Microwave Background, CMB) e lo spettro di potenza delle fluttuazioni di materia derivante dalle survey di galassie.

Finora abbiamo parlato di tre neutrini (ν_e, ν_μ, ν_τ), tuttavia questo e' solo lo schema del Modello Standard. Precise misure elettrodeboli della risonanza dello Z^0 hanno vincolato il numero delle specie di neutrini leggeri attivi con grande precisione, $N_\nu = 2.9840 \pm 0.0082$, consistente entro $\sim 2\,\sigma$ con le tre famiglie aspettate in base alle predizioni del Modello Standard. Invece, il numero effettivo di neutrini termalizzati e' stato fissato al valore cosmologico standard $N_{\rm eff} = 3.046$, che eccede leggermente l'intero 3 per via del disaccoppiamento non istantaneo: l'annichilazione e^+e^-, che avviene circa all'energia del disaccoppiamento dei neutrini ($\sim 1\ MeV$), fornisce l'energia in eccesso. Usufruendo degli attuali dati cosmologici, gli effetti di $N_{\rm eff}$ sono rintracciabili nello spettro delle anisotropie della radiazione cosmica di fondo sia a livello di ampiezza dei picchi sia a livello di deformazione dei picchi stessi a $\ell > 600$. Quindi e' di capitale importanza l'uso dei recenti dati di CMB ad alti multipoli, provenienti dagli esperimenti South Pole Telescope e Atacama Cosmology Telescope, al fine di comprovare o escludere la presenza di una componente extra di radiazione: la radiazione oscura.

Questi ulteriori gradi di liberta' relativistici possono essere dovuti a neutrini sterili, che hanno lo stesso effetto degli attivi sugli osservabili cosmologici. Questa ipotesi da' luogo ad un'interessante connessione fra cosmologia e fisica del neutrino. Infatti, recenti risultati da esperimenti Short–Base–Line sulle oscillazioni dei neutrini

suggeriscono la presenza di neutrini sterili che possono spiegare l'eccesso di radiazione trovato nella CMB.

Questa tesi e' volta a fornire limiti sui parametri cosmologici legati alla fisica del neutrino, ovvero la densita' totale di materia oscura calda e il numero effettivo di gradi di liberta' relativistici, usufruendo dei recenti dati cosmologici. L'obiettivo e' anche di testare la stabilita' di questi vincoli in modelli cosmologici non minimali, variando le nostre assunzioni teoriche a priori riguardo al modello ΛCDM. Infine questa tesi e' dedicata allo studio della possibile connessione fra la cosmologia e la fisica del neutrino alla luce degli ultimi risultati di esperimenti sulle oscillazioni.

La tesi e' organizzata come segue.

Nel Capitolo 1 introdurremo brevemente il Modello Cosmologico Standard per un Universo omogeneo ed isotropo in espansione. In particolare calcoleremo le equazioni di Friedmann e forniremo l'evidenza della materia oscura.

Nel Capitolo 2 introdurremo la teoria delle perturbazioni lineari e ci focalizzeremo sulla radiazione di fondo cosmica, discutendone i diversi effetti che danno luogo alle anisotropie e calcolandone lo spettro di potenza. Infine presenteremo lo spettro di potenza di materia cosi' come puo' essere estratto dalle survey di galassie.

Il Capitolo 3 sara' dedicato ai neutrini: prima di tutto introdurremo i neutrini dal punto di vista della fisica delle particelle, poi ci concentreremo sul fondo cosmico di neutrini e discuteremo gli effetti della massa dei neutrini sulle equazioni della teoria delle perturbazioni lineari e sugli osservabili cosmologici. Infine mostreremo gli effetti del numero effettivo di gradi di liberta' relativistici sempre in relazione agli osservabili cosmologici.

Nel Capitolo 4 spiegheremo i metodi statistici che andremo ad applicare nei capitoli successivi al fine di estrarre da dati cosmologici informazioni sui parametri cosmologici legati alla fisica del neutrino.

Nei capitoli successivi verra' presentato il lavoro che ho condotto durante il Dottorato di Ricerca.

Nel Capitolo 5 condurremo una ricerca della radiazione oscura, parametrizzandola come numero effettivo di gradi di liberta' relativistici, $N_{\rm eff}$, e studiandone il comportamento dal punto di vista della teoria delle perturbazioni attraverso i parametri relativi alle perturbazioni dei neutrini: la velocita' del suono effettiva ed il parametro di viscosita'. Inoltre verificheremo la presenza di degenerazioni fra i parametri relativi alle perturbazioni dei neutrini ed altri parametri cosmologici (il parametro dell'equazione di stato dell'energia oscura e il running dell'indice dello spettro di potenza di materia), degenerazioni che possono portare a conclusioni errate riguardo ai valori assunti da tali parametri relativi alle perturbazioni dei neutrini. Tale verifica sara' condotta su dati simulati degli esperimenti Planck e COrE. Infine controlleremo la stabilita' dei risultati relativi alla radiazione oscura nel caso di un Universo non piatto e sottolineeremo come tali risultati siano fortemente dipendenti dall'assunzione di una prior sulla costante di Hubble.

Nel Capitolo 6 ci concentreremo sulla fisica del neutrino come possibile ponte fra due branche della fisica: la cosmologia e la fisica delle particelle. Useremo sia dati cosmologici sia dati da esperimenti Short–Base–Line su oscillazioni di neutrino per verificare la consistenza dei risultati cosmologici sulla massa dei neutrini sterili nel caso di modelli 3+1 e 3+2.

Nel Capitolo 7 sottolineeremo come i limiti cosmologici sulla massa dei neutrini

siano fortemente dipendenti dal modello assunto nell'analisi. Stimeremo di quanto tali risultati cambiano al variare delle nostre assunzioni teoriche rispetto a reionizzazione e curvatura. In particolare, data l'attuale assenza di informazioni precise riguardo la storia della reionizzazione cosmica, verificheremo i limiti sulla massa dei neutrini nell'ottica di uno scenario relativo alla reionizzazione il piu' generale possibile utilizzando un approccio basato sulle principal components. Per quanto riguarda la curvatura, studieremo come i vincoli sulla massa dei neutrini perdano in definizione se si assume un Universo non piatto. Infine vedremo come l'informazione derivante dallo spettro di potenza relativo all'effetto Sunyaev Zel'dovich termico possa rompere la degenerazione fra σ_8 (la radice del quadrato della media delle fluttuazioni di densita' calcolate su un volume sferico di raggio $8\mathrm{Mpc}h^{-1}$) e la somma delle masse dei neutrini; come conseguenza, cio' comportera' un miglioramento nei vincoli sulla massa dei neutrini.

Nel Capitolo 8 calcoleremo il contributo degli effetti Sunyaev Zel'dovich e dei foregrounds alle anisotropie della CMB. Poiche' il contributo di tali anisotropie secondarie risulta dominante su piccole scale dove gli effetti della massa dei neutrini e di un numero non standard di neutrini lasciano un'impronta rilevante, sara' importante nei futuri esperimenti ad alta precisione avere una chiara rilevazione di SZ ed una perfetta sottrazione dei foregrounds.

Introduction

The connection between cosmological observations and neutrino physics is one of the most interesting and hot topics in astroparticle physics.

Earth based experiments demonstrated that neutrinos oscillate and therefore have mass. However oscillation experiments cannot measure the absolute mass value, but only the squared mass differences. In particular the experiments on the oscillation of atmospheric neutrinos provide only the modulus of the mass squared difference between the second and the third mass eigenstates. Since we don't know the sign of this measure, there are two possible hierarchies: the normal one and the inverted one. The two measured mass squared differences imply that at least two neutrinos are massive today.

Unlike the oscillation experiments, cosmology probes the sum of the neutrino masses and, at the state of art, is the only viable alternative to the beta decay experiments in this field and exceeds it in accuracy. This is possible because neutrinos leave key signatures through their free-streaming properties in several cosmological datasets: the temperature anisotropies power spectrum of the Cosmic Microwave Background (CMB) and the power spectrum of matter fluctuations which is one of the basic products of galaxy redshift surveys.

So far we have spoken about three neutrinos (ν_e, ν_μ, ν_τ), but this is only the Standard Model scheme. Precision electroweak measurements at the Z^0-resonance pin down the number of light active neutrino species with high accuracy, $N_\nu = 2.9840 \pm 0.0082$, consistent within $\sim 2\,\sigma$ with the known three families of the SM. Instead, the effective number of thermally excited neutrino species has been fixed at the cosmological standard value of $N_{\rm eff} = 3.046$, that slightly exceeds the integer 3 because of the non-instant decoupling of neutrinos, so e^+e^-annihilation, that took place at the energy of neutrino decoupling ($\sim 1\,MeV$), provides residual neutrino heating. At the state of art of the current precision of cosmological data, the effects of $N_{\rm eff}$ influence the Cosmic Microwave Background temperature anisotropy power spectrum both on the amplitude and the shape at $\ell > 600$. So it is crucial to use the recent high multipole CMB data from South Pole Telescope and Atacama Cosmology Telescope experiments, in order to assess or rule out the presence of an extra–Dark Radiation component.

These extra relativistic degrees of freedom may consist of sterile neutrinos, which have the same effects on the cosmological observables of the active ones. This hypothesis gives raise to an interesting interplay between cosmology and neutrino physics. Actually, recent results from Short–Base–Line neutrino oscillation experiments suggest the presence of additional sterile neutrinos that can explain the excess of radiation found in CMB data.

The present thesis is aimed to provide constraints on cosmological parameters related to neutrino physics, namely the total hot dark matter density and the effective number of relativistic degrees of freedom, from recent cosmological data. The goal is also to test the robustness of these constraints in non minimal cosmologies, varying our theoretical assumptions about the ΛCDM model. Finally this thesis is devoted to study the possible connection between cosmology and neutrino physics in light of the most updated oscillation experiments results.

The present thesis is organized as follows.

In Chapter 1 we briefly introduce the Cosmological Standard Model for an expanding homogeneous and isotropic Universe. In particular the Friedmann equations are calculated and the Dark Matter evidence is provided.

In Chapter 2 we introduce the linear perturbation theory and we focus on the Cosmic Microwave Background, discussing the effects that give rise to its anisotropies and calculating its power spectrum. Finally the matter power spectrum is presented as it can be extracted from galaxies surveys.

Chapter 3 is dedicated to neutrinos: first of all we introduce neutrinos from the point of view of particle physics, then we focus on the Cosmic Neutrino Background and we discuss the neutrino mass effects on the equations of the linear perturbation theory and on the cosmological observables. Finally we show the effects of a non standard effective number of relativistic degrees of freedom.

In Chapter 4 we explain the statistical methods we are going to apply in subsequent chapters in order to extract information on cosmological parameters related to neutrino physics from cosmological data.

In subsequent chapters the work I carried out during my Ph.D is presented.

In Chapter 5 we perform a new search for Dark Radiation, parametrizing it with an effective number of relativistic degrees of freedom parameter, $N_{\rm eff}$, and studying its behavior from the point of view of perturbation theory through the neutrino perturbation parameters: the effective sound speed and the viscosity parameter. Moreover we investigate possible misleading degeneracies between the neutrino perturbation parameters and other cosmological parameters, as the dark energy equation of state parameter and the running of the scalar spectral index, by performing mock analyses based on the future experiments Planck and COrE. Finally we check the stability of the results about $N_{\rm eff}$ if we assume a non-flat Universe and we underline how these results depend sensitively on the assumption of an HST prior on the Hubble constant.

In Chapter 6 we look at neutrino physics as a link between cosmology and particle physics. We make use of both cosmological data and Short–Base–Line experiments data in order to verify the consistency of the cosmological results on sterile neutrino mass in a 3+1 and 3+2 schemes, with 1 and 2 massive sterile neutrinos, respectively.

In Chapter 7 we point out that the impressive cosmological bounds on neutrino masses are model dependent. So we investigate how these constraints change if we change our theoretical assumptions about reionization and curvature. In particular, given our lack of knowledge about reionization history, we investigate the bounds on the neutrino mass in a more general reionization scenario based on a principal component approach. Concerning curvature, we study how the neutrino mass bounds are weakened by assuming a non-flat Universe. Finally we will see how the information on the temperature Sunyaev Zel'dovich power spectrum can break the

degeneracy between σ_8 (the root mean square of density fluctuations on a spherical volume of $8\mathrm{Mpc}h^{-1}$) and the sum of neutrino masses; as an aftermath, this will lead to a better constraint on the neutrino mass.

In Chapter 8 we calculate the contribution of Sunyaev Zel'dovich effects and foregrounds to the CMB anisotropies. Since these secondary anisotropies contribution is dominant on small angular scales where neutrino mass and non-standard neutrino number leave key signatures, it will be important to have a clear detection of SZ and a perfect subtraction of foregrounds in future high precision data.

Chapter 1

The Cosmological Standard Model

1.1 The Hubble law

The Universe is isotropic and homogeneous at large scale (more than 100 Mpc) [1, 2]. Combining the isotropy respect to any point in the space with the cosmological principle that state that there is no preferred direction in the Universe, one obtains the isotropy respect to any point and this implies the homogeneity.

The spectrum of a galaxy shows some absorption lines produced by the relatively colder outer layers of the atmosphere. Each line is characterized by a wavelength different from that observed in the laboratory. This difference defines the redshift

$$z = (\lambda_{obs} - \lambda_{em})/\lambda_{em}$$

where λ_{obs} is the observed wavelength and λ_{em} is the emitted one equal to the wavelength that would be observed in the rest frame. This quantity is found to be greater than zero. In 1929 Hubble plotted the distance of 50 near galaxies as a function of z and discovered the law $z = (H_0/c)r$, where H_o is a constant, $H_0 = 73.8 \pm 2.4 Km/s/Mpc$ following the last data release of the Hubble Space Telescope [3], or $H_0 = 100h$ Km/s/Mpc where $h = 0.72 \pm 0.07$. Since the values of z in Hubble analysis were small, he made use of the classical Doppler effect formula: $z = v/c$, where v is the radial velocity of the source. So the Hubble law becomes: $v = H_0 r$. The Universe expands homogeneously and isotropically. This model can be mathematically described as follows: considering three galaxies in the positions $\overrightarrow{r_1}$; $\overrightarrow{r_2}$; $\overrightarrow{r_3}$, they define a triangle of side $r_{12} = |\overrightarrow{r_1} - \overrightarrow{r_2}|$, $r_{23} = |\overrightarrow{r_2} - \overrightarrow{r_3}|$, $r_{31} = |\overrightarrow{r_3} - \overrightarrow{r_1}|$. An isotropic and uniform expansion implies that the triangle doesn't change its shape and its sides obey to the expansion rules: $r_{12} = a(t)r_{12}(t)$, $r_{23} = a(t)r_{23}(t)$,$r_{31} = a(t)r_{31}(t)$, where $a(t)$ is called scale factor, it is a function of the time normalized at 1 at the present time and it is independent on the

point and on the direction. The scale factor describes how the distances increase or decrease with time. At any time t an observer placed in galaxy 1 beholds the other galaxies recede with speed: $v_{12}(t) = \frac{dr_{12}(y)}{dt} = \dot{a}r_{12}(t_0) = \frac{\dot{a}}{a}r_{12}(t)$ and $v_{31}(t) = \frac{dr_{31}(t)}{dt} = \dot{a}r_{31}(t_0) = \frac{\dot{a}}{a}ar_{31}(t)$. An observer in 2 would find the same relation between the observed receding velocity and the distance. Since these relations can be applied to any three galaxies, in the Universe it holds that $H = \frac{\dot{a}}{a}$. The present status of receding galaxies implies that in the past they were merged together in an infinitesimal volume, as predicted by the Big Bang theory.

1.2 The Friedmann-Robertson-Walker metric

In the Minkowsky metric the distance between two events in the four dimensional space time (assuming the speed of light $c = 1$) is:

$$ds^2 = \eta_{\alpha\beta}dx^\alpha dx^\beta \qquad \text{with } \eta_{\alpha\beta} = \begin{pmatrix} 1 & 0 & 0 & 0 \\ 0 & -1 & 0 & 0 \\ 0 & 0 & -1 & 0 \\ 0 & 0 & 0 & -1 \end{pmatrix}$$

where the spatial part is Euclidean. In this kind of Universe subject to gravity and to the homogeneous and isotropic expansion, the most general metric can be written as:

$$ds^2 = g_{\mu\nu}dx^\mu dx^\nu$$

where $g_{\mu\nu}$ is the metric tensor. Splitting the temporal, spatial and mix component, we obtain:

$$ds^2 = g_{00}dt^2 + 2g_{oi}dx^i dt - \sigma_{ij}dx^i dx^j.$$

Applying the isotropy, it means no preferred direction $g_{oi} = 0$; moreover, the time synchronization implies that $d\tau = \sqrt{g_{00}}dt$, so $g_{00} = 1$. Because of the isotropy the spatial metric ds_3^2 can be dependent only on $|r|$ and on $dx^2 + dy^2 + dz^2 = dr^2 + r^2(d\theta^2 + \sin^2\theta d\phi^2)$, where $r^2(d\theta^2 + \sin^2\theta d\phi^2)$ is the surface element. So we can rewrite:

$$ds_3^2 = a^2(t)\lambda^2(r)\left[dr^2 + r^2(d\theta^2 + \sin^2\theta d\phi^2)\right],$$

or $ds_3^2 = a^2(t)\left[\lambda'^2(r'^2)dr'^2 + r'^2(d\theta^2 + \sin^2\theta d\phi^2)\right]$, where $r' = \lambda r$ and $\lambda' = \lambda/(rd\lambda/dr + \lambda)$. The unknown function $\lambda(r)$ is obtained by imposing the homogeneity. To do this we need to look at a spherical hypersurface in a four dimensional Euclidean space. The spherical four dimensional coordinates are:

$$\begin{aligned} x_1 &= \arccos\chi \sin\theta \sin\phi \\ x_2 &= \arccos\chi \cos\theta \\ x_3 &= \arccos\chi \sin\theta \cos\phi \\ x_4 &= \arcsin\chi. \end{aligned}$$

The conditions for a three dimensional space to be spherical are: $a^2 = x_1^2+x_2^2+x_3^2+x_4^2$, differentiating this relation: $x_4 dx_4 = -(x_1 dx_1 + x_2 dx_2 + x_3 dx_3)$, so we obtain

$$\begin{aligned} ds^2 &= dx_1^2 + dx_2^2 + dx_3^2 + dx_4^2 = dx_1^2 + dx_2^2 + dx_3^2 + \frac{(x_1 dx_1 + x_2 dx_2 + x_3 dx_3)^2}{x_4^2} = \\ &= a^2[d\chi^2 + \sin^2\chi(d\theta^2 + \sin^2\theta d\phi^2)] \end{aligned}$$

that is the same of the above general formula if $\sin\chi = r$ and $d\chi = \lambda dr$, that means if $\lambda = \frac{1}{\sqrt{1-r^2}}$. For any line element $a^2 = x_1^2 + x_2^2 + x_3^2 + kx_4^2$, we obtain $ds_3^2 = a^2[d\chi^2 + F(\chi)(d\theta^2 + \sin^2\theta d\phi^2)]$, where

$$F(\chi) = \begin{cases} \sin\chi & k = 1 \\ \chi & k = 0 \\ \sinh\chi & k = -1 \end{cases} \qquad \text{and } d\chi = \lambda dr \text{ with } \lambda = \frac{1}{\sqrt{1-r^2}}.$$

This homogeneous and isotropic metric is called Friedmann-Robertson-Walker metric [4] and it turns out to be:

$$ds^2 = dt^2 - a^2(t)\left[\frac{dr^2}{1-kr^2} + r^2(d\theta^2 + \sin^2\theta d\phi^2)\right]$$

The variables r, θ, ϕ are called the comoving coordinates of the point in the space. If the expansion of the Universe was perfectly homogeneous and isotropic, these coordinates would be constant for any point at any time. The constant k is an adimensional number and in principle can assume any value but these three cases are considered:

- k=0 spatially flat Universe;
- k>0 positive curvature, close Universe;
- k<0 negative curvature, open Universe.

The Friedmann-Robertson-Walker metric can be rewritten as

$$ds^2 = dt^2 - a^2(t)\left[dr^2 + S_k^2(r)d\Omega^2\right], \tag{1.1}$$

where

$$S_k(r) = \begin{cases} R\sin(r/R) & (k = +1) \\ r & (k = 0) \\ R\sinh(r/R) & (k = -1) \end{cases}$$

where R is the curvature radius $R = 1/k$.

1.3 The relation between the redshift and the scale factor

The photon path in the space-time is described by a nil four-dimensional geodetic. So for any infinitesimal segment of the photon path it holds that $ds = 0$, that means $c^2dt^2 = a^2(t)dr^2$. Supposing a photon were emitted at time t_e with wavelength λ_e and received at time t_0 with wavelength λ_0, it would pan out:

$$c\int_{t_e}^{t_0}\frac{dt}{a(t)} = \int_0^r dr = r.$$

The next wave would be emitted at $t_e + \lambda_e/c$ and observed at $t_0 + \lambda_0/c$, so

$$c\int_{t_e+\lambda_e/c}^{t_0+\lambda_0/c}\frac{dt}{a(t)} = r.$$

Comparing the two equations above one obtains:

$$\int_{t_e}^{t_0}\frac{dt}{a(t)} = \int_{t_e+\lambda_e/c}^{t_0+\lambda_0/c}\frac{dt}{a(t)}$$

this means that the integral of $dt/a(t)$ between the emitting time and the observing time is the same for any wave. After subtracting $\int_{t_e+\lambda_e/c}^{t_0}\frac{dt}{a(t)}$ we obtain

$$\int_{t_0}^{t_0+\lambda_0/c}\frac{dt}{a(t)} = \int_{t_e}^{t_e+\lambda_e/c}\frac{dt}{a(t)}.$$

In the meantime between two subsequent waves the Universe expansion is negligible so $a(t)$ can be considered constant in the integral:

$$\frac{1}{a(t_0)}\int_{t_0}^{t_0+\lambda_0/c}dt = \frac{1}{a(t_e)}\int_{t_e}^{t_e+\lambda_e/c}dt$$

or

$$\lambda_e/a(t_e) = \lambda_0/a(t_0).$$

Using the redshift definition $z = (\lambda_{obs} - \lambda_{em})/\lambda_{em}$ and assuming $a(t_0) = 1$, we find the relation between the redshift and the scale factor:

$$1 + z = a(t_0)/a(t_e) = 1/a(t_e)$$

1.4 Distances

The cosmological observables of objects at astronomical distances are: redshift z, flux f, luminosity L, and, if the object has an extension greater than a light point, the angular diameter $\delta\theta$.

The standard candle is an object of known luminosity used to determine the luminosity distances:

$$d_L = \left(\frac{L}{4\pi f}\right)^{1/2}.$$

In the case of a static Euclidean Universe the luminosity distance would be equal to the exact distance of the object. In such a Universe the propagation of light would be described by the law $f = L/4\pi d^2$. The expansion of the Universe implies that the observed flux from a source at redshift z decreases of a factor $(1+z)^{-2}$. First of all the expansion of the Universe makes the energy of any photon of the standard candle decrease. If a photon is emitted with energy $E_e = hc/\lambda_e$ when the scale factor is $a(t_e)$, it will be observed at $a(t_0) = 1$ with a greater wavelength: $\lambda_0 = \lambda_e/a(t_e) = (1+z)\lambda_e$. So the energy is decreased: $E_0 = hc/\lambda_0 = hc/\left[\lambda_e(1+z)\right] = E_e/(1+z)$. Secondly, the time interval between the photon detections increases because of the Universe expansion. If two photons are emitted from the same source in the same direction with a time interval δt_e, the exact distance between theme is $c\delta t_e$, but at the time of detection the distance between them will increase up to $c\delta t_e(1+z)$. To sum up, in an expanding Universe the relation between the luminosity distance and the physical distance is

$$d_L = S_k(r)(1+z),$$

where $S_k(r)$ is defined in the FRW metric (1.1). In the particular case of a spatially flat Universe it is

$$d_L = d_P(t_0)(1+z),$$

where $d_p(t_0)$ is the proper distance of the object nowadays and can be calculated by integrating the radial comoving coordinate over a nil geodetic (the photon path):

$$d_p(t) = a(t)\int_0^r dr = a(t)r.$$

An astronomical object is defined a standard ruler if we know its physical length l. Supposing you could measure the redshift and the distance between the edges of a ruler that is perpendicular to the line of sight, if $\delta\theta \ll 1$, using the small angles formula, we would be able to calculate the angular diameter distance

$$d_A = \frac{l}{\delta\theta}.$$

Also the angular diameter distance would be equal to the exact distance in a static Euclidean Universe. In an expanding Universe, using the FRW metric, the distance between the edges of the standard ruler at the emitting time t_e is

$$ds = a(t_e)S_k(r)d\theta.$$

Assuming $ds = l$ we obtain

$$l = S_k(r)\frac{\delta\theta}{(1+z)}.$$

So the angular diameter distance pans out to be:

$$d_A = \frac{S_k(r)}{1+z}.$$

Comparing the last expression with the luminosity distance, one finds the following relation

$$d_A = \frac{d_L}{(1+z)^2}.$$

Finally, in a flat Universe it is

$$d_A = \frac{d_p(t_0)}{1+z} = d_p(t_e).$$

1.5 The energy-momentum tensor

The conservation laws of a homogeneous and isotropic perfect fluid in the restframe of the center of mass are:

$$\dot{\varrho} = 0$$
$$\nabla p = 0$$

where the energy density $\varrho = nmc^2$ (n is the density of particles with mass m) and the pressure in the i direction is $p_i = nmv_i^2$. We can define the tensor

$$T^{\mu\nu} = diag(\varrho, -p_x, -p_y, -p_z) = diag(\varrho, -p, -p, -p) \tag{1.2}$$

where the isotropy has been assumed in the last equality. The conservation laws can be summed up into

$$T^{\mu\nu}_{,\mu} = 0.$$

This relation holds only for two tensors: $g^{\mu\nu}$ e $u^\mu u^\nu$, with $u^\mu \equiv dx^\mu/ds$ the four-velocity and

$$g^{\mu\nu} = \begin{pmatrix} 1 & 0 & 0 & 0 \\ 0 & -\frac{1}{a^2} & 0 & 0 \\ 0 & 0 & -\frac{1}{a^2} & 0 \\ 0 & 0 & 0 & -\frac{1}{a^2} \end{pmatrix}.$$

The only function of the two tensors and of ϱ, p that becomes equal to 1.2 in the Minkowskian approximation is

$$T^{\mu\nu} = (\varrho + p)u^\mu u^\nu - pg^{\mu\nu}. \tag{1.3}$$

In the restframe respect to the matter it is $u^\mu = (1, 0, 0, 0)$ and so the tensor components become:

$$T^{00} = \varrho, \qquad T^{ii} = \frac{p}{a^2}, \qquad T \equiv T^{\mu\mu} = \varrho - 3p.$$

The covariant generalization of the conservation equation is

$$T^{\mu\nu}_{;\mu} = 0 \text{ where } T^{\mu\nu}_{;\mu} = T^{\mu\nu}_{,\mu} + \Gamma^\mu_{\mu\beta}T^{\beta\nu} + \Gamma^\nu_{\mu\beta}T^{\mu\beta} \tag{1.4}$$

where the Γ are the Christoffel symbols defined as: $\Gamma^\alpha_{\mu\nu} = \frac{1}{2}g^{\alpha\beta}(g_{\nu\beta,\mu} + g_{\beta\mu,\nu} - g_{\mu\nu,\beta})$.

In the FRW metric with $k = 0$ the Christoffel symbols are all nil except $\Gamma^i_{j0} = \Gamma^i_{0j} = H\delta^i_j$ and $\Gamma^0_{ij} = a\dot{a}\delta_{ij}$. As an aftermath in the FRW metric the equation 1.4 in the case $\nu = 0$ gives the continuity equation:

$$\dot{\varrho} + 3H(\varrho + p) = 0. \tag{1.5}$$

1.6 The Friedmann equation

The Einstein equation is

$$R_{\mu\nu} - \frac{1}{2} g_{\mu\nu} R = 8\pi T_{\mu\nu}$$

where $R_{\mu\nu} = \Gamma^{\alpha}_{\mu\nu,\alpha} - \Gamma^{\alpha}_{\mu\alpha,\nu} + \Gamma^{\alpha}_{\beta\alpha}\Gamma^{\beta}_{\mu\nu} - \Gamma^{\alpha}_{\beta\nu}\Gamma^{\beta}_{\alpha\mu}$ is the Ricci tensor and $R = g^{\mu\nu}R_{\mu\nu}$ is the scalar curvature. In the FRW metric with $k = 0$ Christoffel symbols are all nil unless $\Gamma^{i}_{j0} = \Gamma^{i}_{0j} = H\delta^{i}_{j}$ e $\Gamma^{0}_{ij} = a\dot{a}\delta_{ij}$. So it is $R_{00} = -3(\dot{H} + H^2) = -3\frac{\ddot{a}}{a}$ and the trace is $R = -6\dot{H} - 12H^2 - 6ka^{-2} = -\frac{6}{a^2}(\dot{a}^2 + a\ddot{a} + k)$. Considering the $(0,0)$ component and the trace of the Einstein equation:

$$\begin{aligned} R_{00} - \frac{1}{2} g_{00} R &= 8\pi T_{00} \\ R &= -8\pi T \end{aligned}$$

using the first equation and the combination of the two, one finds the two Friedmann equations:

$$H^2 = \frac{8\pi}{3}\varrho - \frac{k}{a^2} \tag{1.6}$$

$$\frac{\ddot{a}}{a} = -\frac{4\pi}{3}(\varrho + 3p). \tag{1.7}$$

The two Friedmann equations plus the continuity equation 1.5 describe an expanding homogeneous and isotropic Universe. Nevertheless the two Friedmann equations and the continuity equation are not independent: deriving the first Friedmann equation 1.6 and putting it into the continuity equation 1.5 one finds the second Friedmann equation.

Once we have defined the critical density $\varrho_c = \frac{3H^2}{8\pi}$ and the density parameter $\Omega = \varrho/\varrho_c$, the first Friedmann equation becomes:

$$1 = \Omega - \frac{k}{a^2 H^2}$$

that shows how a Universe with $k = 0$ is characterized by a critical density so $\Omega = 1$. If it is $k = +1$ we will have $\Omega > 1$, while if it is $k = -1$ we will have $\Omega < 1$. After defining the curvature component $\Omega_k \equiv -\frac{k}{a^2H^2}$, we obtain the relation

$$1 = \Omega(a) + \Omega_k(a)$$

that holds at any time.

1.6.1 The relativistic component: radiation

A gas of photons with a distribution which follows the black body law has a pressure $p = \frac{1}{3}\varrho$. Using equation 1.5 we obtain $\dot{\varrho} = -4H\varrho$ and so

$$\varrho_r \sim a^{-4}$$

and using the redshift

$$\varrho_r = \varrho_c \Omega_r (1+z)^4.$$

The radiation density is diluted as a^{-3} because of the volume expansion and as a^{-1} because of the loss of energy due to expansion.

Integrating the Friedmann equation for a spatially flat Universe with a single component (the radiation), we find the behavior of the scale factor as a function of time [5]

$$a \sim t^{1/2}.$$

The energy density of a gas of radiation described by a black body spectrum is

$$\varrho_\gamma = \frac{g}{2\pi^2} \int \frac{E^3 dE}{e^{E/T} + 1} = \frac{g\pi^2}{30} T^4$$

where g are the relativistic particles degrees of freedom.

Since $\varrho_\gamma \sim a^{-4}$, the relation between the temperature and the scale factor is

$$T \sim \frac{1}{a}.$$

Since the present photon background temperature is $T_{CMB} = 2.725\text{K} \approx 10^{-13} GeV$ we obtain $\varrho_\gamma = g \cdot 2.5 \cdot 10^{-34} g/cm^3$.

From the two behavior of matter and radiation $\varrho_m = \varrho_{m,0} a^{-3}$ and $\varrho_r = \varrho_{r,0} a^{-4}$, we can define the equivalence epoch when $\varrho_r = \varrho_m$:

$$a_e = \frac{\varrho_{r,0}}{\varrho_{m,0}} = \frac{\Omega_r}{\Omega_m}.$$

Since $\Omega_r \approx 4.3 \cdot 10^{-5} h^{-2}$, the equivalence took place at redshift

$$1 + z_e = a_e^{-1} = (4.3 \cdot 10^{-5})^{-1} \Omega_m h^2 = 23000 \Omega_m h^2.$$

If $\Omega_m = 0.3$ and $h = 0.7$, we obtain $z_e \approx 3450$.

1.6.2 The non-relativistic component: matter

Matter can be considered as a fluid with nil pressure. Actually $p = nmv^2$ (v^2 mean square velocity of the particles) is much smaller than $\varrho = nmc^2$ in the non-relativistic case. From the continuity equation 1.5 we obtain $\dot{\varrho}/\varrho = -3\dot{a}/a$ or

$$\varrho_m \sim a^{-3} \text{ ,that means } \varrho_m = \varrho_0 \left(\frac{a_0}{a}\right)^3.$$

And using the redshift:

$$\varrho_m = \varrho_0 (1+z)^3 = \varrho_c \Omega_m (1+z)^3$$

where Ω_{matter} and ϱ_c are the present values.

In the case of a spatially flat Universe $k = 0$, the first Friedmann equation 1.6 calculated nowadays becomes $H_0^2 = \frac{8\pi}{3} \varrho_0$, so

$$\left(\frac{\dot{a}}{a}\right)^2 = \frac{8\pi}{3} \varrho_0 a_0^3 a^{-3} = H_0^2 a^{-3}$$

where in the last equality has been assumed $a_0 = 1$. After integrating, we obtain $\frac{2}{3}a^{3/2} = Ht$. The conclusion is that the behavior of the scale factor during the Matter Dominated Era (MDE) is

$$a \sim t^{2/3}.$$

Finally the present critical density $\varrho_{c,0} = \frac{3H_0^2}{8\pi G} \approx 2 * 10^{-29} h^2 g/cm^3$ turns out to be nearly equal to the measured matter density.

1.6.3 The cosmological constant

The present era should be considered dominated by a cosmological constant with $w = -1$, or $P = -\varrho$, so $\varrho_\Lambda = \text{const}$. If $\Omega_\Lambda > 0$ is dominating, the expansion is neverending and exponential

$$H^2 = H_0^2 \Omega_\Lambda, \text{ so } a(t) \sim \exp\left(H_0 \sqrt{\Omega_\Lambda} t\right).$$

Taking into account all these components the Friedmann equation becomes:

$$H^2 = \frac{8\pi}{3}\left(\varrho_m a^{-3} + \varrho_r a^{-4} + \varrho_k a^{-2} + \varrho_\Lambda\right)$$

and dividing by H_0^2

$$\left(\frac{H^2}{H_0^2}\right) = (\Omega_r a^{-4} + \Omega_m a^{-3} + \Omega_\Lambda + \Omega_k a^{-2}). \tag{1.8}$$

1.6.4 Other components

For any fluid with equation of state

$$p = w\varrho$$

the density as a function of the scale factor follows the law

$$\varrho \sim a^{-3(1+w)}.$$

In the case of a spatially flat Universe and if the fluid is the dominant component in the Friedmann equation the scale factor grows as

$$a \sim t^{\frac{2}{3(1+w)}}.$$

Any other component can be added to the Friedmann equation 1.8 with the proper dependence on the scale factor. So the most general manner to write the Friedmann equation is:

$$\dot{a}^2 = \frac{8\pi G}{3c^2} \sum_w \varrho_{w,0} a^{-1-3w} - \frac{kc^2}{R_0^2}.$$

1.7 Dark Matter

In the blue band the total luminosity density of the stars within a radius of 100 Mpc of our Galaxy is $j_{\star,B} = 1.2 \times 10^8 L_{Sun,B}\text{Mpc}^{-3}$. In order to convert the luminosity density in a mass density it is necessary to know the mass/luminosity ratio of the stars. Assuming a normal distribution of the type of stars around the Sun, we find $\langle M/L_B \rangle \approx 4 M_{Sun}/L_{Sun} \approx 170{\cdot}000\text{kg/watt}$. In this case the star mass density in the Universe is $\varrho_{\star,0} = \langle M/L_B \rangle j_{\star,B} \approx 5 \times 10^8 M_{Sun}\text{Mpc}^{-3}$. Since the present critical density is defined as $\varrho_{c,0} = 1.4 \times 10^{11} M_{Sun}\text{Mpc}^{-3}$, the density parameter of the stars nowadays is $\Omega_\star = \frac{\varrho_{\star,0}}{\varrho_{c,0}} \approx 0.004$. The contribution of the stars to the density $\Omega_m \approx 0.3$ necessary for a flat Universe is less than 0.5%. Adding black holes, interstellar medium gas, white dwarfs and brown dwarfs, we can calculate the present density parameter for baryons $\Omega_{baryons} = 0.04 \pm 0.01$. So the majority of baryonic matter is invisible. Nevertheless the deficit of matter remains. The consequence is that the majority of the matter is non-baryonic: dark matter (DM) neither absorbs or emits at any wavelength.

1.7.1 Dark Matter in galaxies

Dark matter can be revealed by observing its gravitational effects on visible matter, for example in the orbital velocity of stars in spiral galaxies as our Galaxy or M31. Stars lay on circular orbits around the center of the disk of spiral galaxies. Their velocity is given by the relation $v = \sqrt{\frac{GM(r)}{r}}$, where $M(r)$ is the mass within a radius r. The surface brightness of a spiral galaxy decreases exponentially with distance $I(r) = I_0 exp\left(-\frac{r}{R_S}\right)$ where the scale length R_S is a typically a few kpc (4kpc for our Galaxy, 6 kpc for M31). At distances of a few scale length the mass remains constant so the velocity should decrease as $v \propto 1/\sqrt{r}$. Instead it has been observed that the velocity of the stars in a spiral galaxy remains constant at large distances. This gives rise to the hypothesis of the existence of a dark matter halo that makes the galaxy density parameter reach the value $\Omega_{gal} \approx 0.16$.

1.7.2 Dark Matter in clusters

In 1930 Zwicky, studying the Coma cluster, discovered that the radial velocity dispersion was very high (about 1000 Km/s). Stars and gas were not enough massive to keep the galaxy together at that velocity. The cluster should have contained dark matter. Supposing cluster are Virial object

$$W + 2K = 0,\ K = -\frac{1}{2}W$$

the mass of the cluster can be calculated as

$$\frac{1}{2}M\left\langle v^2 \right\rangle = \frac{1}{2}\alpha\frac{GM^2}{r_h},\ M = \frac{\langle v^2 \rangle r_h}{\alpha G},$$

where r_h is the half mass radius and α is a numerical factor around one depending on the density profile of the cluster. The density parameter of the galaxy clusters is

$$\Omega_{cluster} \approx 0.2,$$

that represents a lower limit of the matter density in the Universe.

1.7.3 CDM vs HDM

The non baryonic Dark Matter can be divided in two categories, depending on the kinematic behavior. Hot Dark Matter (HDM) is made of particles that are still relativistic when they decoupled from the thermal bath. The strong velocity dispersion (free-streaming) of these particles cancels out the density perturbations of this fluid and affects the perturbation evolution and the growth of structures. Instead Cold Dark Matter (CDM) is made of particles that are no more relativistic at decoupling. The features of a Universe containing CDM are very different from the features of a Universe containing HDM. In a CDM Universe the formation of structures is hierarchical: first we have the smaller structures (galaxies) and then the bigger ones (clusters and superclusters) that are younger. On the contrary in a HDM Universe the older structures are the bigger ones, because the smaller perturbations were canceled out by free-streaming. The observations of our Universe reveal that the younger structures are superclusters. This indicates that the majority of the Dark Matter is CDM. This is the reason why the cosmological standard model is called Lambda Cold Dark Matter (ΛCDM) model, because it accounts for the cosmological constant (Lambda) and the Cold Dark Matter. Nevertheless precise measurements of galaxy distribution at large scales compared with the matter power spectrum suggest that a portion of the Universe Dark Matter content is made of HDM.

Chapter 2

Linear perturbation theory

2.1 Introduction

After photon baryon decoupling, matter perturbations grow because of the gravitational collapse and reach the non linear regime starting from the smaller scales. However the linear perturbation theory [6] is able to describe the primeval Universe at any scale and the present Universe at large scales. Moreover the majority of the cosmological observations concern linear perturbations, and the present cosmological neutrino mass bounds arise from these kind of observation. Linear theory takes advantage of the fact that each Fourier mode evolves through an independent equation. It must be stressed that the decomposition in Fourier modes must be performed respect to the comoving coordinates of the system: so the quantity $\frac{2\pi}{k}$ is the comoving wavelength of a perturbation with wave vector $\vec{k}$, while the physical wavelength is

$$\lambda = a(t)\frac{2\pi}{k}.$$

The conformal Friedmann-Robertson-Walker (FRW) metric is

$$ds^2 = a^2\left[d\tau^2 - dr^2 - r^2\left(d\theta^2 + \sin^2\theta d\phi^2\right)\right],$$

where the conformal time τ is related to the usual one through the relation

$$\frac{dt}{a(t)} = d\tau.$$

The conformal Hubble function is defined as

$$\mathcal{H} = \frac{1}{a}\frac{da}{d\tau}$$

which at the usual time is equal to aH.

During the radiation dominated era (RDE) $a(t) \sim t^{1/2}$from which

$$\mathcal{H}(t) = \frac{1}{a(t)}\frac{da(t)}{dt} \sim a(t)^{-2};$$

because $\tau \sim t^{1/2}$, so we get

$$a(\tau) \sim \tau \text{ e } \mathcal{H}(\tau) = \frac{1}{a(\tau)} \frac{da(\tau)}{d\tau} \sim \tau^{-1}.$$

During the matter dominated era (MDE) $a(t) \sim t^{2/3}$, so

$$\mathcal{H}(t) \sim a(t)^{-3/2};$$

because $\tau \sim t^{1/3}$, and we get

$$a(\tau) \sim \tau^2 \text{ e } \mathcal{H}(\tau) \sim 2\tau^{-1}.$$

The continuity equation for a generic component c is

$$\dot{\varrho}_c + 3\mathcal{H}\left(w_c + 1\right)\varrho_c = 0.$$

The non vanishing Christoffel symbols are $\Gamma^j_{0i} = \mathcal{H}\delta^j_i$ and $\Gamma^0_{ij} = \mathcal{H}\delta_{ij}$; the first (0,0) component of the Ricci tensor and the curvature obtained are $R_{00} = -3\dot{\mathcal{H}}$ and $R = -6a^{-2}\left(\dot{\mathcal{H}} + \mathcal{H}^2\right)$, respectively. So, in a matter-radiation Universe, the (0,0) component and the trace of the Einstein equation become

$$\mathcal{H}^2 = \frac{8\pi}{3} a^2 \left(\varrho_m + \varrho_\gamma\right),$$
$$\dot{\mathcal{H}} = -\frac{4\pi}{3} a^2 \left(\varrho_{tot} + 3p_{tot}\right),$$

that represent the two Friedmann equations.

2.2 The Newtonian Gauge

The most general perturbative metric can be written as $g_{\mu\nu} = g^{(0)}_{\mu\nu} + a^2 g^{(1)}_{\mu\nu}$, where

$$g^{(1)}_{\mu\nu} = \begin{pmatrix} 2\psi & w_i \\ w_i & 2\phi\delta_{ij} + h_{ij} \end{pmatrix}$$

where ψ, ϕ are spatial scalar quantities, w_i is a three component vector and h_{ij} is a tensor 3×3 with trace equal to zero.

If we write the perturbative metric as $g_{\alpha\beta} = g^{(0)}_{\alpha\beta} + h_{\alpha\beta}$, we can see that at the first order

$$h^{\mu\nu} = -h_{\alpha\beta} g^{(0)\alpha\mu} g^{(0)\beta\nu},$$

because of the condition $g_{\alpha\gamma} g^{\gamma\beta} = \delta^\beta_\alpha$.

It is straightforward to notice that

$$\nabla \cdot w^\perp = \nabla \times w^\parallel = 0,$$

because the vector w_i can be decomposed in a longitudinal component and a transverse component $w = w^\parallel + w^\perp$. The longitudinal component can be written as the gradient of a scalar function $w^\parallel = \nabla w_s$ because is irrotational. When we

derive the $0i$ components of the Einstein equations we find both longitudinal and transverse terms on G_{0i} and T_{0i}. The curl of these equations selects only transverse terms, while the divergence only longitudinal terms. So the two components are completely decoupled and can be treated separately. Since the density perturbations δ are scalar quantities, only the longitudinal terms, that can be related to scalar quantities, are coupled to the density perturbations. Vectorial terms merge with curl modes, while tensors represent gravitational waves, that couple to matter only for anisotropic perturbations. Moreover, if at the beginning curl modes (vortices) are zero, they will remain zero. Instead, if they are different from zero at the beginning, they will decay as a^{-1}.

The tensor h_{ij} can be written as the sum of three terms with a null trace

$$h_{ij} = h_{ij}^{\parallel} + h_{ij}^{\perp} + h_{ij}^{T},$$

where the divergences $\partial^i h_{ij}^{\parallel}$, $\partial^i h_{ij}^{\perp}$ are longitudinal and transverse, respectively, and h_{ij}^{T} is transverse, so

$$\epsilon_{ijk}\partial_i\partial_k h_{ij}^{\parallel} = 0,\ \partial_i\partial_j h_{ij}^{\perp} = 0,\ \partial_i h_{ij}^{T} = 0.$$

Since $\partial_i h_{ij}^{\parallel}$ is irrotational, $h_{ij}^{\parallel}$ can be written as a scalar function B

$$h_{ij}^{\parallel} = \left(\partial_i\partial_j - \frac{1}{3}\delta_{ij}\nabla^2\right) B.$$

Instead the perturbations $h_{ij}^{\perp}$, h_{ij}^{T} cannot be derived from a scalar function; the first is a vector and the second is a tensor; they cause rotational velocity perturbations and gravitational waves and they are perfectly decoupled from the scalar term.

In conclusion, we have to take into account only the components of w_i and h_{ij} that can be derived from scalar quantities. That's why we build a vector $\vec{E}$ and a tensor $D_{ij}B \equiv B_{ij} - \frac{1}{3}\delta_{ij}B^{,k}_{,k}$ with a zero trace, from two scalar quantities E and B. So we obtain

$$g_{\mu\nu}^{(1)} = \begin{pmatrix} 2\psi & E_{,i} \\ E_{,i} & 2\phi\delta_{ij} + D_{ij}B \end{pmatrix}.$$

Now we can choose a Gauge we are interested to work in. The Newtonian (or longitudinal) Gauge implies four conditions on the perturbative metric that correspond to the four possible coordinate transformations: $w_i = 0$ (from which $E = 0$) and $B = 0$. The result is

$$ds^2 = a^2\left[(1+2\psi)\,d\tau^2 - (1-2\phi)\,dx^i dx_i\right].$$

This choice benefits of the fact that the metric tensor $g_{\mu\nu}$ is diagonal. Moreover ψ represents the gravitational potential so it has a clear physical meaning. The two scalar potentials ψ and ϕ are different only when the impulse-energy tensor T^{μ}_{ν} contains longitudinal components.

2.3 The perturbation equations

The perturbative quantities are

$$\delta = \frac{\delta\varrho}{\varrho}, \text{ where } \frac{\delta\varrho}{\varrho} \equiv \frac{\varrho(x) - \bar{\varrho}}{\bar{\varrho}}$$

and

$$\nabla^i v_i = \theta$$

where δ is the density perturbation and θ is the velocity divergence, there exists a couple of δ and θ for each fluid that the Universe is made up of. Now we focus on a model with only one fluid, it means on an Universe made with only one component. The equations that must be perturbed are

$$T^{\mu}_{\nu;\mu} = 0$$

and

$$G_{\mu\nu} \equiv R_{\mu\nu} - \frac{1}{2} g_{\mu\nu} R = 8\pi T_{\mu\nu}, \text{ (assuming } G = 1).$$

The perturbed impulse-energy tensor for a component with equation of state $p = w\varrho$ where w is a constant is

$$\delta T_{\mu\nu}(\vec{x}, t) = T_{\mu\nu}(\vec{x}, t) - \bar{T}_{\mu\nu}(t)$$

So the perturbed components are

$$\begin{aligned}
&\delta T^0_0 = \delta\varrho \\
&\delta T^1_1 = \delta T^2_2 = \delta T^3_3 = -c_s^2 \delta\varrho \\
&\delta T^i_0 = -\delta T^0_i = (1 + w)\, \varrho v^i,
\end{aligned}$$

where the sound speed is $c_s^2 = \frac{dp}{d\varrho}$.

The perturbed non-zero Christoffel symbols are

$$\begin{aligned}
&\delta\Gamma^0_{ij} = -\delta_{ij} \left[2\mathcal{H} (\phi + \psi) + \dot{\phi} \right] \\
&\delta\Gamma^0_{00} = \dot{\psi} \\
&\delta\Gamma^0_{0i} = \delta\Gamma^i_{00} = \psi_{,i} \\
&\delta\Gamma^i_{j0} = -\delta^i_j \dot{\phi}.
\end{aligned}$$

The covariant derivative of a tensor T^{μ}_{ν} is $T^{\mu}_{\nu;\mu} = T^{\mu}_{\nu,\mu} - \Gamma^{\alpha}_{\nu\beta} T^{\beta}_{\alpha} + \Gamma^{\alpha}_{\beta\alpha} T^{\beta}_{\nu}$, so the equation $T^{\mu}_{\nu;\mu} = 0$ perturbed for the component $\nu = 0$ and with $w = 0$ and $c_s^2 = 0$ becomes

$$\delta T^{\mu}_{0,\mu} - \delta\Gamma^{\alpha}_{0\beta} T^{\beta}_{\alpha} - \Gamma^{\alpha}_{0\beta} \delta T^{\beta}_{\alpha} + \delta\Gamma^{\alpha}_{0\alpha} T^0_0 + \Gamma^{\alpha}_{\beta\alpha} \delta T^{\beta}_0 = 0,$$

where

$$\begin{aligned}
&\delta T^{\mu}_{0,\mu} = \left(\dot{\delta\varrho}\right) + \varrho v_{,i} \\
&\delta\Gamma^{\alpha}_{0\beta} T^{\beta}_{\alpha} = \varrho\delta\Gamma^{0}_{00} = \varrho\dot{\psi} \\
&\Gamma^{\alpha}_{0\beta}\delta T^{\beta}_{\alpha} = \mathcal{H}\delta\varrho \\
&\delta\Gamma^{\alpha}_{0\alpha} T^{0}_{0} = \varrho\left(\delta\Gamma^{0}_{00} + \delta\Gamma^{i}_{i0}\right) = \varrho\left(\dot{\psi} - 3\dot{\phi}\right) \\
&\Gamma^{\alpha}_{\beta\alpha}\delta T^{\beta}_{0} = 4\mathcal{H}\delta\varrho,
\end{aligned}$$

so

$$\begin{aligned}
\left(\dot{\delta\varrho}\right) + \varrho v^{i}_{,i} - \varrho\dot{\psi} - \mathcal{H}\delta\varrho + \varrho\left(\dot{\psi} - 3\dot{\phi}\right) + 4\mathcal{H}\delta\varrho = 0 \Rightarrow \\
\left(\dot{\delta\varrho}\right) + \varrho\theta - 3\varrho\dot{\phi} + 3\mathcal{H}\delta\varrho = 0 \Rightarrow \\
\frac{\left(\dot{\delta\varrho}\right)}{\varrho} + 3\mathcal{H}\frac{\delta\varrho}{\varrho} = -\theta + 3\dot{\phi}.
\end{aligned}$$

After defining the density contrast $\delta = \delta\varrho/\varrho$ and using the non perturbative conservation equation $\dot{\varrho} + 3\mathcal{H}\varrho = 0$, we derive the relation $\left(\dot{\delta\varrho}\right) = \varrho\dot{\delta} + \delta\dot{\varrho}$ and we obtain the equation

$$\dot{\delta} = -\theta + 3\dot{\phi} \tag{2.1}$$

that is the perturbed continuity equation.

The perturbed equation $T^{\mu}_{\nu;\mu} = 0$ in the case of $\nu = i$ and with $c_s^2 \neq 0$ and $w = 0$ is

$$\dot{v}_i = -\mathcal{H}v_i - a^2\nabla_i\psi - a^2\nabla_i c_s^2\delta$$

and the divergence of this equation represents the Euler equation

$$\dot{\theta} = -\mathcal{H}\theta - a^2\nabla^2\psi - a^2\nabla^2 c_s^2\delta. \tag{2.2}$$

In the Fourier space it is assumed that the perturbed variables are the sum of plane waves $\exp^{ikr}$:

$$\phi = \int e^{ikr}\phi_k d^3k, \qquad \psi = \int e^{ikr}\psi_k d^3k$$

and

$$\delta = \int e^{ikr}\delta_k d^3k, \qquad \theta = \int e^{ikr}\theta_k d^3k$$

where $kr \equiv \vec{k}\cdot\vec{r}$ (in what follows the k index will be omitted). In the linear theory, the equations remain the same for each wave, but have a different k. Each perturbed quantity and its derivatives can be written as follows

$$\begin{aligned}
&\phi(x,\tau) \to e^{ikr}\phi_k(\tau) \\
&\nabla\phi(x,\tau) \to i\mathbf{k}e^{ikr}\phi_k(\tau) \\
&\nabla^2\phi(x,\tau) \equiv -g^{ij}\nabla_i\nabla_j\phi(x,\tau) \to -\left(\frac{k}{a}\right)^2 e^{ikr}\phi_k(\tau).
\end{aligned}$$

For example, the Euler equation 2.2 in the case of $w = 0$ becomes

$$\dot{\theta} = -\mathcal{H}\theta + k^2\psi + k^2 c_s^2 \delta.$$

In the same way we find the perturbed Einstein equations:

$$\begin{aligned}
\delta G_0^0 &= 2a^{-2}\left\{-3\left(\frac{\dot{a}}{a}\right)^2\psi - 3\frac{\dot{a}}{a}\dot{\phi} + \nabla^2\phi\right\} = 8\pi\delta\varrho \\
\delta G_i^0 &= 2a^{-2}\partial_i\left\{\frac{\dot{a}}{a}\psi + \dot{\phi}\right\} = 8\pi\left(\bar{\varrho} + \bar{p}\right)v_i \\
\delta G_j^i &= -2a^{-2}\left\{\left[\left(2\frac{\ddot{a}}{a} - \left(\frac{\dot{a}}{a}\right)^2\right)\psi + \frac{\dot{a}}{a}\left(\dot{\psi} + 2\dot{\phi}\right) + \ddot{\phi} + \frac{1}{3}\nabla^2\left(\psi - \phi\right)\right]\delta_j^i + \right. \\
&\quad \left. -\frac{1}{2}\left(\partial^i\partial_j - \frac{1}{3}\nabla^2\delta_j^i\right)\left(\psi - \phi\right)\right\} \\
&\quad = 8\pi\left(-\delta p\delta_j^i + \Sigma_j^i\right)
\end{aligned}$$

where $\Sigma_j^i \equiv T_j^i - \delta_j^i T/3$ ($\Sigma_i^i = 0$) is the anisotropic perturbation tensor, and, before recombination, when photon and baryon are coupled in a single fluid, the dominant contribution to Σ_j^i comes from neutrinos.

Using the variables $\delta \equiv \delta\varrho/\varrho$, θ the Einstein equations in the Fourier space become:

$$\begin{aligned}
-3\left(\frac{\dot{a}}{a}\right)^2\psi - 3\frac{\dot{a}}{a}\dot{\phi} - k^2\phi &= 4\pi a^2\varrho\delta \\
k^2\left(\frac{\dot{a}}{a}\psi + \dot{\phi}\right) &= 4\pi a^2\left(\varrho + p\right)\theta \\
\left(2\frac{\ddot{a}}{a} - \left(\frac{\dot{a}}{a}\right)^2\right)\psi + \frac{\dot{a}}{a}\left(\dot{\psi} + 2\dot{\phi}\right) + \ddot{\phi} - \frac{k^2}{3}(\psi - \phi) &= 4\pi a^2\delta p \\
k^2(\varphi - \psi) &= 12\pi a^2(\varrho + p)\sigma
\end{aligned}$$

where σ is given by $(\varrho + p)\sigma \equiv -\left(\hat{k}_i\hat{k}_j - \frac{1}{3}\delta_{ij}\right)\Sigma_j^i$. So we obtain the set of linear perturbation equations for a single perfect (it means $\Sigma_j^i = 0$, so $\phi = \psi$) decoupled fluid, with equation of state $p = w\varrho$ (in terms of $\mathcal{H}$)

$$\begin{aligned}
&\dot{\delta} = -(w+1)(\theta - 3\dot{\phi}) + 3\mathcal{H}(w - c_s^2)\delta \\
&\dot{\theta} = \mathcal{H}\theta(3w - 1) + k^2\left(\frac{c_s^2}{1+w}\delta + \psi\right) \\
&k^2\left(\dot{\phi} + \mathcal{H}\psi\right) = 4\pi(w+1)a^2\theta\varrho \\
&k^2\phi + 3\mathcal{H}\left(\dot{\phi} + 3\mathcal{H}\psi\right) = -4\pi a^2\varrho\delta.
\end{aligned} \tag{2.3}$$

2.4 Scales greater than the horizon

In the limit $k \ll \mathcal{H}$ (scales greater than the horizon) the set of equations of perturbations when $w = c_s^2$ (that is true both for radiation and matter) becomes

$$\begin{aligned}
&\dot{\delta} = -(w+1)\left(\theta - 3\dot{\psi}\right) \\
&\dot{\theta} = \mathcal{H}\theta(3w-1) \\
&3\mathcal{H}\left(\dot{\psi} + \mathcal{H}\psi\right) = -4\pi a^2 \varrho\delta.
\end{aligned}$$

A solution of this system is $\dot{\psi} = 0$ because, assuming $\dot{\psi} = 0$ and deriving the first equation, we get

$$\ddot{\delta} = \mathcal{H}\dot{\delta}(3w-1)$$

that gives $\delta = \text{const}$. Concerning the third equation we have $3\mathcal{H}^2\psi = -4\pi a^2\varrho\delta$ and, using the Friedmann equation, we find

$$\delta = -2\psi.$$

So $\delta = \text{const}$ implies $\psi = \text{const}$. In conclusion, the gravitational potential remains constant at scales greater than the horizon.

2.5 The Jeans length

In a spatially flat Universe a physical process that begins at t_i and propagates at speed v along a radial geodesic ($vdt = a(t)dx$) can affect only the wavelength smaller than the causal horizon that is defined as $d(t_i, t) = a(t)\int_{t_i}^{t} dx = a(t)\int_{t_i}^{t} \frac{vdt'}{a(t')}$. This horizon represents the maximum physical distance on which the signal can propagate between t_i and t.

Before decoupling the sound perturbations propagate with a peculiar velocity c_s^2 that defines a peculiar length $d_s(t_i, t)$, called sound horizon. If the sound speed is constant and if both t_i and t are within the same era (RDE or MDE) the sound horizon is proportional (unless a factor of about unity) to c_s/H, that is called Jeans length. More precisely the Jeans length and wavenumber are:

$$\begin{aligned}
k_J(t) &= \left(\frac{4\pi G\bar{\varrho}(t)a^2(t)}{c_s^2(t)}\right)^{1/2}, \\
\lambda_J(t) &= 2\pi\frac{a(t)}{k_J(t)} = 2\pi\sqrt{\frac{2}{3}}\frac{c_s^2}{H(t)}.
\end{aligned}$$

In order to understand the meaning of the numerical factors, we should look at the perturbation equations in the Newtonian limit at small scales $k \gg \mathcal{H}$. In the case of a perfect fluid with a null pressure and a sound speed much smaller than the speed of light (because of the Newtonian limit) equation 2.3 is the Fourier transform of the Poisson equation

$$k^2\phi = -4\pi a^2\varrho\delta = -\frac{3}{2}\mathcal{H}^2\delta, \tag{2.4}$$

where the unperturbed Friedmann equation has been used. By using this in the equation 2.1 we get

$$\dot{\delta} = -\theta - \frac{9}{2}\frac{\mathcal{H}^2}{k^2}\delta\left(2\frac{\dot{\mathcal{H}}}{\mathcal{H}} + \frac{\dot{\delta}}{\delta}\right) \simeq -\theta.$$

So in the Newtonian limit the set of perturbed equations becomes

$$\begin{aligned}
\dot{\delta} &= -\theta \\
\dot{\theta} &= -\mathcal{H}\theta + c_s^2 k^2 \delta + k^2\phi \\
k^2\phi &= -\frac{3}{2}\mathcal{H}^2\delta.
\end{aligned}$$

Deriving the first equation we find

$$\ddot{\delta} + \mathcal{H}\dot{\delta} + \left(k^2 c_s^2 - \frac{3}{2}\mathcal{H}^2\right)\delta = 0, \tag{2.5}$$

which in the Minkowskian limit ($H = 0$) this equation represents the wave equation of a fluid: $\ddot{\delta} + c_s^2\nabla^2\delta = 0$. This implies that c_s is really the sound speed. It is evident that the perturbations do not grow up if $k^2 c_s^2 - \frac{3}{2}\mathcal{H}^2 > 0$, it means if the physical scale of the perturbation $\lambda = 2\pi a/k$ is smaller than the Jeans length,

$$\lambda_J = c_s\sqrt{\frac{\pi}{\varrho}},. \tag{2.6}$$

The last expression is the same of the definition of the Jeans length if we consider $\frac{3}{2}\mathcal{H}^2 = 4\pi a^2\varrho$ from the Friedmann equation and $\mathcal{H} = aH$. In conclusion, the perturbation oscillations are dumped on scales smaller than λ_J. Physically speaking, in a sound speed fluid the modes with $k > k_J$ are expected to oscillate with an angular frequency $\omega = kc_s$ due to the presence of both gas pressure and gravitational compression; these modes are Jeans unstable. Instead for the modes with $k < k_J$, the pressure cannot compensate the gravitational compression and so the density perturbations can grow monotonically. These Jeans instability explains some fundamental aspects of the inhomogeneous Universe: before recombination the photon-baryon fluid has a sound speed $c_s \simeq c/\sqrt{3}$ and oscillates on scales smaller than λ_J, after recombination, c_s and λ_J become negligible, k_J grows to infinity and the structure appear.

Mathematically speaking,

$$c_s = \left(\frac{dp}{d\varrho}\right)^{1/2} = w^{1/2} \text{ assuming } c = 1.$$

For photons $c_s = 1/\sqrt{3}$, so $\lambda_J \simeq \mathcal{H}^{-1}/a$, and the perturbation growth is forbidden on all scales smaller than the horizon. Before decoupling, baryon have nearly the same speed as photons, so baryonic perturbations are dumped. After decoupling, baryonic perturbations grow rapidly, because baryon are free to fall into the potential wells of the dark matter.

2.6 The evolution of the perturbations

The gravitational instability consist on the fact that for $k \gg \mathcal{H}$ perturbations can grow freely. So in the Newtonian limit the equation of the evolution of the perturbations (2.5) can be written as

$$\ddot{\delta} + \mathcal{H}\dot{\delta} - \frac{3}{2}\mathcal{H}^2\delta = 0.$$

Using the variable $\alpha \equiv \log a$ we find

$$\delta'' + \left(\frac{\mathcal{H}'}{\mathcal{H}} + 1\right)\delta' - \frac{3}{2}\delta = 0, \tag{2.7}$$

where $'$ indicates the derivative respect to α.

Dividing the first Friedmann equation by the second for a Universe with more than one component we get $\frac{\dot{\mathcal{H}}}{\mathcal{H}^2} = -\frac{1}{2}\sum_w(1+3w)$. So for a single fluid with parameter w it is

$$\frac{\mathcal{H}'}{\mathcal{H}} = -\frac{1}{2} - \frac{3}{2}w.$$

Using the last expression the equation 2.7 for matter ($w = 0$) becomes

$$\delta'' + \frac{1}{2}\delta' - \frac{3}{2}\delta = 0$$

that is a linear homogeneous differential equation at the second order with constant coefficients and the solutions are linear combinations of $\delta = Ae^{m\alpha} = Aa^m$ with $m_\pm = 1,\ -3/2$. So the growth and the dumping are given by

$$\delta_+ = Aa^1, \qquad \delta_- = Ba^{-3/2},$$

respectively. The second solution becomes more and more negligible respect to the first one and so can be omitted. In the conformal time we have $\delta_+ \sim \tau^2$ and $\mathcal{H} \sim 2\tau^{-1}$ during the MDE, so $\mathcal{H}^2\delta_+ = A\tau^2\frac{2}{\tau^2} = \text{const}$. From the last equation and using the Poisson equation $k^2\phi = -\frac{3}{2}\mathcal{H}^2\delta$, it results

$$\phi = \text{const},$$

that means the gravitational potential is constant during the MDE.

2.7 Two components solution: matter and radiation

The solution we have just obtained is true for matter perturbations during the MDE. In the RDE we need to add one more fluid. If the perturbations of matter δ_m, θ_m and radiation δ_γ, θ_γ are put into the set of equations of perturbations, we will have

two pairs of conservation equations plus the Einstein equation with two components:

$$\begin{aligned}
\dot{\delta}_m &= -\left(\theta_m - 3\dot{\phi}\right) \\
\dot{\theta}_m &= -\mathcal{H}\theta_m + k^2\psi \\
\dot{\delta}_\gamma &= -\left(\theta_\gamma - 3\dot{\phi}\right) \\
\dot{\theta}_\gamma &= k^2\left(\frac{3c_s^2}{4}\delta_\gamma + \psi\right) \\
k^2\left(\dot{\phi} + \mathcal{H}\psi\right) &= 4\pi(1+w)a^2\theta_{tot}\varrho_{tot} \\
k^2\phi + 3\mathcal{H}\left(\dot{\phi} + \mathcal{H}\psi\right) &= -4\pi a^2\varrho_{tot}\delta_{tot}
\end{aligned}$$

where $\varrho_{tot} = \varrho_m + \varrho_\gamma$ and $\varrho_{tot}\delta_{tot} = (\delta\varrho_{tot}) = \varrho_m\delta_m + \varrho_\gamma\delta_\gamma$. In the newtonian limit we will have

$$\begin{aligned}
\dot{\delta}_m &= -\left(\theta_m - 3\dot{\phi}\right) \\
\dot{\theta}_m &= -\mathcal{H}\theta_m + k^2\psi \\
\dot{\delta}_\gamma &= -\left(\theta_\gamma - 3\dot{\phi}\right) \\
\dot{\theta}_\gamma &= k^2\left(\frac{1}{4}\delta_\gamma + \psi\right) \ (c_s^2 = 1/3 \text{ for the radiation component}) \\
k^2\phi &= -4\pi a^2\left(\varrho_m\delta_m + \varrho_\gamma\delta_\gamma\right) = -\frac{3}{2}\mathcal{H}^2\left(\Omega_m\varrho_m + \Omega_\gamma\varrho_\gamma\right).
\end{aligned}$$

After deriving the equations respect to $\dot{\delta}$ we can calculate two coupled equations

$$\ddot{\delta}_m + \mathcal{H}\dot{\delta}_m - \frac{3}{2}\mathcal{H}^2\left(\Omega_m\delta_m + \Omega_\gamma\delta_\gamma\right) = 0 \tag{2.8}$$

$$\ddot{\delta}_\gamma + \frac{1}{4}k^2\delta_\gamma = 0. \tag{2.9}$$

In the RDE $\Omega_m \approx 0$ and $\Omega_\gamma \approx 1$, moreover, the second equation shows that radiation oscillates rapidly around zero, because it is on scales smaller than the horizon $k > \mathcal{H}$. Until photons and baryons are merged, they can be considered as a single fluid with perturbation δ_γ. The oscillations of this fluid cause the acoustic effect on the cosmic microwave background. After averaging on the oscillations, and putting $\langle\delta_\gamma\rangle \approx 0$, we get $\Omega_m\delta_m + \Omega_\gamma\delta_\gamma \approx 0$, and so

$$\ddot{\delta}_m + \mathcal{H}\dot{\delta}_m = 0$$

that is a differential equation. The solution is $\delta_m = \text{const}$ or $\delta_m \sim \tau^{-1}$. In conclusion the matter perturbations can't grow if they cross the horizon during the RDE.

2.8 The present era of the cosmological constant

From recent cosmological data we know that after the MDE has been settled down an epoch characterized by a cosmological constant Λ as the dominant component

of the energy of the Universe. The equation of state of this cosmological constant is $w = -1$, it means $p_\Lambda = -\varrho_\Lambda$. The equation 2.8 can be generalized in the case of matter and cosmological constant:

$$\ddot{\delta}_m + \mathcal{H}\dot{\delta}_m - \frac{3}{2}\mathcal{H}^2 \left(\Omega_m \delta_m + \Omega_\Lambda \delta_\Lambda\right) = 0.$$

Assuming $\Omega_m = \text{const}$ and using $\alpha \equiv \log a$, the general solution becomes

$$m_\pm = \frac{1}{4}\left(-1 \pm \sqrt{1 + 24\Omega_m}\right),$$

so

$$\delta_m = A a^{m_\pm}.$$

The last formula shows how the cosmological constant slows down the growth of the perturbations: as $\Omega_m \to 0$, $m \to 0$. The numerical solution is

$$m = \Omega_m^{+0.6}.$$

It must be stressed that in presence of a cosmological constant it is not true that $\mathcal{H}^2\delta_+$ is constant, so the gravitational potential is no more constant, but it decreases proportionally to a scale independent damping factor $g(\tau) = \psi(\tau)/\psi(\tau_m)$, where τ_m is during the MDE. On scales within the Hubble radius during the MDE and the ΛDE the Poisson equation 2.4 is used to derive the following relationship between the matter perturbations and the gravitational potential fluctuations

$$\delta_m = -\frac{k^2\psi}{4\pi a^2 \varrho_m}.$$

So δ_m is proportional to ψ, and this explains why the gravitational potential decrease reduces the growth of matter perturbations.

2.9 The Cosmic Microwave Background

After the Big Bang, as the temperature of the Universe decreases, the different species of particles decouple from the thermal equilibrium because their interaction rate drops down the Hubble parameter H, so their mean free path becomes greater than the horizon scale (or Hubble distance) c/H. This process causes firstly the neutrino decoupling at $z \approx 10^{11}$, then the formation of the light atomic nuclei at $z \approx 10^8$, and finally the baryon decoupling at $z \approx 10^3$. In the primordial highly ionized Universe, matter and radiation are merged in a single fluid and they interact through Thomson scattering $\gamma + e^- \to \gamma + e^-$ with $\sigma \approx 6.65 \cdot 10^{-29}\text{m}^2$ and the rate is $\Gamma = \frac{c}{\lambda} = \sigma n_e c$, where n_e is the numerical density of electrons. The characteristic time associated with this interaction is $\tau = 1/\Gamma$. Since $n_e \sim a^{-3}$, $\tau \sim a^3$, and because of the equilibrium between matter and radiation, τ must be smaller than the expansion rate H^{-1}. This condition is satisfied during the RDE when $1/H = 2t$, while $\tau \sim t^{3/2}$. After the equivalence, at redshift 3450, during the MDE $a \sim t^{2/3}$ and $1/H = 3t/2$, while $\tau \sim t^2$; so decoupling takes place at $z \approx 1100$ (about 350000 years after the Big Bang, when the temperature of the Universe is about 3000 K).

Photons that undergo the last scattering at $z = 1100$ (Last Scattering Surface, LSS) form the cosmic background radiation. This radiation at different epochs is well represented by a black body spectrum at different temperatures $I = \frac{2h\nu^3}{e^{\frac{h\nu}{kT}}-1}$. Nowadays it is $T_{0,\gamma CMB} = 2.725 \pm 0.001$K, so, since $\varrho_\gamma = \sigma T^4 \sim \frac{1}{a^4}$, $\Omega_r \approx 4.3 \cdot 10^{-5}$. Each cm^3 of the Universe is filled with 411 CMB photons, the mean energy of each one is $E_{mean} = 6.34 \cdot 10^{-4}$eV, it corresponds to a wavelength of about 2 mm in the microwave region.

Half of this black body is slightly redshifted to lower temperature, while the other part is slightly blueshifted at higher temperature. This effect is called dipole distortion and is a typical Doppler effect due to the motion of the satellite respect to the reference framework where the CMB is isotropic. After the subtraction of the motion of the satellite around the Earth, of the Earth around the Sun ($v \approx 30$km/s), of the Sun around the Galactic Center ($v \approx 220$km/s), and of the Galaxy around the center of mass of the Local Group ($v \approx 80$km/s), it will be found that moves in the direction of the Hydra Constellation with a velocity $v_{LG} = 630 \pm 20\text{km/s} = 0.0021c$.

After the dipole distortion subtraction from the CMB spectrum, it remains the temperature fluctuations

$$\left\langle \left(\frac{\delta T}{T}\right)^2 \right\rangle^{1/2} = 1.1 \cdot 10^{-5}$$

where the average is on alla the possible directions. These fluctuations are very small ($\Delta T \approx 30\mu$K, with $T \approx 3$K), nevertheless they are very important in determining the cosmological parameters. These anisotropies represent a picture of the distribution of matter when the baryons decoupled from photons and recombined themselves with electrons to build the neutral hydrogen, at redshift 1100 and at temperature 3000K.

In what follows we will assume an instantaneous decoupling, but this is not completely true, the LSS is not exactly a surface but a shell. If decoupling starts at τ_D and ends at τ_{LS}, during $\Delta\tau$ the radiation free streams on scale $\lambda_D = (\lambda\Delta\tau)^{1/2}$ where λ is the photon mean free path and λ_D turns out to be shorter than the thickness of the LSS. As a consequence all the fluctuations on scales smaller than λ_D are dumped (Silk-Damping), because there photons can spread freely both from overdensities and from underdensities. This effect becomes more and more efficient as it approaches the last scattering instant.

2.9.1 Primary anisotropies

The temperature variation along the line of sight $\hat{n}$ is

$$\frac{\Delta T}{T}(\hat{n}) = \int_0^\infty \left\{ \left[g(z) \left(\left(\frac{\Delta T}{T}\right)_g + \left(\frac{\Delta T}{T}\right)_a + \vec{v}\cdot\hat{n} \right) \right] + e^{-\tau} H^{-1} \dot{\psi} \right\} dz$$

where $g(z) = e^{-\tau} \frac{\sigma_T n_e x_i}{1+z}$ (with $x_i = \frac{n_p}{n_p+n_H}$ ionization fraction, and $n_e x_i$ free electron density) is the visibility function, that can be approximated as a Kronecker delta at

the time of recombination $g(z) \simeq \delta(z - z_{rec})$. In this case it becomes

$$\frac{\Delta T}{T}(\hat{n}) = \left[\left(\frac{\Delta T}{T}\right)_g (z_{rec}) + \left(\frac{\Delta T}{T}\right)_a (z_{rec}) + (\vec{v}\cdot\hat{n})\,(z_{rec})\right] + \int_0^\infty e^{-\tau} H^{-1}\dot{\psi} dz$$

where the first term represents the gravitational effect, the second the adiabatic effect and the third the Doppler effect. These three effects give raise to the primary anisotropies, that were produced at the time of recombination and so are multiplied by the visibility function. The last term is the Integrated Sachs-Wolfe (ISW) effect that gives rise to the secondary anisotropies produced afterwards along the line of sight.

The Doppler effect

The Doppler effect is due to the bulk motion (peculiar velocity) during decoupling (Sunyaev & Zel'dovich 1970).

The gravitational effect

A photon emitted inside a density fluctuation must climb a gravitational potential well. The perturbative metric for a point $dr = d\theta = d\phi = 0$ is

$$ds^2 = a^2(1 + 2\psi)d\tau^2 \equiv a'^2 d\tau^2$$

where $a' \equiv a(1 + \psi)$ at the first order. Using the relation between the redshift and the scale factor $1 + z' = a'^{-1}$, we find

$$\frac{dz}{z} = -\frac{da}{a} = -\psi,$$

so the photons emitted in a gravitational potential well ψ are redshifted of a quantity $-\psi$ (where ψ is a negative quantity for an overdensity). As a consequence in Fourier space the temperature drops down of a factor

$$\frac{\Delta T_k}{T} = \psi_k.$$

The physical meaning is that an overdensity produces a potential well and photons lose energy to climb it, so they are redshifted and the region appears colder.

The adiabatic effect

The adiabatic effect is so defined because it implies initial adiabatic conditions, that means that radiation and matter perturbations are equal in each point. For a baryon-photon fluid $\varrho_{tot} = \varrho_\gamma + \varrho_b$ with $\varrho_\gamma \sim a^{-4}$ e $\varrho_b \sim a^{-3}$, so

$$\delta\varrho_\gamma \sim -4a^{-5}da = -4\varrho_\gamma\frac{da}{a} \qquad \text{and} \qquad \delta\varrho_b \sim -3a^{-4}da = -3\varrho_b\frac{da}{a},$$

and the adiabatic condition turns out to be

$$\delta_b \equiv \frac{\delta\varrho_b}{\varrho_b} = \frac{3}{4}\frac{\delta\varrho_\gamma}{\varrho_\gamma} \equiv \frac{3}{4}\delta_\gamma \Rightarrow \delta_b = \frac{3}{4}\delta_\gamma.$$

So the ratio number of baryons/number of photons is constant, this means $\delta(n_\gamma/n_b) = 0$, because $n_\gamma \sim \varrho_\gamma^{3/4}$ and $n_b \sim \varrho_b$. Finally the adiabatic condition implies that the entropy per particle is constant because it is proportional to the number of photons.

Concerning the temperature fluctuations, since $\varrho_\gamma \sim T^4$, it comes up

$$\frac{\Delta T}{T} = \frac{1}{4}\delta_\gamma = \frac{1}{3}\delta_m.$$

At large scales δ_m and ψ are nearly constant and bounded together by the relation 2.4 $\delta_m = -2\psi$. So it is

$$\frac{\Delta T}{T} = -\frac{2}{3}\psi.$$

The physical meaning is that photons from an overdensity are blueshifted and the region appears hotter.

We can now examine how this effect can determine the CMB temperature fluctuations. The Euler and the continuity equations can be used to derive the relation between the temperature fluctuations and the gravitational potentials for each k mode:

$$\frac{d}{d\tau}\left[(1+R)\,\dot{\Theta}\right] + \frac{k^2}{3}\Theta = -\frac{k^2}{3}(1+R)\psi + \frac{d}{d\tau}\left[(1+R)\,\dot{\phi}\right], \tag{2.10}$$

where the variable Θ is defined as

$$\Theta(\vec{x},t) \equiv \frac{\Delta T}{T}(\vec{x},t) = \frac{1}{3}\delta_m,$$

and $R = 3\varrho_b/4\varrho_\gamma$. The solution of this equation depends on the epoch, because the potentials evolve differently in different epochs. In the MDE the potential is constant and assuming R constant the previous equation becomes

$$(1+R)\ddot{\Theta} + \frac{k^2}{3}\Theta = -\frac{k^2}{3}(1+R)\psi, \tag{2.11}$$

the term on the right is constant, so, using the function $g(\tau) \equiv k^2\Theta/3 + k^2(1+R)\psi/3$, this equation can be written as

$$\ddot{g} + \frac{k^2}{3(1+R)}g = 0$$

that is the equation of a harmonic oscillator. The solution is

$$\Theta(\tau) = -(1+R)\psi + C_1\cos(kc_s\tau) + C_2\sin(kc_s\tau)$$

where C_1 and C_2 depending on the initial conditions and $c_s = [3(1+R)]^{-1/2}$ is the sound speed of the baryon-photon fluid. In equation 2.11 the term $k^2\Theta/3$ is related to the radiation pressure and it counteracts the gravitational collapse of

the perturbations due to the potential ψ. These two effects reflect the oscillating behavior of the gas in the potential wells and, as an aftermath, the oscillation of the temperature fluctuations.

When photons and baryons are still merged in a single relativistic fluid with $w = 1/3$ and $R = 0$, the solution becomes

$$\Theta(\tau) = -\psi + C_1 \cos(kc_s\tau) + C_2 \sin(kc_s\tau).$$

Assuming initial adiabatic conditions

$$\begin{cases} \dot{\Theta}(0) = 0 \\ \Theta(0) = -\frac{2}{3}\psi \end{cases}$$

the Cauchy problem has the following solution

$$\Theta(\tau) = -\psi + \frac{1}{3}\psi \cos(kc_s\tau).$$

that oscillates in time for each k mode.

The $R = 0$ approximation is too strong, so we can assume only $R =$ constant because the time scale of R variations is of the order of the expansion of the Universe and it is much greater than the time scale of the temperature fluctuations. In this case, the solution for initial adiabatic conditions is

$$\Theta(\tau) = -(1+R)\psi + \frac{1}{3}(1+3R)\psi \cos(kc_s\tau).$$

The oscillation amplitude depends on the factor $(1 + R)$ that is proportional to the baryon density. This is due to the fact that baryons contribute only to the mass of the fluid, not to its pressure. Actually the term $k^2\Theta/3$ in 2.11 is independent from R. In conclusion baryons determine the strength of compression and rarefaction of the fluid within the potential wells, and so the amplitude of the oscillations. This turns out in the first important dependence of the anisotropies from the cosmological parameters, in this case Ω_b.

The Sachs-Wolfe effect

The Sachs-Wolfe effect (Sachs & Wolfe 1967) is the sum of the gravitational effect and the adiabatic effect

$$\frac{\Delta T}{T} = \psi - \frac{2}{3}\psi = \frac{1}{3}\psi.$$

Using the Fourier transformer of the Poisson equation 2.4 $\psi_k = -\frac{3}{2}\mathcal{H}^2\delta_k/k^2$, we obtain the total Sachs-Wolfe effect

$$\frac{\Delta T_k}{T} = \frac{\psi_k}{3} = -\frac{\mathcal{H}^2}{2}\frac{\delta_k}{k^2} = -\frac{H_o^2}{2}\frac{\delta_{k,0}}{k^2}, \tag{2.12}$$

where has been used the fact that δ increases as $a \sim \tau^2 \sim H^{-2}$, so in the MDE, as we have already seen, the gravitational potential is constant. We can see that the gravitational effect is dominant, it means that in an overdensity the CMB is

intrinsically denser (adiabatic term), but photons must climb a deeper potential well (gravitational term), and in conclusion the overdensity appears colder.

In the previous paragraph about the adiabatic effect, a solution $\Theta(\tau)$ has been obtained from the differential equation arising from the combination of the Euler equation and the continuity equation with adiabatic initial conditions. Now we can combine this solution with the gravitational effect in order to obtain the total Sachs-Wolfe effect on the LSS

$$\frac{\Delta T}{T}(\tau_{LS}) = [\Theta(\tau) + \psi]_{\tau_{LS}} = \frac{1}{3}\psi \cos(kc_s\tau_{LS}).$$

When the term $kc_s\tau_{LS}$ is a multiple of π the absolute values of the fluctuations are maxima. Since c_s and τ_{LS} are fixed, the temperature fluctuation is an oscillating function of k. For each k mode there is a spatial scale $\lambda \sim 1/k$. The maxima anisotropies correspond to scales that undergo maximum compression or rarefaction at the moment of the last scattering. So the fluctuation spectrum, that is the distribution of power at different scales, is expected to reflect the oscillating behavior of $\Delta T/T$. Finally the odd peaks ($kc_s\tau = (2n+1)\pi$) that correspond to compressions are higher than the par ones ($\psi\cos(kc_s\tau) > 0$) that correspond to rarefactions. This effect is related to a high baryon density.

2.9.2 Secondary anisotropies

After the last scattering, photons and baryons are no longer coupled together. Photons simply propagate freely along geodetic of the space-time from the last scattering surface to the observer. The causes of the secondary anisotropies are all due to gravity.

The Integrated Sachs-Wolfe effect

The Integrated Sachs-Wolfe effect [7] is related to a varying gravitational potential $\dot{\psi} \neq 0$ and its contribution to the anisotropies consists of the variation of the potential integrated along the photon's path. We can distinguish two ISW effects, the Early ISW and the Late ISW, depending on the epoch the effect has been produced in.

The first one comes from the LSS and is mainly due to the presence of neutrinos. The LSS takes place at redshift $z_{LS} = 1100$, while the matter-radiation equality at redshift $z_{rm} = 3450$. So the scale factor $a = 1/(1+z)$ and the ratio between the matter energy density and the radiation energy density $\Omega_m/\Omega_r \propto a$ (that is equal to 1 at the equivalence) are increased of a factor about 3 between these two events. As a consequence at the last scattering the matter density parameter Ω_m and the radiation density parameter Ω_r are of the same order, so the approximation $\Omega_{tot} = \Omega_m$ fails. Since the LS is settled down not well within the MDE, the potential is not constant, but it is $\dot{\psi} < 0$ as in the RDE, and this causes the Early ISW effect.

Instead the second effect arises along the line of sight, that's why in temperature fluctuation formula this term cannot be multiplied by the visibility function. More precisely the Late ISW effect is located at the time of the ΛDE ($z = 0.3$) when the potential decreases $\dot{\psi} < 0$.

Sunyaev-Zel'dovich effect

Travelling toward us from the LSS, CMB photons pass through the hot ionized gas contained in clusters of galaxies. The high energy free electrons cause inverse Compton scattering on CMB photons and this pans out in a distortion of the Planck spectrum. More precisely the intensity decreases at frequencies below 220 GHz, at 220 GHz the effect is null, and the intensity increases at frequencies above 220 GHz. This process is called thermal Sunyaev Zel'Dovich effect [8, 9] and is related to the temperature of the intracluster gas. Instead the kinetic Sunyaev Zel'Dovich effect is related to the proper motion of the cluster and consists of a Doppler effect. Both these effects give a contribution to the temperature anisotropies power spectrum at small scales, where the secondary anisotropies are dominant.

2.9.3 Spherical harmonics

What we have seen so far must be translated in something that can be observed. To do this we need to project the fluctuations on an ideal celestial sphere, it means passing from the Fourier space to the spherical harmonics. A function of θ and ϕ can be written as $f(\theta,\phi) = \sum_{l,m} a_l^m Y_{m,l}(\theta,\phi)$, where $Y_{l,m}$ are the spherical harmonics $Y_{m,l} = (-1)^m \left[\frac{2l+1}{4\pi}\frac{(l-m)!}{(l+m)!}\right] e^{im\phi} P_l^m(\cos\theta)$ and $P_l^m(\cos\theta)$ are the Legendre polynomials. In the case of the temperature fluctuations in a given direction $\hat{n}$ and for a single Fourier mode we get

$$\frac{\Delta T}{T}(\hat{n}) = \left(\frac{\Delta T}{T}\right)_k e^{i\vec{k}\cdot\hat{n}D}$$

where D is the distance from the LSS. Using the identity

$$e^{i\vec{k}\cdot\hat{n}D} = 4\pi \sum_{l,m} i^l j_l(kD) Y_{lm}^*(\hat{k}) Y_{lm}(\hat{n}),$$

where j_l are the Bessel function, we can rewrite the expression for the temperature fluctuations with the multipoles ℓ

$$\frac{\Delta T}{T}(\hat{n}) = \sum_{lm} a_{lm}^k Y_{lm}(\hat{n})$$

with

$$a_{lm}^k = 4\pi \left(\frac{\Delta T}{T}\right)_k i^l j_l(kD) Y_{lm}^*.$$

The a_{lm} coefficients depend on the Bessel functions that have the maximum for $\ell = kD$, so each k mode contributes essentially to the multipole $\ell_k = kD$. The observed anisotropies arise from the overposition of all the k modes $a_{lm} = \sum_k a_{lm}^k$. Moreover, by definition it is $\frac{\Delta T}{T} = \frac{T-\langle T\rangle}{\langle T\rangle}$, so $\langle \Delta T/T\rangle = 0$ and

$$\langle a_{lm}\rangle = 0.$$

These coefficients satisfy the relation

$$\langle a_{l'm'}^* a_{lm}\rangle = C_\ell \delta_{ll'mm'}$$

where it has been defined the angular power spectrum

$$C_\ell \equiv \left\langle |a_{lm}|^2 \right\rangle .$$

If the field of the temperature fluctuations is Gaussian with nil mean, it will be completely characterized by its variance, which is C_ℓ. Since $\theta = \pi/\ell$ and a spatial scale referred to a wavenumber k is subtended by an angle $\theta = 1/kD$, the ℓ multipoles are proportional to the Fourier modes k: $\ell \propto k$.

Practically, it is used the expression

$$\left\langle \left(\frac{\Delta T}{T}\right)^2 \right\rangle = \frac{2\ell+1}{4\pi} \ell C_\ell d(\log \ell)$$

where $\frac{2\ell+1}{4\pi}\ell C_\ell$ is the contribution to the temperature fluctuations in a logarithmic interval of multipoles and it is in μK^2.

2.9.4 The spectrum

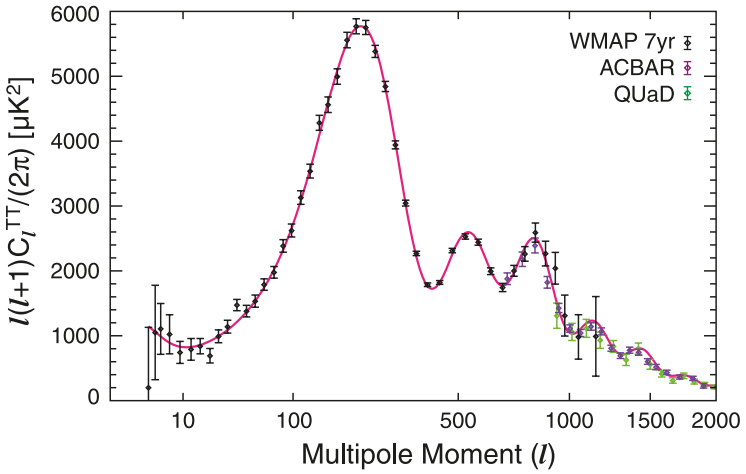

Figure 2.1. The WMAP 7-year temperature power spectrum as reported in [10] , along with the temperature power spectra from the ACBAR (Reichardt et al. 2009) and QUaD (Brown et al. 2009) experiments. The solid line shows the best-fitting 6-parameter flat ΛCDM model to the WMAP data alone.

The temperature anisostropies power spectrum as observed by the WMAP satellite in its 7 year data release is reported in Figure 2.1. The big error bars at low multipoles are due to the fact that the theory is statistical, so it is averaged on more than one Universe, but the experimental observations can be performed only on our Universe. The smaller the scale the greater the number of objects of such dimension that can be observed. At low multipoles the scales are nearly as larger as the Universe, so there is just one object that can be observed.

The nearly constant behavior at low multipoles is related to the only gravitational effect, actually this effect is dominant in equation 2.12 at small k. At larger multipoles the spectrum shows the acoustic oscillations of all those perturbations on scales smaller than the Jeans scale. At $\ell \approx 200$ we can notice the peak that defines the acoustic horizon. This is extremely important from a cosmological point of view because it demonstrates that the Universe is flat. Actually in an open Universe with a negative curvature the angular diameter distance of the anisotropies form the LSS would be greater than in the case of a flat Universe; so a certain k mode would correspond to a greater multipole $\ell = kD_A$. In an open Universe the spectrum would appear shifted at higher ℓ. Viceversa, a close Universe with a positive curvature would be characterized by a spectrum shifted to lower ℓ. Instead, in a spatially flat Universe with nil curvature and $\Omega_m = 0.3$ and $H_0 = 0.72$Km/s/Mpc, assuming that the last scattering took place during the MDE, the horizon at decoupling is

$$\frac{c}{H(z_{LS})} = \frac{c}{H_0\sqrt{\Omega_m}\,(1+z_{LS})^{3/2}} \approx 0.2\text{Mpc}$$

and nowadays the anisotropies angular distance is

$$D_A = \frac{d_{hor}(t_0)}{z_{LS}} \approx 13\text{Mpc},$$

so they are subtended by an angle

$$\theta = \frac{c/H(z_{LS})}{D_A} \approx \frac{0.2\text{Mpc}}{13\text{Mpc}} = 0.015\text{rad} = 1^\circ$$

that corresponds to a multipole $\ell \approx 200$ that is exactly the position where the first peak is observed. In conclusion the Universe is (nearly) spatially flat with a nil curvature.

2.10 CMB polarization

CMB polarization arises from the Thomson scattering between photons and electrons on the baryon-photon fluid quadrupole located on the LSS. The polarized fraction of temperature anisotropy is small since only those photons that last scattered in an optically thin region could have a quadrupole anisotropy. The fraction depends on the duration of the last scattering. For the standard thermal history, it is 10%. Since temperature anisotropies are at the 10^{-5} level, the polarized signal is at the 10^{-6} level.

Polarization is so useful because it can only be generated by Thomson scattering and so cannot be generated after recombination because the Universe is transparent for photons. Thus the polarization spectrum of the CMB is a direct snapshot of conditions on the last scattering surface, while temperature anisotropies can also be generated between the last scattering and the present. As an aftermath, the first thing we learn from polarization spectrum is when the last scattering occurred, i.e. what fraction of photons last scattered at $z \approx 1000$ when the Universe recombined, and what fraction rescattered when the intergalactic medium reionized at $z_{reion} \gtrsim 5$ (see Section 7.2.1).

In Thomson scattering the incident light sets up oscillations of the target electron in the direction of the electric field **E**, i.e. the polarization. The scattered radiation intensity thus peaks in the direction normal to, with the polarization parallel to, the incident polarization. If the incoming radiation field were isotropic, orthogonal polarization states from incident direction separated by 90° would balance so that the outgoing radiation would remain unpolarized. Conversely, if the incident radiation field possesses a quadrupolar variation in intensity or temperature (which possess intensity peaks at $90° = \pi/2$ separations), the result is a linear polarization of the scattered radiation. A reversal in sign of the temperature fluctuation corresponds to a 90° rotation of the polarization, which reflects the spin-2 nature of polarization. Given the tight coupling between photons and electrons, the photon distribution function has a dipole term $T_1 = \hat{\mathbf{n}} \cdot \mathbf{v}$, where $\mathbf{v}$ is the velocity of the fluid. The quadrupole moment is generated if there is a gradient in the velocity field across the mean free path of the photon λ_p and it is $T_2 = \lambda_p n^i n^j \partial_i v_j$ in the rest frame of the electron.

The quadrupoles due to the velocity gradient in the baryon-photon fluid produce scalar modes, while tensor modes are related to the gravitational redshift of the primordial stochastic gravitational waves background caused by the initial accelerated expansion of the Universe predicted by inflation [1]. Scalar modes produce only electric E-modes, while tensor modes produce both E-modes and magnetic B-modes in the same quantity. The CMB polarization field can be decomposed in two components: curl free E-modes coming from the LSS where they are produced both by scalar and tensor perturbations of the metric, and B-modes produced only by tensor perturbations due to the crossing of gravitational waves in the primordial plasma. Moreover E-modes and B-modes are mixed by the gravitational lensing, due to the presence of large scale structure along the line of sight. This effect converts E-modes in B-modes and gives the chance to understand the process of large scale structure formation and, as an aftermath, the neutrino mass that influences this process.

With polarization there are three additional power spectra that can be measured: E and B autocorrelation plus E and T cross-correlation. These spectra are related to the parameters of the ΛCDM model, as the temperature power spectrum, and so they add important additional information on the physics of the Universe.

2.10.1 Statistic of Polarization

The CMB radiation field is characterized by a 2×2 intensity tensor I_{ij} and it is a function of the direction on the sky $\mathbf{n}$ that are used to define its components ($\hat{\mathbf{e}}_\mathbf{1}$, $\hat{\mathbf{e}}_\mathbf{2}$). The Stokes parameters Q and U are defined as $Q = (I_{11} - I_{22})/4$ and $U = I_{12}/2$, and the temperature anisotropy is given by $T = (I_{11} + I_{22})/4$ (the factor 4 relates fluctuations in intensity to those in temperature). Polarization on CMB maps is pictured with "vectors" of length $P = \sqrt{Q^2 + U^2}$ that form an angle $\alpha = \frac{1}{2} \arctan\left(\frac{U}{Q}\right)$ with $\hat{\mathbf{e}}_\mathbf{1}$. These are not real vectors since they return the same

[1] The inflation is a process that took place at energies about 10^{12}TeV, 10^{-36}s after the Big Bang, when the Universe was dominated by a scaler field that produced an accelerating expansion and an exponential growth of the scale factor

after a 180 degrees rotation, and so they do not have a direction. In principle there is a fourth Stokes parameter V that describes circular polarization, but it can be ignored since this kind of polarization cannot be generated through Thomson scattering. Q and U transform under rotation of angle ψ as

$$\begin{aligned} Q' &= Q\cos 2\psi + U\sin 2\psi \\ U' &= -Q\sin 2\psi + U\cos 2\psi \end{aligned}$$

where $\hat{\mathbf{e}}'_{\mathbf{1}} = \cos\psi\hat{\mathbf{e}}_{\mathbf{1}} + \sin\psi\hat{\mathbf{e}}_{\mathbf{2}}$ and $\hat{\mathbf{e}}'_{\mathbf{2}} = -\sin\psi\hat{\mathbf{e}}_{\mathbf{1}} + \cos\psi\hat{\mathbf{e}}_{\mathbf{2}}$. The Stokes parameters are not invariant under rotations in the plane perpendicular to $\mathbf{n}$. For this reason it is more convenient to work with scalar and pseudoscalar polarization fields $E(\mathbf{n})$ and $B(\mathbf{n})$, which are invariant under rotations. In the small scale limit $\mathbf{n}$ is close to $\hat{\mathbf{z}}$ and we can parametrize the direction in the sky with two–dimensional angle θ relative to a fixed coordinate system perpendicular to $\hat{\mathbf{z}}$. So we have, in terms of Stokes parameters,

$$\begin{aligned} E(\ell) &= \int d^2\theta \left[Q(\theta)\cos(2\phi_l) + U(\theta)\sin(2\phi_l)\right] e^{-i\ell\cdot\theta} \\ B(\ell) &= \int d^2\theta \left[U(\theta)\cos(2\phi_l) - Q(\theta)\sin(2\phi_l)\right] e^{-i\ell\cdot\theta}, \end{aligned}$$

where $E(\ell)$ and $B(\ell)$ are the two components of the two scalar fields in Fourier space. To obtain them in real space we can perform a Fourier transform

$$\begin{aligned} E(\theta) &= (2\pi)^{-2}\int d^2\ell e^{-i\ell\cdot\theta}E(\ell) \\ B(\theta) &= (2\pi)^{-2}\int d^2\ell e^{-i\ell\cdot\theta}B(\ell). \end{aligned}$$

These two quantities describe completely the polarization field. They can be expressed directly in terms of real space quantities $Q(\theta)$ and $U(\theta)$ as

$$\begin{aligned} E(\theta) &= -\int d^2\theta'\omega(\tilde{\theta})\left[Q(\theta')\cos(2\tilde{\phi}_l) + U(\theta')\sin(2\tilde{\phi}_l)\right] \\ &= -\int d^2\theta'\omega(\tilde{\theta})Q_r(\theta') \\ B(\ell) &= -\int d^2\theta'\omega(\tilde{\theta})\left[U(\theta')\cos(2\tilde{\phi}_l) - Q(\theta')\sin(2\tilde{\phi}_l)\right] \\ &= -\int d^2\theta'\omega(\tilde{\theta})U_r(\theta'). \end{aligned} \tag{2.13}$$

The variables $(\tilde{\theta},\ \tilde{\phi})$ are the polar coordinates of the vector $\theta - \theta'$ and Q_r and U_r are the Stokes parameters in the polar coordinate system centered at θ. Hence, if θ is zero, $Q_r = \cos 2\phi' Q(\theta') - \sin 2\phi' U(\theta')$ and $U_r = \cos 2\phi' U(\theta') - \sin 2\phi' Q(\theta')$. The window is found to be $\omega(\theta) = 1/\pi\theta^2$ with $\theta \neq 0$ and $\omega(\theta) = 0$ with $\theta = 0$. By construction, $E(\theta)$ and $B(\theta)$ are rotationally invariant: the Stokes parameters Q_r and U_r do not depend on the coordinate system as they are defined relative to the $\theta - \theta'$ vector, and the weight function ω is also rotationally invariant. The variable B is a pseudoscalar because it is the average of U_r and it changes sign under parity. The window extends to infinity and so the quantities E and B are non–local. This

is not the only possible choice: one can construct versions of E and B from Q and U that are finite using different types of windows. The structure of polarization can be tested without measuring the whole sky (as long as the measured field is contiguous).

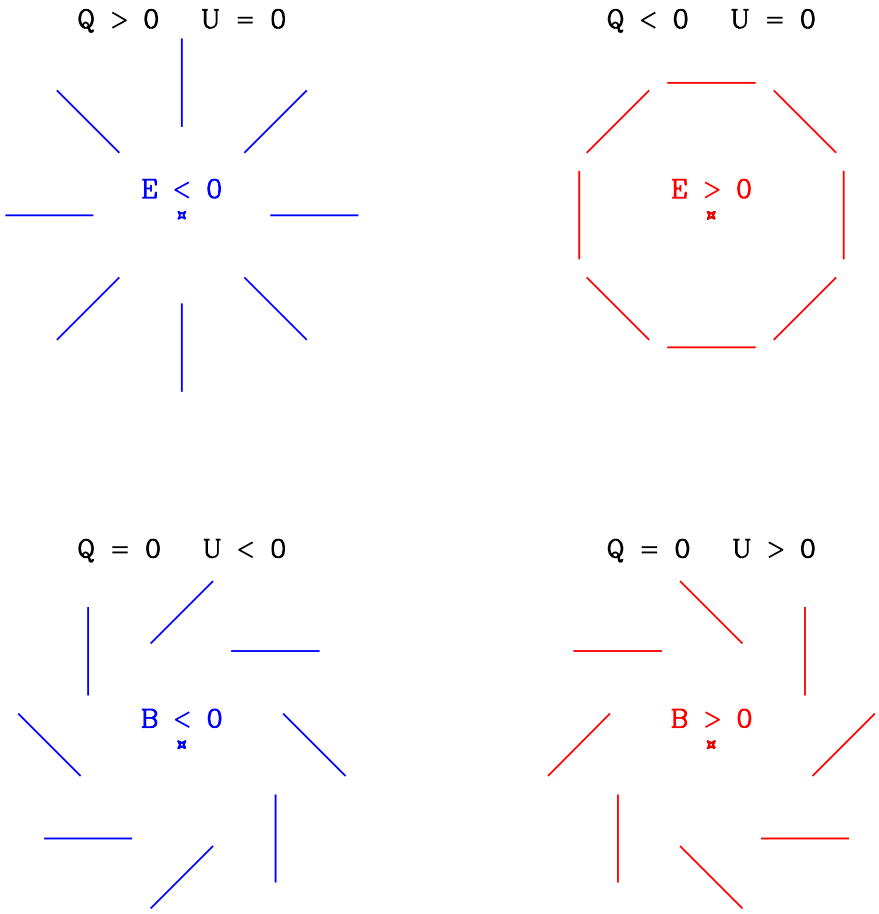

Figure 2.2. Polarization patterns that lead to positive and negative values of the E and B fields. The Stokes parameters are measured in the polar coordinate system centered at the cross. All four patterns are invariant under rotation but the two patterns that generate B are not invariant under reflections.

E type polarization is the only pattern that is produced by density perturbations in this model. Radial polarization pattern is found around the cold spots of E. This relation comes directly from equation 2.14. To obtain B type polarization we can rotate all polarization "vectors" by 45°. Hot and cold spots of the B field

correspond to places where polarization vectors circulate in opposite directions. From Figure 2.2 [11] we can see that such polarization pattern is not invariant under reflections (parity transformation). This is the main distinction between E and B type of polarization: under parity operation E transforms as a scalar and B as a pseudoscalar. Scalar perturbations cannot induce B type of polarization because polarization is invariant under the reflection across the axis determined by the $\hat{\mathbf{k}}$ (direction of Fourier mode) and $\mathbf{n}$ (line of sight), because polarization amplitude only depends on the angle between $\hat{\mathbf{k}}$ and $\mathbf{n}$. Therefore any integration around this circle will produce only E and B.

2.11 Matter power spectrum

The density fluctuations field $\delta(\vec{r})$ is defined in a tridimensional space, but it is useful to express it through its Fourier component in a large comoving volume V:

$$\delta(\vec{r}) = \frac{V}{(2\pi)^3} \int \delta_{\vec{k}} e^{-i\vec{k}\cdot\vec{r}} d^3k,$$

where the different components are $\delta_{\vec{k}} = \frac{1}{V} \int \delta(\vec{r}) e^{i\vec{k}\cdot\vec{r}} d^3r$. The Fourier transformer consists in breaking the function $\delta(\vec{r})$ in an infinite number of sin waves each one with a comoving wave number $\vec{k}$ and a comoving wavelength $\lambda = 2\pi/k$. Each Fourier component is a complex number and can be written as $\delta_{\vec{k}} = |\delta_{\vec{k}}| e^{i\phi_k}$.

When $|\delta_{\vec{k}}| \ll 1$, each Fourier component follows the equation 2.8, until the proper wavelength $a(t)2\pi/k$ remains greater than the Jeans length and smaller than the Hubble scale c/H. The phase ϕ_k remains constant until the amplitude $|\delta_{\vec{k}}|$ remains small. Even after the fluctuations with a small proper wavelength have reached the amplitude $|\delta_{\vec{k}}| \approx 1$ and have collapsed, the growth of the perturbations with a greater wavelength is still described by equation 2.8. This implies that we can use the linear perturbation theory to study the large structure formation even if the smaller structure (such as galaxies) have been already undergone the collapse.

The mean squared of the Fourier components amplitudes defines the power spectrum

$$P_k(t_H) = \left\langle \left| \delta_{\vec{k}} \right|^2 \right\rangle$$

where the mean is on all possible direction of the wavenumber $\vec{k}$ and t_H means that the spectrum is calculated at the time of the horizon crossing of the perturbation: different scales cross the horizon at different times and so the spectrum is not calculated at the same time for every the perturbations. If the phases ϕ_k of the different Fourier components are uncorrelated, $\delta(\vec{r})$ will be a Gaussian field. If a Gaussian field is homogeneous and isotropic, all its statistical properties are contained in the power spectrum. In this case the δ values must be calculated using the Gaussian probability distribution

$$p(\delta) = \frac{1}{\sqrt{2\pi}\sigma} \exp\left(-\frac{\delta}{2\sigma^2}\right)$$

where the standard deviation σ is related to the power spectrum

$$\sigma = \frac{V}{(2\pi)^3}\int P_k d^3k = \frac{V}{2\pi^2}\int P_k k^2 dk.$$

The present observed power spectrum depends on the inflation that predicts that the power P_k in a volume k^{-3} at the time t_H of the horizon crossing is scale invariant (independent from k): $\frac{P_k(t_H)}{k^{-3}} = A$, where A is a constant. This kind of spectrum

$$P_k(t_H) = Ak^{-3} \tag{2.14}$$

is called scale invariant: different scale perturbations share the same amplitude if calculated at t_H. Moreover, since $dP = P_k d^3k = Ak^{-3}k^2dk = Adk/k = Ad(\log k)$, the power per logarithmic unit is constant

$$dP/d(\log k) = A.$$

For the observations is more useful to have the spectrum at a given time t_F, for instance at decoupling, instead that at t_H different for each scale. The difference is that at a given instant the perturbations that have already undergone the horizon crossing have had the time to grow. Consider a perturbation that has had the horizon crossing during the MDE when the scale factor is a and $H = (2/3)t^{-1} = a^{-3/2}H_0$ and $k = aH = aa^{-3/2}H_0 = a^{-1/2}H_0$. A perturbation of wavenumber k has the horizon crossing when $a = (k/H_0)^{-2}$. This perturbation can grow between a and an arbitrary fixed instant a_F as $\delta_k \sim (a_F/a) = (k/k_F)^2$ (because it is within the MDE), if k_F is the scale that crosses at a_F. So smaller scales cross the horizon before larger scales and so they have more time to grow. In conclusion a perturbation of scale k^{-1} can grow between the time of its horizon crossing and a_F of a factor $(k/k_F)^2$. So we have that

$$\delta_k(t_F) = (k/k_F)^2\delta_k(t_H),$$
$$P_k(t_F) = (k/k_F)^4 P_k(t_H).$$

Using equation 2.14, on scales that undergo the horizon crossing after the equivalence, the spectrum is the Harrison Zel'Dovich

$$P_k(t_F) = Ak.$$

Smaller scale perturbation cross the horizon during the RDE and so they can't grow. Their spectrum remains the initial one $P_k \sim k^{-3}$ until the equivalence. After the equivalence, perturbations within the horizon grow all at the same rate for any k, so the shape of the spectrum doesn't change and it is proportional to k on large spatial scales and to k^{-3} on small spatial scales. Figure 2.3 [12] shows that the maximum power is located at the scale that has undergone the horizon crossing at the equivalence k_{eq}. To sum up, we can say that we assume an initial Harrison Zel'Dovich power spectrum modified by a transfer function $T(k)$ such that $T^2(k) = 1$ for $k \ll k_{eq}$ and $T^2(k) = k^{-4}$ for $k \gg k_{eq}$.

It must be stressed that the power spectrum observed in the visible matter through the galaxies surveys P_k^* is not the perturbation power spectrum. The visible

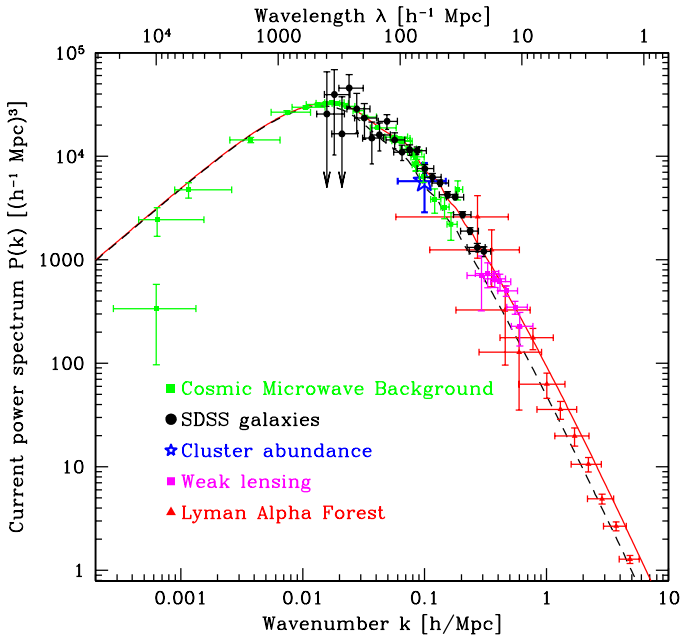

Figure 2.3. Cosmological constraints on the current matter power spectrum $P(k)$. The solid curve shows the theoretical prediction for a flat ΛCDM model with $\Omega_m = 0.28$, Hubble parameter $h = 0.72$ and baryon fraction $\Omega_b/\Omega_m = 0.16$. The dashed curve shows that replacing 7% of the cold dark matter by neutrinos, corresponding to a neutrino mass sum $\sum m_\nu = 1\text{eV}$, suppresses small scale power by about a factor two [12].

matter spectrum is obtained by a galaxies catalogue with angular positions and redshifts, this produces a fluctuations field $\delta(x) = (\varrho(x) - \varrho_0)/\varrho_0$ where $\varrho(x)$ is that galaxies density number and ϱ_0 its mean on the volume V. Then we take the Fourier transformer $\delta_k = V^{-1} \int \delta(x) e^{ikx} d^3x$ and we calculate the power spectrum defined as $P_k^* = |\delta_k|^2$ where the mean is over all the possible directions of k. Another way to calculate the spectrum is based on the relation between the spectrum and the galaxy correlation function $\xi(r)$:

$$P_k^* = \int \xi(r) e^{ikx} d^3x = 2\pi \int \xi(r) \frac{\sin(kr)}{kr} r^2 dr,$$

where has been assumed an isotropic correlation depending only on the absolute value of r. Finally the galaxy spectrum is considered proportional to the perturbation spectrum through a bias factor b:

$$P_k^* = b^2 P_k.$$

The theory we have just seen about the spectrum assumes that it is a mathematical object continuous and defined in each point. Practically the observations give only a sample of the galaxy distribution, so we need to introduce a window function W. The top-hat window function is equal to V^{-1} inside a spherical volume of radius R and zero otherwise. In the Fourier space it is

$$W_k = 3 \frac{\sin(kr) - kr\cos(kr)}{(kr)^3}.$$

The observed spectrum arises from the convolution of P_k with W_k. Nevertheless only the statistical properties of the spectrum not its convolution can be derived from observations. The variance of the field (the mean squared fluctuations on a spherical volume of radius R) are

$$\sigma_R^2 = \int P_k(k) W_k(kr) d^3k.$$

Starting from this expression, we can define a fundamental quantity in the power spectrum measurements: the σ_8 parameter that is the root mean squared of the fluctuations over a volume of radius $8h^{-1}$Mpc (where $h = H_o/(100\text{km/s/Mpc}) = 0.72$ adimensional) for a density field passed through a top-hat window. For linear density perturbations it is $\sigma_8 \approx 1$.

Chapter 3

Neutrino effects in Cosmology

3.1 Neutrinos

The first hint for the existence of neutrinos was noticed in the neutron beta decay: $n \to p + e^- + \overline{\nu}_e$; the energy spectrum of the electron was different from the one expected in a two bodies decay with only two lines. In 1933 Fermi suggested the hypothesis of the emission of a light neutral particle during the process.

Neutrinos are fermions (spin 1/2), more precisely neutrinos are neutral leptons.

By the early 1990s precision electroweak measurements of the Z^0 neutral boson decay Branching Ratio (BR) at Large Electron Proton collider pin down the number of light active neutrino species with high accuracy, $N_\nu = 2.9840 \pm 0.0082$ [13], consistent within $\sim 2\,\sigma$ with the known three families of the Standard Model (ν_e, ν_μ, ν_τ). Actually the BR in the invisible channels is three times the BR in one of the visible leptonic channels (e^+e^- and $\mu^+\mu^-$). These are active neutrino that means neutrino which undergo weak interactions.

Following the Pontecorvo hypothesis (1957), earth based experiments demonstrated that neutrinos oscillate and therefore have mass. Assuming that only two neutrinos (ν_e and ν_μ) are involved in the oscillation, the oscillation probability is related to the neutrino mass through this formula

$$P_{\nu_e \to \nu_\mu} = \sin^2(2\theta) \sin^2 \pi \frac{L}{L_v} \text{ where } L_v = 2.48 \frac{E}{\Delta m^2}.$$

The value of L represents the distance travelled by neutrino from the source to the detector, and it is expressed in km if E is in GeV and Δm^2 is in eV^2. Varying L one can find the minimum or the maximum oscillation probability. However oscillation experiments cannot measure the absolute mass value, but only the mass square differences. In particular experiments on the oscillation of atmospheric neutrinos provide only the modulus of the mass square difference between the second and the third mass eigenstates. Since we don't know the sign of this measure, there are two possible hierarchies (see Figure 3.1: the normal one (Δm^2_{23} positive) [14]

$$|\Delta m^2_{23}| \approx 2.55^{+0.06}_{-0.09} \times 10^{-3} \text{eV}^2 \ (1\sigma \text{ range})$$

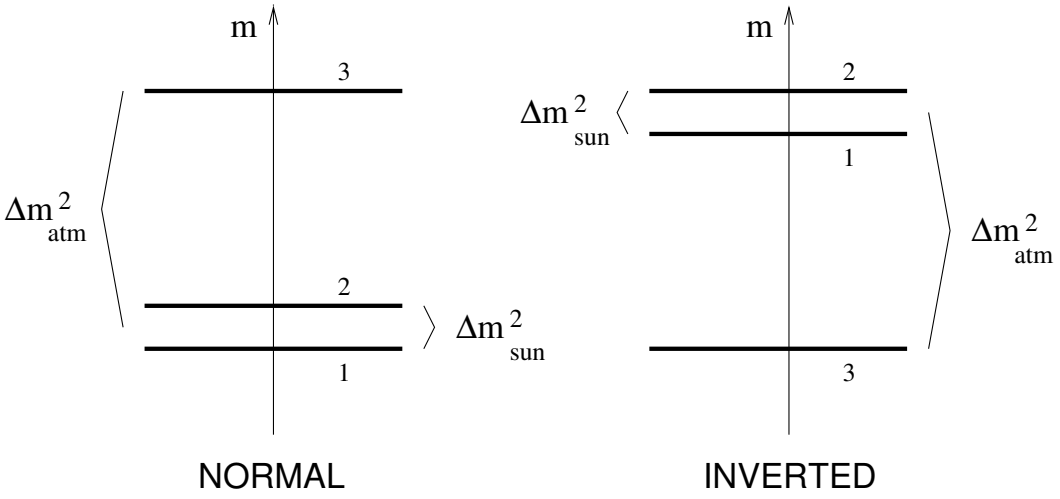

Figure 3.1. The two neutrino schemes allowed: normal hierarchy (NH) and inverted hierarchy (IH).

and the inverted one (Δm^2_{23} negative) [14]

$$|\Delta m^2_{23}| \approx 2.43^{+0.07}_{-0.06} \times 10^{-3}\text{eV}^2 \ (1\sigma \text{ range}).$$

Instead the experiments on solar neutrino oscillations and on neutrinos from reactor provide [14]

$$\Delta m^2_{12} \approx 7.62^{+0.19}_{-0.19} \times 10^{-5}\text{eV}^2 \ (1\sigma \text{ range}).$$

The two mass square differences imply that at least two neutrinos are massive.

3.1.1 Sterile Neutrinos

The number of massive neutrinos states might be larger than the number of electroweak flavors. These extra neutrinos must be sterile, i.e. neutrinos who do not undergo weak interactions, in order to not violate the LEP results. Therefore they must be singlets of the Standard Model gauge group and so they are insensitive to weak interactions, except those induced by mixing with active neutrinos.

Following [15], in sterile neutrino oscillation models, under the assumptions of CPT invariance and negligible matter effects, the probability for a neutrino produced with flavor α and energy E, to be detected as a neutrino of flavor β after traveling a distance L, is given by:

$$\begin{aligned} P(\nu_\alpha \to \nu_\beta) = \quad & \delta_{\alpha\beta} - 4\sum_{i>j} \mathcal{R}(U^*_{\alpha i}U_{\beta i}U_{\alpha j}U^*_{\beta j}) \sin^2 x_{ij} + \\ & 2\sum_{i>j} \mathcal{I}(U^*_{\alpha i}U_{\beta i}U_{\alpha j}U^*_{\beta j}) \sin 2x_{ij} \end{aligned} \tag{3.1}$$

where $\mathcal{R}$ and $\mathcal{I}$ indicate the real and imaginary parts of the product of mixing matrix elements, respectively; $\alpha, \beta \equiv e, \mu, \tau$, or s, (s being the sterile flavor); $i, j = 1, \ldots, 3+n$ (n being the number of sterile neutrino species); and $x_{ij} \equiv 1.27\Delta m^2_{ij} L/E$.

In defining x_{ij}, we take the neutrino mass splitting $\Delta m^2_{ij} \equiv m^2_i - m^2_j$ in eV^2, the neutrino baseline L in km, and the neutrino energy E in GeV. For antineutrinos, the oscillation probability is obtained from Eq. 3.1 by replacing the mixing matrix U with its complex-conjugate matrix. Therefore, if the mixing matrix is not real, neutrino and antineutrino oscillation probabilities can differ. For 3+n neutrino species, there are, in general, $2+n$ independent mass splittings, $(3+n)(2+n)/2$ independent moduli of parameters in the unitary mixing matrix, and $(2+n)(1+n)/2$ Dirac CP-violating phases that may be observed in oscillations. In SBL neutrino experiments that are sensitive only to $\nu_\mu \to \nu_\mu$, $\nu_e \to \nu_e$, and $\nu_\mu \to \nu_e$ transitions, the set of observable parameters is reduced considerably. In this case, the number of observable parameters is restricted to n independent mass splittings, $2n$ moduli of mixing matrix parameters, and $n-1$ CP-violating phases. Therefore, for (3+2) sterile neutrino models ($n = 2$ case), for example, there are two independent mass splittings, Δm^2_{41} and Δm^2_{51}, both defined to be greater than zero, four moduli of mixing matrix parameters $|U_{e4}|$, $|U_{\mu 4}|$, $|U_{e5}|$, $|U_{\mu 5}|$, and one CP-violating phase. The convention used for the CP-phase is:

$$\phi_{45} = arg(U^*_{\mu 5} U_{e5} U_{\mu 4} U^*_{e4}). \tag{3.2}$$

In that case, the general oscillation formula in Eq. 3.1 becomes:

$$\begin{aligned} P(\nu_\alpha \to \nu_\alpha) = 1 - 4[&(1 - |U_{\alpha 4}|^2 - |U_{\alpha 5}|^2) \cdot \\ &(|U_{\alpha 4}|^2 \sin^2 x_{41} + |U_{\alpha 5}|^2 \sin^2 x_{51}) + \\ &|U_{\alpha 4}|^2 |U_{\alpha 5}|^2 \sin^2 x_{54}] \end{aligned} \tag{3.3}$$

and

$$\begin{aligned} P(\nu_\alpha \to \nu_{\beta \neq \alpha}) = &4|U_{\alpha 4}|^2 |U_{\beta 4}|^2 \sin^2 x_{41} + \\ &4|U_{\alpha 5}|^2 |U_{\beta 5}|^2 \sin^2 x_{51} + \\ 8|U_{\alpha 5}||U_{\beta 5}||U_{\alpha 4}||U_{\beta 4}| &\sin x_{41} \sin x_{51} \cos(x_{54} - \phi_{45}) \end{aligned} \tag{3.4}$$

The formulas for antineutrino oscillations are obtained by substituting $\phi_{45} \to -\phi_{45}$. For the case of (3+1) sterile neutrino models ($n = 1$ case), the corresponding oscillation probabilities are obtained from Eqs. 3.3 and 3.4 by setting $x_{51} = x_{54} = 0$ and $|U_{\alpha 5}| = 0$. Note that, under the above assumptions, no CP violation is allowed for (3+1) models.

Recently hints for the existence of sterile neutrinos come from Short Base Line experiments, like MiniBooNE (Mini Booster Neutrino Experiment). The MiniBooNE experiment was designed to perform a search for $\nu_\mu \to \nu_e$ oscillations in a region of Δm^2 and $\sin^2 2\theta$ very different from that allowed by standard, three-neutrino oscillations, as determined by solar and atmospheric neutrino experiments. This search was motivated by the LSND (Liquid Scintillator Neutrino Detector) experimental observation of an excess of $\overline{\nu}_e$ events in a $\overline{\nu}_\mu$ beam which was found compatible with two-neutrino oscillations at $\Delta m^2 \sim 1\, eV^2$ and $\sin^2 2\theta < 1$. If confirmed, such oscillation signature could be attributed to the existence of a light, mostly-sterile neutrino, containing small admixtures of weak neutrino eigenstates, produced by oscillations of the active ones. In addition to a search for $\nu_\mu \to \nu_e$

oscillations, MiniBooNE has also performed a search for $\overline{\nu}_\mu \rightarrow \overline{\nu}_e$ oscillations, which provides a test of the LSND two-neutrino oscillation interpretation that is independent of CP or CPT violation assumptions. Neutrino and antineutrino data from LSND and MiniBooNE could be explained by (3+2) models with 3 active neutrinos plus two additional massive sterile neutrinos, requiring a large CP violation [15]. Otherwise the (3+1) models could fit the data only if Non Standard Interactions are allowed.

3.2 The Cosmic Neutrino Background

Neutrinos were produced in the primeval plasma by frequent weak interactions $p + e^- \rightarrow n + \nu_e$. When they were still in thermal equilibrium, they had a Fermi-Dirac momentum distribution at temperature T:

$$f_{eq}(p) = \left[e^{p/T} + 1\right]^{-1}.$$

When the Universe cooled down, the weak interactions rate Γ_ν went down the expansion rate H and neutrinos decoupled from the plasma. The mean value of the weak interaction rate is

$$\Gamma_\nu = \langle \sigma_\nu n_\nu v \rangle = \langle \sigma_\nu n_\nu \rangle\,, \text{ assuming } v \simeq c \text{ and } c = 1$$

where $\sigma_\nu \propto G_F^2 p^2 \simeq G_F^2 k_B^2 T^2$ is the cross section of the electron-neutrino interactions with $G_F^2 = 1.15 \cdot 10^{-5}\text{GeV}^{-2}$ Fermi constant and $n_\nu \simeq k_B^3 T^3$ neutrinos numerical density with $k_B = 1.381 \cdot 10^{-23}\text{J/K} = 8.619 \cdot 10^{-5}\text{eV/K}$. In order to estimate the temperature which the decoupling took place at, we match the mean value of the weak interaction rate with the expansion rate

$$H = \sqrt{\frac{8\pi\epsilon}{3M_P^2}} \simeq \frac{k_B^2 T^2}{10^{19}\text{GeV}},$$

where ϵ is the total energy density and M_P is the Planck mass. So it results

$$\frac{\Gamma}{H} = \left(\frac{k_B T}{1\text{MeV}}\right)^3,$$

and the neutrino decoupling temperature is $T_{dec} \approx 1\text{MeV}$ (approximately one second after the Big Bang).

At this energy electrons and protons are in thermal equilibrium because the electron mass is 0.511 MeV, so there is equilibrium between electron-positron annihilation and pairs production:

$$\gamma\gamma \longleftrightarrow e^+ e^-,$$

so at $k_B T \approx 1\text{MeV}$ electrons and positrons has nearly the same number density of photons. When the temperature further drops down, photons have no more the energy to produce pairs and the reaction proceeds only in the direction of the annihilation and this causes an increase in photons. The cross section of the

annihilation that produces neutrinos is smaller, so the annihilations produce only an excess in photons not in neutrinos.

If the decoupling process can be considered instantaneous, the momentum spectrum remains the same, because the momentum and the temperature are equally redshifted by the Universe expansion; in other words, after decoupling the neutrino number density remains constant in a comoving volume. Neutrinos with a mass of about one eV are relativistic at decoupling, this is the reason why the momentum distribution is independent from the neutrino mass even after decoupling and the neutrino energy doesn't appear in the exponent of $f_e(p)$.

In order to estimate the temperature ratio between the neutrino background and the photon background, we take into account that after decoupling the annihilations produced the photon excess but didn't transfer entropy to neutrinos. The entropy density of a sea of relativistic particles is $s = \frac{2\pi^2}{45} g^* T^3$, where g^* is the number of degrees of freedom: photons have two degrees of freedom (the two polarization states), electrons and positrons have two degrees of freedom (spin up and spin down) each one. Each degree of freedom has a multiplying factor, which for bosons is 1 and for fermions is 7/8. Before the first annihilation it was $g^* = 2 \times 7/8(\text{electron}) + 2 \times 7/8(\text{positrons}) + 2(\text{photons}) = 11/2$, but then $g^* = 2$. If the electron-positron annihilations happens at constant entropy and produces only photons, by imposing the entropy conservation, we obtain the final result

$$\frac{T_\gamma}{T_\nu} = \left(\frac{11}{4}\right)^{1/3} \approx 1.4.$$

If the present photons background temperature is $T_\gamma = 2.725K$, the cosmic neutrino background temperature will turn out to be $T_\nu = 1.95K$. The numerical density per cm^3 of neutrinos and antineutrinos for each flavor is $n_\nu = \frac{3}{11} n_\gamma$, $n_\nu = 113$. Remembering that the energy density is proportional to the fourth power of the temperature, the neutrino physical density is:

$$\Omega_\nu = 3 \times \frac{7}{8} \times (4/11)^{4/3}\, \Omega_r = 0.68 \Omega_r = 1.68 \times 10^{-5} h^{-2}.$$

This relation is true if neutrinos behave as relativistic particles, that is if their rest mass is negligible respect to their kinetic energy. The kinetic energy per particle is $3k_B T \simeq 5 \times 10^{-4}$eV, the neutrino energy density formula we have just seen is verified only if the mass of all flavor is smaller than this value. If the mass is greater than this value, nowadays neutrinos will be non-relativistic.

The light neutrino regime implies that the neutrino mass is much smaller than the plasma energy $k_B T \simeq 1$MeV at decoupling and so they don't have had influence on the decoupling process. In this case the cosmic neutrino density is similar to the one we have just derived, but in the energy part there is the rest mass instead of the kinetic term:

$$\Omega_\nu = \frac{1.68 \times 10^{-5} h^{-2}}{3} \frac{m_\nu c^2}{5 \times 10^{-4}\text{eV}} = \frac{m_\nu c^2}{93.1 h^2 \text{eV}}.$$

If neutrinos have mass we can write

$$\Omega_\nu = \frac{\sum m_\nu c^2}{93.1 h^2 \text{eV}},$$

where the sum is over all neutrino flavors with $m_\nu c^2 \ll 1\text{MeV}$. The present contribution of the neutrino species to the mass density is

$$\Omega_\nu h^2 = \frac{N_\nu m_\nu}{93.1\text{eV}}. \tag{3.5}$$

Just by putting $\Omega_\nu \leq 1$ we can already find a cosmological upper limit on the sum of neutrino masses $m_\nu \leq \frac{47\text{eV}}{N_\nu}$. Light neutrinos can explain the observed dark matter density $\Omega_{dm} \simeq 0.3$ if the neutrino mass is $m_\nu c^2 \simeq 14\text{eV}$. This kind of neutrino is far from the present limits. Anyway it is not a good candidate for dark matter because it remains relativistic until the last phases of the evolution of the Universe and so hampers the galaxies formation. Actually, considering the thermal energy of the neutrinos $3k_BT$, the redshift of the non-relativistic transition is

$$1 + z_{nr} \simeq \frac{m_\nu c^2}{3k_BT};$$

for example a good neutrino candidate for the dark matter with a 10eV mass undergoes the non-relativistic transition at $z_{nr} \simeq 20{\cdot}000$.

3.3 Free-streaming

Sound waves can't propagate in a collisionless fluid, nevertheless, single particles stream with a peculiar velocity (for neutrinos it corresponds to the thermal one v_{th}). It is therefore possible to define a horizon that represents the typical distance on which the particles travel between the time t_i and the time t. During the radiation dominated epoch and the matter dominated epoch, for $t \gg t_i$, this horizon tends asymptotically to v_{th}/H. So a free-streaming length can be defined, as the Jeans length, but with v_{th} instead of c_s

$$k_{FS} = \left(\frac{4\pi G\varrho(t)a^2(t)}{v_{th}^2(t)}\right)^{1/2}, \qquad \lambda_{FS}(t) = 2\pi\frac{a(t)}{k_{FS}(t)} = 2\pi\sqrt{\frac{2}{3}}\frac{v_{th}(t)}{H(t)}.$$

As long as neutrinos are relativistic, they travel at light speed and their free-streaming length is equal to the Hubble radius. When they become non-relativistic, their thermal velocity decreases

$$v_{th} \equiv \frac{\langle p\rangle}{m} \simeq \frac{3T_\nu}{m} = \frac{3T_{\nu 0}}{m}\left(\frac{a_0}{a}\right) \simeq 150(1+z)\left(\frac{1\text{eV}}{m}\right)\text{km/s},$$

where the present neutrino temperature is $T_{\nu 0} = (4/11)^{1/3}T_{\gamma 0}$ with $T_{\gamma 0} = 2.725\text{K}$. During the matter dominated era, the free-streaming length and wavenumber are

$$\begin{aligned}
\lambda_{FS}(t) &= 7.7\frac{1+z}{\sqrt{\Omega_\Lambda + \Omega_m(1+z)^3}}\left(\frac{1\text{eV}}{m}\right)h^{-1}\text{Mpc} \\
k_{FS}(t) &= 0.82\frac{\sqrt{\Omega_\Lambda + \Omega_m(1+z)^3}}{(1+z)^2}\left(\frac{m}{1\text{eV}}\right)h\text{Mpc}^{-1}.
\end{aligned}$$

So, after the non relativistic transition and during the matter dominated era, the free-streaming length keep growing, but only at the rate $(aH)^{-1} \propto t^{1/3}$, it means more slowly then the scale factor $a \propto t^{2/3}$. Moreover, the comoving free-streaming length λ_{FS}/a nowadays decreases as $\left(a^2H\right)^{-1} \propto t^{-1/3}$; as a consequence, for those neutrinos who undergo the non-relativistic transition during the matter dominated epoch, the comoving free-streaming wavenumber has reached a minimum k_{nr} at the time of the transition, it means when $m = \langle p \rangle = 3T_\nu$ and $(a_0/a) = (1+z) = 2.0 \times 10^3 (m/1\text{eV})$. This minimum value is

$$k_{nr} \simeq 0.018 \Omega_m^{1/2} \left(\frac{m}{1\text{eV}}\right)^{1/2} h\text{Mpc}^{-1}.$$

The physical effect of the free-streaming is to damp the neutrinos density perturbation at small scales: neutrinos can't be bounded in regions smaller than the free-streaming length. On scales larger than the free-streaming length, the neutrino velocity can be considered negligible, and, after the non relativistic transition, neutrino perturbations behave as the cold dark matter perturbations. In particular, free-streaming has no effect on modes $k < k_{nr}$.

3.4 The phases space

The phases space is described by six parameters: three positions x^i and their conjugate momenta P_i, i.e. the spatial part of the quadrimomentum, for a mass m particle $P_i = mU_i$, where $U_i = dx_i/\sqrt{ds^2}$. The relationship between the conjugate momenta and the proper momenta, measured by an observer from a fixed point in the spatial coordinates, is $P_i = a(1-\phi)p_i$. Assuming no metric perturbations, P_i would remain constant, while p_i would decrease with the expansion as a^{-1}.

The particle distribution provides the number of particles in a volume $dx^1dx^2dx^3dP_1dP_2dP_3$ of the phase space

$$f(x^i, P_j, \tau)dx^1dx^2dx^3dP_1dP_2dP_3 = dN,$$

where f is a scalar function and it is invariant under canonical transformations of the coordinates. The zero order distribution is the Fermi-Dirac for fermions (+ sign) and the Bose-Einstein for bosons (-sign):

$$f_0 = f_0(\epsilon) = \frac{g_s}{h^3} \frac{1}{e^{\epsilon/k_B T_0} \pm 1},$$

where $\epsilon = a\left(p^2 + m^2\right)^{1/2} = \left(P^2 + a^2m^2\right)^{1/2}$, $T_0 = aT$ is the temperature of the particles nowadays and the factor g_s is the number of spin degrees of freedom. Obviously neutrinos have the Fermi-Dirac distribution.

In order to eliminate the metric perturbations in the definition of the momenta, P_i can be replaced by $q_i \equiv ap_i$ that can be seen as the proper momentum corrected by the effect of the homogeneous expansion. So the comoving trimomentum q_i can be written using its modulus and its direction as $q_i = q\hat{n}_i$, where $\hat{n}^i\hat{n}_i = \delta_{ij}\hat{n}^i\hat{n}^j = 1$. So the phase space variables change and $f(x^i, P_j, \tau)$ is replaced by $f(x^i, q, \hat{n}_j, \tau)$.

Notice that since q_i are not the conjugate momenta, d^3xd^3q is not the phase space volume element and fd^3xd^3q is not the number of particles. From the relations $P_\mu P^\mu = m^2$ and $P_i = (1-\phi)q_i$, we can get $P_0 = (1+\psi)\epsilon$. In the CDM+HDM models, both massless and massive neutrinos were ultra-relativistic at decoupling, so in the Fermi-Dirac distribution ϵ can be simply replaced by q. In a homogeneous Universe the neutrino phase space distribution would be isotropic $f(x^i, P_j, \tau) = f_0(P, \tau)$ and the energy-momentum tensor would be diagonal with the isotropic pressure terms

$$\begin{aligned} T_0^0 &= \bar{\varrho}_\nu = \frac{4\pi}{a^4}\int q^2 dq \epsilon f_0(q), \\ T_i^i &= -\bar{p}_\nu = -\frac{4\pi}{3a^4}\int q^2 dq \frac{q^2}{\epsilon} f_0(q). \end{aligned}$$

Spatial metric perturbations produce variations in the neutrino phase space distribution depending on time, position and momentum. This will turn out in an anisotropic stress σ in the perturbated energy-momentum tensor $\delta T_{\mu\nu}$, so it would be written as

$$\left(\bar{\varrho} + \bar{P}\right)\sigma \equiv -\left(\hat{k}_i\hat{k}_j - \frac{1}{3}\delta_{ij}\right)\Sigma_j^i,$$

where $\Sigma_j^i \equiv T_j^i - \delta_j^i T_k^k/3$.

Using the quadrimomentum components and the distribution function, the general expression for the energy-momentum tensor is:

$$T_{\mu\nu} = \int dP_1 dP_2 dP_3 (-g)^{-1/2} \frac{P_\mu P_\nu}{P^0} f(x^i, P_j, \tau), \tag{3.6}$$

where g is the determinant of $g_{\mu\nu}$. It is useful to rewrite the determinant as a zero degree term plus a perturbed term that takes into account the anisotropies, it means a function $\Psi \ll 1$ in the new variables q and n_i:

$$f(x^i, P_j, \tau) = f_0(q)\left[1 + \Psi(x^i, q, \hat{n}_j, \tau)\right], \qquad \text{con } P_j = (1-\Psi)\, q_j. \tag{3.7}$$

Now the anisotropic stress appears at the first order. Using the relations $\int d\Omega \hat{n}_i\hat{n}_j = 4\pi\delta_{ij}/3$ and $\int d\Omega \hat{n}_i = \int d\Omega \hat{n}_i\hat{n}_j\hat{n}_k = 0$, the equation 3.6 at the first order in the perturbations becomes:

$$T_0^0 = a^{-4}\int q^2 dq d\Omega \sqrt{q^2 + a^2m^2} f_0(q)\,(1+\Psi)\,, \tag{3.8}$$

$$T_i^0 = a^{-4}\int q^2 dq d\Omega q\hat{n}_i f_0(q)\Psi, \tag{3.9}$$

$$T_j^i = -a^{-4}\int q^2 dq d\Omega \frac{q^2\hat{n}_i\hat{n}_j}{\sqrt{q^2 + a^2m^2}} f_0(q)\,(1+\Psi)\,, \tag{3.10}$$

where $(-g)^{-1/2} = a^{-4}(1 - \psi + 3\phi)$ and $dP_1dP_2dP_3 = (1-3\phi)q^2dqd\Omega$.

3.5 The Vlasov equation

The Vlasov equation (or collisionless Boltzman equation [16]) expresses the conservation of the number of particles along the path lines inside the phase space. Using

the variables $x^i, q, \hat{n}_j, \tau$, it is:

$$\frac{Df}{d\tau} = \frac{\partial f}{\partial \tau} + \frac{dx^i}{d\tau}\frac{\partial f}{\delta x^i} + \frac{dq}{d\tau}\frac{\partial f}{\partial q} + \frac{d\hat{n}_i}{d\tau}\frac{\partial f}{\partial \hat{n}_i} = 0.$$

The function f can be expanded as in 3.7 keeping only the first order perturbation terms. At the zero degree $dx^i/d\tau = P^i/P^0 = -P_i/P_0 = -q_i/\epsilon$. From the geodetic equation $P^0\dot{P}^0 + \Gamma^0_{\mu\nu}P^\mu P^\nu = 0$, we get $dq/d\tau = q\dot{\phi} + \epsilon\hat{n}_i\partial_i\psi$ at the first order. Moreover at the zero degree we have $d\hat{n}_i/d\tau = 0$, because with no metric perturbations the momenta have fixed direction. So the Vlasov equation results to be

$$f_0\dot{\Psi} - \frac{q_i}{\epsilon}f_0\partial_i\Psi + \left(q\dot{\phi} + \epsilon\hat{n}_i\partial_i\psi\right)\frac{\partial f_0}{\partial q} = 0,$$

and in the Fourier space (after dividing by f_0)

$$\dot{\Psi} - i\frac{q}{\epsilon}\left(\vec{k}\cdot\hat{n}\right)\Psi = -\left(\dot{\phi} + i\frac{\epsilon}{q}\left(\vec{k}\cdot\hat{n}\right)\psi\right)\frac{\partial \ln f_0}{\partial \ln q}.$$

The last equation describes how the neutrino phase space distribution reflects the metric perturbations.

3.6 Neutrino perturbations during the relativistic regime

When neutrinos are ultra-relativistic ($\epsilon = q$), the Vlasov equation becomes:

$$\dot{\Psi} - i\left(\vec{k}\cdot\hat{n}\right)\Psi = -\left(\dot{\phi} + i\left(\vec{k}\cdot\hat{n}\right)\psi\right)\frac{\partial \ln f_0}{\partial \ln q}.$$

The momentum q does not appear in the homogeneous equation, while the zero degree term has a fixed dependence on q once the distribution has been fixed. This reflects the fact that in a given point and in a given direction neutrinos are equally blueshifted and redshifted, so their spectrum remains a black body with a temperature variation $\delta T_\nu(x^i, q.\hat{n}_j, \tau)$ in a given point and in a given direction expressed by

$$\begin{aligned} f(x^i, q, \hat{n}_j, \tau) &= \left(\exp\left[\frac{q}{a\left(T_\nu + \delta T_\nu\right)}\right] + 1\right)^{-1} \\ &= f_0(q) + \frac{\partial f_0(q)}{\partial T_\nu}\delta T_\nu(x^i, \hat{n}_j, \tau). \end{aligned}$$

Since f_0 is a function of q/aT_ν, we find $\partial f_0/\partial T_\nu = -(q/T_\nu)\partial f_0/\partial q$ and

$$f(x^i, q, \hat{n}_j, \tau) = f_0(q) - \frac{\partial f_0(q)}{\partial \ln q}\frac{\delta T_\nu}{T_\nu}(x^i, \hat{n}_j, \tau).$$

This result can be considered as the phase space perturbation Ψ and so

$$\Psi(x^i, q, \hat{n}_j, \tau) = -\frac{\partial \ln f_0(q)}{\partial \ln q}\frac{\delta T_\nu}{T_\nu}(x^i, \hat{n}_j, \tau).$$

The conclusion is that the presence of $\partial \ln f_0/\partial \ln q$ in the Vlasov equation implies that the spectrum remains a Planck spectrum.

For massless neutrinos the unperturbed energy density and the pressure are $\bar{\varrho}_\nu = -3\bar{p}_\nu = T^0_0 = -T^i_i$; using equation 3.10

$$\bar{\varrho}_\nu = -3\bar{p}_\nu = a^{-4}\int q^2 dq d\Omega q f_0(q).$$

The perturbations for energy density $\delta\varrho_\nu$, pressure δp_ν, energy flux $\delta T^0_{i\nu}$ and stress tensor $\Sigma^i_{j\nu} = T^i_{j\nu} + p_\nu \delta_{ij}$ (the subscript ν stands for massless neutrinos) are given by

$$\begin{aligned}
\delta\varrho_\nu &= 3\delta p_\nu = a^{-4}\int q^2 dq d\Omega q f_0(q)\Psi, \\
\delta T^0_{i\nu} &= a^{-4}\int q^2 dq d\Omega q \hat{n}_i f_0(q)\Psi, \\
\Sigma^i_{j\nu} &= -a^{-4}\int q^2 dq d\Omega q \left(\hat{n}_i\hat{n}_j - \frac{1}{3}\delta_{ij}\right) f_0(q)\Psi.
\end{aligned}$$

At zero degree the unperturbed energy flux and stress tensor are nil. In order to reduce the number of variables, we can integrate in q the neutrino distribution function and define the quantity:

$$F_\nu(\vec{k}, \hat{n}_j, \tau) \equiv \frac{\int q^2 dq q f_0(q)\Psi}{\int q^2 dq q f_0(q)}.$$

After integrating the Vlasov equation in $q^2 dq q f_0(q)$ and dividing by $\int q^2 dq q f_0(q)$, we obtain the following collisionless Boltzman equation for massless neutrinos:

$$\dot{F}_\nu - i\left(\vec{k}\cdot\hat{n}\right)F_\nu = 4\left(\dot{\phi} + i\left(\vec{k}\cdot\hat{n}\right)\psi\right).$$

The number of variables can be further reduced by noticing that the equation depends on the direction $\hat{n}$ only through the angle $\vec{k}\cdot\hat{n}$, this is a consequence of the isotropy of the background. As an aftermath we can expand the perturbations in series of Legendre polynomials respect to this angle:

$$F_\nu(\vec{k}, \hat{n}, \tau) = \sum_{l=0}^{\infty}(-i)^l(2l+1)F_{\nu l}(\vec{k}, \tau)P_l(\hat{k}\cdot\hat{n}).$$

The perturbed quantities can be written as a function of the new variable and its expansion:

$$\begin{aligned}
\delta_\nu &= \frac{1}{4\pi}\int d\Omega F_\nu(\vec{k}, \hat{n}, \tau) = F_{\nu 0}, \\
\theta_\nu &= \frac{3i}{16\pi}\int d\Omega \left(\vec{k}\cdot\hat{n}\right)F_\nu(\vec{k}, \hat{n}, \tau) = \frac{3}{4}kF_{\nu 1}, \\
\sigma_\nu &= \frac{3}{16\pi}\int d\Omega \left[\left(\vec{k}\cdot\hat{n}\right)^2 - \frac{1}{3}\right]F_\nu(\vec{k}, \hat{n}, \tau) = -\frac{1}{2}F_{\nu 2},
\end{aligned}$$

the density contrast is given by the monopole term, the velocity gradient is the dipole term and the anisotropic stress is the quadrupole term. Using the orthonormality

of the Legendre polynomials, the recursive relation $(l+1)P_{l+1} = (2l+1)P_l - lP_{l-1}$ and the Vlasov equation, we find

$$\begin{aligned}
\dot{\delta}_\nu &= \frac{4}{3}\theta_\nu + 4\dot{\phi}, \\
\dot{\theta}_\nu &= -\frac{k^2}{4}\delta_\nu - k^2\sigma_\nu - k^2\psi, \\
\dot{F}_{\nu l} &= \frac{k}{2l+1}\left[(l+1)F_{\nu(l+1)} - lF_{\nu(l-1)}\right], \quad l \geq 2.
\end{aligned}$$

This set of equations describes the evolution of massless neutrinos distribution within the phase space. Notice that the first two equations are related , respectively, to the continuity equation and the Euler equation.

Assuming adiabatic initial condition during the RDE ($\delta_\nu = \delta_\gamma$), on scales greater than the horizon the neutrino distribution is static with local density and temperature perturbations proportional to the metric fluctuations. Using the first two perturbed Einstein equations in Fourier space, with little algebra we can find:

$$\delta_\nu = \delta_\gamma = -2\psi = 4\frac{\delta T_\nu}{T_\nu}, \qquad \theta_\nu = \theta_\gamma = -\frac{1}{2}k^2\tau\psi.$$

After the Hubble crossing, it means on scales smaller than the free-streaming scale, the different multipoles are populated one by one with a peak at $\tau \simeq l/k$.

In order to compare the evolution of neutrinos and photons before recombination, we combine the Euler equation and the continuity equation in a second order equation:

$$\ddot{\delta}_\nu = -\frac{1}{3}k^2\delta_\nu - \frac{4}{3}k^2\psi + 4\ddot{\phi} - \frac{4}{3}k^2\sigma_\nu.$$

With no σ this equation would be similar to those of photons before recombination. The physical meaning of the different terms is the following: $-\frac{1}{3}k^2\delta_\nu$ is the force arising from the relativistic pressure, $-\frac{4}{3}k^2\psi$ is the gravitational force, $4\ddot{\phi}$ stands for the expansion effect: a local growth of ϕ is equivalent to a local decrease of the scale factor and so an increase in the temperature and density of the black body. The neutrino anisotropic stress becomes important within the Hubble radius and acts as the viscosity force of a fluid. The neutrino overdensities δ_ν do not oscillate and are damped. As shown in Figure 3.2, the photon density contrast oscillates between the horizon crossing and the equivalence, while the neutrino density contrast is suddenly damped after the first oscillation. After the recombination δ_ν and δ_γ remain constant, they don't take part in the gravitational collapse because of the free-streaming and of the relativistic pressure. Notice that after decoupling, photons are free-streamed as relativistic neutrinos and δ_γ approaches -4ψ.

The homogeneous part of the relativistic Vlasov equation is:

$$\Psi(\vec{k}, \hat{n}, q, \tau) = -\frac{\delta T_\nu}{T_\nu}\left(\vec{k}\cdot\hat{n}\right)e^{i(\vec{k}\cdot\hat{n})\tau}\frac{\partial \ln f_0}{\partial \ln q}.$$

It reflects the free propagation through plane waves of the temperature perturbations: the free-streaming. In the basis of $F_{\nu l}(\vec{k}, \tau)$ this implies that $F_{\nu l}(\vec{k}, \tau) \propto j_l(k\tau)$, where $j_l(k\tau)$ are the first type Bessel spherical functions, so the contribution to δ_ν is proportional to $\sin(k\tau)/k\tau$; this contribution goes to zero after the horizon crossing

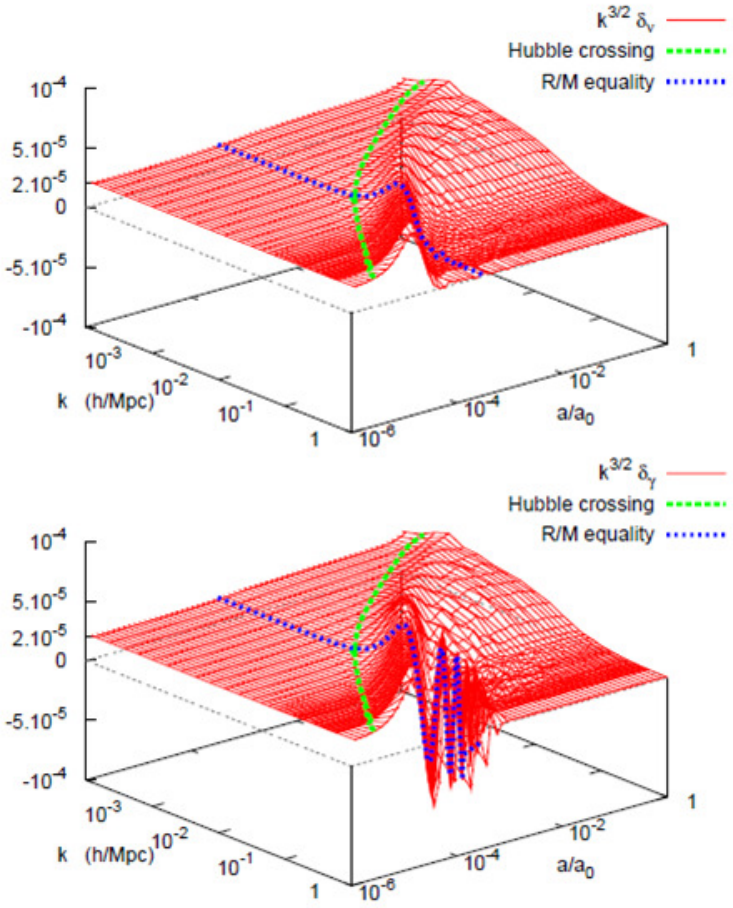

Figure 3.2. [17] The evolution of density perturbations in massless neutrinos compared with the evolution of density perturbations for photons, as a function of the scale factor and the Fourier wave number. The model is with three massless neutrinos. The time increases from left to right.

of the perturbations. Taking into account also the inhomogeneous solution, the global solution decreases during the RDE, because ϕ and ψ decrease. Instead during the MDE ϕ and ψ are constant, and the global solution is $\Psi = \psi\partial \ln f_0/\partial \ln q$. In the basis of $F_{\nu l}$ the global solution for δ_ν is

$$\delta_\nu = -4\psi(k) + \alpha(k)\sin(k\tau)/(k\tau), \quad \tau > \tau_{eq},$$

where the constant $\alpha(k)$ can be obtained by comparing this solution and the RDE one. The first term is the steady state where the relativistic pressure counterbalances the gravitational force in any potential well.

To sum up, during the relativistic regime the effects of free-streaming and relativistic pressure lead to a suppression of the neutrino density contrast within the Hubble radius: during the RDE δ_ν is more or less nil, while δ_b and δ_γ oscillate;

during the MDE it remains constant, while δ_b increases.

3.7 Neutrino perturbations during the non-relativistic regime

Also massive neutrinos obey to the collisionless Boltzman equation. Nevertheless the massive neutrinos distribution function is more complicated because of the mass. The unperturbed energy density and pressure of massless neutrinos are:

$$\begin{aligned}\bar{\varrho}_h &= a^{-4}\int q^2 dq d\Omega \epsilon f_0(q),\\ \bar{p}_h &= -\frac{1}{3}a^{-4}\int q^2 dq d\Omega \frac{q^2}{\epsilon} f_0(q),\end{aligned}$$

where the index h stands for HDM and $\epsilon = \sqrt{q^2 + a^2 m_\nu^2}$. Instead the perturbed quantities are:

$$\begin{aligned}\delta\varrho_h &= a^{-4}\int q^2 dq d\Omega \epsilon f_0(q)\Psi,\\ \delta p_h &= \frac{1}{3}a^{-4}\int q^2 dq d\Omega \frac{q^2}{\epsilon} f_0(q)\Psi,\\ \delta T^0_{ih} &= a^{-4}\int q^2 dq d\Omega q\hat{n}_i f_0(q)\Psi,\\ \Sigma^i_{jh} &= -a^{-4}\int q^2 dq d\Omega \frac{q^2}{\epsilon}\left(\hat{n}_i\hat{n}_j - \frac{1}{3}\delta_{ij}\right) f_0(q)\Psi.\end{aligned}$$

The comoving energy $\epsilon(q,\tau)$ depends on both the time and the momentum, so we cannot cancel the dependence on q by integrating, as we have done in the case of massless neutrinos. We can expand Ψ in Legendre series:

$$\Psi(\vec{k},\hat{n},q,\tau) = \sum_{l=0}^{\infty}(-i)^l(2l+1)\Psi_l(\vec{k},q,\tau)P_l(\hat{k}\cdot\hat{n}).$$

So the perturbed quantities (energy density, pressure, energy flux and anisotropic stress) in the Fourier space are:

$$\begin{aligned}\delta\varrho_h &= 4\pi a^{-4}\int q^2 dq \epsilon f_0(q)\Psi_o,\\ \delta p_h &= \frac{4\pi}{3}a^{-4}\int q^2 dq \frac{q^2}{\epsilon} f_0(q)\Psi_0,\\ (\bar{\varrho}_h + \bar{p}_h)\,\theta_h &= 4\pi k a^{-4}\int q^2 dq q f_0(q)\Psi_1,\\ (\bar{\varrho}_h + \bar{p}_h)\,\sigma_h &= -\frac{8\pi}{3}a^{-4}\int q^2 dq \frac{q^2}{\epsilon} f_0(q)\Psi_2.\end{aligned}$$

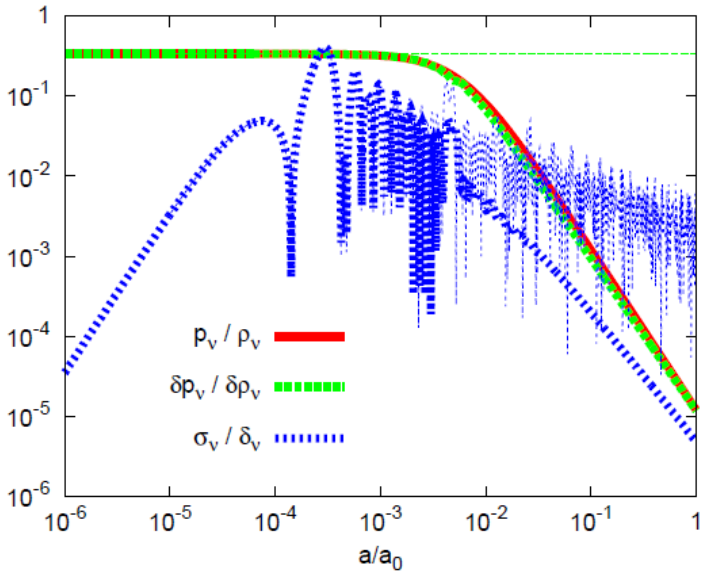

Figure 3.3. Evolution of neutrino isotropic pressure perturbations δp_h and of the anisotropic stress σ_h in units of the density perturbation, compared with the evolution of the parameter w of the equation of state. The modes are $k = 0.1hMpc^{-1}$ and undergo the Hubble crossing when $a/a_0 = 2.5 \times 10^{-5}$). The thin lines refer to massless neutrinos for which $w = 1/3$. Thick lines refer to neutrinos with $m = 0.1$ eV that have the non-relativistic transition at $a/a_0 = 5 \times 10^{-3}$. After the non-relativistic transition, pressure perturbation and anisotropic stress are negligible respect to the density perturbations.

The Vlasov equation becomes:

$$\begin{aligned}
\dot{\Psi}_0 &= \frac{qk}{\epsilon}\Psi_1 - \dot{\phi}\frac{\partial \ln f_o}{\partial \ln q}, \\
\dot{\Psi}_1 &= \frac{qk}{3\epsilon}\left(\Psi_2 - 2\Psi_0\right) + \frac{\epsilon k}{3q}\psi\frac{\partial \ln f_0}{\partial \ln q}, \\
\dot{\Psi}_l &= \frac{qk}{(2l+1)\epsilon}\left[(l+1)\Psi_{l+1} - l\Psi_{l-1}\right], \quad l \geq 2.
\end{aligned}$$

When neutrinos of a given family are inside the non relativistic regime (it means when the momenta verify $q \ll \epsilon \simeq am$) the above expressions of the perturbed quantities show that both δp_h and $(\bar{\varrho}_h + \bar{p}_h)\,\sigma_h$ are suppressed respect to $\delta\varrho_h$ (as shown in Figure 3.3).

As expected the Euler equation and the continuity equation become more and more similar to those of ordinary matter:

$$\begin{aligned}
\dot{\delta}_h &= -\theta_h + 3\dot{\phi}, \\
\dot{\theta}_h &= -\frac{\dot{a}}{a}\theta_h + k^2\psi.
\end{aligned}$$

As in the case of cold dark matter (and baryons after recombination), this leads to a second order equation for the evolution of perturbations

$$\ddot{\delta}_h + \frac{\dot{a}}{a}\dot{\delta}_h = -k^2\psi + 3\left(\ddot{\phi} + \frac{\dot{a}}{a}\dot{\phi}\right).$$

Neutrinos become non relativistic during the MDE when ϕ and ψ are nearly constant and $a \propto \tau^2$. In this case the solution of the above equation is:

$$\begin{aligned}\delta_h &= A\ln\tau + B - \frac{(k\tau)^2}{6}\psi \\ &= \tilde{A}\ln a + \tilde{B} - \frac{2}{3}\left(\frac{k}{aH}\right)^2\psi,\end{aligned}$$

where A and B (or $\tilde{A}$ and $\tilde{B}$) are constant of integration. The last term is the solution of the homogeneous equation and grows as τ^2 as well as the scale factor. This solution has a simple physical explanation:

- $k > k_{nr}$

  The modes that are inside the Hubble radius at the time of the non-relativistic transition have a density contrast δ_h much smaller than δ_{cdm} because of the free-streaming, but grows faster than δ_{cdm} because of the term $\tilde{A}\ln a$. When the first and the third term of the solution become equal, δ_h approaches the following behavior

  $$\delta_h \to -\frac{2}{3}\left(\frac{k}{aH}\right)^2\psi \propto a,$$

  that is the solution of the Poisson equation in a Universe matter dominated. So in an infinite time δ_h will be equal to δ_{cdm} at any scale. After decoupling baryons have the same behavior, but, since baryons have no free-streaming, δ_b suddenly reach δ_{cdm}. Instead neutrinos with masses around 1 eV or smaller are still far from reaching this asymptotic value, unless for scales close to k_{nr}; on smaller scales δ_h remains smaller than $\delta_{cdm} \simeq \delta_b$.

- $k > k_{nr}$

  The modes that are outside the Hubble radius at the time of the non-relativistic transition have a density contrast that is independent on time and are of the same order of δ_{cdm}. After the horizon crossing the solution becomes

  $$\delta_h \to -\frac{2}{3}\left(\frac{k}{aH}\right)^2\psi \propto a,$$

  and reaches δ_{cdm}.

To sum up, drawing the three behavior at an instant close to the end of the MDE, the expected scenario would be $\delta_h = \delta_{cdm} = \delta_b$ for $a_0H_0 < k < k_{nr}$ while for $k > k_{nr}$ the ratio $\delta_h/\delta_{cdm} = \delta_h/\delta_b$ would be smaller than one and decreasing to zero as k increases to infinite. These conclusions are nearly unchanged during the present cosmological constant dominated era. All these characteristics discussed so far are well depicted in Figure 3.4.

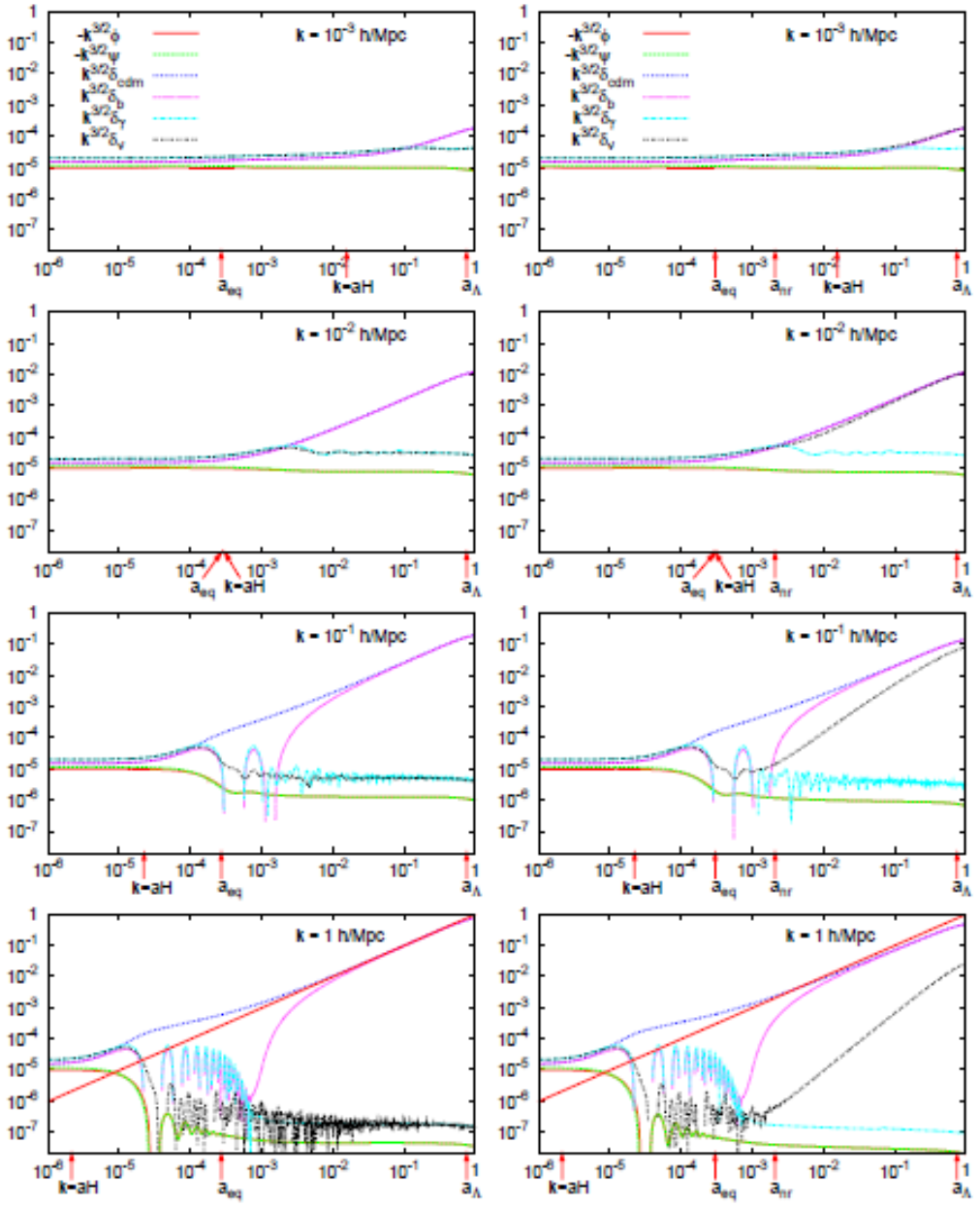

Figure 3.4. Evolution of metric perturbations and density perturbations as a function of the scale factor for modes in the range $10^{-3}h\mathrm{Mpc}^{-1} < k < 1h\mathrm{Mpc}^{-1}$ (from the top panel to the bottom panel) in case of two cosmological models: ΛCDM (on the left panels) with three massless neutrinos and ΛMDM (on the right) with three neutrinos sharing the same mass 0.46 eV. Both models consider $\Omega_m = 0.3$ and $\Omega_\Lambda = 0.7$ and $k^{3/2}\psi = -10^{-5}$ as initial condition.

The matter power spectrum nowadays and at any time after the non-relativistic transition is

$$P(k) = \begin{cases} \langle \delta_{cdm} \rangle & k < k_{nr} \\ \left[1 - \Omega_\nu / \Omega_m\right]^2 \langle \delta_{cdm}^2 \rangle & k \gg k_{nr} \end{cases} \tag{3.11}$$

where $\Omega_m = \Omega_{cdm} + \Omega_b + \Omega_\nu$.

3.8 Massive neutrinos and the suppression of matter perturbations growth

During the MDE ϕ and ψ are constant and so, using the Poisson equation $k^2\phi = -4\pi\delta\varrho$, within the Hubble radius the density contrast $\delta_{cdm} = \delta_b$ grows as $\left[a^2\left(\bar{\varrho}_{cdm} + \bar{\varrho}_b\right)\right]^{-1}$, it means linearly with the scale factor $\delta_{cdm} \propto a$.

During the MDE on scales smaller then the free-streaming scale the neutrino perturbations δ_ν do not contribute to the gravitational clustering. Since neutrinos have free-streaming $\delta_\nu \ll \delta_{cdm}$, and since $\bar{\varrho}_\nu < \bar{\varrho}_{cdm}$ one finds $\delta\bar{\varrho}_\nu \ll \delta\bar{\varrho}_{cdm}$: neutrinos are negligible in the Poisson equation. On the contrary neutrinos take part in the background expansion through the Friedmann equation. Physically speaking the clustering cannot counterbalance the expansion and the expansion slightly exceeds the clustering. As a consequence, ϕ and ψ slightly decay and δ_{cdm} increases more slowly than the scale factor.

In order to estimate the intensity of this effect, one considers the following equation:

$$\ddot{\delta}_{cdm} + \frac{\dot{a}}{a}\dot{\delta}_{cdm} = -k^2\psi + 3\left(\ddot{\phi} + \frac{\dot{a}}{a}\dot{\phi}\right).$$

Within the Hubble radius the zero degree term is dominated by the comoving gradient $-k^2\psi$ if the anisotropic stress is negligible. This gradient is given by the Poisson equation, so, replacing it, we obtain

$$\ddot{\delta}_{cdm} + \frac{\dot{a}}{a}\dot{\delta}_{cdm} = 4\pi a^2 \delta\varrho,$$

where $\delta\varrho$ is the total density perturbation. During the MDE with no neutrinos, should be $\delta_{cdm} = \delta_b$, the global density perturbation should be $\delta\varrho = \left(\bar{\varrho}_{cdm} + \bar{\varrho}_b\right)\delta_{cdm}$, the expansion rate should be $3\left(\dot{a}/a\right)^2 = 8\pi a^2\left(\bar{\varrho}_{cdm} + \bar{\varrho}_b\right) \propto a^{-1}$, the scale factor $a \propto \tau^2$, and the above equation should be

$$\ddot{\delta}_{cdm} + \frac{2}{\tau}\dot{\delta}_{cdm} - \frac{6}{\tau^2}\delta_{cdm} = 0,$$

with two solutions $\delta_{cdm} \propto \tau^2$ and $\delta_{cdm} \propto \tau^{-3}$; not considering the decreasing solution, the final solution is $\delta_{cdm} \propto a$.

Now we move to the case of massive neutrinos, during the MDE and on scales $k \gg k_{nr}$. The neutrino perturbation $\delta\varrho_\nu$ does not contribute to the Poisson equation $\delta\varrho = \left(\bar{\varrho}_{cdm} + \bar{\varrho}_b\right)\delta_{cdm}$, instead the neutrino background density contributes to the

expansion rate: $3\left(\dot{a}/a\right)^2 = 8\pi a^2\left(\bar{\varrho}_{cdm} + \bar{\varrho}_b + \bar{\varrho}_\nu\right)$. Assuming ϱ_ν dominated by non relativistic neutrinos, the slope would be about a^{-3}, and the number

$$f_\nu \equiv \frac{\varrho_\nu}{\left(\varrho_{cdm} + \varrho_b + \varrho_\nu\right)} = \frac{\Omega_\nu}{\Omega_m}$$

would remain approximatively constant. The evolution equation can be rewritten as

$$\ddot{\delta}_{cdm} + \frac{2}{\tau}\dot{\delta}_{cdm} - \frac{6}{\tau^2}\left(1 - f_\nu\right)\delta_{cdm} = 0.$$

Looking for solutions like $\delta_{cdm} \propto \tau^{2p}$, we find two roots

$$p_\pm = \frac{-1 \pm \sqrt{1 + 24\left(1 - f_\nu\right)}}{4},$$

so the increasing solution for the CDM density contrast is

$$\delta_{cdm} \propto a^{p_+} \simeq a^{1-\frac{3}{5}f_\nu},$$

where we have assumed $f_\nu \ll 1$. As expected, the growth of δ_{cdm} is reduced because one of the component of the Universe takes part to the expansion rate but is not involved in the gravitational clustering. The Poisson equation

$$-k^2\phi \propto a^{p_+-1} \simeq a^{-\frac{3}{5}f_\nu}$$

shows how during the MDE the gravitational potential decreases for the same reason.

In conclusion, at the end of the MDE and during the present cosmological constant dominated era, as already seen in the case of no neutrinos, ψ decreases as $g(a)$ and δ_{cdm} increases as $ag(a)$ (where the damping factor is normalized to 1 $g(a) = 1$ for $a \ll a_\Lambda$). The combined effect of neutrinos and cosmological constant on the growth of δ_{cdm} can be approximated as

$$\delta_{cdm} \propto \left[ag(a)\right]^{p_+} \simeq \left[ag(a)\right]^{1-\frac{3}{5}f_\nu}. \tag{3.12}$$

3.9 Neutrino mass effects on matter power spectrum

In order to understand the effects of neutrinos on matter power spectrum we focus on the difference between the ΛCDM model and ΛMDM (Lambda Mixed[1] Dark Matter) model, respectively with massless neutrinos and with massive neutrinos.

1. $k < k_{nr}$ (large scales)

   Neutrino perturbations are not affected by free-streaming and in the non relativistic regime are practically indistinguishable from the CDM perturbations. In particular within the Hubble radius neutrinos take part on the Poisson equation with $\delta_\nu = \delta_{cdm}$, and so the density contrast grows as a. Once Ω_m has been fixed, this branch of the matter power spectrum is neither affected by the value of f_ν nor by the value of the neutrino mass.

[1] Cold Dark Matter plus Hot Dark Matter related to massive neutrinos.

2. $k \gg k_{nr}$ and $k \gg k_{eq}$ (small scales)

   The two spectra are very different. First of all the radiation-matter equivalence does not take place at the same value of the scale factor, because $(a_{eq}/a_0) = \Omega_r / (\Omega_r + \Omega_{cdm}) = (1 - f_\nu)^{-1} \Omega_r / \Omega_m$, where Ω_r contains the densities of photons and three massless neutrinos. Since the two models share the same values of Ω_m and Ω_r, the ratio between the two values of the scale factor at the equivalence is $a_{eq}^{f_\nu} / a_{eq}^{f_\nu=0} = (1 - f_\nu)^{-1}$. At the equivalence and at any time before the non relativistic transition, the two models are equivalent, unless for a shift in the scale factor of the quantity we have just seen above. So the identity

$$\delta_{cdm}^{f_\nu}[a] = \delta_{cdm}^{f_\nu=0}[(1 - f_\nu)\, a] \tag{3.13}$$

   holds until $a \leq a_{nr}$. Suddenly after the instant of $a = a_{nr}$, in the model with massive neutrinos the mechanism described in the last section is activated and the growth of the matter perturbations is reduced. As shown in Fig. 3.5, the presence of neutrino masses leads to an attenuation of the linear matter power spectrum on small scales. Assuming f_ν independent on time for $a \geq a_{nr}$, the growth of CDM perturbations will follow equation 3.12 and will increase exponentially with the scale factor

$$\delta_{cdm}^{f_\nu}[a_0] = \left(\frac{a_0 g(a_0)}{a_{nr}}\right)^{1-\frac{3}{5}f_\nu} \delta_{cdm}^{f_\nu}[a_{nr}]\,.$$

   The case of massless neutrinos follows the behavior of massive neutrinos until $a = (1 - f_\nu)\, a_{nr}$, it means until the scale factor reaches the value of the non relativistic transition for massive neutrinos, shifted backwards by the factor given in 3.13. At this moment the exponential growth of $\delta_{cdm}^{f_\nu=0}$ as a function of the scale factor takes the exponent $\left(1 - \frac{3}{5} f_\nu\right)$. This exponent increases to one, so $\delta_{cdm}^{f_\nu=0}$ becomes a linear function of a. One can write

$$\delta_{cdm}^{f_\nu=0}[a_0] \simeq \left(\frac{a_0 g(a_0)}{(1 - f_\nu)\, a_{nr}}\right) \delta_{cdm}^{f_\nu=0}[(1 - f_\nu)\, a_{nr}]\,,$$

   but this expression slightly overestimates the growth of perturbations in the case of massless neutrinos, because it assumes that after the instant of $a = a_{nr}$ the slope becomes suddenly linear. Numerical results show a slightly slow growth

$$\delta_{cdm}^{f_\nu=0}[a_0] \simeq \left(\frac{a_0 g(a_0)}{(1 - f_\nu)^{1/2}\, a_{nr}}\right) \delta_{cdm}^{f_\nu=0}[(1 - f_\nu)\, a_{nr}]\,.$$

   Using this result, we can calculate the ratio between the present values of δ_{cdm} in the two models

$$\frac{\delta_{cdm}^{f_\nu}[a_0]}{\delta_{cdm}^{f_\nu=0}[a_0]} = (1 - f_\nu)^{1/2} \left(\frac{a_0 g(a_0)}{a_{nr}}\right)^{-\frac{3}{5}f_\nu}.$$

   Moreover from equation 3.11, the ratio between the matter power spectra of the two models can be calculated:

$$\frac{P(k)^{f_\nu}}{P(k)^{f_\nu=0}} = (1 - f_\nu)^3 \left(\frac{a_0 g(a_0)}{a_{nr}}\right)^{-\frac{6}{5}f_\nu}.$$

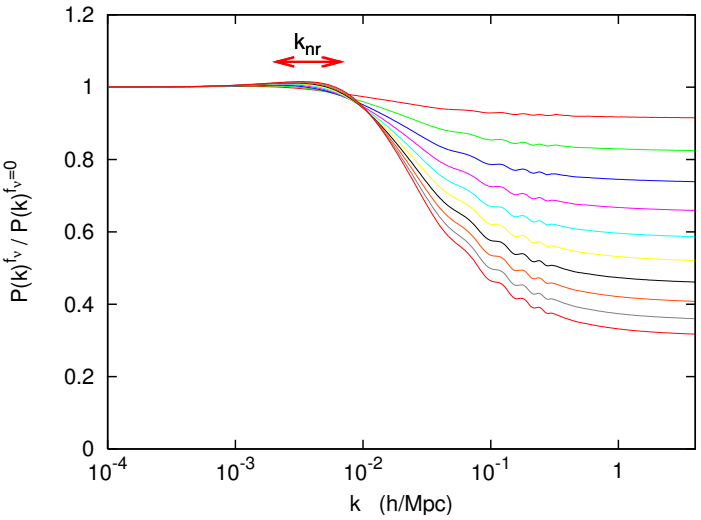

Figure 3.5. Ratio of the matter power spectrum including three degenerate massive neutrinos with density fraction f_ν to that with three massless neutrinos. The parameters $(\omega_{\rm m}, \Omega_\Lambda) = (0.147, 0.70)$ are kept fixed, and from top to bottom the curves correspond to $f_\nu = 0.01, 0.02, 0.03, \ldots, 0.10$. The individual masses m_ν range from 0.046 eV to 0.46 eV, and the scale $k_{\rm nr}$ from $2.1 \times 10^{-3} h\,{\rm Mpc}^{-1}$ to $6.7 \times 10^{-3} h\,{\rm Mpc}^{-1}$ as shown on the top of the figure. $k_{\rm eq}$ is approximately equal to $1.5 \times 10^{-2} h\,{\rm Mpc}^{-1}$.

Replacing (a_o/a_{nr}) with $2000 m_\nu/1{\rm eV}$ and assuming that all the neutrino families N_ν share the same mass m_ν, one can write m_ν as $(\omega_\nu/N_\nu)\,93.1{\rm eV}$, where $\omega_\nu = h^2\Omega_\nu$. The result depends only on $f_\nu, N_\nu, \omega_m(\omega_m = h^2\Omega_m), \Omega_\Lambda$ and it is

$$\frac{P(k)^{f_\nu}}{P(k)^{f_\nu=0}} = (1-f_\nu)^3 \left(1.9 \times 10^5 g(a_0)\omega_m f_\nu/N_\nu\right)^{-\frac{6}{5}f_\nu}.$$

Figure 3.5 shows the ratio of the matter power spectrum for ΛMDM over that of ΛCDM, for different values of f_ν, but for fixed parameters $(\omega_{\rm m}, \Omega_\Lambda)$. Here the ΛMDM model has three degenerate massive neutrinos. As expected from the analytical results, this ratio is a step-like function, equal to one for $k < k_{\rm nr}$ and to a constant for $k \gg k_{\rm eq}$. The value of the small-scale suppression factor is plotted in Figure 3.6 as a function of f_ν and of the number N_ν of degenerate massive neutrinos, for fixed $(\omega_{\rm m}, \Omega_\Lambda)$. The semi-analytical expression is a found to be a good approximation of the exact numerical results. Finally, considering $f_\nu < 0.07$, we find a linear expression:

$$\frac{P(k)^{f_\nu}}{P(k)^{f_\nu=0}} \simeq -8 f_\nu.$$

In conclusion the combined effect of equivalence shift and reduction of CDM fluctuation growth during the MDE turn out in a damping of the perturbations at

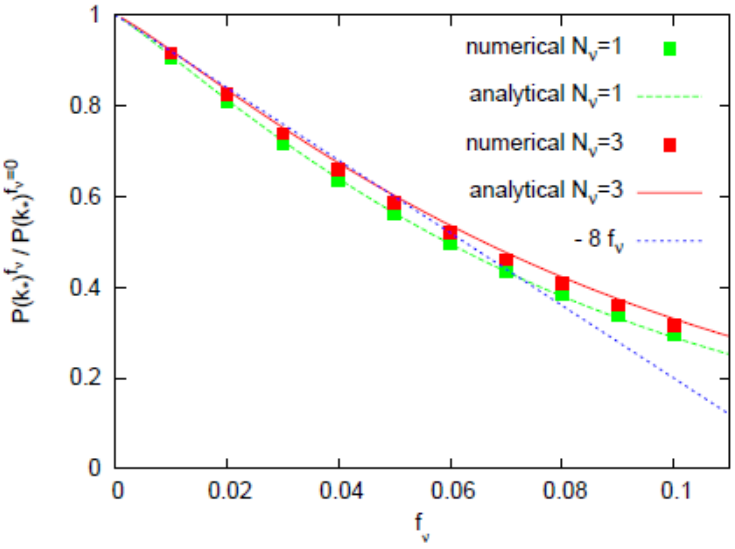

Figure 3.6. Ratio between the matter power spectrum in the case of massless neutrinos and the matter power spectrum in the case of massive neutrinos, as a function of the neutrino density f_ν. The initial conditions are the scale $k = 5h$ Mpc^{-1} and the parameters $(\omega_m, \Omega_\Lambda) = (0.147, 0.7)$. The cases $N_\nu = 1$ and $N_\nu = 3$ degenerate in mass are considered. The numerical results are compared with the linear approximation of the analytical expression.

small scales for $k > k_{nr}$, as can be seen in Figure 3.7. The reason is that relativistic neutrinos represent a radiation component at decoupling and so they cause a delay in the equivalence. This is important because the perturbation growth becomes strong only during the MDE. So, because of the equivalence delay, the small scales, that cross the horizon before the equivalence, grow slowly for a longer time and in the matter power spectrum the small scale perturbations are suppressed. On the other side, the large scale perturbations, that in any case will cross the horizon after the equivalence, independently on neutrinos, are not affected by the equivalence delay and so there is no suppression in the matter power spectrum.

3.10 Neutrino mass effects on CMB

The strongest neutrino mass effect on CMB is related to the equivalence delay. Since neutrinos are still relativistic at decoupling they must be considered as a radiation component at the equivalence, so $\varrho_b + \varrho_{cdm} = \varrho_\gamma + \varrho_\nu$. From this equation we obtain

$$a_{eq} = \frac{\omega_r}{\omega_b + \omega_{cdm}},$$

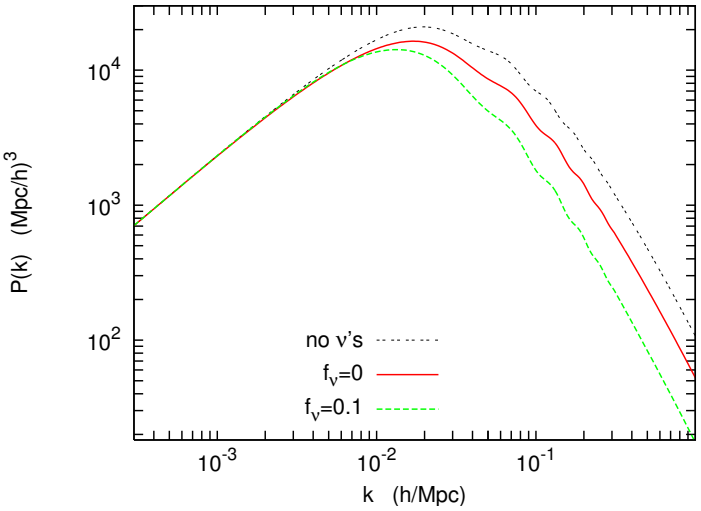

Figure 3.7. Matter power spectrum $P(k)$ for three models: the neutrinoless ΛCDM model with no neutrinos, a more realistic ΛCDM model with three massless neutrinos ($f_\nu \simeq 0$), and finally a ΛMDM model with three massive degenerate neutrinos and a total density fraction $f_\nu = 0.1$. In all models, the values of (ω_b, ω_m, Ω_Λ, A_s, n, τ) have been kept fixed.

where ω_r is the present radiation density assuming neutrinos remained massless and is related to the equation:

$$\varrho_r = \left[1 + \frac{7}{8}\left(\frac{4}{11}\right)^{4/3} N_\mathrm{eff}\right] \varrho_\gamma,$$

where N_eff is the effective number of relativistic degrees of freedom. If f_ν increases a_{eq} increases proportionally to $[1 - f_\nu]^{-1}$: the equivalence is delayed.

The equivalence delay related to the higher radiation content due to the presence of neutrinos causes an enhancement of the early Integrated Sachs Wolfe (ISW) effect (see section 2.9.2), because decoupling is not well settled down during the MDE but happens when the gravitational potential is still varying as in the RDE. This effect results in an increase of the perturbation peaks at low multipole $\ell \lessapprox 200$. If a certain scale oscillates more time during the time scale of potential variation, the average of positive and negative contributions is nil. If at Last Scattering the potential varies with a characteristic time scale τ_{LS}, the perturbation scales evolving with the same time are $k^{-1} = \tau_{LS} c_s$, that is approximately the dimension of the horizon at that epoch. Since the relation between multipoles and scales is $l \propto k d_{LS}$ where d_{LS} is the Last Scattering surface distance, scales $k = (\tau_{LS} c_s)^{-1}$ correspond to multipoles $l \approx 200$, that is the first peak. So the early ISW effect and the subsequent enhancement of the peaks are more pronounced around the first peak, as can be seen in Figure 3.8.

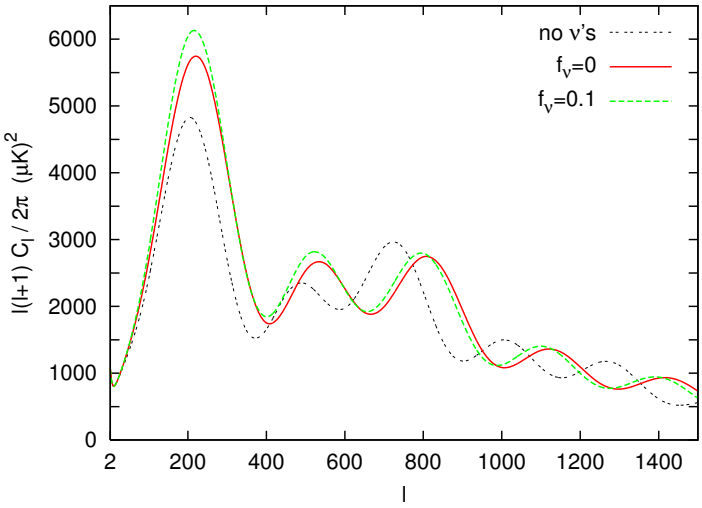

Figure 3.8. CMB temperature anisotropy spectrum C_l^T for three models: the neutrinoless ΛCDM model with no neutrinos, a more realistic ΛCDM model with three massless neutrinos ($f_\nu \simeq 0$), and finally a ΛMDM model with three massive degenerate neutrinos and a total density fraction $f_\nu = 0.1$. In all models, the values of ($\omega_{\rm b}$, $\omega_{\rm m}$, Ω_Λ, A_s, n, τ) have been kept fixed.

Besides the early ISW, the potential variation directly affects CMB anisotropies. The oscillations follow the equation 2.10

$$\frac{d}{d\tau}\left[(1+R)\,\dot{\Theta}\right] + \frac{k^2}{3}\Theta = -\frac{k^2}{3}\,(1+R)\,\psi - \frac{d}{d\tau}\left[(1+R)\,\dot{\phi}\right].$$

in the case constant potentials. But when the potentials are varying the last term is dominant and produces the enhancement of the peaks located at the scales that cross the horizon before the equivalence. Since the equivalence takes place at redshift $z_{eq} \approx 24000 h^2 \Omega_m$ (with $\Omega_r = 4.13 \times 10^{-5} h^{-2}$), the scales affected are such that $k > k_{eq} \approx (14\text{Mpc})^{-1} h^2 \Omega_m$.

3.11 The effective number of relativistic degrees of freedom

In a standard physics scenario the particles contributing to the total value of the relativistic degrees of freedom $g_* \simeq 10.75$ are electrons, three neutrinos (and their antiparticles), and photons. Any extra relativistic degrees of freedom can be parameterized in terms of an excess with respect to the standard effective neutrino number $N_{\rm eff} = 3$. More precisely it is $N_{\rm eff} \simeq 3.046$ after accounting for QED

corrections and non-instantaneous decoupling of neutrinos that means that neutrinos are still in thermal contact with the primordial plasma when the electron-positron annihilations start, and so neutrinos carry out a portion of the energy released by these processes. The effective number of relativistic degrees of freedom appears in the total radiation energy density:

$$\varrho_r = \left[1 + \frac{7}{8}\left(\frac{4}{11}\right)^{4/3} N_{\rm eff}\right] \varrho_\gamma,$$

where ρ_γ is the energy density of photons.

A first effect of $N_{\rm eff}$ is related to the primordial helium abundance Y_P. Changing $N_{\rm eff}$ affects the freeze-out temperature T_{freeze} during Big Bang Nucleosynthesis (BBN) [2] and therefore the final neutron to proton ratio n_n/n_p [18]. Larger $N_{\rm eff}$ means earlier freeze-out, larger n_n/n_p, and larger Y_p. However, as shown in [19], one should be careful when comparing the effective number of relativistic degrees of freedom at the times of BBN and Last Scattering, since they may be related to different physics. This is because the energy density in relativistic species may change from the time of BBN ($T \sim$ MeV) to the time of LS ($T \sim$ eV). For instance, if one of the active neutrinos has a mass in the range eV $< m <$ MeV and decays into sterile particles such as other neutrinos etc. with lifetime $t(\text{BBN}) < \tau < t(\text{LS})$, then the effective number of relativistic degrees of freedom at LS would be different from the number at BBN. Such a massive active neutrino is disfavored by experimental results on neutrino oscillations that seem to indicate a mass lighter than 1 eV. One could instead consider sterile neutrinos mixed with active ones which could be produced in the early Universe by scattering, and subsequently decay. The mixing angle must then be large enough to thermalize the sterile neutrinos. One finds that such a sterile neutrino must have a mass of a few MeV, otherwise with a KeV mass the decay time would be longer than the age of the Universe and so it would certainly not have decayed at $t(\text{LS})$.

The effect of $N_{\rm eff}$ on cosmological observables (e.g. CMB anisotropy power spectrum and galaxy power spectrum) is mainly related to the dependence of $N_{\rm eff}$ on the epoch of matter-radiation equality a_{eq}. In particular, as it has been shown in the previous paragraph for massive neutrinos, for what concern the CMB, an increase in a_{eq} changes the extent of the early Integrated Sachs Wolfe effect. The relation between a_{eq} and $N_{\rm eff}$ is given by equating energy densities:

$$\rho_{rad} = \rho_m \quad \Longleftrightarrow \quad a_{eq} = \frac{1 + 0.227 N_{\rm eff}}{40484\,\Omega_m\,h^2}\,.$$

[2] The Big bang Nucleosynthesis starts with the merging of neutrons and protons in deuterium, and proceeds through subsequent merging to the formation of the heavier nuclei, until each free neutron is bounded on an atomic nuclei. Since the deuterium binding energy is greater than the hydrogen ionization energy of a factor $B_D/Q = 1.6 \times 10^5$, the deuterium production is activated at temperature 1.6×10^5 times greater than the recombination temperature $T_{rec} = 3740$K, it means at $T_{nuc} \approx 6 \times 10^8$K, at time $t_{nuc} \approx 300$s. The nucleosynthesis is dismissed at time $t \simeq \tau_n \approx 10$min, when the temperature was $T \approx 4 \times 10^8$K.

This shows a linear relationship for $a_{eq}(N_{\rm eff})$, which transfers to the baryon to photon ratio at equality [20]:

$$\begin{aligned} R_{eq} &= \frac{3\rho_b}{4\rho_\gamma}\Big|_{a_{eq}}\,, \\ &= 30496\,\Omega_b\,h^2\,a\,\Big|_{a_{eq}}\,, \\ &= \frac{1+0.227N_{\rm eff}}{1.3276}\,\frac{\Omega_b}{\Omega_m}\,. \end{aligned}$$

The presence of baryons in the relativistic cosmic fluid slows down the sound speed according to the definition,

$$c_s \equiv 1/\sqrt{3(1+R)}\,, \tag{3.14}$$

and so this quantity is also affected at equality by the effective neutrino number. This reflects in the size of sound horizon at a generic time τ [20]:

$$\begin{aligned} r_s &\equiv \int_0^\tau d\tau'\,c_s(\tau')\,, \\ &= \int_0^a \frac{da}{a^2H}\,c_s(a)\,, \\ &\approx \frac{2}{3k_{eq}}\sqrt{\frac{6}{R_{eq}}}\,\ln\left\{\frac{\sqrt{1+R}+\sqrt{R+R_{eq}}}{1+\sqrt{R_{eq}}}\right\}\,, \\ &= \frac{6.612\times10^{-3}}{H_0\sqrt{\Omega_m\Omega_b h^2}}\,\ln\left\{\frac{\sqrt{1+R}+\sqrt{R+R_{eq}}}{1+\sqrt{R_{eq}}}\right\}\,. \end{aligned} \tag{3.15}$$

The last equations come from assuming the Universe is matter dominated during recombination. As can be seen, the sound horizon depends on $N_{\rm eff}$ through R_{eq}.

In [21] the authors claim that changing the number of allowed neutrinos makes an increasing difference at high ℓ that is not related to early ISW effect. In contrast, using qualitative arguments, they demonstrate that this difference is predominantly due to increased Silk Damping, caused by the increased expansion rate. As already explained in section 2.9, temperature anisotropies on scales smaller than the photon diffusion length are damped by the diffusion, a phenomenon known as Silk damping. Diffusion causes the drop in power toward high ℓ and makes the power spectrum sensitive to the angular scale of the diffusion length, τ_d. To second order in λ_{mfp}/λ, where λ_{mfp} is the photon means free path, the temperature fluctuations are suppressed by $\exp[-(2r_d/\lambda)^2]$ where the mean squared diffusion distance at recombination is

$$r_d^2 = (2\pi)^2\int_0^{a*}\frac{da}{a^3\sigma_T n_e H}\left[\frac{R^2+\frac{6}{15}(1+R)}{6(1+R^2)}\right]$$

where n_e is the number density of free electrons, σ_T is the Thompson cross-section, $a*$ is the scale factor at recombination and the factor in square brackets is due to the directional and polarization dependence of Thompson scattering. If we approximate $a*$ as independent on H, then $r_d \propto 1/\sqrt{H}$. This is expected for a random walk process:the distance increases as the square root of time. Increasing H (which happens when we increase $N_{\rm eff}$) leads to smaller r_d which would decrease the

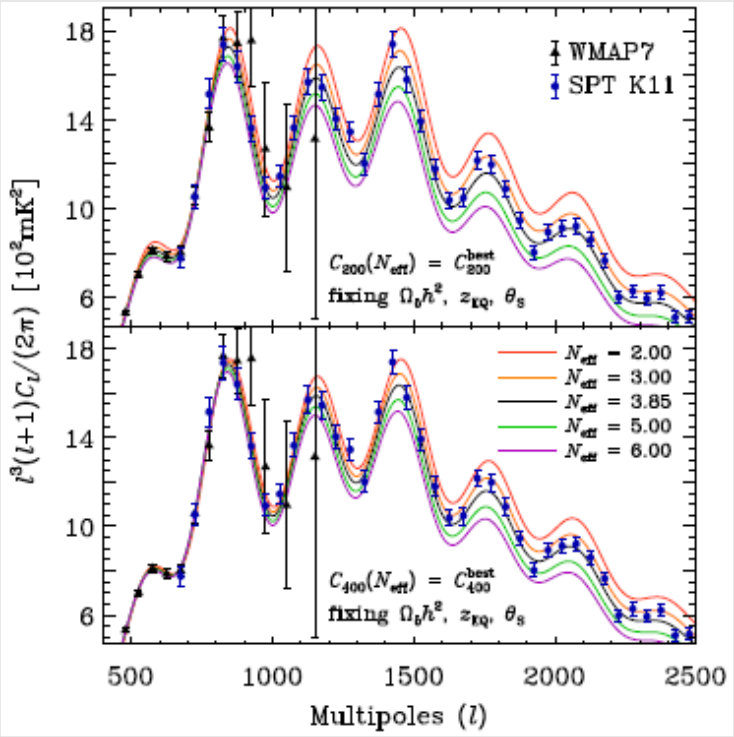

Figure 3.9. Top panel: WMAP and SPT power spectrum measurements, and theoretical power spectra normalized at $\ell = 200$. The black central curve is for the best-fit ΛCDM + $N_{\rm eff}$ model assuming BBN consistency. The other model curves are for $N_{\rm eff}$ varying from 2 to 6 with ρ_b, θ_s and z_{EQ} held fixed. Larger $N_{\rm eff}$ corresponds to lower power. Bottom panel: Same as above except normalized at $\ell = 400$ where the ISW contribution is negligible. We see most of the variation remains [21].

amount of damping. Nevertheless to keep the angular size of the sound horizon θ_s ($\theta_s = r_s/D_A$) fixed at the observed value, the angular diameter distance D_A must also decrease as $1/H$. Since D_A decreases by more than would be necessary to keep θ_d fixed, θ_d increases, which means the damping is increased, as can be seen in Figure 3.9.

Chapter 4

Statistical methods in Cosmology

4.1 Inference methods in cosmology and Bayes theorem

In cosmology linear perturbation theory is a stochastic theory. For a given model with parameters p_i the theory predicts its probability. The likelihood $\mathcal{L}(d_n, p_i)$ is defined as the probability to observe data d_n given a model with parameters p_i. Nevertheless the likelihood can be used to solve the inverse problem that is to estimate how likely is a theoretical model once the experimental data are given, or to infer the confidence intervals on p_i from the data.

The Bayesian method is based on a theoretical model characterized by N free parameters p_i and N priors $P(p_i)$ that represent our knowledge of the parameters before the experimental data. These priors can be simply flat probability distribution in the interval of physically possible values of the parameters. For instance in the case of f_ν, it is reasonable to define $P(f_\nu) = 1$ in the interval $0 < f_\nu < 1$ and $P(f_\nu) = 0$ otherwise. Priors can also depend on data from previous experiments. For instance, if the Hubble constant is one of the free parameters, its prior can be obtained from the results of the Hubble Space Telescope Key Project and it can be defined as a gaussian with central value 73.8 Km/s/Mpc and standard deviation $\sigma = 2.4$ Km/s/Mpc [3]. Given the likelihood $\mathcal{L}(d_n, p_i)$ and the prior $P(p_i)$ we can calculate the posterior of any parameter p_i taking into account the data.

Now we move to the case of CMB probability function. If the theory provides the value of the temperature T in each point of the sky, each measure will be the sum of a constant signal T and noise that follows a Gaussian distribution with nil mean and variance σ_T^2 (standard deviation σ_T). So the free parameters of the theory are two: T and σ_T. If only one measure d is available, the probability to get d from

the theory would be

$$P\left[d|T,\sigma_T\right] \equiv \mathcal{L}\left(d;T,\sigma_T\right) = \frac{1}{\sqrt{2\pi\sigma_T^2}} \exp\left\{-\frac{\left(d-T\right)^2}{2\sigma_T^2}\right\}.$$

In the case of N_m independent measures the total probability function is the product of each probability function

$$P\left[\{d_i\}\,|T,\sigma_T\right] \equiv \mathcal{L}\left(\{d_i\}\,;T,\sigma_T\right) = \frac{1}{\left(\sqrt{2\pi\sigma_T^2}\right)^{N_m}} \exp\left\{-\frac{\sum_{i=1}^{N_m}\left(d_i-T\right)^2}{2\sigma_T^2}\right\}.$$

Notice that, even if the data have a Gaussian distribution, the probability function is Gaussian only respect to T, but not respect to σ_T^2. In order to evaluate the parameters we need the posterior $P\left[T,\sigma_T|\,\{d_i\}\right]$, while so far we have only the likelihood $P\left[\{d_i\}\,|T,\sigma_T\right]$. The relation between these two quantities is given by

$$P\left[B\cap A\right] = P\left[B|A\right]P\left[A\right] = P\left[A|B\right]P\left[B\right];$$

and from the last equality we get the Bayes theorem:

$$P\left[B|A\right] = \frac{P\left[A|B\right]P\left[B\right]}{P\left[A\right]}.$$

In the case of CMB it is:

$$P\left[T,\sigma_T|\,\{d_i\}\right] = \frac{P\left[\{d_i\}\,|T,\sigma_T\right]P\left[T,\sigma_T\right]}{P\left[\{d_i\}\right]}.$$

Since the denominator does not depend on T nor on σ_T, it does not affect the width of the probability function nor the position of the peak in the parameter space, so it is negligible. If we make the conservative assumption of a flat prior $P\left[T,\sigma_T\right]$, we obtain

$$\mathcal{L} \propto P\left[T,\sigma_T|\,\{d_i\}\right],$$

where the proportionality constant is independent on the parameters and so not important. The best fit values of the parameters are located where the probability function has a peak, so they can be found by differentiating $\mathcal{L}$ respect to each parameter. The derivative respect to T is

$$\frac{\partial\mathcal{L}}{\partial T} = \frac{\sum_{j=1}^{N_m}\left(d_j-T\right)}{\sigma_T^2\left(\sqrt{2\pi\sigma_T^2}\right)^{N_m}} \exp\left\{-\frac{\sum_{i=1}^{N_m}\left(d_i-T\right)^2}{2\sigma_T^2}\right\},$$

putting it equal to zero one finds

$$\sum_{i=1}^{N_m}\left(d_i-T\right) = 0,$$

so the maximum of the probability function is located where

$$T = \bar{T} = \frac{1}{N_m} \sum_{i=1}^{N_m} d_i,$$

that represents the expected value. Similar for σ_T^2 the derivative is

$$\frac{\partial \mathcal{L}}{\partial \sigma_T^2} = \mathcal{L} \left\{ -\frac{N_m}{2\sigma_T^2} + \frac{\sum_{i=1}^{N_m} (d_i - T)^2}{2\sigma_T^4} \right\}$$

putting it equal to zero one finds the most likely value of the variance

$$\sigma_T^2 = \frac{\sum_{i=1}^{N_m} \left(d_i - \bar{T} \right)^2}{N_m}.$$

The error related to these best fit values is proportional to the width of the probability function. The width can be calculated assuming that $\mathcal{L}$ is Gaussian respect to the parameters, that means $\ln \mathcal{L}$ is quadratic respect to the parameters. The variance (the square of the error) of a Gaussian distribution is minus the inverse of two times the quadratic coefficient. With simple algebra it results

$$\begin{aligned} \ln \mathcal{L}(T) &= \ln \mathcal{L}(\bar{T}) + \frac{1}{2} \frac{\partial^2 \ln \mathcal{L}}{\partial T^2} \bigg|_{T=\bar{T}} (T - \bar{T})^2 \\ &= \ln \mathcal{L}(\bar{T}) - \frac{N_m}{2\sigma_T^2} (T - \bar{T})^2, \end{aligned}$$

so the width of the probability function is $\sigma_T / N_m^{1/2}$. This value represents the 1σ error in the evaluation of T. Notice that the uncertainty on the evaluation of T is not equal to σ_T. The probability function can be rewritten using the best fit values of the parameters:

$$\mathcal{L} = \frac{1}{\sqrt{2\pi C_N}} \exp \left\{ -\frac{\left(T - \bar{T} \right)^2}{2C_N} \right\}, \tag{4.1}$$

where the variance due to the noise is

$$C_N = \frac{\sigma_T^2}{N_m}.$$

This probability function has exactly the same maximum and width of the previous one.

This analysis implies the existence of a theory that predicts the exact value of the temperature in each point of the sky; such a theory does not exist, and we have only a distribution of the temperature from which we can calculate T in each pixel. In the case of a Gaussian distribution the probability that the temperature lies in the interval T and $T + dT$ is

$$P(T)dT = \frac{1}{\sqrt{2\pi C_S}} \exp \left\{ \frac{-T^2}{2C_S} \right\} dT,$$

where C_S is the expected variance due only to the signal, independent on the noise. In order to have the probability function one has to calculate the convolution between this "a priori" probability and the likelihood 4.1, where $\bar{T}$ is now replaced by the estimated value of the temperature Δ. So we have

$$P\left[\Delta|C_S\right] = \sum_t P\left[\Delta|T\right] P\left[T|C_S\right],$$

that means the likelihood is the integral over all possible values of the temperature. This is called marginalization and the results is

$$\mathcal{L} = \int_{-\infty}^{+\infty} \frac{dT}{\sqrt{2\pi C_S}} \exp\left\{\frac{-T^2}{2C_S}\right\} \frac{1}{\sqrt{2\pi C_N}} \exp\left\{\frac{-(\Delta - T)^2}{2C_N}\right\}.$$

The argument of the exponential can be rewritten as

$$-\frac{T^2 C}{2C_S C_N} + \frac{\Delta T}{C_N} - \frac{\Delta^2}{2C_N} = -\frac{C}{2C_S C_N}\left[T - \frac{C_S \Delta}{C}\right]^2 + \frac{C_S \Delta^2}{2CC_N} - \frac{\Delta^2}{2C_N}$$

where $C = C_S + C_N$ is the covariance matrix. Changing the integration variable from T to $x = T - C_S\Delta/C$, and after integrating, the result is

$$\begin{aligned}\mathcal{L} &= \frac{1}{\sqrt{2\pi C_N}} \exp\left\{-\frac{\Delta^2}{2C}\right\} \int_{-\infty}^{+\infty} \frac{dx}{\sqrt{2\pi C_S}} \exp\left\{-\frac{Cx^2}{2C_S C_N}\right\} \\ &= \frac{1}{\sqrt{2\pi C}} \exp\left\{-\frac{\Delta^2}{2C}\right\}.\end{aligned}$$

This is the likelihood for an experiment with just one pixel. As expected, the measured temperatures lie along a Gaussian distribution with the variance given by the sum of the variance due to the noise and the one due to the signal.

In the case of N_P pixels it is

$$\mathcal{L} = \frac{1}{(2\pi)^{N_P/2} \left(\det C\right)^{1/2}} \exp\left\{-\frac{1}{2}\Delta C^{-1} \Delta\right\},$$

where now Δ is an array of data of the N_P measures and the total covariance matrix C is $N_P \times N_P$ and is symmetric (so it has $N_P(N_P+1)/2$ elements). If C is diagonal and proportional to the identity (that means the elements on diagonal are equal), it is

$$\mathcal{L} = \frac{1}{(2\pi)^{N_P/2} \left(C_S + C_N\right)^{N_P/2}} \exp\left\{-\frac{1}{2}\frac{\sum_{i=1}^{N_P} \Delta_i^2}{C_S + C_N}\right\}.$$

In this case the C_S values are those who maximize the likelihood. Differentiating respect to C_S one obtains

$$\frac{\partial \mathcal{L}}{\partial C_S} = \mathcal{L}\left\{-\frac{N_P}{2(C_S + C_N)} + \frac{\sum_{i=1}^{N_P} \Delta_i^2}{2(C_S + C_N)^2}\right\}$$

and putting it equal to zero one finds the value of C_S that gives the maximum

$$C_S = \frac{1}{N_P} \sum_{i=1}^{N_P} \Delta_i^2 - C_N.$$

In order to estimate the signal of a CMB experiment we can calculate the variance of the data (the first term on the right in the previous equation) and compares it with the mean noise per pixel (the second term on the right). If the data have a variance greater than the noise, the signal is simply the difference.

One can also calculate the error on C_S in the same way:

$$\frac{\partial^2 \ln \mathcal{L}}{\partial C_S^2} = \left\{ \frac{N_P}{2(C_S + C_N)^2} - \frac{\sum_{i=1}^{N_P} \Delta_i^2}{(C_S + C_N)^3} \right\},$$

at the likelihood peak $\sum_{i=1}^{N_P} \Delta_i^2$ can be replaced by $N_P(C_S + C_N)$, so

$$\sigma_{C_S} = \sqrt{\frac{2}{N_P}}(C_S + C_N).$$

The last equation is a simplified formula useful to calculate the precision of a given experiment in determining the cosmological parameters. The general formula provides the errors on C_ℓ

$$\sigma_{C_\ell} = \sqrt{\frac{2}{(2\ell+1)f}}(C_\ell + C_{N,\ell}).$$

The only difference respect to the simplified version is that the number of pixels (or the number of independent measures) is replaced by $(2\ell + 1)f$, where f is the sky coverage fraction of the experiment.

This is the Bayesian method provide confidence intervals: a c.i. I at n% is defined as the interval where the cumulative is equal to n% that is $\int_I P(p_i)dp_i = n/100$ and where each point $P(p_i)$ is greater than its value outside I. It must be underlined that once a model is fixed, the Bayesian method provides always confidence intervals of the parameters, no matter how wrong the model could be and if it is consistent with the data. So the Bayesian method is strongly dependent on the input model. That's why we have to take into account the χ^2 that evaluates the consistency between the model and the data.

4.2 Monte Carlo Markov Chains

Monte Carlo methods are algorithms based on random sampling. An important subclass of Monte Carlo methods are Monte Carlo Markov Chains (MCMC) methods that are Markov process, i.e. the next sample depends on the present one, but not on the previous ones. The sequence of steps is called Chain and each step corresponds to some particular value of the parameters for which the likelihood is evaluated.

It is an efficient way to sample the likelihood surface (target distribution) if the parameter space is very large, as in the cosmological analyses, and using a grid becomes time consuming.

The aim of MCMC methods is to simulate posterior distribution. In particular one simulates sampling the posterior distribution $P(\alpha|x)$, of a set of parameter α given event x, obtained via Bayes Theorem

$$P(\alpha|x) = \frac{P(x|\alpha)P(\alpha)}{\int P(x|\alpha)P(\alpha)d\alpha},$$

where $P(x|\alpha)$ is the likelihood of event x given the model parameters α and $P(\alpha)$ is the prior probability density; α denotes a set of cosmological parameters and event x is the set of observed $\hat{C}_\ell$.

It works as follows [22, 23]:

1. Start with a set of cosmological parameters $\{\alpha_1\}$, compute the C_ℓ^1 and the likelihood $\mathcal{L}_1 = \mathcal{L}(C_\ell^{1th}|\hat{C}_\ell)$.

2. Take a random step in parameter space starting from the present one to obtain a new set of cosmological parameters $\{\alpha_2\}$. The distribution of the steps is called proposal distribution and is taken to be Gaussian in each direction i with r.m.s. given by σ_i. We will refer below to σ_i as the "step size", that is important to optimize the chain efficiency.

3. Compute the C_ℓ^{2th} for the new set of cosmological parameters and their likelihood $\mathcal{L}_2$.

4. (a) Accept the new step as a new point in the chain if it complies with the Metropolis-Hastings algorithm where the probability of acceptance is

$$p(acceptance) = min[1, \mathcal{L}_2/\mathcal{L}_1].$$

   Then go to step 2 after substitution $\{\alpha_1\} \to \{\alpha_2\}$.

   (b) If the condition is not verified, draw a random number x from a uniform distribution from 0 to 1. If $x \geq \mathcal{L}_2/\mathcal{L}_1$, do not accept the new step and repeat the previous point in the chain[1] and return to step 2. If $x < \mathcal{L}_2/\mathcal{L}_1$, accept the new step as in 4.(a).

5. Repeat from step 2 until the convergence test (see below) is verified.

After an initial "burn-in" in a starting low probability region, further samples can be thought as coming from the stationary distribution. So if this initial part of the chains is discarded in the post-analysis, the chain will have no dependence on the starting location.

The choice of the step size is crucial to improve the chain efficiency and speed up convergence. If the step size is too big, the acceptance rate will be very small; if the step size is too small the acceptance rate will be high but the chain will exhibit poor mixing, that is the coverage of all the target distribution. Both situations will lead to slow convergence.

The classic convergence test is the Gelman-Rubin criterion [24]. This method not only tests convergence but can also diagnose poor mixing. The idea is that there are two ways to estimate the mean of the parameters - either treat the combined chains as a single chain, or look at the means of each chain. If the chains have converged these should agree within some tolerance. Let us consider M chains starting at well-separated points in parameter space; each has $2N$ elements, of which we consider only the last N: $\{y_i^j\}$ where $i = 1, ..., N$ and $j = 1, ...M$, i.e. y denotes a

[1] The MCMC gives to each point in parameter space a weight proportional to the number of steps the chain has spent at that particular location.

chain element (a point in parameter space) the index i runs over the elements in the chain, the index j runs over the different chains. The mean of the chain is defined as

$$\bar{y}^i = \frac{1}{N}\sum_{i=1}^{N} y_i^j,$$

and the mean of the distribution is

$$\bar{y} = \frac{1}{NM}\sum_{ij=1}^{NM} y_i^j.$$

The variance between chains is defined as

$$B_n = \frac{1}{M-1}\sum_{j=1}^{M}(\bar{y}^j - \bar{y})^2,$$

and the average variance within a chain as

$$W = \frac{1}{M(N-1)}\sum_{ij}(y_i^j - \bar{y}^j)^2.$$

Under convergence B_n and W should agree. The quantity

$$\hat{R} = \frac{\frac{N-1}{N}W + B_n(1+\frac{1}{M})}{W}$$

is the ratio of two estimates of the variance in the target distribution and so it should approach unity as convergence is achieved. The numerator of the variance is an estimate of the variance that is unbiased if the distribution is stationary, otherwise is an overestimate. The denominator is an underestimate of the variance of the target distribution if the individual sequences did not have time to converge. The convergence of the Markov chain is then monitored by recording the quantity $\hat{R}$ for all the parameters and running the simulation until the values for $\hat{R}$ are always < 1.01.

A widely used tool for Monte Carlo Markov Chain analysis in cosmology is the publicly available package `CosmoMC` [25], that allows to sample several cosmological parameters spaces analyzing basically any kind of cosmological data. The calculation of theoretical observable is done through `camb` [26] (Code for Anisotropies in the Microwave background) software. The code allows for different sampling algorithms and different convergence tests. However the most used ones and the ones we are going to use in the analysis shown in subsequent chapters are the Metropolis-Hastings sampling algorithm and the Gelman-Rubin convergence test.

4.3 Model selection and Bayesian evidence

It has been shown that in Bayesian inference best fit parameters and confidence intervals depend on the underlying model, i.e. what set of parameters are allowed to vary. The problem of model selection is concerned about determining which

combination of parameters gives the preferred fit to the data. The goal is to make an objective comparison of different models which may have a different number of parameters. Typically the introduction of extra parameters will yield an improved fit to the data set, so a simple comparison of the maximum likelihood value will always favor the model with more parameters, regardless of whether the extra parameters are relevant.

The Bayesian method to select between models is to consider the bayesian evidence ratio. We denote two competing models by M and M'. We assume the M' is a simpler model, which has fewer ($n < n$) parameters in it. We further assume that it is nested in model M, i.e. the n' parameters of model M' are common to M, which has $p = n - n'$ extra parameters in it. These parameters are fixed to fiducial values in M'. We denote by x the data vector, and by θ and θ' the parameters vectors (of length n and n'). The posterior probability, i.e. the probability of the model given the data, of each model comes from Bayes theorem:

$$p(M|x) = \frac{p(x|M)p(M)}{p(x)}$$

and similarly for M'. By marginalization $p(x|M)$, known as the Evidence, is

$$p(x|M) = \int d\theta p(x|\theta M)p(\theta|M),$$

which should be interpreted as a multidimensional integration. Hence the posterior relative probabilities of the two models, regardless of what their parameters are, is

$$\frac{p(M'|x)}{p(M|x)} = \frac{p(M')}{p(M)} \frac{\int d\theta' p(x|\theta' M')p(\theta'|M')}{\int d\theta p(x|\theta M)p(\theta|M)}.$$

With non-committal priors on the models, $p(M') = p(M)$, this ratio simplifies to the ratio of evidences, called Bayes factor,

$$B \equiv \frac{\int d\theta' p(x|\theta' M')p(\theta'|M')}{\int d\theta p(x|\theta M)p(\theta|M)}.$$

Note that, as we have anticipated, if M' is nested the complicated model M will inevitably lead to a higher likelihood (or at least as high), but the evidence will favor the simpler model if the fit is nearly good, through the smaller prior volume. We assume uniform (and hence separable) priors in each parameter, over ranges $\Delta\theta$ (or $\Delta\theta'$) hence $p(\theta|M) = (\Delta\theta_1 ... \Delta\theta_n)^-1$ and

$$B = \frac{\int d\theta' p(x|\theta' M')p(\theta'|M')}{\int d\theta p(x|\theta M)p(\theta|M)} \frac{\Delta\theta_1 ... \Delta\theta_n}{\Delta\theta'_1 ... \Delta\theta'_n}.$$

In the nested case the ratio of prior hypervolumes simplifies to

$$\frac{\Delta\theta_1 ... \Delta\theta_n}{\Delta\theta'_1 ... \Delta\theta'_n} = \Delta\theta_{n'+1} ... \Delta\theta_{n'+p},$$

where $p = n - n'$ is the number of extra parameters in the more complicated model.

Bayes factors are usually interpreted against the Jeffreys scale for the strength of evidence given in Table 4.1. This is an empirically calibrated scale [27], with thresholds at values of the odds of about 3 : 1,12 : 1 and 150 : 1, representing weak, moderate and strong evidence, respectively.

Table 4.1. Empirical scale for evaluating the strength of evidence when comparing two models, the so-called "Jeffreys scale". The probability column refers to the posterior probability of the favored model, assuming non-committal priors on the two competing models, i.e. $p(M') = p(M) = 1/2$ and that the two models exhaust the model space, $p(M'|x) + p(M|x) = 1$

$\lvert \ln B_{01} \rvert$	Odds	Probability	Strength of evidence
< 1.0	$\lesssim 3:1$	< 0.750	Inconclusive
1.0	~ 3	0.750	Weak evidence
2.5	$\sim 12:1$	0.923	Moderate evidence
5.0	$\sim 150:1$	0.993	Strong evidence

4.4 Parameters estimation

The parameters of the basic ΛCDM model are: the physical baryon density, $\omega_b \equiv \Omega_b h^2$; the physical cold dark matter density, $\omega_c \equiv \Omega_c h^2$; the dark energy density in units of the critical density, Ω_Λ; the amplitude of the primordial spectrum at a certain pivot scale, A_s; the power law spectral index of primordial density (scalar) perturbations, n_s; the reionization optical depth, τ. The parameters derived from these six fit parameters are: the age of the Universe, t_0; the Hubble constant, $H_0 = 100h$km s$^-$1 Mpc$-$1; the amplitude of density fluctuations in linear theory on $8h^-1\ Mpc$ scale, σ_8. The ΛCDM parameters best fit to the 7-year WMAP data are given in Table 4.2.

In subsequent chapters we will consider non-minimal cosmological models. In previous chapter we have already seen the ΛMDM (Lambda Mixed Dark Matter) model with massive neutrinos. In particular we will examine the constraints on parameters related to non-standard physics, by allowing the effective neutrino number and the neutrino mass to vary. Furthermore we will also allow for a non standard parametrization of the reionization process and for a non-flat ($\Omega_k \neq 0$) Universe.

4.4.1 One dimensional and two dimensional posterior

In all the analyses of this thesis we compute the likelihood function in the n-dimensional cosmological parameter space (with n parameters), and multiply it by the prior probability distribution functions to derive the n-dimensional posterior probability density distribution function. Marginalizing this over all but one $(n-1)$ of the cosmological parameters gives the one-dimensional posterior probability distribution function for the parameter of interest. This one-dimensional distribution function is used to determine the most likely value of the parameter, as well as limits

Table 4.2. Six parameters ΛCDM fit of 7-year WMAP data [28].

Parameter	7-year Fit
Fit parameters	
$10^2\Omega_b h^2$	$2.258^{+0.057}_{-0.056}$
$\Omega_c h^2$	0.1109 ± 0.0056
Ω_Λ	0.734 ± 0.029
A_s	$(2.43 \pm 0.11) \times 10^{-9}$
n_s	0.963 ± 0.014
τ	0.088 ± 0.015
Derived parameters	
t_0	13.75 ± 0.13 Gyr
H_0	71.0 ± 2.5 km/s/Mpc
σ_8	0.801 ± 0.030

on it. Marginalizing over only $n-2$ of the cosmological parameters, we derive the two-dimensional posterior probability density distribution function $P(x, y)$ where x and y are the two parameters of interest. This is used to derive the constraint contours in the two-dimensional x–y parameter space.

Chapter 5

Neutrino Number: Dark Radiation

5.1 Introduction

One of the major theoretical predictions of the standard scenario is the existence of a relativistic energy component (see Section 3.11 and e.g. [29]), beside CMB photons, with a current energy density given by :

$$\rho_{rad} = \left[1 + \frac{7}{8}\left(\frac{4}{11}\right)^{4/3} N_{\rm eff}\right]\rho_\gamma \ ,$$

where ρ_γ is the energy density of the CMB photons background at temperature $T_\gamma = 2.728K$ and $N_{\rm eff}$ is in principle a free parameter, defined as the effective number of relativistic degrees of freedom. Assuming standard electroweak interactions, three active massless neutrinos and including the (small) effect of neutrino flavor oscillations the expected value is $N_{\rm eff} = 3.046$ with a deviation from $N_{\rm eff} = 3$ that takes into account effects from the non-instantaneous neutrino decoupling from the primordial photon-baryon plasma (see e.g. [30]).

In recent years, thanks to the continuous experimental advancements, the value of $N_{\rm eff}$ has been increasingly constrained from cosmology ([19], [31], [32], [33], [34], [10], [35], [36], [37], [38], [3], [21]), ruling out $N_{\rm eff} = 0$ at high significance.

However, especially after the new ACT [39] and SPT [40] CMB results, the data seem to suggest values higher than the "standard" one, with $N_{\rm eff} \sim 4 - 5$ (see e.g. [35], [36], [3], [21], [41]) in tension with the expected standard value at about two standard deviations.

The number of relativistic degrees of freedom obviously depends on the decoupling process of the neutrino background from the primordial plasma. However, a value of $N_{\rm eff} = 4$ is difficult to explain in the three neutrino framework since non-standard neutrino decoupling is expected to maximally increase this value up to $N_{\rm eff} \sim 3.12$

(see e.g. [42]). A possible explanation could be the existence of a fourth (or fifth) sterile neutrino. The hypothesis of extra neutrino flavor is interesting since recent results from short-baseline neutrino oscillation data from LSND [43] and MiniBooNE [44, 45] experiments are consistent with a possible fourth (or fifth) sterile neutrino specie (see [35, 36] and references therein). Moreover, a larger value for $N_{\rm eff} \sim 4$ could arise from a completely different physics, related to axions (see e.g. [46, 47, 48]), gravity waves ([49]), decaying particles (see e.g. [50, 51, 52]), extra dimensions [53, 54, 55, 56] and dark energy (see e.g. [57, 58] and references therein).

As a matter of fact, any physical mechanism able to produce extra "dark" radiation produces the same effects on the background expansion of additional neutrinos, yielding a larger value for $N_{\rm eff}$ from observations.

Since there is a large number of models that could enhance $N_{\rm eff}$ it is clearly important to investigate the possible ways to discriminate among them. If Dark Radiation is made of relativistic particles as sterile neutrinos it should behave as neutrinos also from the point of view of perturbation theory, i.e. if we consider the set of equations that describes perturbations in massless neutrino in the Newtonian Gauge (the one used in the `CAMB` package [26]) (following the definition presented in [59, 60]):

$$\begin{aligned}
\dot{\delta}_\nu &= \frac{\dot{a}}{a}(1-3c_{\rm eff}^2)\left(\delta_\nu + 3\frac{\dot{a}}{a}\frac{q_\nu}{k}\right) - k\left(q_\nu + \frac{2}{3k}\dot{h}\right), \\
\dot{q}_\nu &= kc_{\rm eff}^2\left(\delta_\nu + 3\frac{\dot{a}}{a}\frac{q_\nu}{k}\right) - \frac{\dot{a}}{a}q_\nu - \frac{2}{3}k\pi_\nu, \\
\dot{\pi}_\nu &= 3c_{\rm vis}^2\left(\frac{2}{5}q_\nu + \frac{8}{15}\sigma\right) - \frac{3}{5}kF_{\nu,3}, \\
\frac{2l+1}{k}\dot{F}_{\nu,l} &- lF_{\nu,l-1} = -(l+1)F_{\nu,l+1},\ l \geq 3\ ,
\end{aligned}$$

it should have an effective sound speed $c_{\rm eff}^2$ and a viscosity parameter $c_{\rm vis}^2$ such that $c_{\rm eff}^2 = c_{\rm vis}^2 = 1/3$. Here the dot indicates the derivative respect to conformal time τ, a is the scale factor, k is the wavenumber, δ_ν is the neutrino density contrast, q_ν is the neutrino velocity perturbation, π_ν is the neutrino anisotropic stress, $F_{\nu,\ell}$ are higher order moments of the neutrino distribution function, finally σ is the shear.

Varying $c_{\rm vis}^2$ modifies the ability for neutrinos to free-stream out of a gravitational potential well. When $c_{\rm vis}^2 = 0$ the Cosmic neutrino Background (CNB) becomes a perfect fluid and is capable of supporting undamped acoustic oscillations, shown in red, dot-dashed on the left-hand panel of Figure 5.1 [41]. An increased $c_{\rm vis}^2$ leads to an overdamping of the perturbations, shown in blue, dashed in the left-hand panel of Figure 5.1. Free streaming of relativistic neutrino will indeed produce anisotropies in the neutrino background yielding a value of $c_{\rm vis}^2 = 1/3$ while a smaller value would indicate possible non standard interactions (see e.g. [61, 62, 63]). A value of $c_{\rm vis}^2$ different from zero, as expected in the standard scenario, has been detected in [64] and confirmed in subsequent papers [65, 66]. More recently, the analysis of [41] confirmed the presence of anisotropies from current cosmological data. Changing $c_{\rm eff}^2$ allows for a neutrino pressure perturbation which is non-adiabatic, i.e., $(\delta p - \delta\rho/3)/\bar{\rho} = (c_{\rm eff}^2 - 1/3)\delta_\nu^{rest}$, where δ_ν^{rest} is the density perturbation in a frame where the neutrino velocity perturbation $q_\nu = 0$. When $c_{\rm eff}^2$ is small the

CNB is partially able to overcome its internal pressure support and nearly cluster. Actually, a value of $c^2_{\rm eff} < 1/3$ ($c^2_{\rm eff} > 1/3$) leads to a decreased (increased) pressure of the CNB in its restframe, which in turn causes the amplitude of the neutrino perturbation increase (decrease), as seen on the right panel of Figure 5.1 in the red, dot-dashed (blue, dashed) curve. Figure 5.2 [41] shows how the CMB temperature power spectrum is modified i this parametrization. Note that an increase (decrease) in $c^2_{\rm eff}$ leads to an increase (decrease) in the neutrino sound horizon. Moreover an increase (decrease) in $c^2_{\rm eff}$ leads to an increase (decrease) in the scale at which neutrino perturbations affect CMB. Recently the analysis of [41] suggested the presence of a lower value for the effective sound speed with $c^2_{\rm eff} = 1/3$ ruled out at more than two standard deviations.

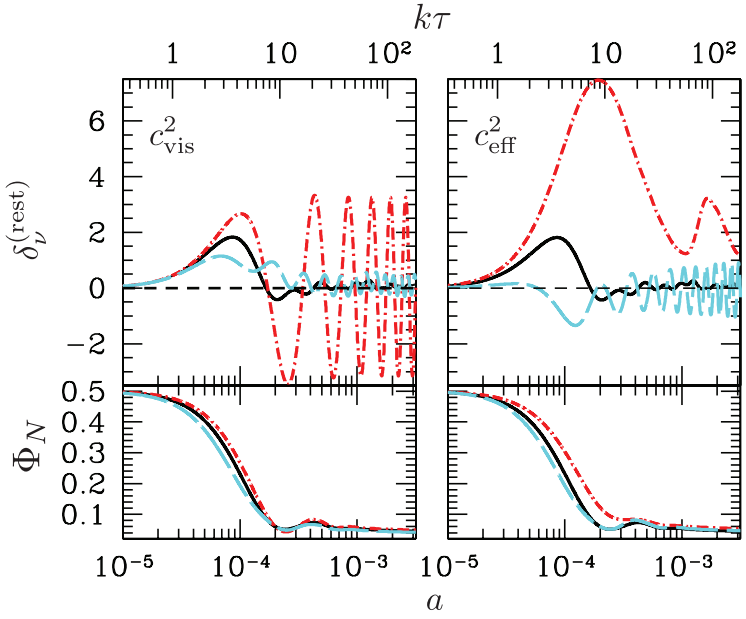

Figure 5.1. The evolution of the neutrino density perturbation in its rest frame for a mode $k = 0.1h\mathrm{Mpc}^{-}1$ as a function of the scale factor a, or the conformal time τ [41]. The black solid curve gives the evolution for the standard case, i.e., when $c^2_{\rm vis} = c^2_{\rm eff} = 1/3$. The left-hand panel shows the evolution when $c^2_{\rm vis} = 0$ (red, dot-dashed) and $c^2_{\rm vis} = 1$ (blue, dashed) with $c^2_{\rm eff} = 1/3$. The right-hand panel shows the evolution when $c^2_{\rm eff} = 0.1$ (red, dot-dashed) and $c^2_{\rm eff} = 0.8$ (blue, dashed) with $c^2_{\rm vis} = 1/3$. The bottom panels show the corresponding evolution of the newtonian potential, Φ_N.

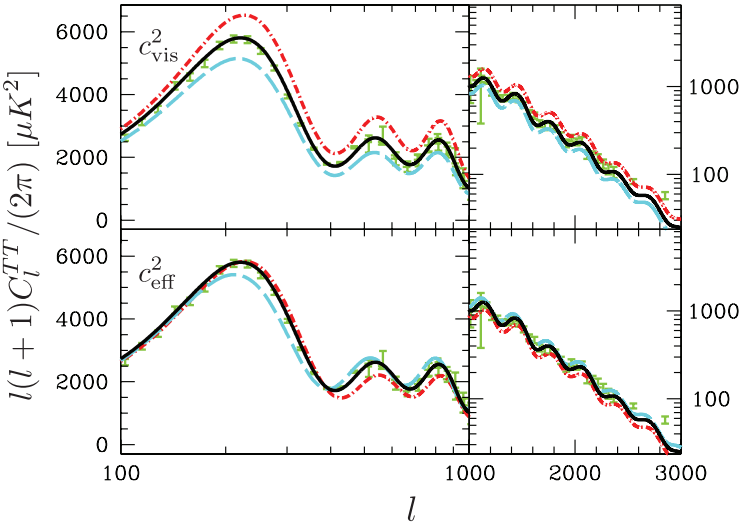

Figure 5.2. Modifications to the CMB temperature power spectrum, C_ℓ^{TT}, as both $c^2_{\rm vis}$ (top panel) and $c^2_{\rm eff}$ (bottom panel) are varied [41]: the black solid curve gives the evolution of the standard case: the top panel shows C_ℓ^{TT} when $c^2_{\rm vis} = 0$ (red, dot-dashed) and $c^2_{\rm vis} = 1$ (blue, dashed); the bottom panel shows $c^2_{\rm eff} = 0.2$ (red, dot-dashed) and $c^2_{\rm eff} = 0.7$ (blue, dashed). The large angular scale measurements are from the 7-year WMAP release [10] and on small angular scales from ACT [67].

5.2 Analysis Method

We perform a MCMC [25] analysis combining the following CMB datasets: WMAP7 [10], ACBAR [68], ACT [39], and SPT [40], and we analyze datasets using out to $l_{\rm max} = 3000$. We also include information on dark matter clustering from the galaxy power spectrum extracted from the SDSS-DR7 luminous red galaxy sample [69]. Finally, we impose a prior on the Hubble parameter based on the last Hubble Space Telescope observations [3].

The analysis method we adopt is based on the publicly available Monte Carlo Markov Chain package `CosmoMC` [25] with a convergence diagnostic done through the Gelman and Rubin statistic. We sample the following six-dimensional standard set of cosmological parameters, adopting flat priors on them: the baryon and cold dark matter densities $\Omega_{\rm b}$ and $\Omega_{\rm c}$, the ratio of the sound horizon to the angular diameter distance at decoupling θ_s, the optical depth to reionization τ, the scalar spectral index n_S, and the overall normalization of the spectrum A_S at $k = 0.002{\rm Mpc}^{-1}$. We consider purely adiabatic initial conditions and we impose spatial flatness. We vary the effective number of relativistic degrees of freedom $N_{\rm eff}$, the effective sound speed $c^2_{\rm eff}$, and the viscosity parameter $c^2_{\rm vis}$. In some cases, we consider only variations in the extra dark radiation component $N_\nu^S = N_{\rm eff} - 3.046$, varying the perturbation parameters $c^2_{\rm vis}$ and $c^2_{\rm eff}$ only for this extra component and assuming $c^2_{\rm eff} = c^2_{\rm vis} = 1/3$

for the standard 3 neutrino component.

In our analysis we always fix the primordial Helium abundance to the observed value $Y_p = 0.24$. This procedure is different from the one adopted, for example, in [40], where the Y_p parameter is varied assuming Big Bang Nucleosynthesis for each values of $N_{\rm eff}$ and $\Omega_{\rm b}$ in the chain. Since the cosmological epoch and the energy scales probed by BBN are dramatically different from the ones probed by CMB and large scale structure we prefer to do not assume standard BBN in our analysis and to leave the primordial Helium abundance as fixed to a value consistent with current observations.

We account for foregrounds contributions including three extra amplitudes: the SZ amplitude A_{SZ}, the amplitude of clustered point sources A_C, and the amplitude of Poisson distributed point sources A_P. We marginalize the contribution from point sources only for the ACT and SPT data, based on the templates provided by [40]. We quote only one joint amplitude parameter for each component (clustered and Poisson distributed). Instead, the SZ amplitude is obtained fitting the WMAP data with the WMAP own template, while for SPT and ACT it is calculated using the [70] SZ template at 148 GHz. Again, this is different from the analysis performed in [40] where no SZ contribution was considered for the WMAP data. For further information about how to deal with secondary anisotropies in CMB analyses see Section 8.

5.3 Results

As stated in the previous section, we perform two different analyses. In the first analysis we vary the amplitude of the whole relativistic contribution changing $N_{\rm eff}$ and the corresponding perturbation parameters $c^2_{\rm vis}$ and $c^2_{\rm eff}$. In the second analysis we assume the existence of a standard neutrino background and vary only the extra component $N^S_\nu = N_{\rm eff} - 3.046$ considering only in this extra component the variations in $c^2_{\rm vis}$ and $c^2_{\rm eff}$.

5.3.1 Varying the number of relativistic degrees of freedom $N_{\rm eff}$.

In Table 5.1 we report the constraints on the cosmological parameters varying $N_{\rm eff}$ with and without variations in perturbation theory. We consider two cases: first we run our analysis fixing the perturbation parameters to the standard values, i.e. $c^2_{\rm eff} = c^2_{\rm vis} = 1/3$, then we let those parameters to vary freely.

As we can see from the results in the left column of Table 5.1, the WMAP7+ACT+SPT+DR7+H0 analysis is clearly suggesting the presence for Dark Radiation with $N_{\rm eff} = 4.08^{+0.71}_{-0.68}$ at 95% c.l.. When considering variations in the perturbation parameters (right column) the constraint is somewhat shifted towards smaller values with $N_{\rm eff} = 3.89^{+0.70}_{-0.70}$. The constraint on the sound speed, $c^2_{\rm eff} = 0.312 \pm 0.026$ is fully consistent with the expectations of a free streaming component. Anisotropies in the neutrino background are detected at high statistical significance with $c^2_{\rm vis} = 0.29^{+0.21}_{-0.16}$ improving previous constraints presented in [64].

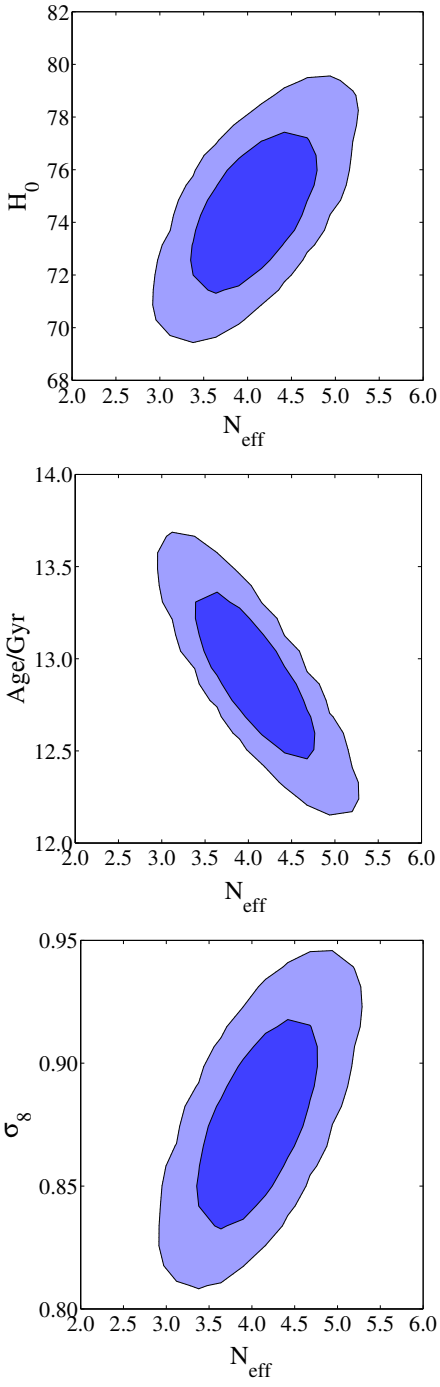

Figure 5.3. 68% and 95% c.l. constraints for the degeneracy between $N_{\rm eff}$ and the Hubble constant H_0, the age of the universe t_0, and the amplitude of mass fluctuations σ_8.

It is interesting to consider the possible degeneracies between $N_{\rm eff}$ and other "indirect" (i.e. not considered as primary parameters in MCMC runs) model parame-

Table 5.1. MCMC estimation of the cosmological parameters assuming $N_{\rm eff}$ relativistic neutrinos. Upper bounds at 95% c.l. are reported for foregrounds parameters. We quote the one-dimensional marginalized 68% and 95% c.l. for the neutrino parameters.

$\Omega_b h^2$	0.02229 ± 0.00038	0.02206 ± 0.00081
$\Omega_c h^2$	0.1333 ± 0.0086	0.1313 ± 0.0094
τ	0.082 ± 0.012	0.083 ± 0.014
H_0	74.3 ± 2.2	74.2 ± 2.1
n_s	0.977 ± 0.011	0.972 ± 0.021
$\log(10^{10} A_s)$	3.195 ± 0.035	3.196 ± 0.035
A_{SZ}	< 1.2	< 1.4
$A_C[\mu\mathrm{K}^2]$	< 14.3	< 14.6
$A_P[\mu\mathrm{K}^2]$	< 25.2	< 24.7
$N_{\rm eff}$	$4.08^{+0.18+0.71}_{-0.18-0.68}$	$3.89^{+0.19+0.70}_{-0.19-0.70}$
$c^2_{\rm eff}$	1/3	$0.312^{+0.008+0.026}_{-0.007-0.026}$
$c^2_{\rm vis}$	1/3	$0.29^{+0.04+0.21}_{-0.06-0.16}$
χ^2_{min}	7594.2	7591.5

ters. In Figure 5.3 we therefore plot the 2D likelihood constraints on $N_{\rm eff}$ versus the Hubble constant H_0, the age of the universe t_0 and the amplitude of r.m.s. mass fluctuations on spheres of $8\mathrm{Mpc}h^{-1}$, σ_8.

As we can see from the three panels in the figure, there is a clear degeneracy between $N_{\rm eff}$ and those three parameters. Namely, an extra radiation component will bring the cosmological constraints (respect to the standard 3 neutrino case) to higher values of the Hubble constant and of σ_8 and to lower values of the age of the universe t_0. These degeneracies have been already discussed in the literature (see e.g. [71]) and could be useful to estimate the effect of additional datasets on our result. The 3% determination of the Hubble constant from the analysis of [3] plays a key role in our analysis in shifting the constraints towards larger values of $N_{\rm eff}$. If future analyses will point towards lower values of the Hubble constant, this will make the standard 3 neutrino case more consistent with observations. If future observations will point towards values of the age of the universe significantly larger than 13 Gyrs, this will be against an extra dark radiation component, since it prefers $t_0 \sim 12.5$Gyrs. Clearly, adding cluster mass function data as presented in [72] and that points towards lower values of σ_8 renders the standard $N_{\rm eff} = 3.046$ case more

consistent with observations. A future and precise determination of σ_8 from clusters or Lyman-α surveys could be crucial in ruling out dark radiation.

5.3.2 Varying only the excess in the relativistic component N_ν^S and assuming 3 standard neutrinos.

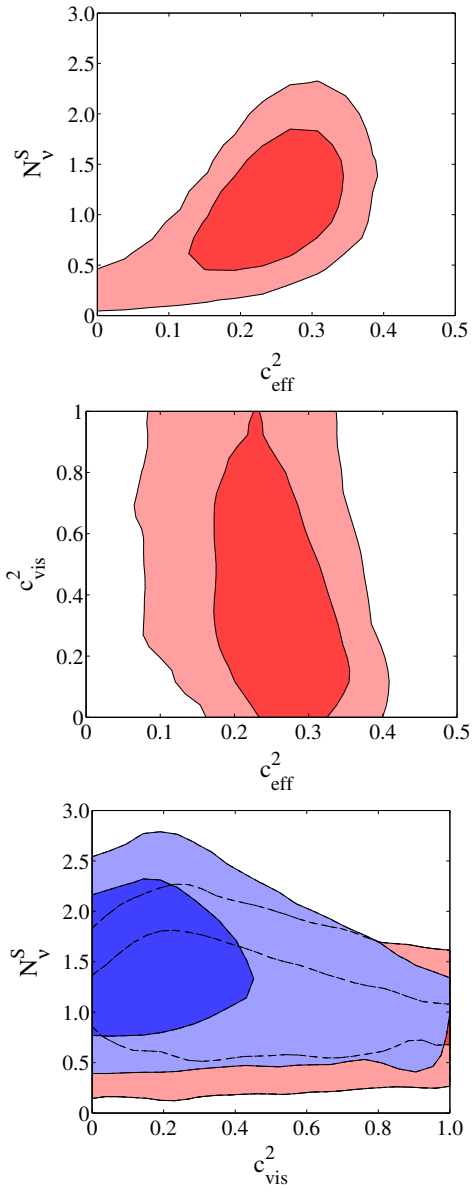

Figure 5.4. 68% and 95% c.l. constraints for the degeneracy between neutrinos parameters. Red contours refer to model (A) in Table 5.2, while blue contours show model (B).

In Table 5.2 we report the constraints considering only an excess N_ν^S in the

number of relativistic degrees of freedom over a standard 3 neutrinos background.

Table 5.2. MCMC estimation of the cosmological parameters considering an extra component N_ν^S and assuming a standard background of 3 relativistic neutrinos. The perturbation parameters refer to the extra component. Both 68% and 95% confidence levels for the neutrino parameters are reported. Upper bounds are at 95% c.l. .

Model :	**varying** $c^2_{\rm eff}$, $c^2_{\rm vis}$	$c^2_{\rm eff} = 1/3$, **varying** $c^2_{\rm vis}$
	(A)	**(B)**
$\Omega_b h^2$	0.02177 ± 0.00066	0.02262 ± 0.00049
$\Omega_c h^2$	0.135 ± 0.010	0.143 ± 0.010
τ	0.086 ± 0.013	0.084 ± 0.013
H_0	72.8 ± 2.1	73.7 ± 2.2
n_s	0.989 ± 0.014	0.978 ± 0.014
$\log(10^{10} A_s)$	3.178 ± 0.035	3.192 ± 0.035
A_{SZ}	< 1.6	< 1.4
$A_C[\mu\mathrm{K}^2]$	< 15.0	< 15.0
$A_P[\mu\mathrm{K}^2]$	< 24.8	< 24.8
N_ν^S	$1.10^{+0.19+0.79}_{-0.23-0.72}$	$1.46^{+0.21+0.76}_{-0.21-0.74}$
$c^2_{\rm eff}$	$0.24^{+0.03+0.08}_{-0.02-0.13}$	$1/3$
$c^2_{\rm vis}$	< 0.91	< 0.74
χ^2_{min}	7590.5	7592.0

As we can see for the results in the table, the evidence for an extra background is solid with $N_\nu^S = 1.46^{+0.76}_{-0.74}$ at 95% c.l. when only variations in the $c^2_{\rm vis}$ component are considered, while the constraint is $N_\nu^S = 1.10^{+0.79}_{-0.72}$ when also variations in $c^2_{\rm eff}$ are considered. Again, the data provide a good determination for $c^2_{\rm eff}$ with $c^2_{\rm eff} = 0.24^{+0.08}_{-0.13}$ at 95% c.l., in marginal agreement at about 2σ with the standard $c^2_{\rm eff} = 1/3$ value. This lower value of $c^2_{\rm eff}$, also found in [41], could hint for a dark radiation component with a varying equation of state, ruling out a a massless sterile neutrino. It will be certainly interesting to investigate if this signal remains in future analyses. No significant constraint is obtained on $c^2_{\rm vis}$.

In Figure 5.4 we show the degeneracy between the parameters N_ν^S, $c^2_{\rm eff}$, and $c^2_{\rm vis}$ by plotting the 2D likelihood contours between them. As we can see a degeneracy is

present between $c^2_{\rm eff}$ and N^S_ν: models with lower values of N^S_ν are more compatible with $c^2_{\rm eff} = 0$ since the effect of $c^2_{\rm eff}$ on the CMB spectrum is smaller. No apparent degeneracy is present between $c^2_{\rm vis}$ and the remaining parameters since $c^2_{\rm vis}$ is weakly constrained by current data.

Since oscillation experiments have clearly established that neutrino are massive, it is interesting to perform a similar analysis but letting the 3 neutrino standard background with $c^2_{\rm eff} = c^2_{\rm vis} = 1/3$ to be massive, and varying the parameter Σm_ν that consider the sum of masses of the 3 active neutrinos. The extra dark radiation component is assumed massless and we treat the perturbations in it as in the previous sections. In Table 5.3 we report the results of this analysis.

Table 5.3. MCMC estimation of the cosmological parameters considering $N_\nu = 3.04$ massive neutrinos. Values and 68% - 95% errors for the neutrino parameters are reported. Upper bounds are at 95% c.l. .

$\Omega_b h^2$	0.02174 ± 0.00063
$\Omega_c h^2$	0.135 ± 0.011
τ	0.087 ± 0.014
H_0	72.7 ± 2.1
n_s	0.989 ± 0.015
$\log(10^{10} A_s)$	3.179 ± 0.036
A_{SZ}	< 1.6
$A_C[\mu\mathrm{K}^2]$	< 15.9
$A_P[\mu\mathrm{K}^2]$	< 26.1
$\sum m_\nu[\mathrm{eV}]$	< 0.79
N^S_ν	$1.12^{+0.21+0.86}_{-0.26-0.74}$
$c^2_{\rm eff}$	$0.241^{+0.03+0.09}_{-0.02-0.12}$
$c^2_{\rm vis}$	< 0.92
χ^2_{min}	7590.7

As we can see, when masses in the active neutrinos are considered, there is a slightly stronger evidence for the extra background with $N^S_\nu = 1.12^{+0.86}_{-0.74}$. This is can be explained by the degeneracy present between $\sum m_\nu$ and N^S_ν, well known in the literature (see e.g. [35]) and clearly shown in Figure 5.5 where we report the 2D marginalized contours in the plane $\sum m_\nu - N^S_\nu$.

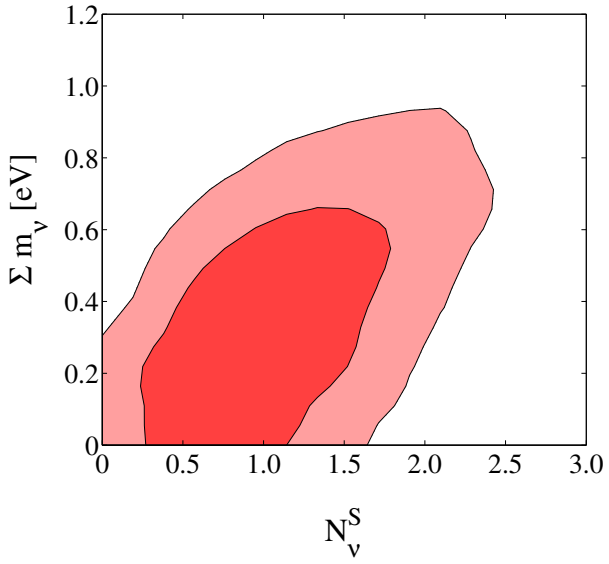

Figure 5.5. Degeneracy in the plane $\sum m_\nu - N_\nu^S$ at 68% and 95% c.l. .

5.3.3 Profile likelihood analysis

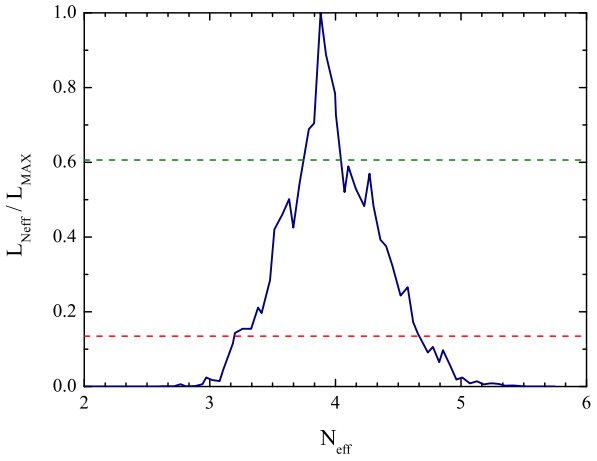

Figure 5.6. Maximum Likelihood ratio $L_{N_{\rm eff}}/L_{max}$ for $N_{\rm eff}$. The dashed lines represent the 68% and 95% c.l. for a Gaussian likelihood ($L_{N_{\rm eff}}/L_{max} = 0.6065$ and $L_{N_{\rm eff}}/L_{max} = 0.135$) respectively.

Recently, in [73], a model-independent analysis for the extra relativistic degrees of freedom in cosmological data has been performed claiming no statistically significant evidence for it. This simple analysis consists in extracting the maximum likelihood

value L as a function of $N_{\rm eff}$ over the parameter space sampled in the chains, with a bin width of 0.5 and constructing a profile likelihood ratio by considering $ln(L_{N_{\rm eff}}/L_{max})$ as a function of $N_{\rm eff}$; where L_{max} is the maximum likelihood in the entire chains.

Here we perform a similar analysis, using however a smaller bin width of 0.05 and considering the case where the whole number of relativistic degrees of freedom $N_{\rm eff}$ is varied while $c^2_{\rm vis} = c^2_{\rm eff} = 1/3$. The resulting likelihood ratio $L_{N_{\rm eff}}/L_{max}$, plotted in Figure 5.6, clearly indicates a preference for a dark radiation component finding that the best fit model has $N_{\rm eff} = 3.88$ with a $\Delta\chi^2 = 14.56$ respect to the best fit model with $N_{\rm eff} = 3.046$.

We should however point out that the ratio $L_{N_{\rm eff}}/L_{max}$ presented in Figure 5.6 is rather noisy. Bayesian methods such as MCMC are indeed known to be inaccurate for this purpose (see for example the discussion in [74, 75]). Other methods more appropriate for a frequentist analysis have been presented, for example, in [76, 77, 78, 34, 79].

5.4 Future Planck and COrE CMB data analysis

Now we generate mock CMB data for a cosmology with dark radiation perturbation parameters different from their standard values and then we fit these simulated data via the usual MCMC analysis to an extended non minimal cosmology with standard dark radiation parameters, but varying both the constant and the time varying dark energy equation of state, or the scalar spectral index and its running.

We generate a mock data set for the ongoing Planck [80] CMB experiment, with $c^2_{\rm vis}$ different from its standard value and with $w = -1$ and $n_s = 0.96$. Then we fit these mock data using a MCMC analysis to different extensions of the minimal cosmological model in which the dark radiation is standard. The three possible extensions we consider are: *(a)* a ΛCDM model with a running spectral index $n_{\rm run}$, *(b)* the wCDM model in which we include the possibility of a dark energy equation of state parameter w different from -1, and *(c)* the $w(a)$CDM model in which we assume an equation of state evolving with redshift. The reconstructed values of the dark energy equation of state and of the running spectral index will be, in general, different from the values used in the mocks and, in the case of the dark energy equation of state w, different from the value expected within the ΛCDM model. We shall also explore the impact of future CMB data from the COrE mission [81], performing an equivalent forecast to the one we present here for Planck.

In the following we shall present the reconstructed values of n_s, $n_{\rm run}$, w, w_0 and w_a which will result from a fit of Planck and COrE mock data (generated with non standard values for the dark radiation perturbation parameters, $c^2_{\rm vis} = 0.1$) to a cosmology with a standard value for the dark radiation parameter $c^2_{\rm vis} = 1/3$ but with a running spectral index or a time varying dark energy component. We do not consider here $c^2_{\rm eff} \neq 1/3$ due to the tighter current bounds on this parameter, when compared to the current constraints on $c^2_{\rm vis}$.

Table 5.4. Constraints on the cosmological parameters for each of the Plank and COrE mock data sets described in the text. We report the mean and the standard deviation of the posterior distribution. We have set $c^2_{\rm eff} = 1/3$ and $c^2_{\rm vis} = 0.1$ in the mock data sets used as fiducial models. Then, we have fitted these data to a model with canonical values for the dark radiation perturbation parameters, i.e. $c^2_{\rm eff} = 1/3$ and $c^2_{\rm vis} = 1/1$.

	ΛCDM + $n_{\rm run}$ (Planck)	ΛCDM + $n_{\rm run}$ (COrE)	wCDM (Planck)	wCDM (COrE)	$w(a)$CDM (Planck)	$w(a)$CDM (COrE)
w	-1	-1	-0.70 ± 0.05	-0.63 ± 0.05	—	—
$N_{\rm eff}$	3.04	3.04	3.04	3.04	3.04	3.04
n_s	1.002 ± 0.004	0.999 ± 0.002	1.007 ± 0.004	1.004 ± 0.002	1.007 ± 0.004	1.007 ± 0.002
$n_{\rm run}$	-0.035 ± 0.005	-0.038 ± 0.003	0	0	0	0
w_0	—	—	—	—	-1.19 ± 0.10	-0.99 ± 0.05
w_a	—	—	—	—	0.77 ± 0.23	0.88 ± 0.06

5.4.1 ΛCDM + $n_{\rm run}$

For this scenario we consider the following set of parameters:

$$\{\omega_b,\, \omega_c,\, \theta_s,\, \tau,\, n_s,\, \log[10^{10} A_s],\, n_{\rm run}\}\ .$$

In general, the spectrum of the scalar perturbations is not exactly a power law but it varies with scale. Therefore one must consider the scale dependent running of the spectral index $n_{\rm run} = dn_s/d\ln k$. Following [82], the power spectrum for the scalar perturbations reads

$$P(k) \equiv A_s k^{n(k)} \propto \left(\frac{k}{k_0}\right)^{n_s + \ln(k/k_0)(dn/d\ln k) + \cdots}\ ,$$

being $k_0 = 0.05\ {\rm Mpc}^{-1}$ the pivot scale. The correlation between n_s and $n_{\rm run}$ is shown in Figure 5.7. As stated in [83], the parameter that is constrained by cosmological data is the effective spectral index $n' = n_s + \ln(k/k_0)(dn/d\ln k)$. This is the reason for the circular allowed regions in the $n_s - n_{\rm run}$ plane. The first and second columns of Table 5.4 show that, if a cosmology with $n_{\rm run} = 0$ but with non standard dark radiation perturbation parameters ($c^2_{\rm vis} = 0.1$) is fitted to a cosmology with standard dark radiation parameters but with $n_{\rm run} \neq 0$, the reconstructed value of the running spectral index will differ from zero at a high statistical significance.

Finally, for the case of the simulated cosmology here with $c^2_{\rm vis} < 1/3$, the reconstructed value of n_s is consistent with a Harrison-Zel'dovich scale invariant primordial power spectrum within one sigma. Setting the properties of dark radiation

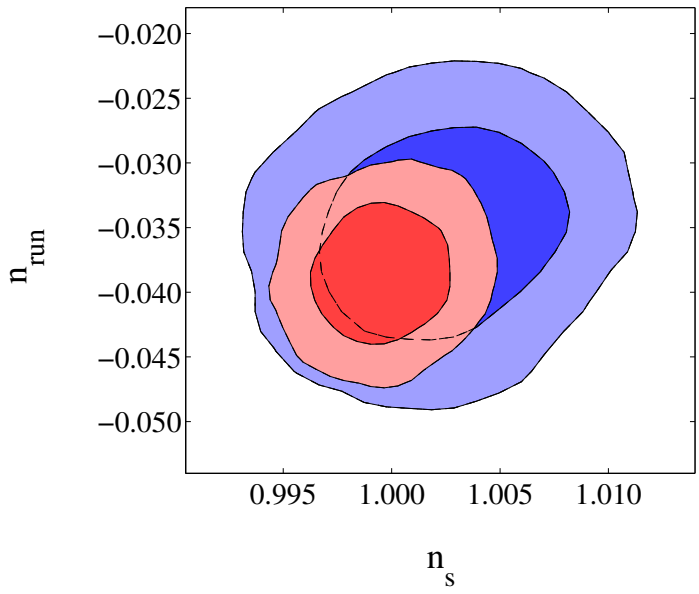

Figure 5.7. 68% and 95% CL allowed regions in the $n_s - n_{\rm run}$ plane from MCMC fits of Planck (blue regions) and COrE (red regions) CMB mock data.

is therefore mandatory since it is highly correlated with the spectral index of the spectrum of primordial perturbations, key to distinguish among the different inflationary models.

5.4.2 wCDM

Here we consider a cosmological model including a dark energy fluid characterized by a constant equation of state parameter w (the ratio of the pressure to energy density of the dark energy fluid) as a free parameter. We consider the following set of parameters:

$$\{\omega_b,\, \omega_c,\, \theta_s,\, \tau,\, n_s,\, \log[10^{10} A_s],\, w\}\ .$$

As stated in [36], there exists a degeneracy between the number of the extra dark radiation species and the dark energy equation of state. A value of $w > -1$ shifts the positions of the CMB acoustic peaks to lower multipoles ℓ; this effect could be compensated by a decrease of $c^2_{\rm vis}$ or by an increase of $N_{\rm eff}$. As we have already seen in Section 3.11, one of the main effects of a $N_{\rm eff} > 3.04$ comes from the change of the epoch of the radiation matter equality, and consequently, from the shift of the CMB acoustic peaks, see Section 3.11 and Ref. [21] for a detailed study. The position of the acoustic peaks is given by the so-called acoustic scale θ_s, which reads

$$\theta_s = \frac{r_s}{D_A},$$

where D_A and r_s are the comoving angular diameter distance to the last scattering surface and the sound horizon at the recombination epoch z_{rec}, respectively. Although

D_A almost remains the same for different values of $N_{\rm eff}$, r_s becomes smaller when $N_{\rm eff}$ is increased (see after Figure 5.10). Thus the positions of the acoustic peaks are shifted to higher multipoles (smaller angular scales) by increasing the value of $N_{\rm eff}$ [84]. A dark energy component with $w > -1$ will decrease the comoving angular diameter distance to the last scattering surface D_A, shifting the positions of the CMB acoustic peaks to larger angular scales, i.e. to lower multipoles ℓ, compensating, therefore, the effect induced by an increase of $N_{\rm eff}$. The reconstructed MCMC values for w (see the third and fourth columns of Table 5.4) are larger than the value used in the input cosmology $w = -1$, excluding the ΛCDM scenario with high significance. A dark radiation component which deviates from its standard behavior could therefore be confused with the presence of a dark energy fluid with $w \neq -1$.

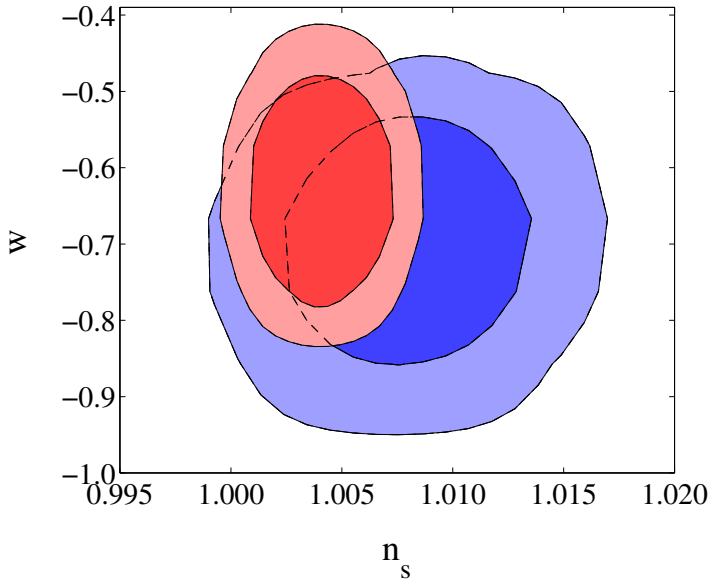

Figure 5.8. Same as Figure 5.7 but in the $w - n_s$ plane.

5.4.3 $w(a)$CDM model

We also consider models of the dark energy in which the equation of state of the dark energy component varies with time. We use a parameterization that has been extensively explored in the literature [85, 86, 87, 88]:

$$w(a) = w_0 + w_a(1 - a) \ ,$$

where w_0 is the equation of state parameter at present, while $w_a = -2dw/d\ln a|_{a=1/2}$ [86, 89]. We consider the following set of parameters:

$$\{\omega_b, \omega_c, \theta_s, \tau, n_s, \log[10^{10} A_s], w_0, w_a\} \ .$$

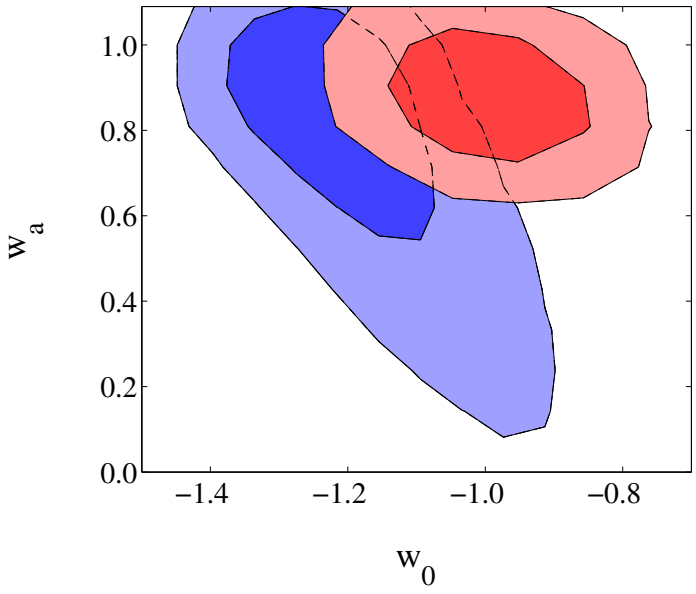

Figure 5.9. Same as Figure 5.7 but in the $w_0 - w_a$ plane.

The fifth and sixth columns of Table 5.4 show the reconstructed values of w_0 and w_a after fitting the Plank and COrE mock data generated with a non standard viscosity parameter $c^2_{\rm vis} = 0.1$ but with $w = -1$ to a cosmology with standard dark radiation but with the time varying dark energy equation of state $w(a)$ used here. The correlation between w_0 and w_a is shown in Figure 5.9. The reconstructed values that we find for Planck (COrE) mock data are $w_0 = -1.19 \pm 0.10$ and $w_a = 0.77 \pm 0.23$ ($w_0 = -0.99 \pm 0.05$ and $w_a = 0.88 \pm 0.06$) at 68 % CL, values which are consistent with the current constraints on these two dark energy parameters, see Ref. [10]. Therefore it is crucial to unravel the nature of the dark radiation component since if it turns out to be non standard, future cosmological data might be misinterpreted as a time varying dark energy fluid.

5.5 The impact of assuming flatness on $N_{\rm eff}$

As we have already seen in Section 3.11, a larger neutrino number increases the early ISW as the neutrino mass. Moreover changing the neutrino effective number essentially changes the expansion rate H at recombination. So it changes the size of sound horizon at recombination as well ($r_s \propto 1/H$) and the damping at recombination ($r_d \propto 1/sqrtH$). If these distances vary according to H then they also vary according to any parameter correlated with H. If we allow for an open universe with nonzero curvature the effective neutrino number is slightly reduced. The theory confirms this because $\theta_s = r_s/D_A$ is constrained by observation which means if $N_{\rm eff}$ is reduced and $\Omega_k > 0$ then r_s and D_A both increase (see Figure 5.10). However, if the parameter space favors a closed universe then there will appear to

be a higher number of effective neutrinos. This is one of the primary reasons for expecting correlation between $N_{\rm eff}$ and Ω_k.

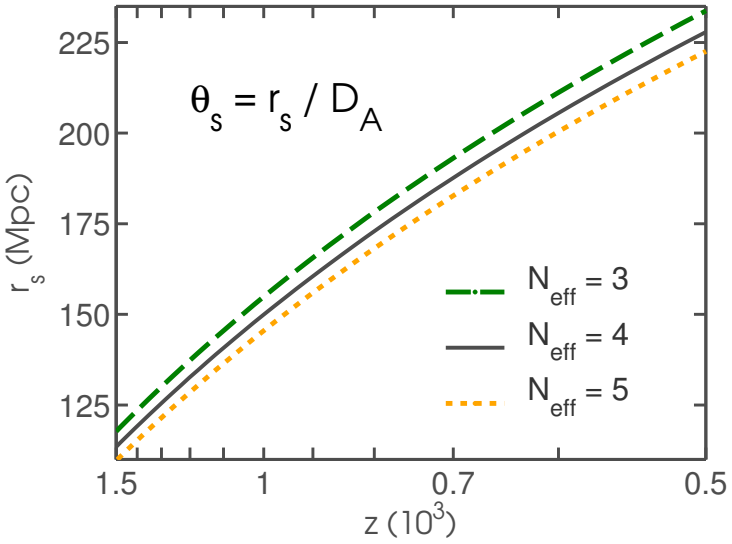

Figure 5.10. A demonstration of how the sound horizon r_s changes with the effective neutrino number $N_{\rm eff}$ under the matter dominated approximation.

For this analysis we use the same method of Section 5.2, but here the CMB anysotropy datasets are combined with Baryonic Acoustic Oscillation (BAO) data of Percival [90], instead of SDSS-DR7. We also performed a run without high multipole datasets (SPT and ACT), in order to test the impact of these recent data. Moreover we have a slightly different parameter space: we let $N_{\rm eff}$ varying, but we do not account for neutrino perturbation parameters ($c^2_{\rm eff}$ and $c^2_{\rm vis}$). Instead we consider the spatial curvature Ω_k.

Figure 5.11 demonstrates the correlation between Ω_k and $N_{\rm eff}$, which agrees with the prediction. Interestingly, the effect of the additional CMB datasets (ACT and SPT) increases the correlation between these parameters with respect to WMAP 7-year data alone. This may be due in part to the considerable improvement in $N_{\rm eff}$ whereas the uncertainty in the curvature is not noticeably improved by the addition of small scale anisotropy measurements. These results suggest that an open universe with fewer neutrinos would look similar to a flat universe with more neutrinos. We also note that when including $N_{\rm eff}$ as a free parameter in the ΛCDM+Ω_k model, the 1σ constraint of $\Omega_k = -0.0023^{+0.0054}_{-0.0056}$ found in Ref. [10] does not deteriorate significantly for the same combination of datasets (i.e. WMAP+BAO+H_0). This is due to the presence of the BAO data and the H_0 prior in the analysis, since both probes are sensitive to the geometry of the Universe. Therefore, BAO and H_0 help to break the degeneracy between $N_{\rm eff}$ and Ω_k.

Table 5.5 provides a summary of parameter values for runs where Ω_k and $N_{\rm eff}$ vary. Here we find $N_{\rm eff} = 4.03 \pm 0.45$ and $10^3\Omega_k = -4.46 \pm 5.24$ at the 68% confidence level. Therefore, even when Ω_k is allowed to vary, $N_{\rm eff} = 3$ is still disfavored with $\sim$

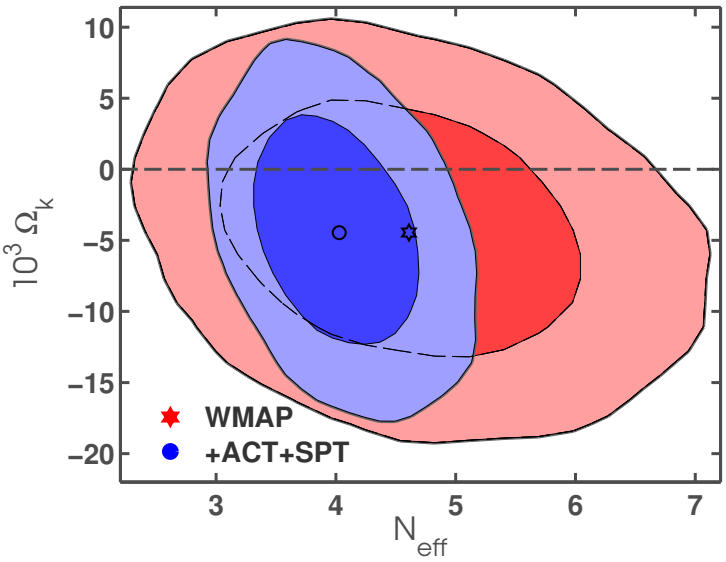

Figure 5.11. Correlation between Ω_k and $N_{\rm eff}$. The credible intervals are given at the 68% and 95% confidence levels and the markers indicate the locations of the marginalized values. WMAP+BAO+H_0 is shown in red while WMAP+ACT+SPT+BAO+H_0 is in blue. Note that the effect of adding additional datasets is significant.

Table 5.5. Summary of constraints while varying Ω_k and $N_{\rm eff}$. All datasets include BAO and H_0 for improved parameter constraints. Errors are at the 68% CL. See Figure 5.11.

Parameter	WMAP7+$N_{\rm eff}$+Ω_k	...+ACT+SPT
$100\Omega_b h^2$	2.26 ± 0.056	2.27 ± 0.045
$\Omega_c h^2$	0.136 ± 0.0169	0.129 ± 0.00915
Ω_Λ	0.721 ± 0.0179	0.723 ± 0.0158
n_s	0.9837 ± 0.0157	0.9863 ± 0.0147
τ	0.0887 ± 0.0148	0.0894 ± 0.0149
H_0 (km/s/Mpc)	74.88 ± 3.40	73.44 ± 2.03
$N_{\rm eff}$	4.61 ± 0.96	4.03 ± 0.45
$10^3\,\Omega_k$	-4.45 ± 5.85	-4.46 ± 5.24

95% confidence.

5.6 The impact of a new median statistics H_0 prior

We have seen that dark radiation can predict a larger value for $N_{\rm eff}$. It is therefore crucial to carefully investigate this result, to see if it can be strengthened or weakened by, for example, considering a slightly different choice of data. As it has been shown (see Figure 5.3 and discussion, and Ref. [21]) that $N_{\rm eff}$ is degenerate with the value of the Hubble constant H_0. Assuming a prior on the value of the Hubble constant is therefore a key step in the determination of $N_{\rm eff}$ from the data. The prior on the Hubble constant used in most recent analyses, labeled HST, is a Gaussian one based on the results of Ref. [3] with $H_0 = 73.8 \pm 2.4$km/s/Mpc, including systematics.

While this 3% determination of H_0 is certainly impressive, one might wonder if a slightly different Hubble constant prior could change the preference for $N_{\rm eff} > 3$. There are several indications that a different Hubble constant prior could be more appropriate. For instance, a number of measurements result in a significantly lower value of H_0; e.g., the Ref. [91] summary value is $H_0 = 62.3 \pm 4$km/s/Mpc. In addition, a standard analysis, under the assumption of $N_{\rm eff} = 3.046$, of CMB data alone is able (in a flat universe) to constrain the Hubble constant. Recently such analyses yield $H_0 \sim 70$km/s/Mpc, more than one standard deviation away from the HST value. For example, the analysis of ACT and WMAP7 data in Ref. [39] gives $H_0 = 69.7 \pm 2.5$km/s/Mpc. Clearly, there is also observational evidence for a significantly smaller value of H_0 than the HST estimate. Furthermore, it is possible that using a prior with a lower value of H_0 could result in a $N_{\rm eff}$ determined from CMB anisotropy and other large-scale data that is consistent with the other cosmological $N_{\rm eff}$ determinations.

There are many measurements of H_0, over 550.[1] Most recent estimates lie in the interval 60–75km/s/Mpc, with error bars on some individual estimates probably being too small, since these measurements are mutually inconsistent (this is likely a consequence of underestimated systematic errors in some cases). Clearly, what is needed is a convincing summary observational estimate of H_0.[2] To date, the best technique for deriving such a summary estimate — that does not make use of the error bars of the individual measurements — is the median statistics technique; Ref. [95] includes a detailed description of this technique.

The median statistics technique has been used to analyse a number of cosmological data sets. These include Type Ia supernova apparent magnitude data, to show that the current cosmological expansion is accelerating, [95, 96, 97]; CMB temperature anisotropy data, in one of the first analyses to show that these data were consistent with flat spatial hypersurfaces, [98]; and, collections of measurements of the cosmological clustered mass density, in one of the earliest analyses to show that this makes up around 25–30% of the current epoch cosmological energy budget, [99].

[1] See cfa-www.harvard.edu/∼huchra/.

[2] And not just for the case at hand, but for many different cosmological parameter analyses, see, e.g., Refs. [92, 93, 94].

These successes support the idea that a median statistics estimate of the Hubble constant provides an accurate summary estimate.

The median statistics technique has been used thrice to analyse Huchra's list (at three different epochs). From an analysis of 331 measurements (up to the middle of 1999), Ref. [95] found an median statistics summary $H_0 = 67$km/s/Mpc; from 461 measurements (up to the middle of 2003), and from 553 measurements (up to early 2011), Refs. [100, 101] both found a median statistics summary $H_0 = 68$km/s/Mpc. While the estimated statistical error bar (given by the scatter in the central H_0 values) has decreased as the sample size has increased, the larger (and dominant) systematic error bar (estimated from the scatter in the summary values of H_0 determined by different techniques) has changed much less.

For our analyses here we estimate H_0 using the method of Ref. [101] but now excluding from the Huchra list of 553 measurements the 16 H_0 measurements derived from CMB data assuming $N_{\rm eff} = 3.046$. We exclude these 16 CMB measurements as we want an external and independent prior on H_0 to use in our analysis of the latest CMB datasets. From a median statistics analysis of the 537 non-CMB measurements we find $H_0 = 68 \pm 2.8$km/s/Mpc (one standard deviation error), identical to that found in Ref. [101] from an analysis of the 553 measurements. In what follows we refer to the Gaussian prior based on this value as the median statistics (MS) H_0 prior. Our goal here is to discuss the implications of assuming the MS prior for H_0, instead of the usual HST prior, for current CMB and large-scale structure parameter inference. We focus much of our attention on the value of $N_{\rm eff}$ and the evidence for dark radiation, but we also consider how the MS prior changes the estimated value of other parameters, including the dark energy equation of state parameter w and the spectral index of primordial fluctuations n_s.

5.6.1 Analysis Method

Here the analysis is very similar to the one presented in section 5.2, with three changes: (i) we consider two different H_0 priors: the median statistics (MS) prior of $H_0 = 68 \pm 2.8$km/s/Mpc as well as, for comparison, the HST prior [3] used in previous analyses; (ii) we consider an extended case where we assume massive neutrinos, we enlarge our parameter space varying the total mass of neutrinos $\sum m_\nu$; (iii) we allow the Helium abundance Y_p to vary consistently with standard BBN following Ref. [40]. This means that each theoretical CMB angular spectrum is computed assuming a value for Y_p derived by BBN nucleosynthesis from the input values of $\Omega_b h^2$ and $N_{\rm eff}$ of the theoretical model considered. The small uncertainty on Y_p derived from the experimental errors on the neutron half-life produces negligible changes in the CMB angular spectra so we ignore it. In a latter case we also vary Y_p as a free parameter. In addition, where indicated, we also present constraints on the dark energy equation of state parameter w (the ratio of the pressure to energy density of the dark energy fluid), assumed to be redshift independent, although the corresponding dark energy density is time dependent.[3] We consider massless neutrinos, adiabatic initial conditions, and a spatially-flat universe.

[3] This is the widely-used wCDM parametrization of dark energy. It is not a complete parametrization, as it cannot describe the evolution of spatial inhomogeneities, nor is it an accurate approximation

5.6.2 Results

Neutrinos

Table 5.6. Cosmological parameter values and 68% confidence level errors assuming $N_{\rm eff}$ relativistic neutrinos or $N_{\rm eff} = 3.046$ massive neutrinos. 95% c.l. upper bounds are listed for the sum of neutrino masses and foregrounds parameters. We also list the derived Hubble constant, the non-relativistic matter density parameter $\Omega_{\rm m} = \Omega_c + \Omega_b$, and σ_8, the amplitude of density inhomogeneities averaged over spheres of radius $8h^{-1}$ Mpc, where h is the Hubble constant in units of 100km/s/Mpc.

Parameters	No Prior	HST Prior		MS Prior	
		73.8 ± 2.4km/s/Mpc		68 ± 2.8km/s/Mpc	
$\Omega_b h^2$	0.02258 ± 0.00050	0.02248 ± 0.00039	0.02210 ± 0.00037	0.02211 ± 0.00040	0.02188 ± 0.00036
$\Omega_c h^2$	0.134 ± 0.010	0.1317 ± 0.0080	0.1142 ± 0.0029	0.1256 ± 0.0080	0.1181 ± 0.0032
θ_s	1.0395 ± 0.0016	1.0397 ± 0.0016	1.0415 ± 0.0014	1.0400 ± 0.0017	1.0409 ± 0.0014
τ	0.085 ± 0.014	0.084 ± 0.013	0.083 ± 0.013	0.080 ± 0.013	0.081 ± 0.014
n_s	0.984 ± 0.017	0.979 ± 0.012	0.9659 ± 0.0091	0.964 ± 0.012	0.9536 ± 0.0090
$N_{\rm eff}$	4.14 ± 0.57	3.98 ± 0.37	3.046	3.52 ± 0.39	3.046
$\sum m_\nu$[eV]	0.0	0.0	< 0.36	0.0	< 0.60
H_0[km/s/Mpc]	75.2 ± 3.6	74.2 ± 2.0	69.3 ± 1.4	70.9 ± 2.1	66.8 ± 1.8
$\log(10^{10} A_s)$	3.183 ± 0.043	3.191 ± 0.035	3.205 ± 0.034	3.219 ± 0.036	3.226 ± 0.034
$\Omega_{\rm m}$	0.277 ± 0.019	0.280 ± 0.016	0.284 ± 0.017	0.294 ± 0.017	0.315 ± 0.024
σ_8	0.882 ± 0.033	0.876 ± 0.028	0.782 ± 0.032	0.857 ± 0.028	0.757 ± 0.043
A_{SZ}	< 1.4	< 1.3	< 0.97	< 1.1	< 0.96
$A_C[\mu{\rm K}^2]$	< 14.5	< 14.7	< 12.8	< 14.1	< 13.1
$A_P[\mu{\rm K}^2]$	< 24.9	< 25.5	< 26.6	< 26.1	< 26.6
$\chi^2_{\rm min}$	7593.4	7593.2	7592.0	7594.8	7595.1

Table 5.6 and Figure 5.12 show that the H_0 prior plays a crucial role in determining constraints on $N_{\rm eff}$ from the data. With the HST H_0 prior we find a central $N_{\rm eff}$ value that is 2.5σ larger than 3.046, while the median statistics prior results in

of more physically motivated time-varying dark energy models, [102, 103]. It is preferable to use a consistent and physically motivated dark energy model, e.g., that proposed in Refs. [104, 105], for such an analysis, but this is a much more involved undertaking, so instead we patch up the wCDM parametrization by assuming that the acoustic spatial inhomogeneities travel at the speed of light. This extended wCDM parametrization should provide reasonable (qualitative) indications of what might be expected in a consistent, physically-motivated model of time-varying dark energy.

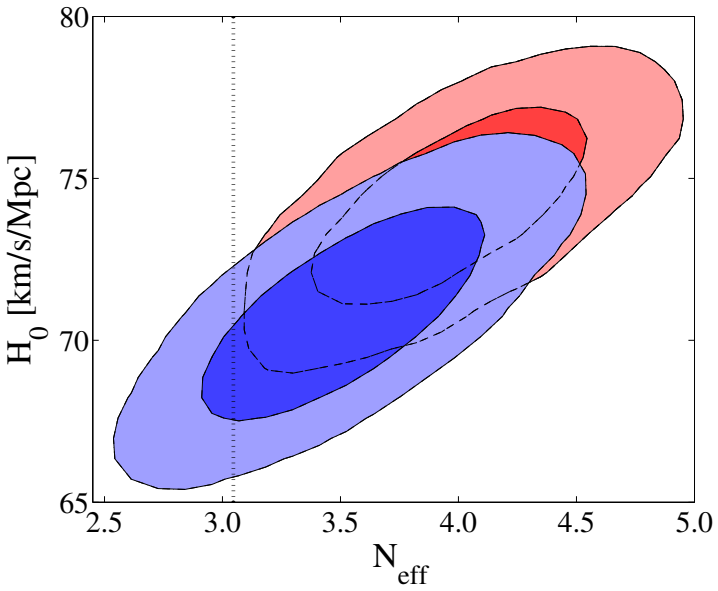

Figure 5.12. Constraints in the $N_{\rm eff}$-H_0 plane. Elliptical two-dimensional posterior probability distribution function contours show the 68% and 95% c.l. limits. Red contours and regions (closer to the upper right corner) assume the HST prior with $H_0 = 73.4 \pm 2.4$km/s/Mpc, while blue contours and regions (closer to the lower left corner) are obtained using the median statistics prior with $H_0 = 68 \pm 2.8$km/s/Mpc. The dotted black vertical line corresponds to $N_{\rm eff} = 3.046$.

an $N_{\rm eff}$ that is consistent with 3.046 (being only 1.2σ larger).

The HST prior is therefore at least partially responsible for the current indication for dark radiation. However, as we can see from the central values of H_0 and $N_{\rm eff}$ obtained when a flat prior on H_0 is assumed, the CMB anisotropy and large-scale structure data considered here prefers a larger value of $N_{\rm eff}$ (being 1.9σ larger than 3.046) and a somewhat larger value of H_0. This is clear also from the $\chi^2_{\rm min}$ values of the best fit that are higher when the median statistics H_0 prior is assumed, compared to the case of the HST prior (see the last line of Table 5.6).

The H_0 prior is crucial also in the determination of the $\sum m_\nu$ limits if we instead limit ourselves to the case of 3, standard, massive neutrinos. In Table 5.6, columns 3 and 5, we quote the cosmological parameters and the upper limits on $\sum m_\nu$ in case of the HST and of the MS prior. As we can see, the upper limit on $\sum m_\nu$ is considerably weaker when the MS prior is considered, with the 95% c.l. upper limit moving from $\sum m_\nu < 0.36$ eV in the case of the HST prior to $\sum m_\nu < 0.60$ eV in the case of the MS prior. This can be clearly explained by the CMB degeneracy between H_0 and $\sum m_\nu$ as illustrate in Figure 5.13. Namely, lower values of the Hubble parameter are in better agreement with current CMB data when $\sum m_\nu$ is increased. Dataset preferring higher values for H_0 will therefore provide stronger

constraints on $\sum m_\nu$ when combined with the CMB data.

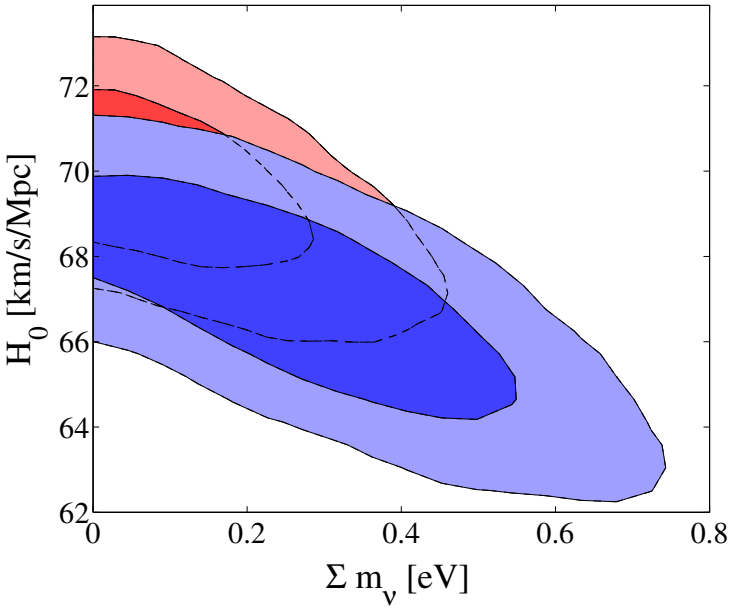

Figure 5.13. Constraints in the $\sum m_\nu$-H_0 plane. Elliptical two-dimensional posterior probability distribution function contours show the 68% and 95% c.l. limits. Red contours and regions (closer to the upper left corner) assume the HST prior with $H_0 = 73.4 \pm 2.4$km/s/Mpc, while blue contours and regions (closer to the lower right corner) are obtained using the median statistics prior with $H_0 = 68 \pm 2.8$km/s/Mpc.

Beside the $N_{\rm eff}$–H_0 degeneracy, it is interesting to note that there also is a degeneracy between $N_{\rm eff}$ and n_s. When the HST prior is assumed, n_s is 1.8σ below 1, while for the median statistics case it is 3σ below unity.

In Figure 5.14 we show the contours in the two-dimensional $\Omega_{\rm m}$–σ_8 parameter space, for the two Gaussian H_0 priors. Here σ_8 is the amplitude of density inhomogeneities averaged over spheres of radius $8h^{-1}$ Mpc. In this figure we also show the fit to the central value and the two standard deviation limits of the constraint from the normalization of the galaxy cluster mass function from Ref. [106], i.e., $\sigma_8 = (0.25/\Omega_{\rm m})^{0.47}[0.813 \pm 0.013 \pm 0.024]$. Here the first error bar represents the statistical, and the second the systematic, error (see their Sec. 10). We derive the 2σ cluster constraints shown in Figure 5.13 by adding these errors in quadrature and then doubling.

From Figure 5.14 we see that both H_0 priors give results that are not far off from what the measured normalization of the cluster mass function demands. Qualitatively, the HST H_0 prior is more consistent with the cluster data if $\Omega_{\rm m} \sim 0.25$, near the low end of current indications, see, e.g., Ref. [99], while the median statistics case prefers a larger $\Omega_{\rm m} \sim 0.27$, more consistent with current measurements, see, e.g., Ref. [99].

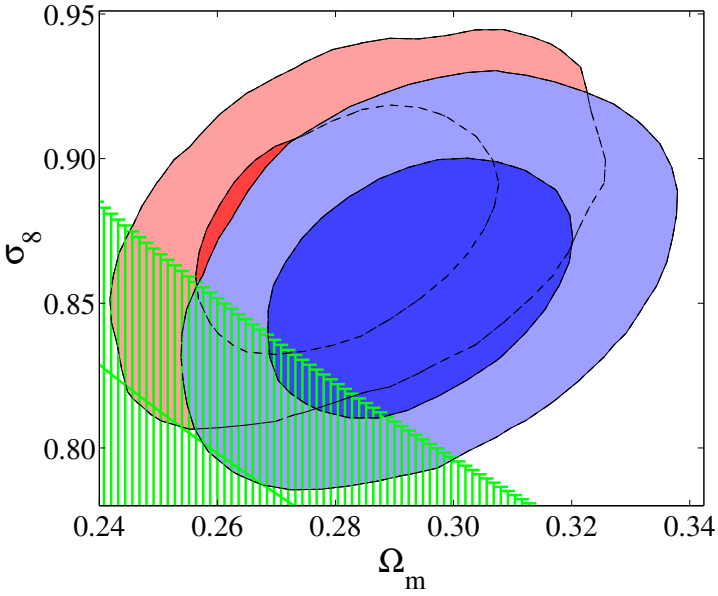

Figure 5.14. Constraints in the Ω_m–σ_8 plane. Elliptical two-dimensional posterior probability density function contours show the 68% and 95% confidence level limits. Red contours (closer to the upper left corner) assume the HST prior with $H_0 = 73.8 \pm 2.4$km/s/Mpc; blue contours (closer to the lower right corner) are obtained with the median statistics prior where $H_0 = 68 \pm 2.8$km/s/Mpc. The green region (in the lower left corner) demarcates the central value and 2σ limits from the cluster mass function normalization data, [106].

Helium mass abundance

One assumption made in the previous paragraph is that the Helium abundance is varied consistently with BBN. Current CMB data produce only weak constraints on this quantity and allowing Y_p to vary freely would make the standard case of $N_{\rm eff} = 3.046$ in better agreement with data due to an anti-correlation between $N_{\rm eff}$ and Y_p in CMB data (see, for example, the discussion in [107]). In order to check the impact of the H_0 priors in this case, we have performed two analysis varying the Helium abundance Y_p and $N_{\rm eff}$. The results are reported in Table 5.7.

As we can see, when Y_p is allowed to vary, the standard case of $N_{\rm eff}$ is more consistent with current data in both cases. In the case of the MS prior we have $N_{\rm eff} = 2.75 \pm 0.46$ that is perfectly consistent with the expectations of the standard scenario. However the value obtained for the Helium abundance is probably too high in the case of the MS prior: $Y_p = 0.334 \pm 0.033$ that is about two standard deviations away from the conservative experimental bound of $Y_p < 0.2631$ obtained from an analysis of direct measurements in [108].

The larger helium abundance obtained in the case of the MS prior respect to

Table 5.7. Cosmological parameter values derived assuming a varying Y_p. Errors are at 68% c.l. while upper bounds at 95% c.l. are reported for foregrounds parameters.

Parameters	HST Prior	MS Prior
$\Omega_b h^2$	0.02274 ± 0.00042	0.02246 ± 0.00043
$\Omega_c h^2$	0.1246 ± 0.0091	0.1138 ± 0.0085
θ_s	1.0429 ± 0.0027	1.0454 ± 0.0029
τ	0.087 ± 0.014	0.085 ± 0.014
n_s	0.986 ± 0.013	0.972 ± 0.013
$N_{\rm eff}$	3.52 ± 0.48	2.75 ± 0.46
H_0[km/s/Mpc]	72.7 ± 2.2	68.2 ± 2.3
Y_p	0.310 ± 0.034	0.334 ± 0.033
$\log(10^{10} A_s)$	3.175 ± 0.037	3.197 ± 0.036
$\Omega_{\rm m}$	0.279 ± 0.015	0.293 ± 0.016
σ_8	0.872 ± 0.029	0.847 ± 0.029
A_{SZ}	< 1.7	< 1.6
$A_C[\mu{\rm K}^2]$	< 15.4	< 15.3
$A_P[\mu{\rm K}^2]$	< 23.1	< 23.4
$\chi^2_{\rm min}$	7592.0	7590.4

the HST prior can be clearly seen from the direction of the degeneracies in the 2D contours plots in Figure 5.15. Namely, a lower $N_{\rm eff}$ prefers an higher Y_p and a lower prior for H_0 shifts the constraints towards lower $N_{\rm eff}$ and higher values for Y_p.

wCDM

The standard ΛCDM cosmological model has some conceptual problems that are partially alleviated in some models in which the dark energy density varies slowly in time (and so weakly in space), [104, 105]. Furthermore, as we have already underlined many times, observational constraints on cosmological parameters are model dependent, i.e., the observational estimate of a cosmological parameter, e.g., $N_{\rm eff}$, depends on the cosmological model used to analyse the data. It is therefore of interest to examine the observational cosmological constraints on $N_{\rm eff}$

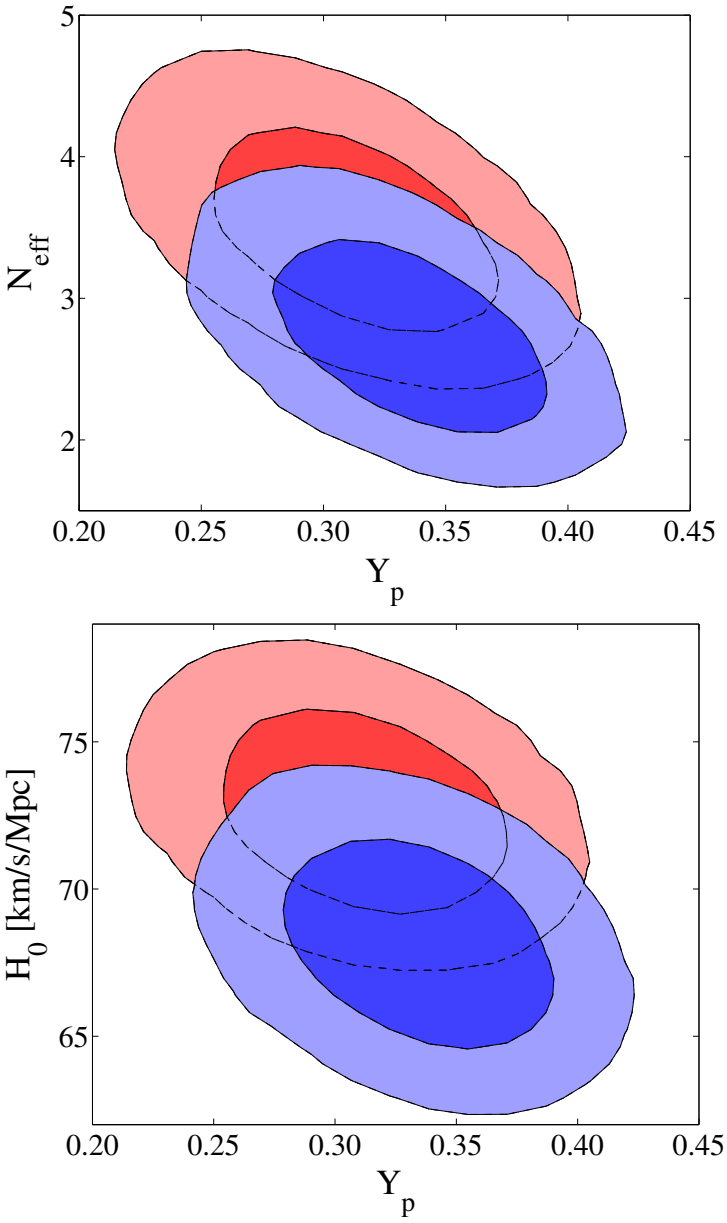

Figure 5.15. Constraints in the Y_p - $N_{\rm eff}$ plane (top) and Y_p -H_0 (bottom). Elliptical two-dimensional posterior probability distribution function contours show the 68% and 95% c.l. limits. Red contours and regions (closer to the upper left corner) assume the HST prior with $H_0 = 73.4 \pm 2.4$km/s/Mpc, while blue contours and regions (closer to the lower right corner) are obtained using the median statistics prior with $H_0 = 68 \pm 2.8$km/s/Mpc.

in a cosmological model in which the dark energy density varies in time, such as that of Ref. [104, 105]. However, to get an indication of what could be expected

Table 5.8. Cosmological parameter values derived assuming the wCDM parametrization of time-evolving dark energy. Errors are at 68% c.l. while upper bounds at 95% c.l. are reported for foregrounds parameters.

Parameters	HST Prior		MS Prior	
$\Omega_b h^2$	0.02200 ± 0.00040	0.02290 ± 0.0054	0.02206 ± 0.00040	0.02279 ± 0.00053
$\Omega_c h^2$	0.1162 ± 0.0039	0.1347 ± 0.0085	0.1141 ± 0.0040	0.1291 ± 0.0084
θ_s	1.0414 ± 0.0015	1.0396 ± 0.0016	1.0414 ± 0.0015	1.0400 ± 0.0016
τ	0.080 ± 0.013	0.089 ± 0.015	0.081 ± 0.013	0.089 ± 0.015
n_s	0.956 ± 0.010	0.997 ± 0.019	0.959 ± 0.011	0.993 ± 0.019
$N_{\rm eff}$	3.046	4.42 ± 0.54	3.046	4.16 ± 0.53
H_0[km/s/Mpc]	72.1 ± 2.4	72.8 ± 2.3	66.7 ± 2.6	68.0 ± 2.4
w	-1.09 ± 0.10	-0.86 ± 0.11	-0.90 ± 0.10	-0.76 ± 0.10
$\log(10^{10} A_s)$	3.223 ± 0.039	3.150 ± 0.050	3.210 ± 0.041	3.149 ± 0.051
$\Omega_{\rm m}$	0.267 ± 0.018	0.298 ± 0.022	0.307 ± 0.226	0.329 ± 0.025
σ_8	0.856 ± 0.044	0.831 ± 0.047	0.790 ± 0.046	0.775 ± 0.047
A_{SZ}	< 0.94	< 1.5	< 0.95	< 1.4
$A_C[\mu{\rm K}^2]$	< 13.0	< 15.0	< 13.0	< 14.9
$A_P[\mu{\rm K}^2]$	< 27.0	< 23.9	< 26.7	< 24.7
$\chi^2_{\rm min}$	7598.1	7592.7	7595.1	7592.1

from such an analysis, we determine the observational constraints on $N_{\rm eff}$ in a cosmological model in which the time-evolving dark energy density is parametrized by the wCDM parametrization (made complete by assuming that the acoustic spatial inhomogeneities propagate at the speed of light) described above. Table 5.8 shows the observational constraints derived under these assumptions.

From Table 5.8 we see that the MS prior changes the best fit w in the standard case with $N_{\rm eff} = 3.046$ to $w \sim -0.9$, with $w = -1$ off by one standard deviation. When both w and $N_{\rm eff}$ are allowed to vary freely the geometrical degeneracy with H_0 makes the HST and MS H_0 priors much less effective. In this case the evidence for dark radiation is again significant: for the MS H_0 prior case we find $N_{\rm eff} = 4.16 \pm 0.53$, and a dark energy equation of state parameter $w = -0.76 \pm 0.10$, i.e., excluding a cosmological constant at more than two standard deviations. A scale-invariant HZ primordial spectrum with $n_s = 1$ is fully consistent with both priors. While some of these values indicate significant tensions with the standard ΛCDM model, it is important to keep in mind the strong degeneracies between $N_{\rm eff}$, H_0 and w, as well as the fact that the wCDM parametrization used in the analysis has been arbitrarily

Table 5.9. Similar constraints as in Table 5.8, but now also including the SNeIa data in the analysis.

Parameters	HST Prior + SNeIa		MS Prior + SNeIa	
$\Omega_b h^2$	0.02203 ± 0.00038	0.02260 ± 0.00046	0.02190 ± 0.00038	0.02230 ± 0.00046
$\Omega_c h^2$	0.1156 ± 0.0037	0.1317 ± 0.0079	0.1157 ± 0.0038	0.1249 ± 0.0077
θ_s	1.0414 ± 0.0015	1.0400 ± 0.0016	1.0411 ± 0.0015	1.0401 ± 0.0016
τ	0.081 ± 0.013	0.086 ± 0.014	0.080 ± 0.013	0.083 ± 0.014
n_s	0.957 ± 0.010	0.985 ± 0.015	0.956 ± 0.010	0.972 ± 0.016
$N_{\rm eff}$	3.046	4.08 ± 0.43	3.046	3.63 ± 0.42
H_0[km/s/Mpc]	71.0 ± 1.6	74.0 ± 2.0	68.8 ± 1.6	70.6 ± 2.1
w	-1.050 ± 0.069	-0.967 ± 0.075	-0.989 ± 0.070	-0.946 ± 0.076
$\log(10^{10} A_s)$	3.222 ± 0.038	3.178 ± 0.043	3.221 ± 0.038	3.198 ± 0.044
$\Omega_{\rm m}$	0.273 ± 0.014	0.282 ± 0.015	0.291 ± 0.015	0.295 ± 0.016
σ_8	0.843 ± 0.035	0.863 ± 0.038	0.823 ± 0.036	0.836 ± 0.038
A_{SZ}	< 0.94	< 1.3	< 0.94	< 1.2
$A_C[\mu\mathrm{K}^2]$	13.0	14.8	< 13.1	< 14.0
$A_P[\mu\mathrm{K}^2]$	27.0	24.8	< 27.0	< 26.0
$\chi^2_{\rm min}$	8128.4	8124.0	8126.2	8125.6

completed to allow for an accounting of the evolution of density inhomogeneities.

In order to try to break these degeneracies, and derive more reliable constraints on the parameters, we perform a new analysis that also include the SDSS supernova Type Ia (SNeIa) apparent magnitude data, [109]. From Table 5.9 we see that the inclusion of the SNeIa data bring the results back to the previous dichotomy: the HST prior clearly shows a preference for $N_{\rm eff} > 3.046$ while the MS prior results in a value of $N_{\rm eff}$ that is in much better agreement with the standard scenario. The constraints on the equation of state are $w = -0.967 \pm 0.075$ for the HST prior and $w = -0.946 \pm 0.076$ for the MS prior. The HZ spectrum with $n_s = 1$ is again in tension with the observations for the MS H_0 prior at a little less than two standard deviations.

Chapter 6

Sterile Neutrinos: Cosmology and SBL

6.1 Introduction

As we have seen in previous Chapters, recent cosmological data have provided a clear evidence (more than 5 standard deviations) for the existence of the primordial neutrino background and have strongly constrained the absolute neutrino mass scale (see e.g. Ref. [110]). On the other hand, neutrino oscillations experiments have not only firmly established that neutrino are massive and mixed particles (for reviews, see e.g. Refs. [111, 112, 113]), but have also provided precise measurements of the three-neutrino mixing parameters (see the recent global fits in Refs. [14, 114]). Moreover, with the continuous experimental improvements, a clear interplay between neutrino physics and cosmology is emerging.

However, the measurements of CMB anisotropies made by the ACT (Atacama Cosmology Telescope) [39] and SPT (South Pole Telescope) [40] experiments, when combined with the measurements of the Hubble constant H_0 and galaxy clustering data, have provided interesting hints for an extra relativistic weakly interacting component, coined dark radiation (see previous Chapter). Parameterizing this energy component with the effective number of neutrino species $N_{\rm eff}$, the recent data bound it to $N_{\rm eff} = 4.08 \pm 0.8$ at 95% C.L. (see Section 5.3 and Ref. [21, 115, 41, 79]) whereas the standard prediction for only three active neutrino species is $N_{\rm eff} = 3.046$ [30]. While this result should be taken with some grain of salt, since it is derived from a combination of cosmological data and some tension does exist between the data (see Section 5.6 and Ref. [116]) it is anyway interesting since a fourth, or fifth, neutrino species seems also suggested by short–baseline (SBL) oscillation experiments.

As we have seen in section 3.1, models with one additional $\sim$ 1 eV massive sterile neutrino, i.e. the so called (3+1) models, were introduced to explain LSND SBL antineutrino data [43] by means of neutrino oscillations. A much better

fit to SBL appearance data and, to a lesser extent, to disappearance data, is provided by models with two sterile neutrinos (3+2) [117, 118] which can also explain both the MiniBooNE neutrino [44] and antineutrino data [45] if CP violation is allowed [15]. CP violation can even occur in (3+1) scenarios with only one relevant mass squared difference in presence of non standard neutrino interactions (NSI). Therefore, the (3+1) NSI model can also nicely explain current data [119]. To sum up the appearance and disappearance data of LSND, MiniBooNE and several other SBL experiments can be explained by the mixing of the three active neutrinos with one or two additional sterile neutrinos in the so-called 3+1 and 3+2 models (see Refs. [120, 121, 122, 123, 124, 125]).

So the cosmological extra relativistic degrees of freedom may consist of sterile neutrinos (it means neutrinos which don't undergo weak interactions). In a cosmological framework it is important to point out that, if sterile neutrinos exist, their mass influences cosmological observables in an analogous way to that of active neutrinos, it means by changing the epoch of equivalence and by suppressing perturbations via free-streaming.

Here we aimed to determine the masses of the sterile neutrinos in 3+1 and 3+2 models using data from SBL experiments and recent cosmological data and check if the results are mutually compatible. Finally, we combine the bounds from the two different analyses to have a joint probability for the masses of sterile neutrinos. Previous analyses discussing the interplay between SBL and cosmological data may be found in Refs. [126, 18, 36, 35]. We also notice here that bounds on extra–radiation from Big Bang Nucleosynthesis (BBN) [108, 18, 35, 127] may be quite severe, pointing toward a more constrained value for $N_{\rm eff}$ than what is implied by CMB data. Recent analyses on BBN constraints are indicating a favored value of $N_{\rm eff}$ smaller than 4 [108]. This result would imply that the 3+2 scheme might be already considered as disfavored by BBN data.

6.2 Current Cosmological Constraints

Here we summarize the cosmological constraints from current data on the active neutrino masses and on the sterile neutrino thermal abundance and masses. We have modified the Boltzmann CAMB code [26] incorporating the extra massive sterile neutrino parameters and extracted cosmological parameters from current data using a Monte Carlo Markov Chain (MCMC) analysis based on the publicly available MCMC package `CosmoMC`[25]. We consider here a flat ΛCDM scenario plus three (N_{ν_s}) active (sterile) massive neutrino species, described by a set of cosmological parameters

$$\{\omega_b, \omega_c, \theta_s, \tau, n_s, \log[10^{10} A_s], m_\nu, m_{\nu_s}, N_{\nu_s}\} \ , \tag{6.1}$$

where $\omega_b \equiv \Omega_b h^2$ and $\omega_c \equiv \Omega_c h^2$ are the physical baryon and cold dark matter densities, θ_s is the ratio between the sound horizon and the angular diameter distance at decoupling, τ is the optical depth, n_s is the scalar spectral index, A_s is the amplitude of the primordial spectrum [1], m_ν is the active neutrino mass, m_{ν_s}

[1] The pivot scale assumed in this study corresponds to $k_0 = 0.05$ Mpc^{-1}.

is the sterile neutrino mass and N_{ν_s} is the number of thermalized sterile neutrino species. We assume that both active and sterile neutrinos have degenerate mass spectra (m_ν and m_{ν_s} are the individual masses, not the sum of the masses). The flat priors assumed on these cosmological parameters are shown in Table 6.1.

Table 6.1. Flat priors for the cosmological parameters considered here.

Parameter	Prior
$\Omega_b h^2$	0.005-0.1
$\Omega_c h^2$	0.01-0.99
θ_s	0.5-10
τ	0.01-0.8
n_s	0.5-1.5
$\ln(10^{10} A_s)$	2.7-4
m_{ν_s} [eV]	0-3
m_ν [eV]	0-3
N_{ν_s}	0-6

Here our basic data set is the seven–year WMAP data [10, 28] (temperature and polarization) with the routine for computing the likelihood supplied by the WMAP team. We consider two cases: we first analyze the WMAP data together with the luminous red galaxy clustering results from SDSSII (Sloan Digital Sky Survey) [69] and with a prior on the Hubble constant from HST (Hubble Space Telescope) [128], referring to it as the "run1" case. We then include to these data sets Supernova Ia Union Compilation 2 data [129], and we will refer to this case as "run2". In addition, we also add to the previous data sets the BBN measurements of the ^{4}He abundance, considering separately helium fractions of $Y_p^1 = 0.2561 \pm 0.0108$ (see Ref. [130]) and of $Y_p^2 = 0.2565 \pm 0.0010$ (stat.) ± 0.0050 (syst.) from Ref. [131]. Finally, we also consider the Deuterium abundance measurements $\log(D/H) = -4.56 \pm 0.04$ from Ref. [132].

It is important to clarify that CMB anisotropies also depend on the value of Y_p but since Y_p is constrained loosely by current CMB/LSS data, it is consistent to fix it to value $Y_p = 0.24$ in the CMB runs and to consider it as an independent parameter constrained by BBN observations.

Given a cosmological model, we predict the theoretical primordial abundance of Y_p and $\log(D/H)$ by making use of the public available PArthENoPE BBN code (see [133]).

Since running cosmomc and getting at the same time the theoretical predictions from Parthenope for BBN would be exceedingly time-consuming we perform

importance sampling obtaining the predicted values for Y_p and $\log(D/H)$ with an interpolation routine using a grid of Parthenope predictions for each (ω_b, N_{ν_s}), as in [134].

Table 6.2. 1D marginalized bounds on the active and sterile neutrino parameters using the two combinations of data sets described in the text (r1 refers to "run 1" and r2 refers to "run 2", respectively).

Parameter	68% CL(r1)	95% CL(r1)	68% CL (r2)	95% CL (r2)
N_{ν_s}	< 2.5	< 4.1	< 2.0	< 3.2
m_ν [eV]	< 0.13	< 0.30	< 0.10	< 0.20
m_{ν_s} [eV]	< 0.22	< 0.46	< 0.20	< 0.50

Table 6.3. 1D marginalized 95% CL bounds on N_{ν_s}, m_{ν_s} and m_ν after combining the results of "run 2" with those coming from different measurements of BBN light element abundances.

	Y_p^1 [130]	Y_p^2 [131]	$Y_p^1 + D$ [132]	$Y_p^2 + D$ [132]
N_{ν_s}	< 2.3	< 1.7	< 1.7	< 1.4
m_ν [eV]	< 0.17	< 0.15	< 0.15	< 0.15
m_{ν_s} [eV]	< 0.62	< 0.67	< 0.69	< 0.68

Table 6.2 shows the 1D marginalized bounds on N_{ν_s}, m_{ν_s} and m_ν arising from the two different analyses performed here on cosmological data sets. The marginalized limits have been computed setting a lower limit of 0 in all the three neutrino parameters here explored. The bounds obtained on the parameters associated to the dark matter candidates considered here are consistent with those obtained in Ref. [47] after taking into account the differences in the thermal abundances of sterile neutrinos and QCD thermal axions. When we marginalize over all the cosmological parameters, see Table 6.2, the 95% CL upper bound for N_{ν_s} is 4.1 (3.2) using "run1" ("run2") data sets. Therefore, current cosmological data does not exclude at the 95% CL the existence of ~ 2 sterile neutrino species with sub-eV masses plus three sub-eV active massive neutrinos. It would be interesting to further explore if a model with sterile neutrinos is preferred over the model with only three active neutrinos (see next Section). The results here are also in very good agreement with those of Ref. [35] even if in the former analysis the two species, i.e. the active and sterile

neutrino states, were not considered to be massive at the same time.

Table 6.3 shows the 95% 1D marginalized bounds on N_{ν_s}, m_{ν_s} and m_ν arising when different combinations of BBN light element abundances measurements are combined with "run 2" results. Note that when measurements of the ^{4}He abundance are added to CMB, galaxy clustering and SNIa data, the 95% CL upper limit on N_{ν_s} is 2.3 (1.7) if $Y_p^1 = 0.2561 \pm 0.0108$ ($Y_p^2 = 0.2565 \pm 0.0010 \pm 0.0050$) is assumed. Since the number of sterile species after adding BBN constraints is smaller than before, the sterile (active) neutrino masses can get slightly larger (smaller) values, since BBN data is insensitive to the dark matter density in the form of massive neutrinos at late times. The combination of Helium and Deuterium abundance measurements compromises the viability of (3+2) models, leading to $N_{\nu_s} < 1.7 - 1.4$ at the 95% CL. However, the two sterile states might not have thermal properties at decoupling and evade BBN constraints. A complete analysis including sterile neutrino mixing parameters and recent reactor neutrino oscillation results [135] is mandatory.

Figure 6.1, top panel, depicts the 68% and 95% CL allowed contours in the m_ν–N_{ν_s} plane. The blue (red) contours denote the allowed regions by "run1" ("run2") data sets. Notice that there exists a degeneracy between these two quantities. This degeneracy is similar to the one found by the authors of Ref. [35]. When the mass energy density in the form of massive neutrinos is increased, the number of extra relativistic species must also be increased to compensate the effect. This will be the case for massless sterile species. In this analysis, the degeneracy is milder respect to those of Figure 5.5 and [35], since sterile neutrinos are massive and therefore they behave as an additional dark matter component at late times. The degeneracy will show up when the active neutrinos have relatively large masses, since, in that case, a tiny amount of sterile neutrino masses will be allowed. The sterile states will then behave as relativistic particles at the decoupling era and will compensate the effect of a large active neutrino mass.

Figure 6.1, middle panel, depicts the 68% and 95% CL allowed contours in the m_ν–m_{ν_s} plane. There exists a very strong anticorrelation between these two quantities, since both contribute to the dark matter energy density at late times and therefore if the mass of the sterile neutrino states grows, the mass of the active ones must decrease. The situation is analogous to that of QCD thermal axions and massive (active) neutrinos, see Ref. [47].

The bottom panel of Figure 6.1 depicts the 68% and 95% CL allowed contours in the N_{ν_s}–m_{ν_s} plane. In this case, the larger the sterile neutrino mass is, the lower its thermal abundance must be, as expected.

6.3 Neutrino oscillations analysis

The short–baseline neutrino oscillation analysis is performed following Refs. [121, 122, 123].

We consider 3+1 and 3+2 neutrino spectra in which ν_e, ν_μ, ν_τ are mainly mixed with ν_1, ν_2, ν_3, whose masses are much smaller than 1 eV and there are one or two additional massive neutrinos, ν_4 and ν_5, which are mainly sterile and have masses of the order of 1 eV. Short-baseline oscillations are generated by the large squared-mass

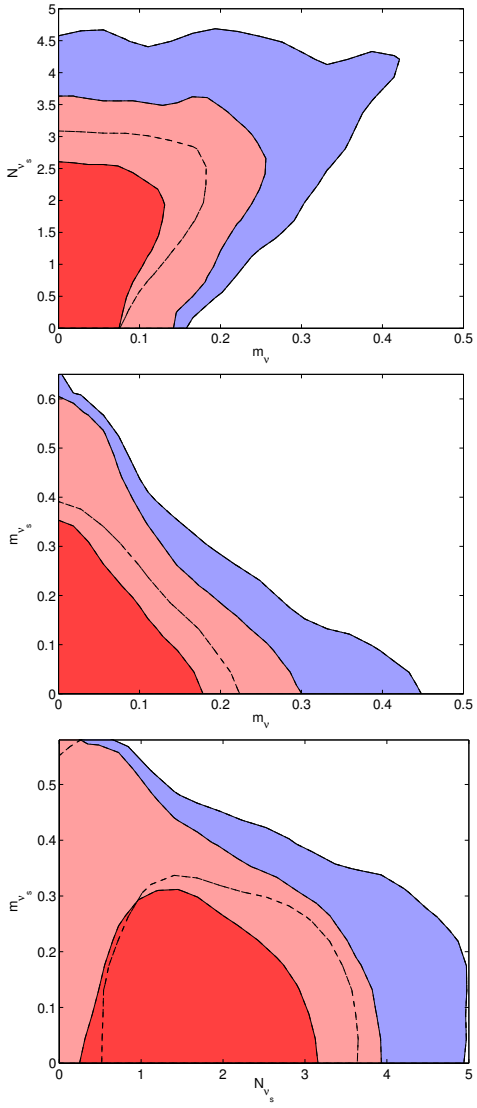

Figure 6.1. The top, middle and bottom panels show the 68% and 95% CL constraints on the plane m_ν-N_{ν_s}, m_ν-m_{ν_s} and m_{ν_s}-N_{ν_s}, respectively. The blue (red) contours denote the allowed regions by "run1" ("run2") data sets, see text for details. The masses of the sterile and active neutrinos are both in eV units.

differences Δm^2_{41} and Δm^2_{51}, with:

$$\Delta m^2_{51} \geq \Delta m^2_{41} \gg \Delta m^2_{31} \gg \Delta m^2_{21}\,. \tag{6.2}$$

The small squared–mass differences Δm^2_{21} and Δm^2_{31} which generate, respectively, solar and atmospheric neutrino oscillations (see Refs.[111, 112, 113]) have negligible effects in SBL oscillations and are ignored in the following. The two heavy neutrino masses m_4 and m_5 which are probed by cosmological data are simply connected to

Table 6.4. Values of $\chi^2_{\rm min}$, number of degrees of freedom (NDF), goodness–of–fit (GoF) and best–fit values of the mixing parameters obtained in our 3+1 and 3+2 fits of short–baseline oscillation data.

	3+1	**3+2**
$\chi^2_{\rm min}$	142.1	134.1
NDF	138	134
GoF	39%	48%
Δm^2_{41} [eV^2]	1.62	0.89
$\vert U_{e4}\vert^2$	0.035	0.018
$\vert U_{\mu 4}\vert^2$	0.0086	0.015
Δm^2_{51} [eV^2]		1.61
$\vert U_{e5}\vert^2$		0.022
$\vert U_{\mu 5}\vert^2$		0.0047
η		1.57π

the squared–mass differences relevant for SBL oscillations by:

$$m_4 \simeq \sqrt{\Delta m^2_{41}}\,, \qquad m_5 \simeq \sqrt{\Delta m^2_{51}}\,. \tag{6.3}$$

We fit the data set of short-baseline neutrino oscillation experiments corresponding to the GLO–HIG analysis in Ref. [123], in which the low-energy MiniBooNE neutrino [136] and antineutrino [137, 138, 139] data corresponding to the so-called "MiniBooNE low–energy anomaly" are not considered, since they induce a strong tension between appearance and disappearance data (see the discussions in Refs. [122, 123]). We made the following two improvements with respect to the analysis presented in Ref. [123]:

1. We used the reactor neutrino fluxes presented in the recent White Paper on light sterile neutrinos [140], which update Refs. [141, 142]. The new fluxes are about 1.3% larger than those we used before, which were taken from the reactor antineutrino anomaly publication [135].

2. We replaced the KamLAND bound on $\vert U_{e4}\vert^2$ with a more powerful constraint obtained from solar neutrino data [143, 144, 145]. Taking into account the recent measurement of $\vert U_{e3}\vert^2$ in the Daya Bay [146] and RENO [147] reactor neutrino experiments ($\vert U_{e3}\vert^2 = \sin^2\vartheta_{13} = 0.025 \pm 0.004$), from Figure 1 of Ref. [145] we inferred the approximate upper bound $\vert U_{e4}\vert^2 = \sin^2\vartheta_{14} \leq 0.02$ at 1σ (see Ref. [148]).

In our analysis of SBL neutrino oscillation data we apply first the standard χ^2 method. The minimum value of χ^2, the number of degrees of freedom, the goodness–of–fit and the corresponding best–fit values of the oscillation parameters are presented in Table 6.4. The results concerning the 3+1 and 3+2 fits are similar to those reported, respectively, in Ref. [123] for the GLO–HIG case and Ref. [121], with small variations due to the consideration of different data sets. From Table 6.4 we can see that in both the 3+1 and 3+2 frameworks the global goodness–of–fit is satisfactory.

The allowed regions of Δm^2_{41} versus the effective SBL oscillation amplitudes $\sin^2 2\vartheta_{e\mu}$, $\sin^2 2\vartheta_{ee}$ and $\sin^2 2\vartheta_{\mu\mu}$ (with $\sin^2 2\vartheta_{\alpha\beta} = 4|U_{\alpha 4}|^2|U_{\beta 4}|^2$) are shown in Figure 6.2. These regions are relevant, respectively, for $\overset{(-)}{\nu}_\mu \leftrightarrows \overset{(-)}{\nu}_e$, $\overset{(-)}{\nu}_e \to \overset{(-)}{\nu}_e$ and $\overset{(-)}{\nu}_\mu \to \overset{(-)}{\nu}_\mu$ oscillation experiments. They are more similar to those shown in Figure 3 of Ref. [123] than the region presented in Ref. [148], because the larger reactor antineutrino fluxes used in this analysis increase the reactor antineutrino anomaly, leading to a larger value of $|U_{e4}|^2$, which tends to cancel the effect of the solar neutrino constraint.

The allowed regions in the Δm^2_{41}-Δm^2_{51} plane obtained in the 3+2 analysis are shown in Figure 6.3. One can see that the allowed regions are similar to those presented in Figure 9 of Ref. [121], with small variations due to the different considered data sets.

Since we want to perform a combined analysis of SBL oscillation data and cosmological data and the cosmological analysis is performed with the Bayesian method, we have also analyzed the SBL oscillation data with a Bayesian approach. We assumed the sampling distribution of the data D:

$$p(D|\theta_M, M) \propto e^{-\chi^2(D,\theta_M)/2}\,, \tag{6.4}$$

where M is the model ($M = 3+1$ or $M = 3+2$), θ_M is the corresponding set of oscillation parameters (listed in Table 6.4) and $\chi^2(D, \theta_M)$ is the corresponding χ^2 function. The sampling probability is the likelihood when considered as a function of the parameters of the model. In each of the two models, we calculated the posterior probability distribution of the oscillation parameters using Bayes' theorem:

$$p(\theta_M|D, M) = \frac{p(D|\theta_M, M)p(\theta_M|M)}{p(D|M)}\,, \tag{6.5}$$

where $p(D|M)$ is easily calculated as a normalization constant. We assumed a flat prior distribution in the logarithmic space of the oscillation parameters, except for the CP–violating phase η in the 3+2 spectrum (see Ref. [121]) for which we used a linear scale in the interval $[0, 2\pi]$. For $\log(\Delta m^2_{41}/\mathrm{eV}^2)$ and $\log(\Delta m^2_{51}/\mathrm{eV}^2)$ we considered the range $[-1, 1]$. For $\log|U_{e4}|^2$, $\log|U_{\mu 4}|^2$, $\log|U_{e5}|^2$, $\log|U_{\mu 5}|^2$ we considered the range $[-4, 0]$.

Since we are interested in combining the results of the analysis of SBL oscillation data with that of the cosmological data, where the only shared parameters are the neutrino masses in Eq.(6.3), we calculated the marginal posterior probability distributions of the squared–mass differences by integrating the posterior probability distribution over the other oscillation parameters taking into account the scale of

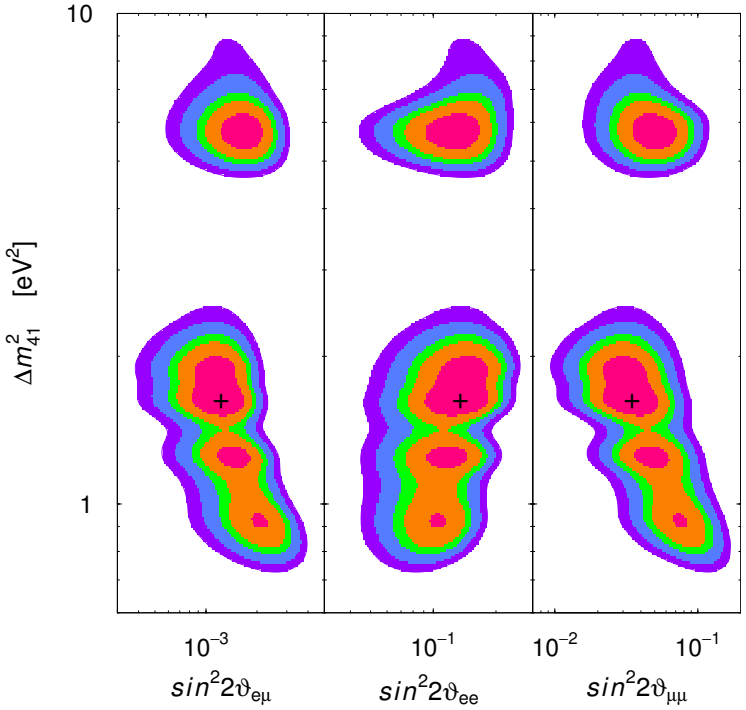

Figure 6.2. Allowed regions in the $\sin^2 2\vartheta_{e\mu}$–Δm^2_{41}, $\sin^2 2\vartheta_{ee}$–Δm^2_{41} and $\sin^2 2\vartheta_{\mu\mu}$–$\Delta m^2_{41}$ planes obtained from the global fit of short–baseline neutrino oscillation data in the 3+1 scheme using the standard χ^2 method. The best-fit point is indicated by a cross (see Table. 6.4).

the flat prior. For example, in the 3+1 model:

$$p(\log \Delta m^2_{41}|D, 3+1) = \int d\log|U_{e4}|^2 \, d\log|U_{\mu 4}|^2 \times p(\log(\Delta m^2_{41}), \log|U_{e4}|^2, \log|U_{\mu 4}|^2|D, 3+1)\,. \quad (6.6)$$

In this way, we obtained the posterior probability distribution of Δm^2_{41} in the 3+1 spectrum plotted in Figure 6.4 (thick green line exhibiting several sharp peaks) and the allowed regions in the Δm^2_{41}–Δm^2_{51} of the 3+2 spectrum shown in Figure 6.5. Comparing with Figure 6.3, one can see that the Bayesian allowed regions are wider than those obtained with the χ^2 method. The difference is due to the different method of marginalization with respect to the other mixing parameters (mixing angles and CP–violating phase): in the χ^2 method one considers only the minimum of the χ^2 in the range of each marginalized parameter, whereas in the Bayesian method one must integrate the posterior probability density over the marginalized parameter space. Since the data do not constrain much the values of the marginalized parameters (see Figures 10–12 of Ref. [121]), the Bayesian integration gives significantly different results from the χ^2 marginalization. The allowed vertical bands with constant value of Δm^2_{41} are due to the fact that one

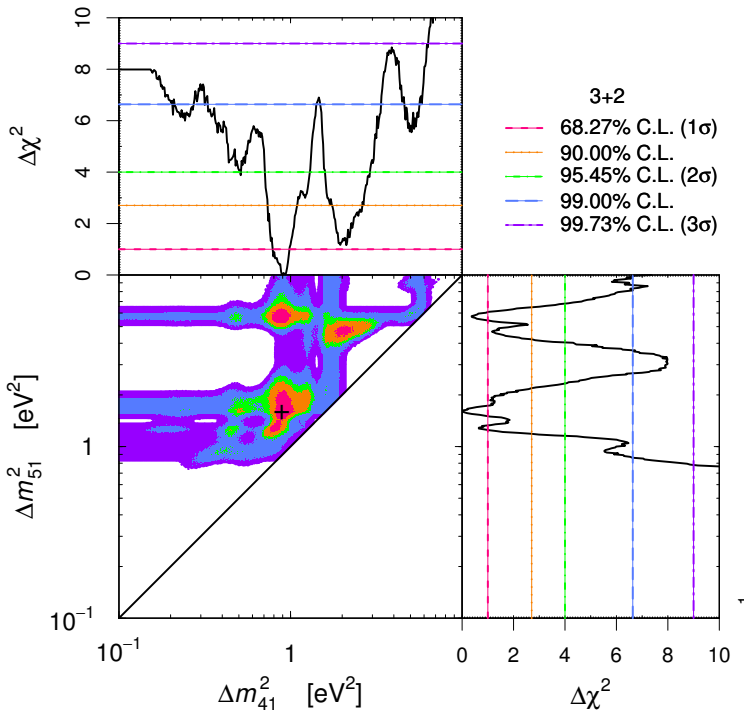

Figure 6.3. Allowed regions in the Δm^2_{41}-Δm^2_{51} plane and corresponding marginal $\Delta\chi^2$'s obtained from the global fit of short–baseline neutrino oscillation data in 3+2 schemes using the standard χ^2 method. The best-fit point is indicated by a cross (see Table. 6.4).

can have a comparable fit for any value of Δm^2_{51} and negligible $|U_{e5}|$ and $|U_{\mu 5}|$, which is effectively equivalent to a 3+1 framework. The same applies to the allowed horizontal bands with constant value of Δm^2_{51}.

6.4 Cosmological analysis

In order to match cosmology with SBL analysis, here the cosmological analysis is performed in two different steps: first by analyzing CMB–only data and then by further adding data from large scale structure and priors on the Hubble parameter. The CMB analysis is performed by employing the following datasets: WMAP7 [10], ACT [39] and SPT [40]. The large scale structure analysis makes use of information on dark matter clustering from the matter power spectrum extracted from the SDSS–DR7 luminous red galaxy sample [69]. Finally, the Hubble parameter prior we use is based on the latest Hubble Space Telescope observations [3].

We analyze datasets up to $\ell_{\rm max} = 3000$. The analysis method we adopt is based on the publicly available Markov Chain Monte Carlo (MCMC) package `CosmoMC` [25] with a convergence diagnostic done through the Gelman and Rubin statistic.

We sample the following six–dimensional standard set of cosmological parameters,

adopting flat priors on them: the baryon and cold dark matter densities $\Omega_b h^2$ and $\Omega_c h^2$, the ratio of the sound horizon to the angular diameter distance at decoupling θ_s, the optical depth to reionization τ, the scalar spectral index n_S and the overall normalization of the spectrum A_S. We account for foregrounds contributions including three extra amplitudes: the SZ amplitude, the amplitude of clustered point sources, and the amplitude of Poisson distributed point–sources (see Section 8). We consider purely adiabatic initial conditions and we impose spatial flatness. Here both active and sterile neutrinos are assumed to be fully thermalized. Sterile neutrino thermalization [149, 150, 151, 152, 153] is realized through oscillations and occurs if the mass splittings and mixing angles with active neutrinos are not too small. An approximate condition is that the relevant squared-mass separation Δm^2 and effective mixing $\sin\theta$ satisfy the following requirement [152]:

$$\Delta m^2 \ \sin^4\theta > 3 \times 10^{-6} \ \mathrm{eV}^2 \, . \tag{6.7}$$

For the 3+1 case, this condition is always fulfilled, as can be seen in Figure 6.3. In the 3+2 case, the situation is more complex, since the allowed regions from the SBL analysis may extend to the case where one of the two additional neutrinos has very small values of the mixing angle and/or the mass splitting, as is shown in the analysis of Ref. [121]. The situation where one of the two sterile neutrinos decouples (and the 3+1 scheme is actually recovered as a limit) is a possible solution for the 3+2 case. Table 6.4 above and Ref. [121] show that for the best fit parameters the values of the mass splittings and effective mixing angles are sufficient to ensure thermalization of both states in the 3+2 case; when the parameters are moved toward the edges of the their allowed ranges, Eq. (6.7) may not be satisfied for both sterile states and full thermalization of one of the two extra–neutrinos may not occur and a dedicated analysis of the thermalization process would be required. In our analysis we assume that full thermalization always occurs in the allowed parameter space. Clearly, a partial or non–standard thermalization could lead to completely different constraints on the sterile neutrino mass [149, 150, 151, 152]. In particular, Ref. [152] shows that in the non thermal case the cosmological energy density in sterile neutrinos does not monotonically increase with the mass and it is constrained to be less then 0.003 at 95% C.L. for masses > 1 eV; as an aftermath, in the matter power spectrum the suppression due to free–streaming is smaller at higher masses. This effect can relax the constraints on the sterile neutrino masses around 1 eV.

The aim is to specifically test 3+1 and 3+2 neutrino mass models, by means of a joint analysis of both cosmological and SBL experiments data. Therefore, contrary to the typical approach (see e.g. Ref. [35, 36, 154]), in the cosmological analysis we do not let the effective number of relativistic degrees of freedom N_{eff} to vary as a free parameter, instead we fix it at the values $N_{\mathrm{eff}} = 3 + 1$ or $N_{\mathrm{eff}} = 3 + 2$ for the 3+1 and 3+2 schemes, respectively. This is consistent with the assumptions done in the oscillation analysis and with the hypothesis of cosmological full thermalization of all neutrino states (including the sterile ones; see the recent discussions in Refs. [149, 150]). Consistently to the analysis of Section 6.3, we fix the three active neutrinos to be massless and we allow the sterile neutrinos to have masses which vary as additional free parameters. Since we are interested to sample the joint sensitivity of cosmological and SBL neutrino data on the sterile–neutrinos mass parameters, in

Table 6.5. MCMC estimation of the cosmological parameters from the analysis of CMB–only data and from CMB data plus matter power spectrum information (SDSS) and a prior on H_0 (HST), in the case of three massless active neutrinos and one massive sterile neutrino (3+1 scheme) and assuming 3 massless active neutrinos plus 2 massive sterile neutrinos (3+2 scheme). Neutrino mass upper bounds are reported at the 95% C.L., unless for the 3+2 CMB+SDSS+HST case where we quote the best–fit value together with the 68% (95%) C.L. interval.

	3+1 CMB only	**3+2** CMB only	**3+1** CMB+SDSS+HST	**3+2** CMB+SDSS+HST
$\Omega_b h^2$	0.0224 ± 0.0004	0.0226 ± 0.0004	0.0224 ± 0.0004	0.0226 ± 0.0004
$\Omega_c h^2$	0.135 ± 0.007	0.156 ± 0.009	0.133 ± 0.004	0.156 ± 0.004
τ	0.085 ± 0.014	0.087 ± 0.015	0.084 ± 0.014	0.086 ± 0.014
H_0	71.5 ± 3.6	73.6 ± 4.4	73.1 ± 1.6	74.6 ± 2.0
n_s	0.970 ± 0.015	0.985 ± 0.016	0.977 ± 0.010	0.990 ± 0.010
$\log(10^{10} A_s)$	3.21 ± 0.05	3.20 ± 0.05	3.19 ± 0.04	3.19 ± 0.04
$\Sigma m\ (eV)$	< 2.88	< 2.48	< 0.73	$0.58^{+0.12\ (+0.45)}_{-0.13\ (-0.42)}$
$\chi^2_{\rm min}$	7529.5	7532.2	7578.5	7581.1

the cosmological analysis we do not employ the neutrino mass fraction f_ν (as it is usually done), but instead we sample directly $\log \Delta m^2_{41}$ and $\log \Delta m^2_{51}$. This implies a flat prior on those parameters.

Before attempting a joint analysis with the SBL data, which have been presented in the previous Section, we report in Table 6.5 the constraints on the cosmological parameters using CMB–only data and CMB data plus SDSS information together with the HST prior, and assuming: a 3+1 model with three massless active neutrinos and one massive sterile neutrino; a 3+2 model with three massless active neutrinos plus two massive sterile neutrinos. The 95% C.L. mass bounds on the sterile neutrinos is 2.88 eV for the 3+1 scheme, while for the 3+2 model the bound on the sum of the masses of the two additional sterile neutrinos is 2.48 eV, both of them share a 2σ upper limit of about 1.24 eV, when CMB–only data are used. These bounds drastically improve when also SDSS data and the HST prior are included in the analysis (see Ref. [155]), reaching the value of 0.73 eV for the 3+1 case and about 1 eV for the 3+2 case. Both the 3+1 and 3+2 schemes are statistically well acceptable,

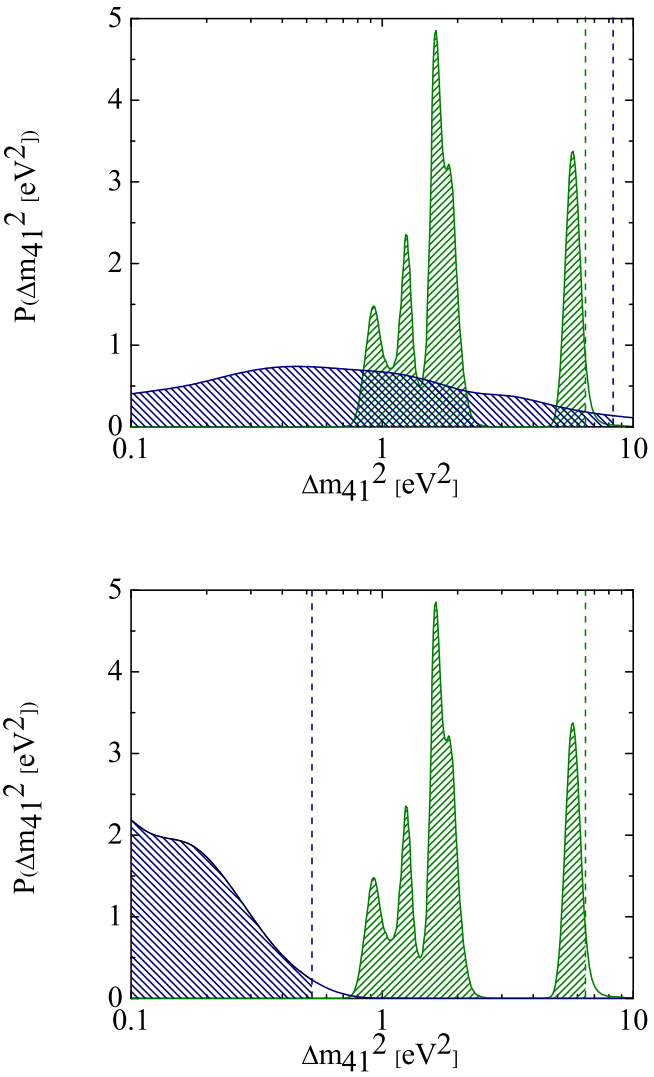

Figure 6.4. Marginal posterior probabilities obtained with a Bayesian analysis for Δm^2_{41} in the 3+1 scheme. The thick [green] solid line exhibiting several sharp peaks (the same in the two panels) refers to the analysis of the short–baseline oscillation data alone. The blue line exhibiting a broad peak stands for the analysis of the cosmological data alone: CMB-only data for the left panel, CMB data implemented with SDSS and HST information for the right panel. In all cases, the shaded regions refer to the 95% coverage of the probability distribution.

with no noticeable preference in the minimal χ^2. The only visible (and expected) difference between the 3+1 and 3+2 schemes is that 2 additional neutrinos require

a larger value of the dark matter abundance $\Omega_c h^2$, to compensate a delay of the equivalence time, which would instead be induced by the presence of an additional light degree of freedom in the 3+2 case [18]. The correction due to non degeneracy between the mass of the first and the second sterile neutrino in the 3+2 model is of the order of precision of present numerical codes and so undetectable using only the present cosmological data (CMB and matter power spectra). Moreover the degeneracies with other cosmological parameters makes the detection of the neutrino mass differences impossible at the state of art (see Ref. [156]). Figure 6.4 shows the marginal posterior probability of the cosmological Bayesian analysis for the 3+1 case, compared with the results of the SBL study. The blue line exhibiting a broad peak stands for the analysis of the cosmological data alone and the left panel refers to CMB-only data, while the right panel refers to the CMB data implemented with SDSS and HST information. The two panels of the figure show how the inclusion of SDSS and HST information is relevant to set the more stringent constraint on the cosmological upper bound on the neutrino mass. The shaded regions refer to the 95% C.L. coverage of the probability distribution, from which the bounds on m_4 of Table 6.5 are derived. When compared with the SBL analysis and its 95% C.L. mass intervals (three slightly discontinued ranges in the interval $0.93\,\text{eV} < m_4 < 1.45\,\text{eV}$ and a higher mass range $2.29\,\text{eV} < m_4 < 2.59\,\text{eV}$), with a best fit at $m_4 = 1.27\,\text{eV}$, we notice that CMB–only and SBL oscillation data are well compatible among them, with a significant overlap of the corresponding 95% C.L. regions. The 95% C.L. cosmological upper bound $m_4 < 2.88\,\text{eV}$ disfavors the higher mass SBL solution, while is perfectly compatible with the lower SBL mass ranges. The combination of the cosmological and SBL datasets will therefore produce a clean allowed interval, as shown in the next Section. Instead, when SDSS and HST information are included in the analysis, SBL oscillations and cosmological data are in tension, with no overlapping 95% C.L. The analysis for the 3+2 scheme is shown in Figure 6.5, where C.L. regions in the Δm^2_{41}–Δm^2_{51} plane are reported. The SBL allowed regions clearly show a preference for at least a non–zero neutrino mass (m_5 with our choice of hierarchy in neutrino masses) and a global preference for $m_4 = 0.95\,\text{eV}$ and $m_5 = 1.27\,\text{eV}$. The cosmological data instead provide upper limits on both sterile neutrino masses, with no clear preference for non–zero values. CMB–only data (left panel) are well compatible with SBL results, with the 95% C.L. upper bound of the cosmological analysis consistent with the corresponding 95% C.L. regions of the SBL analysis and its global best–fit point ($m_4 = 0.95\,\text{eV}$ and $m_5 = 1.27\,\text{eV}$). Also in the 3+2 case, the inclusion of SDSS and HST data produces tension between SBL and cosmological analyses, as is manifest in the right panel of Figure 6.5, where only a partial overlap at the 3σ C.L. is present. Figure 6.5 clearly shows that the whole set of cosmological data will be instrumental in significantly reducing the degeneracy of the allowed solutions of the SBL analysis when the joint analysis will be attempted in the next Section.

6.5 Combined analysis

The combined analysis of the SBL oscillation data and the cosmological observations has been performed by merging the corresponding posterior probabilities. Since the only relevant parameters common to both sectors are the sterile neutrino masses $m_4 \simeq \sqrt{\Delta m^2_{41}}$ and $m_5 \simeq \sqrt{\Delta m^2_{51}}$ we can define a marginal posterior probability for the joint analysis by directly multiplying the SBL and cosmological marginal posterior probabilities relative to the parameter of interest. For example, in the 3+1 case, denoting by $D_{\rm C}$ and $D_{\rm S}$ the cosmological and SBL data we have[2]:

$$\begin{aligned} &p(\log \Delta m^2_{41} | D_{\rm C+S}, 3+1) \propto \\ &p(\log \Delta m^2_{41} | D_{\rm C}, 3+1) \ \times \ p(\log \Delta m^2_{41} | D_{\rm S}, 3+1)\,, \end{aligned} \tag{6.8}$$

where the SBL probability is the one defined in Eq. (6.6) and the cosmological probability is the one used in the analysis of the previous section and obtained through `CosmoMC`.

The combined analysis for the 3+1 scheme is shown in Figure 6.6. As usual, the left panels refers to the case of CMB–only data in the cosmological sector, while the right panel adds SDSS and HST datasets. The horizontal dashed lines identify the credible intervals at 68.27%, 90.00%, 95.45%, 99.00% and 99.73% C.L. In the case of CMB–only data, the inclusion of the cosmological information to the SBL analysis disfavors the higher mass SBL solution around 2.4 eV but maintains the lower mass 95% C.L. allowed intervals ($0.90\,{\rm eV} < m_4 < 1.46\,{\rm eV}$) and ($2.27\,{\rm eV} < m_4 < 2.51\,{\rm eV}$) and the best–fit solution ($m_4 = 1.27\,{\rm eV}$). When SDSS and HST information is added to the analysis, the allowed interval of the global analysis shifts down to lower values of the sterile neutrino mass, due to the more stringent bound from the cosmological sector. The 95% C.L. mass range becomes $0.85\,{\rm eV} < m_4 < 1.18\,{\rm eV}$, and the best fit shifts down to $m_4 = 0.93\,{\rm eV}$.

The combined analysis for the 3+2 scheme is shown in Figure 6.7, again for the case of CMB–only data (left panel) and for the further inclusion of SDSS and HST data (right panel). The global results are that at least one sterile neutrino needs to be massive, with a mass of the order of 1 eV (m_5 with our choice of hierarchy), while the second sterile neutrino can be massless. The marginalized 95% intervals for the two neutrino masses are: $m_4 < 2.51\,{\rm eV}$ and $0.86\,{\rm eV} < m_5 < 3.16\,{\rm eV}$ when CMB–only data are considered; $m_4 < 0.70\,{\rm eV}$ and $0.67\,{\rm eV} < m_5 < 1.35\,{\rm eV}$ for the full analysis which includes also SDSS and HST.

[2] Since we assumed a flat prior for $\theta = \log \Delta m^2_{41}$ in both the SBL and cosmological analyses, using Bayes' theorem (6.5) we have $p(\theta|D_{\rm C+S}) \propto p(D_{\rm C+S}|\theta) = p(D_{\rm C}|\theta) p(D_{\rm S}|\theta) \propto p(\theta|D_{\rm C}) p(\theta|D_{\rm S})$.

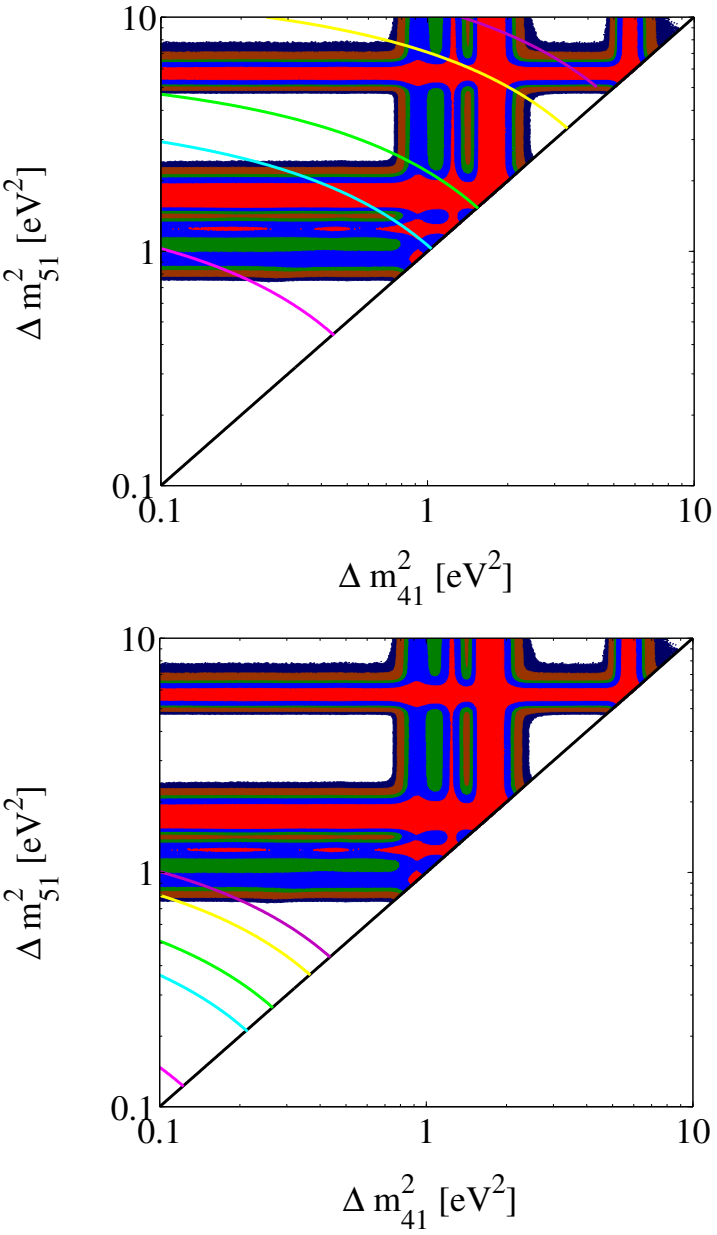

Figure 6.5. Allowed regions in the Δm^2_{41}-Δm^2_{51} plane obtained with a Bayesian analysis. The "boxy" regions (the same in the two panels) refer to the global analysis of the short–baseline oscillation data and are relative to the following confidence levels (from the innermost to the outermost region): 68.27% (red), 90.00% (light blue), 95.45% (green), 99.00% (brown) and 99.73% (dark blue). The arc–shaped solid lines refer to the analysis of the cosmological data: the left panel stands for the CMB–only dataset, while the right panel refers to the inclusion of the SDSS information and HST prior to the CMB data. The different lines refer to the following confidence levels (from the lower curve to the upper curve, in each panel): 68.27% , 90.00%, 95.45%, 99.00% and 99.73% .

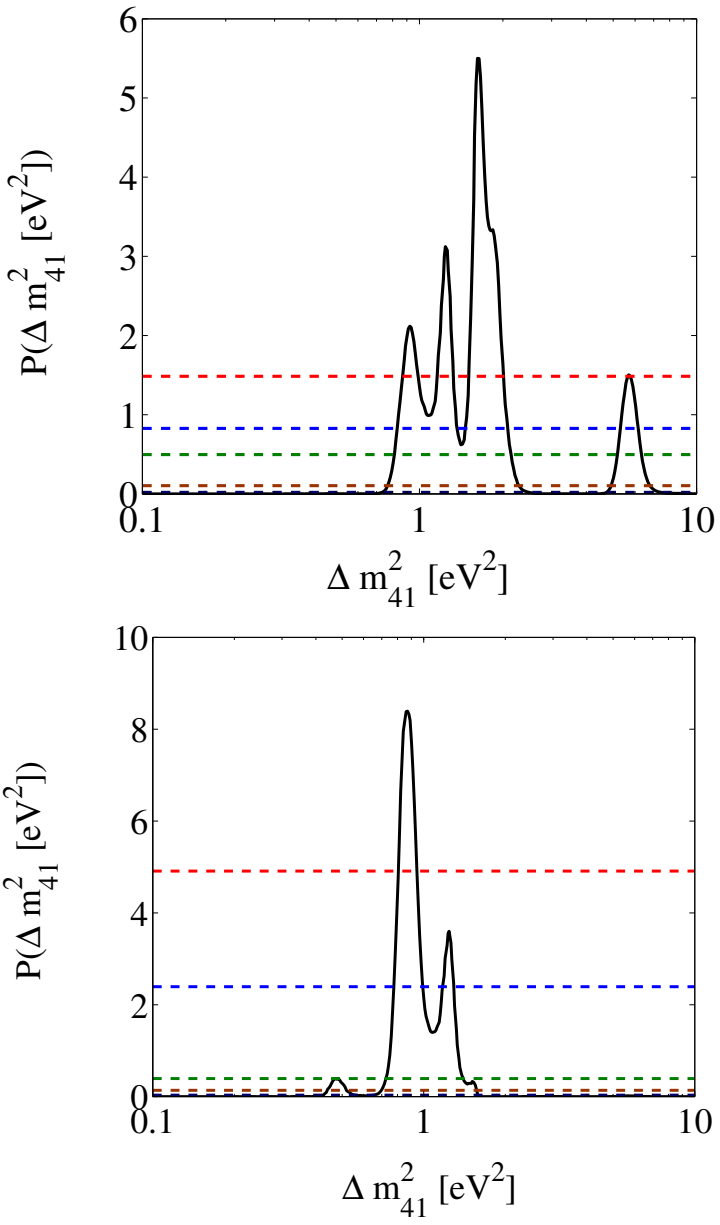

Figure 6.6. Marginal posterior probabilities obtained with a Bayesian analysis for Δm^2_{41} in the 3+1 scheme, for the joint analysis of cosmological and short–baseline data. Left panel: the cosmological analysis employs CMB–only data. Right panel: the cosmological analysis adds SDSS and HST information to the CMB data. The horizontal dashed lines identify (from the lower curve to the upper curve, in each panel) the credible intervals at 68.27%, 90.00%, 95.45%, 99.00% and 99.73% C.L.

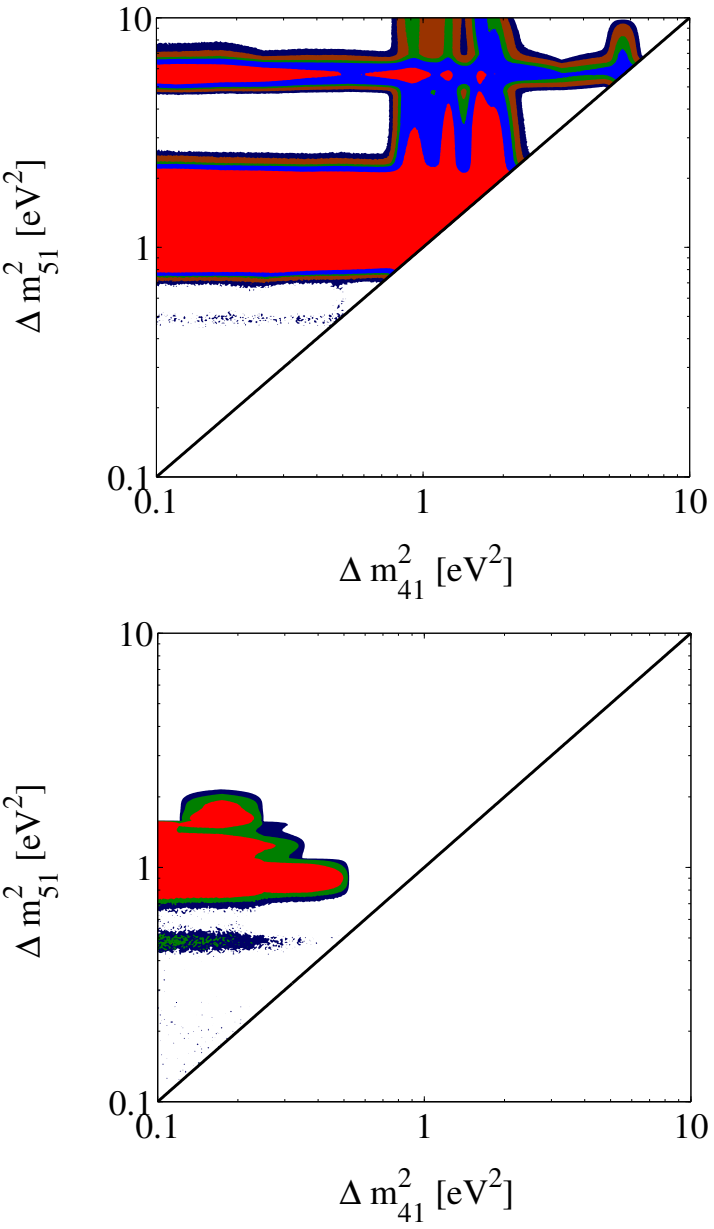

Figure 6.7. Allowed regions in the Δm^2_{41}–Δm^2_{51} plane obtained with a Bayesian approach, for the joint analysis of short–baseline and cosmological data. The different regions (as in Figure 6.5) refer to the following confidence levels (from the innermost to the outermost region): 68.27% (red), 90.00% (light blue), 95.45% (green), 99.00% (brown) and 99.73% (dark blue). Left panel: SBL data plus the CMB–only dataset. Right panel: SBL data plus CMB, SDSS and HST data; in this case only 68.27% (red), 95.45% (green) and 99.73% (dark blue) C.L. are reported.

Chapter 7

Neutrino Mass and Priors: Reionization and Curvature

7.1 Introduction

Precision observation of CMB and large scale structure of galaxies can be used to probe neutrino mass with greater precision than current laboratory experiments. The most recent data release from WMAP after seven years of observations presented a bound on the total neutrino mass of $\Sigma m_\nu < 1.3$eV at the 95% c.l. [10, 28]. This bound is approximately a factor five better than the current laboratory experimental upper limit inferred from a combination of beta-decay experiments and neutrino oscillation data (see e.g. [157]). The CMB bound on neutrino masses is also considered the most conservative limit from cosmology. Indeed, including information from galaxy clustering and luminosity distance data, the constraint can be further improved to $\Sigma m_\nu < 0.55$eV at 95% c.l. [10], while a limit of $\Sigma m_\nu < 0.28$eV at 95% c.l. can be obtained by including redshift-dependent halo bias-mass relations [158].

But cosmological results (see bayesian analysis) are very model dependent. It is however important to be aware of the theoretical modelling behind the constraint based on cosmological measurements. A model of structure formation based on dark matter, adiabatic primordial fluctuations and dark energy is assumed and the removal of one of these assumptions can in principle affect the CMB limit. So it is important to investigate the changes in neutrino mass bounds if we use different theoretical assumptions.

We investigate another possible theoretical caveat that could affect the CMB bound on the sum of the neutrino masses, i.e. the modelling of the reionization epoch. It is often assumed in the current cosmological data analysis that reionization is a sudden event at redshift $z = z_{re}$, i.e. this process is usually described by a single parameter with the free electron fraction x_e increasing from $\sim 10^{-4}$ up to 1 for redshifts $z < z_{re}$ (~ 1.08 for $z < 3$ when taking into account Helium reionization).

While this scenario can properly describe several reionization scenarios, it can't obviously describe more complex reionization scenarios as for example double or not-monotone reionization. Given our current ignorance about the thermal history of the universe at redshifts $z \geq 6$ it is important to consider all the possible reionization scenarios allowed by data when deriving the most conservative constraint on a cosmological parameter such as the sum of the neutrino masses. We indeed assume a more general reionization model following the principal components method suggested by Mortonson and Hu [159] and we derive constraints on the neutrino mass in this different theoretical framework.

7.2 Reionization

The primeval plasma was highly ionized. After decoupling electrons and protons recombined themselves in neutral hydrogen. So the Universe became neutral and it started the Dark Age that finished when the first luminous object turned on. They emitted photoionizing photons and so they activated reionization [160].

The observational evidence of the present ionized Universe is the Gunn-Peterson effect. The Gunn-Peterson trough [161] is a feature of the spectra of the quasars due to the presence of neutral hydrogen in the intergalactic medium. The trough is characterized by suppression of electromagnetic emission from the quasar at wavelengths smaller than the wavelength of Lyman-alpha line at the redshift of the emitted light. The effect is observed only in the spectra of the quasars at redshift greater than 6. This means that at $z < 6$ the Universe is highly ionized.

7.2.1 Reionization effects on CMB

For the temperature spectrum the main effect of reionization is an erasure of the primary anisotropies (from recombination) as $\exp(-2\tau_{reion})$ where

$$\tau_{reion} = c\sigma_T \int dt n_e (1+z)^3$$

is the optical depth nowadays of CMB photons due to Thomson scattering (σ_T is the Thomson cross section) with free electron (n_e is the electron density). This occurs below the scale of the horizon at last scattering since only on these scales there has been enough time to convert the originally isotropic temperature fluctuations into anisotropies [162]. This uniform reduction of power at small scales has the same effect as a change in the overall normalization. Moreover there is a degeneracy between τ_{reion} and others cosmological parameters: the scalar spectral index (n_s) and the amplitude of r.m.s. mass fluctuations on spheres of $8\text{Mpc}h^{-1}$ (σ_8). This degeneracy is due to the fact that the reionization damping can be compensated by an increase in the dark matter density fluctuations. If reionization takes place at redshift between 20 and 5 the difference in the power spectrum is confined to large angles ($\ell < 30$). Here the observations are limited by "cosmic variance": the fact that we only have one sample of the sky and hence only $2\ell + 1$ samples of any given multipole. So cosmic variance is the dominating source of uncertainty on the low-ℓ temperature spectrum.

The same is not true for the polarization spectrum where the reionization signal is not cosmic variance limited. CMB photons cannot spread on large scales $\ell < 30$ before recombination ended. So the polarization signal is expected to be zero at low multipole. The peak at low multipole shown in Figure 7.1 is clearly due to the rescattering of CMB photons during reionization.

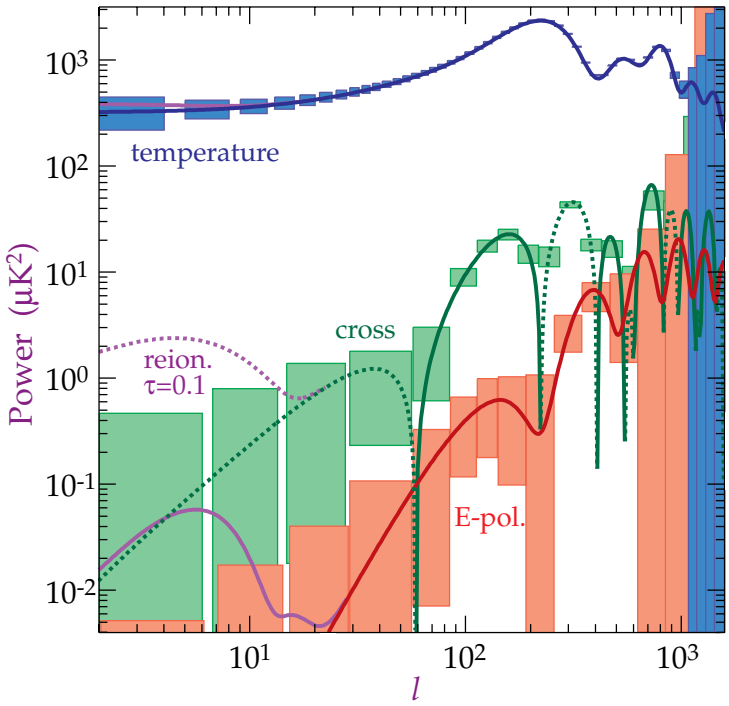

Figure 7.1. Temperature, polarization, and temperature-polarization cross correlation predictions and sensitivity of MAP for a fiducial model $\Omega_0 = 1$, $\Omega_B = 0.1$, $h = 0.5$ cold dark matter. While the reionized model (purple $\tau = 0.1$) is impossible to distinguish from the fiducial model from temperature anisotropies alone, its effect on polarization is clearly visible at low ℓ. Dashed lines for the temperature-polarization correlation represent anticorrelation [162].

Here we would like to point out that, even if we knew the reionization history of the Universe, there is no direct correspondence between the behavior of the fraction of ionized hydrogen at certain redshift and its effect on the E-mode polarization spectrum. For instance, a sudden reionization model produces only one single peak al $\ell < 10$, while models with a partial reionization at higher redshift produce a less high peak, but also a bump at $10 < \ell < 30$ (see Figure 7.2). Moreover we do not know the thermal history of the Universe. For these reasons it is important to analyze cosmological data in the framework of a more general reionization scenario, independent on a particular reionization history.

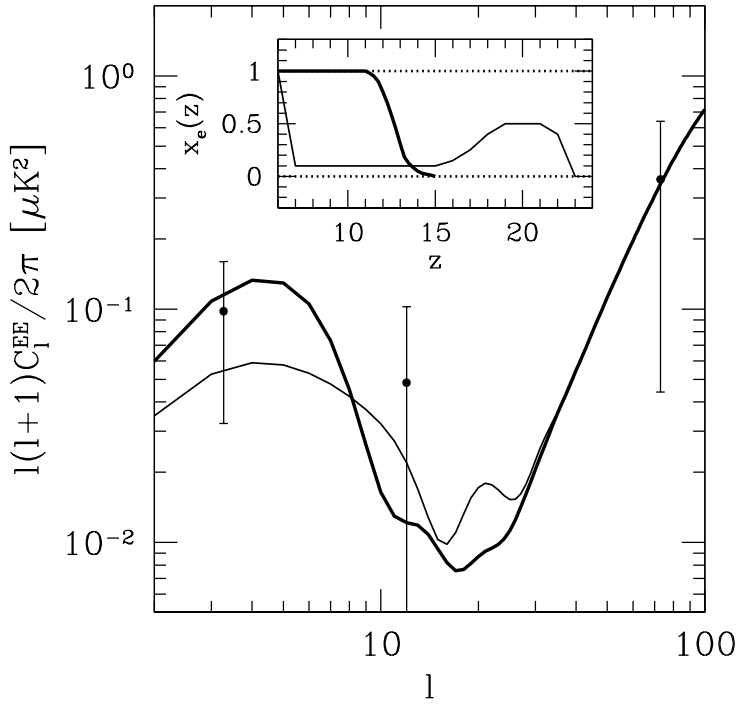

Figure 7.2. E-mode polarization angular power spectra and ionization histories (inset) for a nearly-instantaneous reionization model with optical depth $\tau = 0.105$ (thick curves) and an extended, double reionization history with $\tau = 0.090$ (thin). Points with error bars represent the 3-year WMAP data from Page et al. (2006) [163].

7.3 Principal Components

We adopt the method, developed in Ref. [159], based on principal components that provide a complete basis for describing the effects of reionization on large-scale E-mode polarization. Following Ref. [159], one can parametrize the reionization history as a free function of redshift by decomposing $x_e(z)$ into its principal components:

$$x_e(z) = x_e^f(z) + \sum_\mu m_\mu S_\mu(z),$$

where the principal components, $S_\mu(z)$, are the eigenfunctions of the Fisher matrix that describes the dependence of the polarization spectra on $x_e(z)$ (again, see Ref. [159]), m_μ are the amplitudes of the principal components for a particular reionization history, and $x_e^f(z)$ is the WMAP fiducial model at which the Fisher matrix is computed and from which the principal components are obtained. In what follows we use the publicly available $S_\mu(z)$ functions and varied the amplitudes m_μ for $\mu = 1, ..., 5$ for the first five eigenfunctions. The first 5 modes provide all the information about reionization that are relevant in the E-mode polarization spectrum at large scales where the reionization signal is expected. The eigenfunctions are

computed in 95 bins from redshift $z_{min} = 6$ to redshift $z_{max} = 30$ with $x_e(z) = 1.08$ for $z < 3$, $x_e(z) = 1.0$ for $3 \leq z < 6$ and $x_e(z) = 10^{-4}$ for $z \geq 30$. Hereafter we refer to this method as the MH (Mortonson-Hu) case.

7.4 Analysis method

We have then modified the Boltzmann CAMB code [26] incorporating the generalized MH reionization scenario as in [159] and extracted cosmological parameters from current data using a Monte Carlo Markov Chain (MCMC) analysis based on the publicly available MCMC package `CosmoMC` [25].

We consider here a flat ΛCDM universe described by a set of cosmological parameters

$$\{\omega_b, \omega_c, \omega_\nu, \theta_s, n_s, \log[10^{10} A_s]\}, \tag{7.1}$$

where $\omega_b \equiv \Omega_b h^2$ and $\omega_c \equiv \Omega_c h^2$ are the physical baryon and cold dark matter densities relative to the critical density, ω_ν is the physical energy density in massive neutrinos, θ_s is the ratio of the sound horizon to the angular diameter distance at decoupling, A_s is the amplitude of the primordial spectrum, and n_s is the scalar spectral index. We assume 3 degenerate, massive neutrinos with the same mass (see formula 3.5):

$$m_\nu = 30.8\text{eV} \times \omega_\nu$$

In what follows we will use as standard parameter the value $\Sigma m_\nu = 3 m_\nu$.

The extra parameters needed to describe the reionization are the five amplitudes of the eigenfunctions for the MH case and one single common parameter, the optical depth τ, for the sudden reionization case.

Our basic data set is the seven–year WMAP data [10] (temperature and polarization) with the routine for computing the likelihood supplied by the WMAP team.

7.5 Results

In Table 7.1 we compare the constraints on several cosmological parameters in the case of standard or MH reionization scenario. As we can see from the table, the CMB constraint on the neutrino mass is weakened by $\sim 40\%$ when a more general reionization scenario is considered. This is not simply due to an increase in the parameter space but also due to degeneracies present between the cosmological parameters. Considering the MH reionization scenario renders values of the spectral index n_s in better agreement with the Harrison-Zel'dovich $n_s = 1$ value (see [164]). This changes the relative amplitude of the peaks in the CMB angular spectrum and makes models with higher neutrino mass more consistent with the WMAP data. Introducing a neutrino mass has indeed the effect of decreasing the gravitational potential at recombination, increasing the small scale CMB anisotropy[1]. This can be counterbalanced by decreasing the value of the spectral index n_s as clearly

[1] The effect of neutrino mass on CMB lensing for the WMAP data is negligible.

Table 7.1. 95% c.l. errors on cosmological parameters in the case of sudden reionization and MH reionization. The upper limit on the neutrino mass is relaxed by $\sim 43\%$.

Parameter	WMAP7 (Sudden Reionization)	WMAP7 (MH Reionization)
$\Omega_b h^2$	$0.0221^{+0.0012}_{-0.0012}$	$0.0226^{+0.0015}_{-0.0014}$
$\Omega_c h^2$	$0.117^{+0.013}_{-0.013}$	$0.115^{+0.017}_{-0.017}$
θ_s	$1.038^{+0.005}_{-0.005}$	$1.039^{+0.006}_{-0.005}$
n_s	$0.955^{+0.032}_{-0.033}$	$0.975^{+0.0448}_{-0.0434}$
H_0	$65.7^{+7.6}_{-8.2}$	$66.0^{+10.2}_{-9.0}$
Ω_Λ	$0.674^{+0.091}_{-0.134}$	$0.675^{+0.112}_{-0.148}$
Σm_ν	< 1.15eV	< 1.66eV

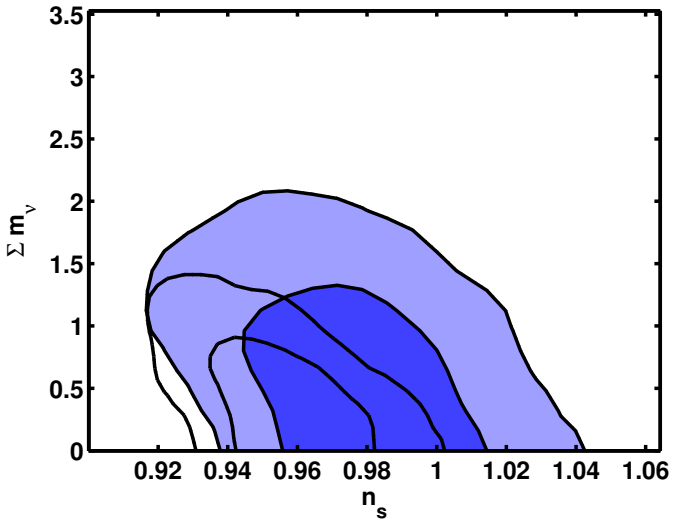

Figure 7.3. Constraints on the Σm_ν vs n_s plane. The filled contours assume MH reionization while the empty contours assume standard, sudden, reionization.

shown by the anti-correlation in the n_s-Σm_ν plane. A general reionization scenario brings higher values of n in agreement with observations, immediately resulting in a better compatibility of larger neutrino masses. It is worth noticing that while in the standard reionization scenario HZ spectra are excluded at about two standard deviations when massive neutrinos are included in the analysis, in the MH case the $n_s = 1$ spectra are well consistent with the data and inside the 1σ c.l. also with $\Sigma m_\nu \sim 0.5$eV.

In Figure 7.3 we show the constraints on the Σm_ν vs n_s plane, while in Figure

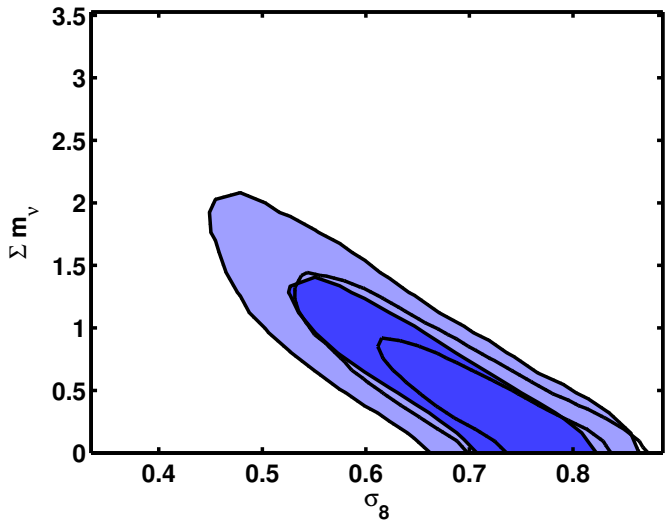

Figure 7.4. Constraints on the Σm_ν vs σ_8 plane. The filled contours assume MH reionization while the empty contours assume standard, sudden, reionization.

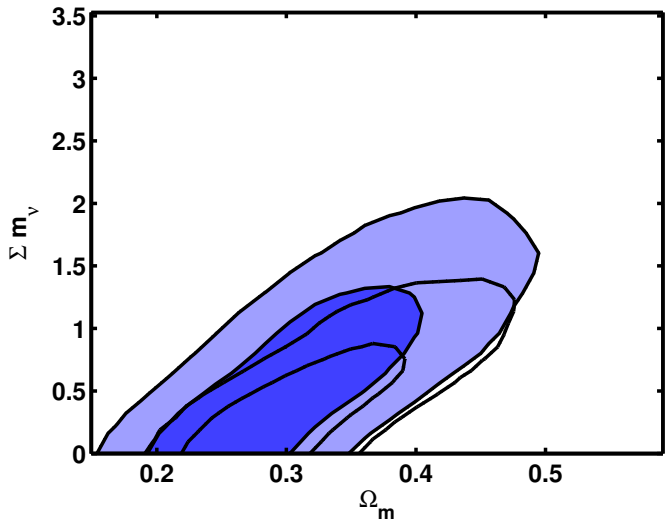

Figure 7.5. Constraints on the Σm_ν vs Ω_m plane. The filled contours assume MH reionization while the empty contours assume standard, sudden, reionization.

7.4 we show the constraints on the Σm_ν vs σ_8 plane. The filled contours assume MH reionization while the empty contours assume standard, sudden, reionization. As we can see, MH reionization allows for values of the spectral index n closer to 1 (as already pointed out in [164]), for a larger neutrino mass and for a lower σ_8 amplitude.

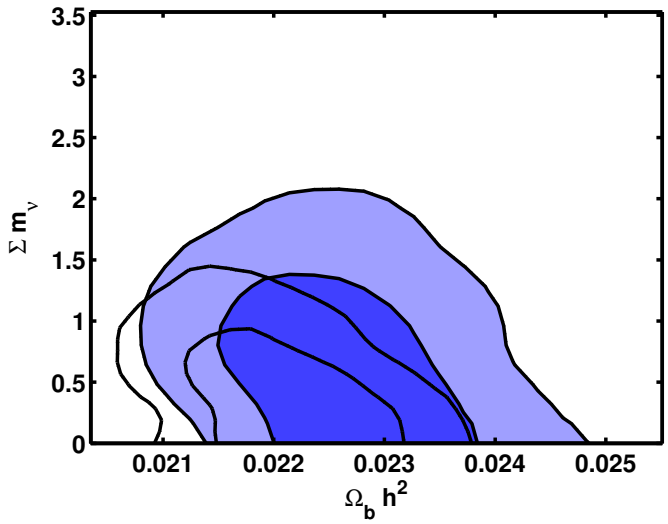

Figure 7.6. Constraints on the Σm_ν vs $\Omega_b h^2$ plane. The filled contours assume MH reionization while the empty contours assume standard, sudden, reionization.

It is interesting to note that a neutrino mass can in principle accommodate lower values of σ_8 with CMB data. When MH reionization is assumed even lower values of σ_8 are consistent with CMB data. A low value of $\sigma_8 \sim 0.77$ is preferred by the recent detection of diffuse Sunyaev-Zel'dovich effect by the South Pole Telescope [165] experiment.

Moreover, correlations exist with the matter density Ω_m, as we show in Figure 7.5 and (even if less pronounced) with the baryon physical density $\Omega_b h^2$ as we show in Figure 7.6.

7.6 The impact of assuming flatness on $\sum m_\nu$

The flatness assumption can represent another source of possible misleading results about neutrino mass in cosmological model dependent analysis.

As in the previous case we make use of `CosmoMC`. But in this case our analysis combines the following CMB anisotropy dataset: not only WMAP 7-year [10] as in the previous analysis, but also the high ℓ data SPT [40], and ACT [39]. Including BAO+H_0 simply means we are using the baryon acoustic oscillation (BAO) data of Percival *et al.* [90] and impose a prior on the Hubble parameter based on the last Hubble Space Telescope observations [3]. We integrate spectral data out to $\ell_{\rm max} = 3000$. We sample from the following parameters: the baryon $\Omega_b h^2$, cold dark matter $\Omega_c h^2$, and dark Ω_Λ energy densities, the scalar spectral index n_s, the optical depth to reionization τ, the Hubble parameter H_0, and the amplitude of SZ spectrum A_{SZ}, which contribution is non negligible if the integration is out $\ell \approx 2000$. We also consider the effective neutrino number $N_{\rm eff}$, spatial curvature Ω_k,

and the sum of neutrino masses $\sum m_\nu$, but in this case we assume a standard sudden reionization scenario.

Table 7.2 shows the results from WMAP+BAO+H0 in the first column and the result of adding the high multipole dataset in the final column for a standard ΛCDM scenario with three massive degenerate neutrinos. Although the constraint greatly improves the two sigma limit for the masses, this is not enough to favor either the standard or inverted hierarchy. However, this is not a surprise because none of the dataset are sensitive enough on their own. Forthcoming data from the Planck experiment and other future experiments will likely improve the mass constraint [166].

Table 7.2. Summary of the constraint on the sum of the neutrino masses. All dataset include BAO and H_0 for improved parameter constraints. Errors are at the 68% CL except for $\sum m_\nu$, which is quoted as a 95% upper limit.

Parameter	WMAP7+BAO+H_0	...+ACT+SPT
$100\Omega_b h^2$	2.26 ± 0.053	2.23 ± 0.038
$\Omega_c h^2$	0.112 ± 0.0036	0.111 ± 0.0029
Ω_Λ	0.719 ± 0.0182	0.726 ± 0.0154
n_s	0.968 ± 0.0124	0.963 ± 0.0092
τ	0.0897 ± 0.015	0.0873 ± 0.014
H_0 (km/s/Mpc)	69.2 ± 1.6	69.9 ± 1.37
$\sum m_\nu$	< 0.57 eV	< 0.45 eV

Finally we investigate the effect of assuming flatness while determining an upper bound on $\sum m_\nu$. We investigate two models. The first assumes three degenerate massive neutrinos, while the second allows for additional relativistic species accounted by $\Delta N_{\rm eff} > 0$. We define the correlation coefficient ρ_{ij} as the ratio of the off-diagonal term of the covariance matrix σ_{ij} to the 1σ errors $\sigma_i \sigma_j$, so that for two parameters denoted by i and j we have $\rho_{ij} = \sigma_{ij}/\sigma_i\sigma_j$. Figure 7.7 shows that $\sum m_\nu$ and Ω_k are strongly correlated with a correlation coefficient of $\rho_{\Omega_k \sum m_\nu} = 0.78$ for both models ($\Delta N_{\rm eff} = 0$ and $\Delta N_{\rm eff} > 0$). Furthermore, the degeneracy considerably increases the uncertainty in the sum of the neutrino masses. In fact, with $\Omega_k \neq 0$ the 95% upper limit on $\sum m_\nu$ more than doubles with respect to the flat case: with $\sum m_\nu < 0.95$ eV for the model assuming only three massive neutrinos and $\sum m_\nu < 1.19$ eV for $\Delta N_{\rm eff} > 0$. The strong correlation between curvature and mass is expected because massive neutrinos with $m_\nu < 0.3$ eV are still relativistic until recombination so they act as an additional radiative component. As a consequence the presence of such massive neutrinos shifts the time of matter-radiation equality a_{eq}. In this case lower

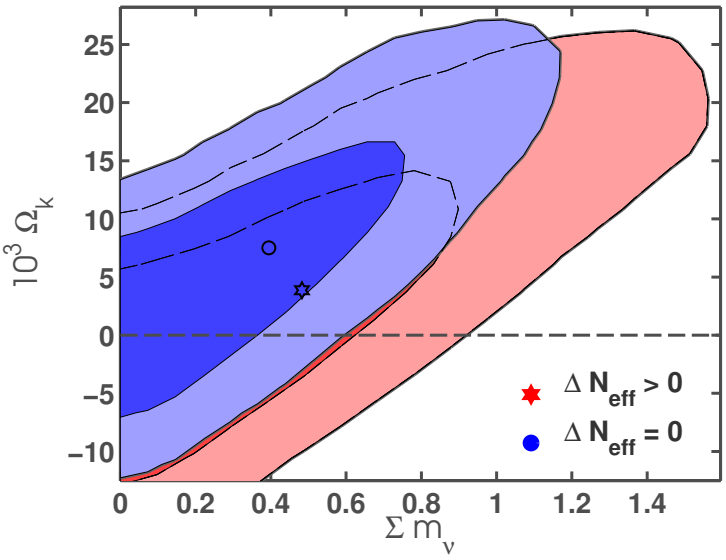

Figure 7.7. Comparison of the correlation between Ω_k and $\sum m_\nu$ under the two $\Delta N_{\rm eff}$ models. The model with three massive neutrinos is shown in blue while the model with additional relativistic species is in red. Intervals are given at the 68% and 95% confidence levels and markers indicate the locations of the marginalized values. Dataset include WMAP7+ACT+SPT+BAO+H_0. The addition of curvature allows $\sum m_\nu$ to be more than twice the previous constraint.

mass neutrinos roughly correspond to higher $N_{\rm eff}$. Neutrinos also leave an imprint on the CMB through the early Integrated Sachs-Wolfe effect (c.f. Section 2.9.2 and Refs. [17, 167]) which changes the position of acoustic peaks. This effect can be compensated by a change in the geometry of the Universe, which weakens the constraints on both $\sum m_\nu$ and Ω_k. See Table 7.3 for a summary of cosmological parameters when curvature and massive neutrinos are considered.

7.7 Neutrino Mass and the Sunyaev Zel'dovich effect

A measurement of the temperature Sunyaev Zel'dovich (tSZ) (see Section 2.9.2) power spectrum (for more details on how to take into account tSZ and, in general, secondary anisotropies and foreground in CMB analysis see Section 8) can be used to determine the sum of neutrino masses by breaking the degeneracy between σ_8 and neutrino mass (see Figure 7.4) that exists with the CMB data alone. The CMB data alone are consistent with high neutrino masses which slows the growth of structure. If the sum of neutrino masses was around 1eV and $\sigma_8 \simeq 0.6$ the measured tSZ power would in fact be higher than that predicted by Sehgal model [168]. The X-ray constraints, $\sigma_8 \simeq 0.8$, which is independent of the tSZ modeling, rules out this

Table 7.3. Summary of the constraint on the sum of the neutrino masses when $\Omega_k \neq 0$. $\Delta N_{\rm eff}$ is an additional relativistic contribution after considering 3.046 massive neutrinos. Dataset include WMAP7+ACT+SPT+BAO+H_0. Errors are at the 68% CL except for $\sum m_\nu$, which is quoted as a 95% upper limit.

Parameter	$\Delta N_{\rm eff} = 0$	$\Delta N_{\rm eff} > 0$
$100\Omega_b h^2$	2.24 ± 0.043	2.26 ± 0.049
$\Omega_c h^2$	0.118 ± 0.0063	0.134 ± 0.0105
Ω_Λ	0.711 ± 0.0216	0.703 ± 0.0239
n_s	0.967 ± 0.011	0.982 ± 0.015
τ	0.0864 ± 0.0144	0.0890 ± 0.0145
H_0 (km/s/Mpc)	70.6 ± 1.62	73.1 ± 2.03
$10^3\,\Omega_k$	7.52 ± 7.74	3.46 ± 8.69
$\sum m_\nu$	< 0.95 eV	< 1.19 eV
$\Delta\, N_{\rm eff}$	0	0.995 ± 0.430

line of argument.

Using CMB dataset of WMAP 7-year [10, 28] and SPT [40], plus BAO data [90] and a prior on H_0 [3], neutrino masses are highly degenerate with σ_8 as shown in Figure 7.8 of paper [169]. Higher neutrino masses lead to lower σ_8 since massive neutrinos slow the growth of structure below the neutrino free-streaming length. As reported in [169], introducing massive neutrinos weakens the CMB+H0+BAO constraints on σ_8 from $\sigma_8 = 0.812 \pm 0.018$ to $\sigma_8 = 0.756 \pm 0.044$. The sum of the neutrino mass is constrained to be less than 0.52eV at 95% CL.

The tSZ power spectrum presents an independent probe of σ_8

$$D^{\rm tSZ} \propto \left(\frac{h}{0.71}\right)^{1.7} \left(\frac{\sigma_8}{0.80}\right)^{8.3} \left(\frac{\Omega_b}{0.044}\right)^{2.8}.$$

This breaks the Σm_ν degeneracy and thereby improves the neutrino mass determination. Models that predict more tSZ power require a lower σ_8 to match the observed tSZ power spectrum. As can be seen in Figure 7.8, lower σ_8 values favor larger neutrino masses.

With massive neutrinos and no modeling uncertainty, adding the tSZ information reduces the uncertainty on σ_8 by a factor of 2-3. The median σ_8 moves up slightly to $\sigma_8 = 0.776 \pm 0.019$ with the Shaw model [170] and to $\sigma_8 = 0.732 \pm 0.017$ with the Sehgal model [168] . In this optimistic scenario, author of paper [169] find $\Sigma m_\nu = 0.15 \pm 0.09$eV or $\Sigma m_\nu = 0.29 \pm 0.10$eV for the Shaw and Sehgal models,

respectively. Note that the X-ray σ_8 measurement mentioned earlier is in tension with the preferred σ_8 of the Sehgal model. With a more realistic 50% modeling uncertainty on the Shaw model, the constraint is $\sigma_8 = 0.768 \pm 0.031$. With this modeling uncertainty, the Sehgal and Shaw model results are consistent at $\sim 0.5\sigma$. The upper limit on Σm_ν is reduced from 0.52eV to 0.40eV at 95% CL with the addition of tSZ information.

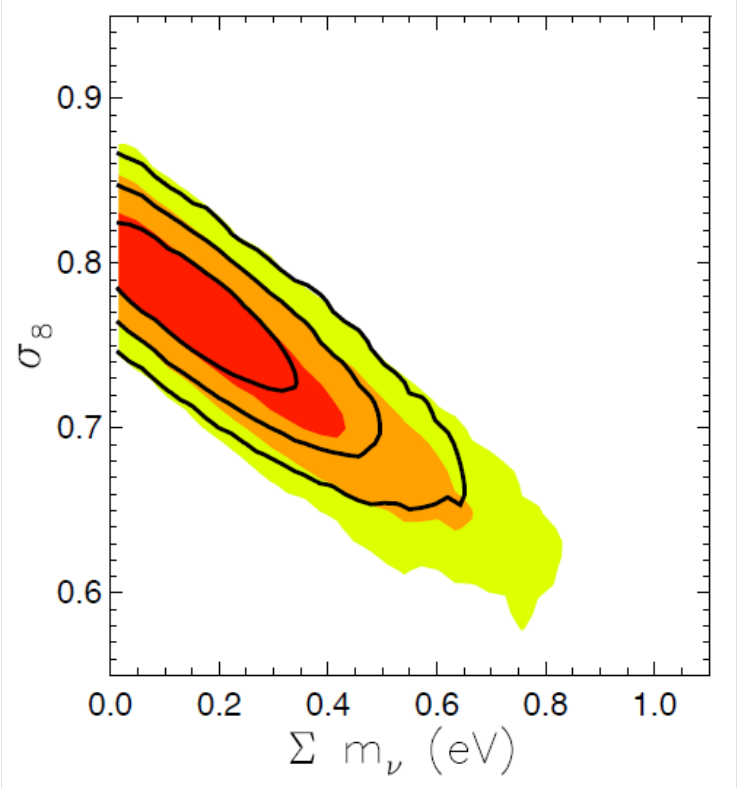

Figure 7.8. 2D likelihood for σ_8 and m_ν. The filled contours show the 1σ, 2σ and 3σ constraints for the CMB+BAO+H0 data. The black solid lines show the constraints with the addition of the tSZ information assuming 50% theory prior.

Chapter 8

Sunyaev Zel'dovich effect and foregrounds

8.1 Introduction

The observation of CMB anisotropies is affected by several systematics and secondary effects due to the fact that the CMB is not the only source of emission in the microwave frequencies and to the formation of structures between the observer and the last scattering surface (see Section 2.9.2 and [171, 172, 173, 174]). The great accuracy of future data requires a compelling description of these effects, in order to separate the different contributions to the anisotropies and to distinguish primordial and secondary effects (see [175]). The observable used to extract most of the cosmological information from the CMB is the angular power spectrum C_ℓ. Secondary effects or unresolved foregrounds provide a contribution to the observed C_ℓ. In order to obtain an unbiased determination of the cosmological parameters from CMB maps it is necessary to correctly describe possible contaminations. On the other hand, both contaminants and secondary effects themselves contain certain cosmological and astrophysical information, especially on the formation of structure at late-times and the large-scale structure of the Universe, so that the separation of these components from primordial CMB fluctuations becomes an important science goal on its own. The Galactic emission and radio point sources are typical examples of foreground contamination in CMB maps. While the bright sources detected in maps can be removed with a suitable mask before the estimation of the angular power spectrum, unresolved point sources will contribute to the total anisotropy power spectrum C_ℓ.

The Sunyaev-Zel'dovich (SZ) effect (see Section 2.9.2 and [8]), caused by the Compton scattering of the CMB photons by the electrons in the Universe, is a well-known secondary anisotropy studied by a variety of experiments. The SZ effect contains cosmological information, since the angular power spectrum of secondary

temperature anisotropy arising from SZ scattering depends on both the gas distribution in galaxy clusters and on the amplitude of the matter density fluctuations σ_8 (see Section 7.7 and [176, 177, 178, 179]). Since the SZ thermal effect has a unique spectral signature relative to the CMB thermal spectrum, the SZ signal can be distinguished from primary CMB anisotropies and other foregrounds using observations at multiple frequencies across the SZ null at ~ 217 GHz ([180]). Such a separation, however, is not feasible with kinetic SZ effect associated with peculiar motions of the electrons scattering the CMB ([8]) as the signal has the same spectrum as that of the CMB. Even for the SZ thermal effect, in realistic experiments, the main obstacles that limit a clear detection of the thermal signal comes from uncertainties in the modeling of the kinetic contribution and the difficulty of separating SZ effects from clustered point sources.

The contribution of unresolved point sources and SZ effect is best seen on small angular scales where they dominate the total CMB angular power spectrum. The use of data at these small angular scales is hence becoming decisive in the analysis of CMB data. Here we analyze large ℓ data (up to $\ell \sim 9000$) from the South Pole Telescope (SPT) at 150 and 220 GHz ([181]) and from Atacama Cosmology Telescope (ACT) ([39, 67]) at 150 GHz combined with Wilkinson Microwave Anisotropy Probe (WMAP) data after 7 years of observation ([10]) to put constraints on the two SZ effects.

In previous studies significant limitations came from uncertainties associated with clustering of dusty star-forming galaxies (DSFG) that contribute to high-frequency CMB data. Such clustering has now been measured with both Herschel ([182]) and Planck ([183]) experiments. In the context of CMB studies, Herschel measurements are most useful as they probe the DSFG clustering down to sub-arcminute angular scales at scales well matched to arcminute scale CMB experiments while Planck measurements are limited to scales greater than $5'$ or $\ell < 2000$. Here we describe the clustering of unresolved point sources we used the same template of [182], where the authors reported a detection of both the linear clustering and the non-linear clustering at a few arcminute scales, corresponding to $\ell \sim 4000$.

In what follows we perform a Monte Carlo Markov Chain (MCMC) analysis constraining both the thermal and the kinetic terms of the SZ effect together with the the Poisson and clustering corrections due to unresolved point sources, including radio sources at lower frequencies such as 150 GHz.

8.2 Parametrizing SZ effect and foregrounds

In this Section we briefly describe the adopted parametrizations and templates for the Sunyaev-Zel'dovich effect, unresolved extragalactic point source foregrounds and lensing.

8.2.1 Sunyaev-Zel'dovich thermal and kinetic effect.

As we have already discussed in Section 2.9.2, the SZ effect has two different contributions, one from the thermal motion of the electrons (thermal SZ effect - tSZ)

and one from the bulk motion of the electrons relative to the CMB (kinetic SZ - *kSZ*). The former contribution has a distinct frequency dependence, while the kSZ effect causes only a Doppler shift of the incident CMB spectrum retaining the black body shape. The total SZ signal in a generic direction $\hat{n}$ is then given by (see for example Section 2 in [39]):

$$\Delta T^{\rm SZ}(\nu) = \frac{f(x)}{f(x_0)} \Delta T_0^{\rm tSZ}(\hat{n}) + \Delta T^{\rm kSZ}(\hat{n}) \ , \tag{8.1}$$

with $x = h\nu/k_B T_{CMB}$ and $f(x) = 2 - x/2\tanh(x/2)$. Here ΔT_0^{tSZ} is the expected thermal contribution at frequency ν_0. From $f(x)$ it can easily seen that the thermal SZ effect vanishes at ~ 218 GHz. We model the SZ contributions to the anisotropy angular power spectrum, relative to a template power spectrum, as

$$D_\ell^{{\rm SZ},ij} = A_{\rm tSZ} \frac{f(\nu_i)}{f(\nu_0)} \frac{f(\nu_j)}{f(\nu_0)} D_{0,\ell}^{\rm tSZ} + A_{\rm kSZ} D_{0,\ell}^{\rm kSZ} \ , \tag{8.2}$$

where $D_\ell = \ell(\ell+1)C_\ell/2\pi$ and $D_{0,\ell}^i$ is the template spectrum for either thermal or kinetic SZ. Here we consider the SZ templates from [70], computed by tracing through a dark matter simulation and processed to include gas in dark matter halos and in the filamentary intergalactic medium. The thermal SZ template describes the power from tSZ temperature fluctuations from all clusters for a Universe normalized with amplitude of matter fluctuations $\sigma_8 = 0.8$. In particular we use the 'standard' model of [70], that was first described in [168], and assuming a σ_8 scaling given by $D_{0,\ell}^{tSZ} \propto (\sigma_8/0.8)^{8.1}$ as found in [70]. For these templates the reference values at $\ell = 3000$ are $D_{0,\ell=3000}^{tSZ} \simeq 8.9\mu K^2$ and $D_{0,\ell=3000}^{kSZ} \simeq 2.1\mu K^2$

8.2.2 Foregrounds from unresolved extragalactic point sources.

The foregrounds contribution to the CMB power spectrum at arcminute angular scales arises essentially from unresolved extragalactic point sources. These sources provide two contributions, a Poisson term due to the random discrete distribution and a clustering term accounting for the large-scale distribution of the sources. We assume the Poisson term as constant in C_ℓ, modeling it as $D_\ell^{\rm Poiss} = A_{\rm Poiss} D_{0,\ell}^{\rm Poiss}$ where $D_{0,\ell}^{\rm Poiss} = (\ell/3000)^2$. The clustered term can be similarly expressed as $D_\ell^{{\rm clust},ij} = A_{\rm clust}(\nu_i, \nu_j) D_{0,\ell}^{\rm clust}$, where $D_{0,\ell}^{\rm clust}$ is the point sources clustering template and $A_{\rm clust}(\nu_i, \nu_j)$ encodes the frequency scaling (see Section 8.3 for further details). Contribution to point sources comes from radio point sources and dusty star-forming galaxies (DSFG). At 220 GHz the main point source contribution is mainly DSFGs while at 150 GHz the point sources are primarily radio sources with a synchrotron spectrum. We therefore neglect the clustering of radio sources and assume that the contribution from radio sources is essentially described only by a Poisson behavior. For clustered DSFGs we adopt the template from [182] where the authors reported a detection of both the linear clustering and the excess of clustering associated with the 1-halo term at arcminute scales. Those data are from the Herschel Multi-tiered Extra-galactic survey (HerMES) ([184]), taken with the Spectral and Photometric Imaging Receiver (SPIRE) onboard the Herschel Space Observatory ([185]).

8.2.3 CMB Lensing

It is well known that gravitational lensing of CMB anisotropies by large-scale structure tends to increase the power at small angular scales (see [186] for a recent review). A proper calculation of this effect is hence necessary in order to prevent an incorrect estimate of the foregrounds and SZ parameters. The calculation of lensed CMB spectra out to $\ell = 9000$ is prohibitively expensive in computational time. Instead, we approximate the impact of lensing by adding a fixed lensing template D_ℓ^{lens} computed by running `camb` ([26]) with and without the lensing option and taking the difference between these spectra. In this run the cosmological parameters of the ΛCDM model are fixed at the best fit values WMAP7. In [181] it has been estimated that the error due to this approximation is less than $0.5\mu\mathrm{K}^2$ at $\ell > 3000$ and is hence negligible with respect to secondary and foregrounds contributions. The lensing contribution is clearly frequency independent.

8.3 Analysis Method and data

We place constraints on the cosmological parameters and on the SZ and foregrounds parameters using the 7-years WMAP data in combination with the SPT data at 150 GHz and at 220 GHz, and the ACT data at 148 GHz. The SPT and ACT datasets are necessary to analyze the smaller scales of the power spectrum where point sources and SZ are dominant. For the SPT data we select the single frequency 15×15 blocks from the full 45×45 covariance matrix provided by the SPT collaboration (see [181]), neglecting the correlation between different frequencies.

We use a 6-parameter flat-ΛCDM cosmological model to describe primary CMB anisotropies and reionization: the baryon and dark matter physical energy densities $\Omega_b h^2$, $\Omega_c h^2$, the reionization optical depth τ, the ratio of the sound horizon to the angular diameter distance at the decoupling θ_s, the amplitude of the curvature perturbation A_s (with flat prior on $\log A_s$) and the spectral index n_s; these two last parameters are both defined at the pivot scale $k_0 = 0.002$ hMpc^{-1}. In addition to the standard cosmological parameters we include the SZ and foreground parameters described in the previous section. We perform a Monte Carlo Markov Chain analysis based on the publicly available package `CosmoMC` ([25]) suitably modified to account for the additional parameters, with a convergence diagnostic based on the Gelman and Rubin statistics. When estimating parameters with point sources and SZ included, the total CMB anisotropy spectra are three, one for each frequency plus the cross-correlation term, because of the frequency dependence of the secondary anisotropies.

In order to study the stability of our results on the assumed parametrization, we perform three different analysis, both with 6 additional parameters describing SZ effect and foregrounds, but considering different parametrizations.

8.3.1 First case: "run1".

In the first case, that we define as "run1" in what follows, we consider the SZ effect parameters A_{tSZ} and A_{kSZ}, the Poissonian contribution A^{150}_{Poiss} and A^{220}_{Poiss} and the

Poisson contribution for the 150×220 GHz cross-correlation $A^X_{\rm Poiss}$. The use of the $A^X_{\rm Poiss}$ extra parameter for the cross correlation of Poisson point source can be justified from the possibility that the contribution at one single frequency comes from more than one point source population and that the two channels are not fully correlated. This possibility has not been considered in previous analyses and is therefore important to evaluate the impact of this assumption. Finally we consider a single clustered point sources parameter, $A_{\rm clust}$, scaling the contribution at different frequencies using the relation of [187]:

$$I_\nu = 8.80 \times 10^{-5} \, (\nu/\nu_0) \, P_\nu \, (13.6K) \ ,$$

with $\nu_0 = 100{\rm cm}^{-1}$, following recent results from Planck ([183]). In what follows we refer to this scaling as "Gispert" scaling.

In summary, the spectra in "run1" are defined as:

$$\begin{aligned}
D_\ell(150) &= D_\ell^{lens} + A_{\rm tSZ} D_{0,\ell}^{\rm tSZ} + A_{\rm kSZ} D_{0,\ell}^{\rm kSZ} \\
&\quad + A_{\rm clust} D_{0,\ell}^{\rm clust150} + A^{150}_{\rm Poiss} D_{0,\ell}^{\rm Poiss} \\
D_\ell(220) &= D_\ell^{lens} + A_{\rm kSZ} D_{0,\ell}^{\rm kSZ} \\
&\quad + A_{\rm clust} D_{0,\ell}^{\rm clust220} + A^{220}_{\rm Poiss} D_{0,\ell}^{\rm Poiss} \\
D_\ell(150\times 220) &= D_\ell^{lens} + A_{\rm kSZ} D_{0,\ell}^{\rm kSZ} \\
&\quad + A_{\rm clust} D_{0,\ell}^{\rm clustcross} + A^{\rm cross}_{\rm Poiss} D_{0,\ell}^{\rm Poiss}
\end{aligned}$$

The thermal SZ effect is negligible at 220 GHz. The contribution of the thermal SZ effect to the cross-correlated power spectrum may not vanish in presence of a spatial correlation between IR sources and the clusters that cause the thermal SZ. Nevertheless as showed in [181] the effect of this correlation is negligible for the SPT data (see par. 7.4 in [181] for further details). We hence do not consider this contribution when fitting the data.

8.3.2 Second case: "run2".

In the second analysis, to which in what follows we refer as "run2", we assume full correlation between the Poisson point sources signal at 150 and 220 GHz as done in previous analyses, i.e. we fix the cross amplitude of Poisson point sources at the square root of the product of the amplitudes at 150 and 220, $A^X_{\rm Poiss} = \sqrt{A^{150}_{\rm Poiss} A^{220}_{\rm Poiss}}$. Moreover, we don't scale the clustered point sources template and we use instead two different parameters for 150 and 220 GHz. This second analysis is more similar to the one presented in [181], however we point out that while here we consider the amplitudes at different frequencies as free parameters, [181] considered the amplitudes at one single frequency and one common frequency spectral index for clustered and point sources as free parameters.

In this second case the foreground spectra are defined as:

$$
\begin{aligned}
D_\ell(150) &= D^{lens}_{\ell,150} + A_{\rm tSZ} D^{\rm tSZ}_{0,\ell} + A_{\rm kSZ} D^{\rm kSZ}_{0,\ell} \\
&\quad + A_{\rm clust150} D^{\rm clust}_{0,\ell} + A^{150}_{\rm Poiss} D^{\rm Poiss}_{0,\ell} \\
D_\ell(220) &= D^{lens}_{\ell,220} + A_{\rm kSZ} D^{\rm kSZ}_{0,\ell} \\
&\quad + A_{\rm clust220} D^{\rm clust}_{0,\ell} + A^{220}_{\rm Poiss} D^{\rm Poiss}_{0,\ell} \\
D_\ell(150 \times 220) &= D^{lens}_{\ell,X} + A_{\rm kSZ} D^{\rm kSZ}_{0,\ell} \\
&\quad + \sqrt{A_{\rm clust150} A_{\rm clust220}} D^{\rm clust}_{0,\ell} \\
&\quad + \sqrt{A_{\rm Poiss150} A_{\rm Poiss220}} D^{\rm cross}_{0,\ell}
\end{aligned}
$$

8.3.3 Third case: "run3".

Finally we combine 150 GHz data of SPT and ACT, using separate parameters for ACT and SPT both for clustered and Poisson point sources, to account for the different masking thresholds of the point sources. In this case we have:

$$
\begin{aligned}
D_\ell(150) &= D^{lens}_{\ell,150} + A_{\rm tSZ} D^{\rm tSZ}_{0,\ell} + A_{\rm kSZ} D^{\rm kSZ}_{0,\ell} \\
&\quad + A_{\rm clustACT} D^{\rm clust}_{0,\ell} + A^{150}_{\rm PoissACT} D^{\rm Poiss}_{0,\ell} \\
&\quad + A_{\rm clustSPT} D^{\rm clust}_{0,\ell} + A^{150}_{\rm PoissSPT} D^{\rm Poiss}_{0,\ell}
\end{aligned}
$$

8.4 Results

In Table 8.1 we report the mean values of the cosmological parameters and their 68% C.L. uncertainty from SPT data at 150 and 220 GHz for the "run1" and "run2" analyses, while in Table 8.2 we list the mean values of the cosmological parameters and their 68% C.L. uncertainty from ACT data ("run3") combined with SPT data at 150 GHz. In order to facilitate the comparison with other works present in the literature we also translate the constraints on the foregrounds amplitudes in to the foreground power spectrum at $\ell = 3000$, $D_{\ell=3000}$. Since a significant correlation exists between thermal and kinetic SZ and since the kinetic SZ is predicted to be small, we also perform an analysis by fixing $D^{\rm kSZ}_{\ell=3000} = 2\,\mu K^2$.

We find that for the "run1" case the thermal SZ anisotropy amplitude is $D^{\rm tSZ}_{\ell=3000} = 2.2 \pm 1.5\,\mu K^2$. While a $\sim 1\sigma$ indication for SZ is present our result is less significant than the one reported by [181] with $D^{\rm tSZ}_{\ell=3000} = 3.2 \pm 1.3\,\mu K^2$ i.e. with a thermal SZ detection at at more than two standard deviations. The result on the kinetic SZ component are compatible, with $D^{\rm kSZ}_{\ell=3000} = 2.7 \pm 1.9\,\mu K^2$ at 68% c.l. from our analysis to be compared with $D^{\rm kSZ}_{\ell=3000} = 2.4 \pm 2.0\,\mu K^2$ from [181].

Although the point sources and SZ parameters do not show significant degeneracies with cosmological parameters (see also [188]), a strong correlation exists between $A_{\rm tSZ}$ and $A_{\rm kSZ}$ and to a smaller extent between $A_{\rm tSZ,kSZ}$ and $A_{\rm clust}$. This can be seen in Figure 8.1 where we show the $2-D$ likelihood constraints in the

Table 8.1. Mean values and 68% error bars from SPT data at 150 and 220 GHz. Run1 case is with only one DSFG clustering amplitude allowed to vary and frequency scaling fixed from [187], consistent with Planck ([183]). Run2 case is with two DSFG clustering amplitudes allowed to vary, without frequency scaling.

	WMAP7+ SPT (run1, kSZ free)	WMAP7+ SPT (run1)	WMAP7+ SPT(run2, kSZ free)	WMAP7+ SPT (run2)
$10^2\Omega_b h^2$	2.267 ± 0.049	2.268 ± 0.051	2.264 ± 0.049	2.269 ± 0.049
$\Omega_c h^2$	0.113 ± 0.005	0.113 ± 0.004	0.1126 ± 0.0052	0.1127 ± 0.0052
τ	0.090 ± 0.015	0.089 ± 0.015	0.089 ± 0.015	0.090 ± 0.014
n_s	0.973 ± 0.013	0.973 ± 0.013	0.972 ± 0.013	0.972 ± 0.012
$\log(10^{10} A_s)$	3.18 ± 0.04	3.18 ± 0.04	3.18 ± 0.045	3.18 ± 0.04
Ω_m	0.278 ± 0.028	0.279 ± 0.029	0.276 ± 0.029	0.276 ± 0.028
σ_8	0.823 ± 0.028	0.825 ± 0.028	0.820 ± 0.0272	0.821 ± 0.026
$A_{\rm tSZ}$	0.24 ± 0.17	0.25 ± 0.16	0.33 ± 0.23	0.52 ± 0.22
$A_{\rm kSZ}$	1.3 ± 0.9	[1]	2.7 ± 1.4	[1]
$A_{\rm clust}$	1.05 ± 0.19	1.08 ± 0.14	–	–
$A_{\rm clust150}$	–	–	0.44 ± 0.27	0.66 ± 0.26
$A_{\rm clust220}$	–	–	8.2 ± 1.7	8.7 ± 1.5
$D^{\rm tSZ}_{\ell 3000}(\mu{\rm K}^2)$	2.2 ± 1.5	2.3 ± 1.4	2.9 ± 2.0	4.7 ± 2.0
$D^{\rm kSZ}_{\ell 3000}(\mu{\rm K}^2)$	2.7 ± 1.9	[2.05]	5.5 ± 3.0	[2.05]
$D^{\rm clust150}_{\ell 3000}(\mu{\rm K}^2)$	6.05 ± 1.06	6.26 ± 0.82	2.51 ± 1.60	3.81 ± 1.53
$D^{\rm clust220}_{\ell 3000}(\mu{\rm K}^2)$	39.11 ± 6.79	40.63 ± 5.08	47.33 ± 9.78	50.47 ± 9.17
$D^{\rm Poiss150}_{\ell 3000}(\mu{\rm K}^2)$	10.03 ± 0.67	10.1 ± 0.7	10.38 ± 0.63	10.33 ± 0.67
$D^{\rm Poiss220}_{\ell 3000}(\mu{\rm K}^2)$	79.5 ± 4.8	80 ± 5	77.89 ± 4.49	76.5 ± 4.0
$D^{\rm Poisscross}_{\ell 3000}(\mu{\rm K}^2)$	26.8 ± 1.4	26.8 ± 1.4	–	–

plane $D^{\rm kSZ}_{\ell=3000} - D^{\rm tSZ}_{l=3000}$ for the "run2" and "run3" case. Fixing the kSZ term slightly improves the detection for the thermal SZ with $D^{\rm tSZ}_{\ell=3000} = 2.3 \pm 1.4\,\mu K^2$ in "run1" but still with less significance than the one in [181] where a value of $D^{\rm tSZ}_{\ell=3000} = 3.5 \pm 1.0\,\mu K^2$ is reported.

Based on the degeneracy direction of Figure 8.1, we constrain the sum of the SZ effects at $\ell = 3000$ to be $D^{\ell=3000}_{\rm tSZ} + 0.5 D^{\ell=3000}_{\rm kSZ} = 3.5 \pm 1.8\ \mu{\rm K}^2$ to be compared $4.5 \pm 1.0\ \mu{\rm K}^2$ of [181] . These amplitudes are consistent but, again, the significance of the detection is worse than [181] who found this sum to be $4.5 \pm 1.0\ \mu{\rm K}^2$.

Table 8.2. Mean values and 68% error bars from ACT data combined with SPT data at 150 GHz

	WMAP7+ SPT+ACT (kSZ free)	WMAP7+ SPT+ACT
$10^2\Omega_b h^2$	2.232 ± 0.047	2.234 ± 0.046
$\Omega_c h^2$	0.1121 ± 0.0050	0.1124 ± 0.0053
τ	0.086 ± 0.014	0.086 ± 0.015
n_s	0.964 ± 0.012	0.964 ± 0.012
$\log(10^{10} A_s)$	3.20 ± 0.043	3.19 ± 0.04
Ω_m	0.274 ± 0.027	0.275 ± 0.028
σ_8	0.812 ± 0.0255	0.813 ± 0.027
$A_{\rm tSZ}$	0.34 ± 0.25	0.38 ± 0.24
$A_{\rm kSZ}$	1.6 ± 1.1	[1]
$A_{\rm clustact}$	0.66 ± 0.56	0.75 ± 0.59
$A_{\rm clustspt}$	0.66 ± 0.43	0.77 ± 0.41
$D^{\rm tSZ}_{\ell 3000}(\mu{\rm K}^2)$	3.1 ± 2.3	3.5 ± 2.2
$D^{\rm kSZ}_{\ell 3000}(\mu{\rm K}^2)$	3.2 ± 2.3	[2]
$D^{\rm clustact}_{\ell 3000}(\mu{\rm K}^2)$	3.9 ± 3.2	4.2 ± 3.2
$D^{\rm Poissact}_{\ell 3000}(\mu{\rm K}^2)$	13.4 ± 2.4	13.5 ± 2.5
$D^{\rm clustspt}_{\ell 3000}\ (\mu{\rm K}^2)$	3.8 ± 2.5	4.5 ± 2.4
$D^{\rm Poissspt}_{\ell 3000}(\mu{\rm K}^2)$	10.2 ± 0.8	10.2 ± 0.8

The small discrepancy with the results presented in [181] comes essentially from the different parametrization used. Adopting a more similar parametrization as in the case of "run2" we found $D^{\rm tSZ}_{\ell=3000} = 2.9 \pm 2.0\,\mu K^2$, $D^{\rm kSZ}_{\ell=3000} = 5.5 \pm 3.0\,\mu K^2$ at 68% c.l., $D^{\ell=3000}_{\rm tSZ} + 0.5 D^{\ell=3000}_{\rm kSZ} = 5.6 \pm 2.6\ \mu{\rm K}^2$, yielding a detection for the thermal SZ with higher significance. In case of fixed kSZ we obtain $D^{\rm tSZ}_{\ell=3000} = 4.7 \pm 2.0\,\mu K^2$, again a more significant detection in better agreement with [181].

The different assumptions in the frequency scaling of the clustered point sources component in "run1" and "run2" is the main explanation for the difference in the

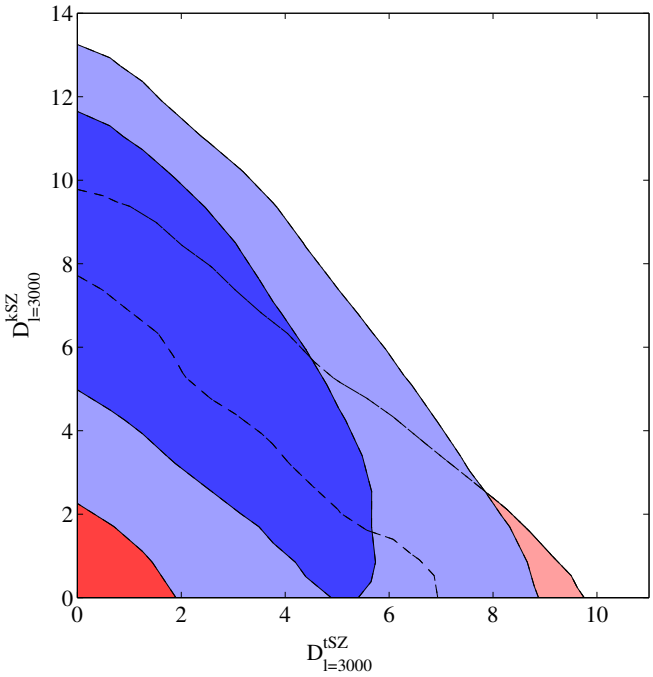

Figure 8.1. Joint two-dimensional posterior probability contours showing 68% and 95% C.L. constraints on $D^{\rm ksz}_{\ell=3000}$ and $D^{\rm tSZ}_{\ell=3000}$ from ACT 150 GHz data (red) and SPT all frequencies data (blue) for the run2 case.

results. In "run1", taking into account Gispert scaling ([187]), we find $D^{\rm clust220}_{\ell=3000} = 39.11 \pm 6.79\,\mu K^2$, while in "run2", when the amplitude of the clustering point sources is allowed to vary, we have $D^{\rm clust220}_{\ell=3000} = 47.33 \pm 9.78\,\mu K^2$, that is more consistent with the corresponding value of $D^{\rm clust220}_{\ell=3000} = 57 \pm 9$ reported in [181]. A small tension therefore exists between the Gispert scaling and the data at 220 GHz, resulting also in a worse determination of the thermal SZ signal. The use of a different parametrization of the point source (just amplitudes in our case while [181] varies one amplitude and one spectral index per component) can explain the remaining differences.

Also with regard to the Poisson point sources component at 150 GHz, our results show a discrepancy compared to those from [181], both in "run1" and "run2". At 150 GHz we find $D^{\rm Poiss150}_{\ell=3000} = 10.03 \pm 0.67\,\mu K^2$ in "run1" and $D^{\rm Poiss150}_{\ell=3000} = 10.38 \pm 0.63\,\mu K^2$ in "run2", while the value in [181] is $D^{\rm Poiss150}_{\ell=3000} = 7.4 \pm 0.6\,\mu K^2$. At 220 GHz we find a better agreement with $D^{\rm Poiss220}_{l=3000} = 79.5 \pm 4.8\,\mu K^2$ in "run1" and $D^{\rm Poiss220}_{\ell=3000} = 77.89 \pm 4.49\,\mu K^2$ in "run2", while the value in [181] is $D^{\rm Poiss220}_{\ell=3000} = 71 \pm 5\,\mu K^2$. The difference is explained in straightforward terms if we take in account that in [181] radio galaxies are included in their "baseline model" with an amplitude $D^{\rm r}_{\ell=3000} = 1.28\,\mu K^2$ with a 15% uncertainty. Clustering of radio galaxies is negligible, so this radio galaxies term is a Poisson like term of the form $\propto \ell^2$. Adding this

component, our Poisson amplitudes are consistent with those reported by [181] within 1σ. In "run1" at 150 GHz we find $D_{\ell=3000}^{\mathrm{Poiss150}} = 10.03 \pm 0.67\,\mu K^2$, while in [181] the correspondent total Poisson contribution at $\ell = 3000$ is about $(8.68 \pm 0.69)\,\mu K^2$.

We can therefore conclude that the current results presented in the literature on the amplitude of the secondary anisotropies should be considered with great care since there is a clear dependence on the parametrization used, on the frequency scaling adopted and on the assumed templates. We stress that, a part for small discrepancies imputable to differences in the parameterization, all our results for the SZ amplitudes from the analysis of SPT data both for our "run1" and "run2" cases, are substantially consistent with the analysis of the same data made by [181], even if we are finding less tight constraints. Our results hence compare in the same way to the recent predictions of tSZ power made by the models of [170], [70] and [189] confirming that these models overestimate the power of the tSZ signal, as already found in [181].

In Figure 8.2 we show the recent CIB power spectra data of the Planck collaboration ([183]) at 217 GHz and small angular scale CMB power spectrum data from SPT, at 220 GHz, with a comparison to scaled measurements from [182]. The Herschel model is shown in terms of the 1-halo and 2-halo contributions to the total power spectrum. For reference, we also show the model used by [190] at 220 GHz to describe the clustering of DSFGs, which overestimated the power at tens of arcminute angular scales and above relative to Herschel and Planck DSFG clustering measurements. [190] used a linear model to analyze their data. At small angular scales non-linear effects are not negligible and using a linear model to interpret the data may lead to a wrong determination of the bias and hence to an overestimation of the power at larger angular scales (see also discussion in [183]). Instead our model shows a good fit of both Planck and SPT CIB.

In Figure 8.3 we show the best fit models for each component compared with the SPT and WMAP7 data. In the "run1", when only one amplitude of clustered DSFGs is allowed to vary when fitting the all frequencies SPT data combined with WMAP7 data, we find that $A_{\mathrm{clust}} = 1.05 \pm 0.19$. This suggests that the combination of [182] model and the frequency scaling for the mean CIB is a good fit of the DSFG clustering at lower CMB frequencies. Higher precision CMB power spectra at 150, 220 and 350 GHz and a direct cross-correlation of Herschel-SPIRE maps against the CMB will be necessary to study if fluctuations scale with frequency as the mean CIB intensity and to improve overall constraints on secondary anisotropies.

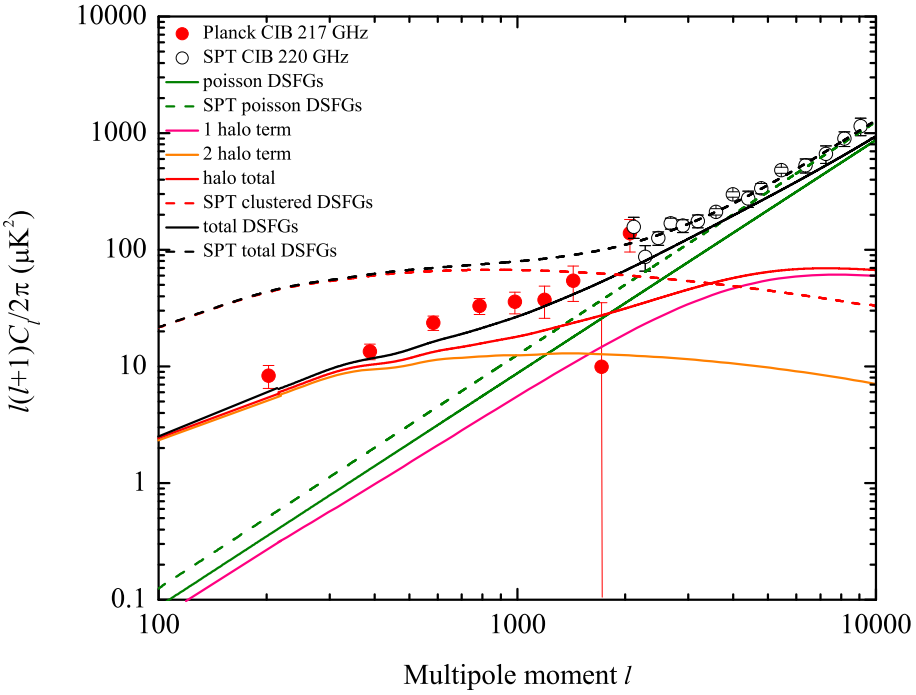

Figure 8.2. Planck DSFG clustering data (red points) at 217 GHz and SPT data at 220 GHz (white points) compared with the combination (solid black line) of the Poisson term (green line) and clustering term (red) of unresolved point sources by scaling the best-fit model to measurements made with Herschel at 350 μm to 217 GHz using the frequency scaling of [187]. We show the 1-halo (pink) and 2-halo (orange) contributions to the clustering term following [182]. The dashed lines are the 220 GHz SPT DSFG power spectrum components from [190], which resulted in an overestimate of Planck DSFG clustering at $\ell < 3000$.

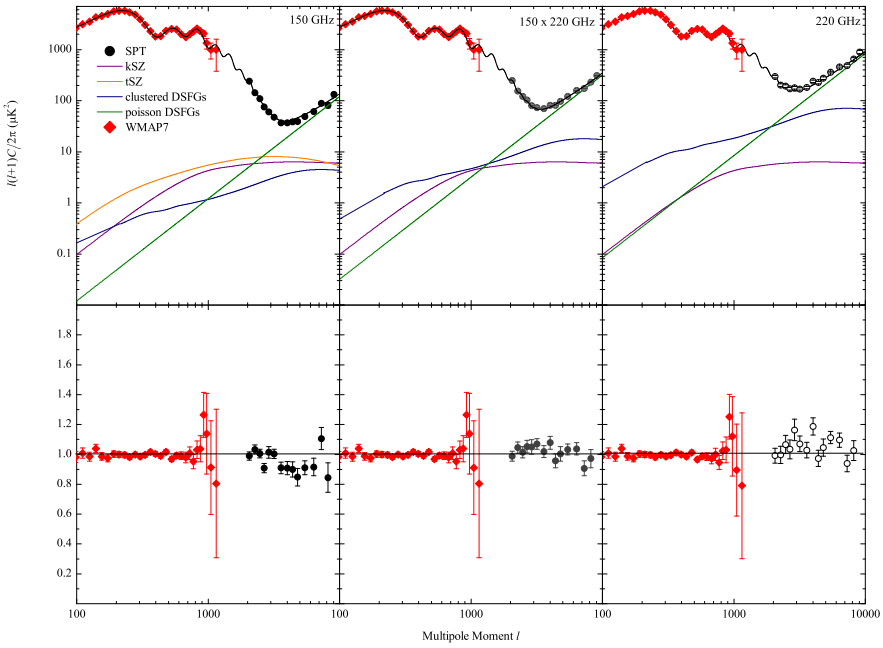

Figure 8.3. Contribution to the angular anisotropy power spectrum from point sources and from SZ effect for the best fit model of the WMAP7+SPT analysis. Left panel is 150 GHz, middle 220 GHz and right panel shows the cross spectra. kSZ term is the orange solid line and the tSZ term at 150 GHz is the purple line. Green lines are the Poisson terms and blue lines are the clustering contributions. The black lines are the total best fit power spectra. Black dots are SPT data and red squares are WMAP7 data. The bottom panels show the residual relative to the total model, including primordial CMB and best-fit secondary anisotropy amplitudes.

Conclusions

At the state of art cosmology can constraint only two quantities related to neutrino physics: the effective number of relativistic degrees of freedom $N_{\rm eff}$ and the total hot dark matter density $\Omega_\nu h^2$. The goal of this thesis is to put new constraints on these parameters from recent cosmological data in the framework of a non minimal cosmological model and also in light of Short–Base–Line results. Here we summarize the main results obtained in the work performed during my Ph.D and presented in this thesis.

As far as concern the effective number of relativistic degrees of freedom $N_{\rm eff}$, we performed a new search for an extra–dark radiation. We have shown that the cosmological data we considered are clearly suggesting the presence of an extra dark radiation component with $N_{\rm eff} = 4.08^{+0.71}_{-0.68}$ at 95% c.l. . Performing an analysis on its effective sound speed $c^2_{\rm eff}$ and viscosity $c^2_{\rm vis}$ parameters, we found $c^2_{\rm eff} = 0.312 \pm 0.026$ and $c^2_{\rm vis} = 0.29^{+0.21}_{-0.16}$ at 95% c.l., consistent with the expectations of a relativistic free streaming component ($c^2_{\rm eff}$=$c^2_{\rm vis}$=1/3). Assuming the presence of 3 standard relativistic neutrinos we constrain the extra dark radiation component with $N^S_\nu = 1.10^{+0.79}_{-0.72}$ and $c^2_{\rm eff} = 0.24^{+0.08}_{-0.13}$ at 95% c.l. while $c^2_{\rm vis}$ is practically unconstrained. Assuming a mass in the 3 neutrino component we obtain further indications for the dark radiation component with $N^S_\nu = 1.12^{+0.86}_{-0.74}$ at 95% c.l. . From these results we conclude that dark radiation currently represents one of the most relevant anomaly for the Λ-CDM scenario.

We have also shown that there is a correlation between $N_{\rm eff}$ and Ω_k that gets stronger when high multipole dataset are added. If CMB data were to favor open models then the neutrino number would decrease. However, even when Ω_k is allowed to vary, $N_{\rm eff} = 3.046$ is still disfavored by the data with 95% confidence.

This dark radiation will be severely constrained in the very near future by the Planck satellite data, where a precision on $N_{\rm eff}$ of about $\Delta N_{\rm eff} \sim 0.2$ is expected (see e.g. [191] and [192]) only from CMB data. For this reason we have generated mock CMB data for the ongoing Planck experiment and the future COrE mission with non standard values for the dark radiation perturbation parameters. Then, we have fitted these data to a canonical dark radiation scenario with $c^2_{\rm vis} = c^2_{\rm eff} = 1/3$ but with a running spectral index or with a dark energy component with $w \neq -1$, finding that non standard values for the dark radiation perturbation parameters may be misinterpreted as a scale invariant power spectrum of primordial fluctuations or as cosmologies with a running spectral index or a time varying dark energy component with high significance.

We have also emphasized the important role played by the HST H_0 prior in establishing the statistical evidence for the existence of this dark radiation. We

have shown that with a new median statistics H_0 prior derived from 537 non-CMB H_0 measurements, there is no significant evidence for $N_{\rm eff} > 3.046$, consistent with the indications from other cosmological data. And it is probably not unreasonable to believe that the converse might also be true: with other cosmological data not inconsistent with $N_{\rm eff} = 3.046$, consistency of the smaller-scale CMB anisotropy data with the predictions of the ΛCDM model apparently demands $H_0 \sim 68$km/s/Mpc.

We have tried to check if these cosmological hints for extra–dark radiation have a counterpart in neutrino physics. Actually this dark radiation can be composed of one or two sterile neutrinos, which may correspond to those in 3+1 or 3+2 models which have been invoked for the explanation of Short–Baseline (SBL) neutrino oscillation anomalies. We have performed analyses of the cosmological and SBL data in the frameworks of both the 3+1 and 3+2 models. Then we have compared the results obtained with the same Bayesian method, to figure out if the indications of cosmological and SBL data are compatible. The results of our analysis show that the cosmological and SBL data give compatible results when the cosmological analysis takes into account only CMB data. But if the information on the matter power spectrum coming from galaxies surveys are also considered there is a tension between the sterile neutrino masses needed to have SBL neutrino oscillations and the cosmological upper limit on the sum of the masses. The combined analysis of cosmological and SBL data gives an allowed region for m_4 in the 3+1 scheme around 1 eV. In the 3+2 scheme, the cosmological data reduce the allowance of the second massive sterile neutrino given by SBL data, leading to a combined fit which prefers the case of only one massive sterile neutrino at the scale of about 1 eV. In conclusion, our analysis shows that cosmological data are marginally compatible with the existence of one massive sterile neutrino with a mass of about 1 eV, which can explain the anomalies observed in SBL neutrino oscillation experiments. The case of massive sterile neutrinos is less tolerated by cosmological data and in any case the second sterile neutrino must have a mass smaller than about 0.6 eV.

Concerning the total hot dark matter density we have seen that priors are very important in Bayesian cosmological analyses and can highly influence cosmological results. For instance, the details of the reionization process in the late universe are not very well known. In the absence of a precise, full redshift evolution of the ionization fraction during the reionization period, a simple parametrization, with a single parameter z_r, has become the standard reionization scheme in numerical analyses. However, more general reionization scenarios are certainly plausible and their impact on the cosmological constraints should be carefully explored. We have investigated the stability of the CMB constraints on neutrino masses in generalized reionization scenarios using a model independent analysis performed through the Principal Components. We have found that a more general treatment of reionization could potentially weaken the current CMB upper limit on $\sum m_\nu$ by $\sim 40\%$.

Furthermore, the constraints on the sum of neutrino masses are weakened by degeneracy with the curvature parameter Ω_k. In this case we have shown that the mass uncertainty more than doubles when Ω_k is allowed to vary.

Future data expected from the Planck [80] satellite on large angular scale CMB polarization and on small scale anisotropies will help in clarifying the thermal history of the Universe and in ruling out exotic reionization scenarios or non-flat Universe that are still in agreement with present-day observations.

Finally looking at the strong degeneracy between σ_8 and $\sum m_\nu$ we have seen how the measured tSZ power can be used to better constraint σ_8 and therefore the sum of neutrino masses. With a conservative 50% model uncertainty, the tSZ power spectrum reduces the σ_8 uncertainty by 30% and tightens the upper limit on the total neutrino masses from 0.52eV to 0.40eV.

Finally, given the great accuracy of future data it will be necessary to have an accurate description of SZ effects and foregrounds in order to separate the different contributions to anisotropies and so obtain an unbiased determination of cosmological parameters related to neutrino physics. For this reason we have provided a new analysis of the foreground contribution to the CMB data making use of the ACT and SPT high multipole data. The foreground contribution from Poisson point sources at 220 and 150 GHz is detected with very high significance (at more than ~ 15 standard deviations) with no particular dependence on the parametrization used. The contribution from clustered point sources is also well detected at 220 GHz. We have found that current CMB data favors a larger contribution at this frequency than the one expected by the Gispert frequency scaling once the data is normalized at 150 GHz. The thermal SZ component is detected at a level slightly above the two standard deviations. However a different parametrization of the components and the assumption of the Gispert scaling could bring this detection to about one standard deviation. The correlation with the kinetic SZ term is present in the data despite the multi-frequency approach. More data at more frequencies are clearly needed to establish a strong detection of the SZ term. We have firmly established the power spectrum of DSFGs that dominate the arcminute scale CMB anisotropies at 220 GHz and higher frequencies. This comes from the recent Herschel results combined with Planck-confirmed frequency spectrum for the CIB mean intensity. In future, additional improvements will come from directly cross-correlating the CMB maps against high-resolution CIB maps from Herschel; for this a Herschel-SPIRE survey at the same large areas as CMB surveys will become useful ([193]).

Conclusioni

Attualmente la cosmologia puo' vincolare solo due quantita' relative alla fisica del neutrino: il numero effettivo di gradi di libera' relativistici $N_{\rm eff}$ e la densita' totale di materia oscura $\Omega_\nu h^2$. L'obiettivo di questa tesi e' di porre nuovi vincoli su tali parametri usufruendo dei recenti dati cosmologici nell'ottica di un modello cosmologico non minimale ed anche alla luce dei risultati da esperimenti Short–Base–Line su oscillazioni di neutrino.

Per quanto concerne il numero effettivo di gradi di liberta' relativistici $N_{\rm eff}$, abbiamo condotto un'innovativa ricerca di un eccesso di radiazione oscura. Abbiamo mostrato come i dati cosmologici considerati indichino con chiarezza la presenza di una componentre extra di radiazione oscura con $N_{\rm eff} = 4.08^{+0.71}_{-0.68}$ al 95% c.l. . Da un'analisi sui parametri relativi alla velocita' effettiva del suono $c^2_{\rm eff}$ e alla viscosita' $c^2_{\rm vis}$ sono stati ricavati i valori $c^2_{\rm eff} = 0.312 \pm 0.026$ e $c^2_{\rm vis} = 0.29^{+0.21}_{-0.16}$ al 95% c.l., consistenti con i valori attesi per una componente relativistica caratterizzata da free-streaming ($c^2_{\rm eff}$=$c^2_{\rm vis}$=1/3). Inoltre assumendo tre neutrini standard, abbiamo posto dei vincoli sulla sola componente in eccesso di radiazione oscura $N^S_\nu = 1.10^{+0.79}_{-0.72}$ con $c^2_{\rm eff} = 0.24^{+0.08}_{-0.13}$ al 95% c.l. mentre $c^2_{\rm vis}$ e' praticamente non vincolato. Infine abbiamo conferito una massa ai tre neutrini standard e abbiamo cosi' ottenuto un'ulteriore indicazione riguardo alla componente relativistica in eccesso $N^S_\nu = 1.12^{+0.86}_{-0.74}$ al 95% c.l. . Da questi risultati abbiamo potuto concludere che la radiazione oscura rappresenta attualmente una delle piu' rilevanti anomalie del modello ΛCDM.

Abbiamo anche mostrato la correlazione esistente tra $N_{\rm eff}$ e Ω_k, correlazione che diventa piu' evidente qualora si tenga conto dei dati ad alti multipoli. Se i dati di CMB favorissero modelli di Universo aperti il numero di neutrini diminuirebbe. Tuttavia, anche lasciando il parametro di curvatura variabile, il valore standard $N_{\rm eff} = 3.046$ risulta comunque sfavorito dai dati al 95%.

Tale radiazione oscura verra' ulteriormente caratterizzata nel prossimo futuro dal satellite Planck che fornira' una precisione su $N_{\rm eff}$ di $\Delta N_{\rm eff} \sim 0.2$ (vedi [191] e [192]) da soli dati di CMB. Per questo motivo abbiamo generato dei dati di CMB fittizi basandoci sulle caratteristiche sperimentali del satellite Planck e sulla futura missione COrE, usando valori non standard dei parametri delle perturbazioni della radiazione oscura. Abbiamo fittato questi dati nel caso di uno scenario in cui la radiazione oscura e' caratterizzata da $c^2_{\rm vis} = c^2_{\rm eff} = 1/3$ (standard), ma in cui e' presente anche un indice spettrale variabile o una componente di energia oscura con $w \neq -1$. Abbiamo riscontrato che valori non standard dei parametri delle perturbazioni di radiazione oscura possono essere erroneamente interpretati come uno spettro di potenza primordiale delle perturbazioni invariante di scala o come dei modelli cosmologici con un indice spettrale variabile o con una componente di

energia oscura variabile nel tempo.

Abbiamo inoltre enfatizzato il ruolo fondamentale che gioca la prior su H_0 da HST nello stabilire l'evidenza statistica della presenza di radiazione oscura. Abbiamo anche mostrato che, utilizzando una nuova prior su H_0 derivante dalla media statistica su 537 misure di H_0 indipendenti da dati di CMB non vi e' alcuna evidenza significativa di $N_{\rm eff} > 3.046$, il che' e' consistente con altri dati cosmologici. Allo stesso modo questo risultato avvalora anche l'ipotesi inversa: con altri dati cosmologici non consistenti con $N_{\rm eff} = 3.046$, l'accordo fra i dati di CMB a piccole scale e le predizioni del modello ΛCDM richiede $H_0 \sim 68$km/s/Mpc.

Abbiamo tentato di verificare se queste indicazioni cosmologiche di una componentre in eccesso di radiazione oscura avessero una controparte nella fisica del neutrino. Effettivamente questa radiazione oscura puo' essere composta da uno o due neutrini sterili, che possono corrispondere a quelli invocati nei modelli 3+1 e 3+2 per spiegare le anomalie degli esperimenti Short–Base–Line (SBL). Abbiamo quindi analizzato dati sia cosmologici sia SBL nel contesto dei modelli 3+1 e 3+2. Abbiamo comparato i risultati ottenuti con il medesimo metodo Bayesiano, per dedurre se le indicazioni cosmologiche e i dati SBL sono compatibili. I risultati della nostra analisi mostrano che i dati cosmologici e i dati SBL danno risultati compatibili qualora l'analisi cosmologica prenda in considerazione solo dati di CMB. Se si aggiungono anche le informazioni sullo spettro di potenza di materia provenienti da survey di galassie vi e' disaccordo tra i valori delle masse dei neutrini sterili necessari per spiegare le oscillazioni degli esperimenti SBL e il limite superiore sulla somma delle masse ricavato dalla cosmologia. L'analisi combinata di dati cosmologici e dati SBL fornisce una regione permessa per m_4 nello schema 3+1 intorno a 1 eV. Nello schema 3+2, i dati cosmologici riducono la regione permessa da dati SBL per la massa del secondo neutrino sterile, determinando una preferenza del fit combinato per il caso di un solo neutrino massivo con massa intorno a 1 eV. In conclusione questa nostra analisi mostra che i dati cosmologici sono solo parzialmente compatibili con l'esistenza di un neutrino sterile massivo con una massa intorno a 1 eV, neutrino che potrebbe spiegare le anomalie osservate nelle oscillazioni dagli esperimenti SBL. Il caso di neutrini sterili massivi e' meno compatibile con i dati cosmologici e in ogni caso il secondo neutrino sterile dovrebbe avere una massa inferiore a circa 0.6 eV.

Per quanto concerne la densita' totale di materia oscura calda abbiamo visto che le assunzioni a priori giocano un ruolo fondamentale nelle analisi Bayesiane quali sono quelle cosmologiche e possono pesantemente influenzarne i risultati. Per esempio, i dettagli del processo di reionizzazione nelle ultime fasi di evoluzione dell'Universo risultano ancora essere in gran parte ignoti. In assenza di una precisa conoscenza dell'evoluzione della frazione di idrogeno ionizzato durante il periodo di reionizzazione, l'uso di un singolo parametro, il redshift di reionizzazione z_r, e' diventato lo schema piu' usato nelle analisi numeriche. Tuttavia scenari piu' generali di reionizzazione sono altrettanto plausibili e il loro impatto sui vincoli cosmologici dovrebbe essere accuratamente studiato. A tal proposito abbiamo analizzato la stabilita' dei vincoli da CMB sulla massa dei neutrini in uno scenario cosmologico generalizzato usando un metodo indipendente dal modello e basato sulle Principal Components. Abbiamo riscontrato che una trattazione piu' generale della reionizzazione puo' rilassare gli attuali limiti superiori da CMB su $\sum m_\nu$ di $\sim 40\%$.

Inoltre, i vincoli sulla somma delle masse dei neutrini possono essre indeboliti

anche dalla degenerazione con il parametro di curvatura Ω_k. In questo caso e' stato mostrato che l'incertezza sulla massa raddoppia quando il parametro Ω_k e' variabile.

I dati futuri aspettati dal satellite Planck [80] sulla polarizzazione della CMB a grandi scale angolari e sulle anisotropie a piccole scale aiuteranno a chiarire la storia termica dell'Universo e ad escludere possibili scenari non standard di reionizzazione o Universi non piatti che sono ancora in accordo con le attuali osservazioni.

Infine concentrandoci sulla forte degenerazione fra σ_8 e $\sum m_\nu$, abbiamo visto che la misura del tSZ puo' essere usata per meglio vincolare σ_8 e quindi la somma delle masse dei neutrini. Con un 50% di incertezza sul modello, lo spettro di potenza del tSZ riduce l'incertezza su σ_8 del 30% e porta il limite superiore sulla massa dei neutrini da 0.52eV a 0.40eV.

In ultima analisi, data l'accuratezza dei futuri dati sara' necessario avere una precisa descrizione degli effetti SZ e dei foreground al fine di separare i diversi contributi alle anisotropie e di ottenere quindi una determinazione dei parametri cosmologici relativi alla fisica del neutrino scevra da contributi spuri. Per questo motivo abbiamo analizzato il contributo dei foreground ai dati di CMB usando i dati ad alti multipoli di ACT e SPT. Il contributo dei foreground dovuto a sorgenti puntiformi con distribuzione Poissoniana a 220 e 150 GHz e' rilevato in maniera significativa (a piu' di $\sim$ 15 deviazioni standard) e non e' stata rilevata alcuna dipendenza dalla parametrizzazione usata. Il contributo dalle sorgenti puntiformi in fase di clustering e' anch'esso ben distinguibile a 220 GHz. Gli attuali dati di CMB sembrano suggerire un contributo a questa frequenza maggiore di quello trovato con lo scaling delle frequenze fornito da Gispert una volta che i dati sono stati normalizzati a 150 GHz. La componente di SZ termico e' rilevata ad un livello di confidenza leggermente al di sotto delle due deviazioni standard. Tuttavia una diversa parametrizzazione delle componenti e l'assunzione dello scaling di Gispert possono portare tale evidenza a circa una deviazione standard. La correlazione con il termine cinetico dell'SZ rimane presente nei dati nonostante l'approccio di analisi su piu' frequenze. Maggiori dati a diverse frequenze sono necessari per stabilire una chiara evidenza del termine di SZ. Tuttavia questa analisi ha stabilito lo spettro di potenza delle galassie con polvere in fase di formazione stellare a 220 GHz e a piu' alte frequenze. Questo e' stato reso possibile dai recenti risultati di Herschel combinati con lo spettro dell'intensita' media del fondo cosmico infrarosso confermato da Planck. Nel futuro ulteriori miglioramenti verranno dalla cross-correlazione delle mappe di CMB con le mappe del fondo cosmico infrarosso di Herschel; per questo e' auspicabile una survey Herschel-SPIRE sulle stesse aree delle mappe di CMB ([193]).

Bibliography

[1] B. Ryeden, *Intorduction to cosmology.* Addison Wesley, 2004.

[2] S. Dodelson, *Modern cosmology.* Academic Press.

[3] A. G. Riess, L. Macri, S. Casertano, H. Lampeitl, H. C. Ferguson, A. V. Filippenko, S. W. Jha, and W. e. Li, "A 3% solution: Determination of the hubble constant with the hubble space telescope and wide field camera 3," *Astrophys. J.*, vol. 732, 2011.

[4] D. D. Reid, D. W. Kittel, E. E. Arsznov, and T. G. B., "The picture of our universe: A view from modern cosmology," *arXiv.org:astro-ph/0209504*, 2002.

[5] J. Lesgourgues, "An overview of cosmology," *arXiv:astro-ph/0409426.*

[6] C. P. Ma and E. Bertschinger, "Cosmological perturbation theory in the synchronous versus conformal newtonian gauge," *Astrophys. J.*, vol. [astro-ph/9401007].

[7] M. J. Rees and D. W. Sciama, "Large scale density inhomogeneities in the universe," *Nature*, vol. 217, 1968.

[8] R. Sunyaev and Y. Zeldovich *Comm. Astrophys. Sp. Phys.*, vol. 4, 1972.

[9] M. Birkinshaw, "The sunyaev-zel'dovich effect," *Phys. Rept.*, vol. 310, 1999.

[10] E. e. Komatsu *arXiv:1001.4538 [astro-ph.CO].*

[11] U. Seljak and M. Zaldarriaga, "Polarization of microwave background: Statistical and physical properties," *astro-ph/9805010.*

[12] M. Tegmark, "Cosmological neutrino bounds for non-cosmologists," *Phys. Scripta T*, vol. 121, 2005.

[13] T. ALEPH, DELPHI, L3, OPAL, and S. Collaborations, vol. 427. 2005.

[14] D. V. Forero, M. Tortola, and J. W. F. Valle, "Global status of neutrino oscillation parameters after neutrino-2012," *arXiv:1205.4018 [hep-ph].*

[15] G. Karagiorgi, Z. Djurcic, J. M. Conrad, M. H. Shaevitz, and M. Sorel, "Viability of $\delta m^2 \sim 1$ ev^2 sterile neutrino mixing models in light of miniboone electron neutrino and antineutrino data from the booster and numi beamlines," *Phys. Rev. D*, vol. 81, 2010.

[16] C. P. Ma and E. Bertschinger, "Cosmological perturbation theory in the synchronous and conformal newtonian gauges," *Astrophys. J.*, vol. 455, 1995.

[17] J. Lesgourgues and S. Pastor, "Massive neutrinos and cosmology," *Phys. Rept.*, vol. 429, 2006.

[18] J. Hamann, S. Hannestad, G. G. Raffelt, and Y. Y. Y. Wong, "Sterile neutrinos with ev masses in cosmology: How disfavoured exactly?," *JCAP*, vol. 1109, 2011.

[19] R. Bowen, S. H. Hansen, A. Melchiorri, J. Silk, and R. Trotta, "The impact of an extra background of relativistic particles on the cosmological parameters derived from microwave background anisotropies," *Mon. Not. Roy. Astron. Soc.*, vol. 334, 2002.

[20] S. Dodelson, *Modern cosmology.* Amsterdam, Netherlands: Academic Pr., 2003.

[21] Z. Hou, R. Keisler, L. Knox, M. Millea, and C. Reichardt, "How additional massless neutrinos affect the cosmic microwave background damping tail," *arXiv:1104.2333 [astro-ph.CO].*

[22] A. Heavens, "Statistical techniques in cosmology," *arXiv:0906.0664 [astro-ph.CO].*

[23] L. Verde, "A practical guide to basic statistical techniques for data analysis in cosmology," *arXiv:0712.3028 [astro-ph].*

[24] A. Gelman and D. B. Rubin, "Inference from iterative simulation using multiple sequences," *Statist. Sci.*, vol. 7, 1992.

[25] A. Lewis and S. Bridle *Phys. Rev. D*, vol. 66, 2002.

[26] A. Lewis, A. Challinor, and A. Lasenby *Astrophys. J.*, vol. 538, 2000.

[27] R. Trotta, "Bayes in the sky: Bayesian inference and model selection in cosmology," *Contemp. Phys.*, vol. 49, 2008.

[28] D. e. Larson *arXiv:1001.4635 [astro-ph.CO].*

[29] E. W. Kolb and M. S. Turner, "The early universe," *Front. Phys.*, vol. 69, 1990.

[30] G. Mangano, G. Miele, S. Pastor, T. Pinto, O. Pisanti, and P. D. Serpico, "Relic neutrino decoupling including flavor oscillations," *Nucl. Phys.*, vol. B729 , 2005.

[31] U. Seljak, A. Slosar, and P. McDonald, "Cosmological parameters from combining the lyman-alpha forest with cmb, galaxy clustering and sn constraints," *JCAP*, vol. 0610 , 2006.

[32] M. Cirelli and A. Strumia, "Cosmology of neutrinos and extra light particles after wmap3," *JCAP*, vol. 0612, 2006.

[33] G. Mangano, A. Melchiorri, O. Mena, G. Miele, and A. Slosar, "Present bounds on the relativistic energy density in the universe from cosmological observables," *JCAP*, vol. 0703 , 2007.

[34] K. Ichikawa, M. Kawasaki, and F. Takahashi, "Constraint on the effective number of neutrino species from the wmap and sdss lrg power spectra," *JCAP*, vol. 0705, 2007.

[35] J. Hamann, S. Hannestad, G. G. Raffelt, I. Tamborra, and Y. Y. Y. Wong, "Cosmology seeking friendship with sterile neutrinos," *Phys. Rev. Lett.*, vol. 105 , 2010.

[36] E. Giusarma, M. Corsi, M. Archidiacono, R. de Putter, A. Melchiorri, O. Mena, and S. Pandolfi, "Constraints on massive sterile neutrino species from current and future cosmological data," *Phys. Rev.*, vol. D83 , 2011.

[37] L. M. Krauss, C. Lunardini, and C. Smith, "Neutrinos, wmap, and bbn," *[arXiv:1009.4666 [hep-ph]]*.

[38] B. A. Reid, L. Verde, R. Jimenez, and O. Mena, "Robust neutrino constraints by combining low redshift observations with the cmb," *JCAP*, vol. 1001, 2010.

[39] J. e. Dunkley, "The atacama cosmology telescope: Cosmological parameters from the 2008 power spectra," *arXiv:1009.0866 [astro-ph.CO]*.

[40] R. e. Keisler, "A measurement of the damping tail of the cosmic microwave background power spectrum with the south pole telescope," *arXiv:1105.3182 [astro-ph.CO]*.

[41] T. L. Smith, S. Das, and O. Zahn, "Constraints on neutrino interactions using cosmological observations," *arXiv:1105.3246 [astro-ph.CO]*.

[42] G. Mangano, G. Miele, S. Pastor, T. Pinto, O. Pisanti, and P. D. Serpico, "Effects of non-standard neutrino-electron interactions on relic neutrino decoupling," *Nucl. Phys.*, vol. B756 , 2006.

[43] A. e. L. C. Aguilar, "Evidence for neutrino oscillations from the observation of anti-neutrino(electron) appearance in a anti-neutrino(muon) beam," *Phys. Rev. D*, vol. 64, 2001.

[44] A. A. e. T. M. C. Aguilar-Arevalo, "A search for electron neutrino appearance at the $\delta m^2 \sim 1\text{ev}^2$ scale," *Phys. Rev. Lett.*, vol. 98, 2007.

[45] A. A. e. M. C. Aguilar-Arevalo, "A search for electron antineutrino appearance at the delta m**2 1-ev**2 scale," *Phys. Rev. Lett.*, vol. 103, 2009.

[46] S. Hannestad, A. Mirizzi, G. G. Raffelt, and Y. Y. Y. Wong, "Neutrino and axion hot dark matter bounds after wmap-7," *JCAP*, vol. 1008, 2010.

[47] A. Melchiorri, O. Mena, and A. Slosar, "An improved cosmological bound on the thermal axion mass," *Phys. Rev. D*, vol. 76, 2007.

[48] K. Nakayama, F. Takahashi, and T. T. Yanagida, "A theory of extra radiation in the universe," *Phys. Lett. B*, vol. 697, 2011.

[49] T. L. Smith, E. Pierpaoli, and M. Kamionkowski, "A new cosmic microwave background constraint to primordial gravitational waves," *Phys. Rev. Lett.*, vol. 97, 2006.

[50] W. Fischler and J. Meyers, "Dark radiation emerging after big bang nucleosynthesis?," *Phys. Rev.*, vol. D83 , 2011.

[51] K. Ichikawa, M. Kawasaki, K. Nakayama, M. Senami, and F. Takahashi, "Increasing effective number of neutrinos by decaying particles," *JCAP*, vol. 0705 , 2007.

[52] K. Nakayama, F. Takahashi, and T. T. Yanagida, "A theory of extra radiation in the universe," *Phys. Lett.*, vol. B697, 2011.

[53] P. Binetruy, C. Deffayet, E. U., and D. Langlois, "Brane cosmological evolution in a bulk with cosmological constant," *Phys. Lett. B*, vol. 477, 2000.

[54] T. Shiromizu, K. i. Maeda, and M. Sasaki, "The einstein equation on the 3-brane world," *Phys. Rev. D*, vol. 62, 2000.

[55] V. V. Flambaum and E. V. Shuryak, "Possible evidence for 'dark radiation' from big bang nucleosynthesis data," *EuroPhys. Lett.*, vol. 74, 2006.

[56] A. Hebecker and J. March-Russell, "Randall-sundrum ii cosmology, ads / cft, and the bulk black hole," *Nucl. Phys. B*, vol. 608, 2001.

[57] E. Calabrese, D. Huterer, E. V. Linder, A. Melchiorri, and L. Pagano, "Limits on dark radiation, early dark energy, and relativistic degrees of freedom," *Phys. Rev. D*, vol. 83, 2011.

[58] J. S. Gagnon and J. Lesgourgues, "Dark goo: Bulk viscosity as an alternative to dark energy," *JCAP*, vol. 1109, 2011.

[59] W. Hu, "Structure formation with generalized dark matter," *Astrophys. J.*, vol. 506 , 1998.

[60] W. Hu, D. J. Eisenstein, M. Tegmark, and M. J. White, "Observationally determining the properties of dark matter," *Phys. Rev.*, vol. D59, 1999.

[61] J. F. Beacom, N. F. Bell, and S. Dodelson, "Neutrinoless universe," *Phys. Rev. Lett.*, vol. 93 , 2004.

[62] S. Hannestad, "Structure formation with strongly interacting neutrinos - implications for the cosmological neutrino mass bound," *JCAP*, vol. 0502 , 2005.

[63] A. Basboll, O. E. Bjaelde, S. Hannestad, and G. G. Raffelt, "Are cosmological neutrinos free-streaming?," *Phys. Rev. D*, vol. 79, 2009.

[64] R. Trotta and A. Melchiorri, "Indication for primordial anisotropies in the neutrino background from wmap and sdss," *Phys. Rev. Lett.*, vol. 95 , 2005.

[65] A. Melchiorri and P. Serra, "Anisotropies in the neutrino background: An update," *Phys. Rev.*, vol. D74, 2006.

[66] F. De Bernardis, L. Pagano, P. Serra, A. Melchiorri, and A. Cooray, "Anisotropies in the cosmic neutrino background after wmap 5-year data," *JCAP*, vol. 0806, 2008.

[67] S. e. Das, "The atacama cosmology telescope: A measurement of the cosmic microwave background power spectrum at 148 and 218 ghz from the 2008 southern survey," *Astrophys. J.*, vol. 729, 2011.

[68] C. L. e. Reichardt, "High resolution cmb power spectrum from the complete acbar data set," *Astrophys. J.*, vol. 694, 2009.

[69] B. A. e. Reid, "Cosmological constraints from the clustering of the sloan digital sky survey dr7 luminous red galaxies," *Mon. Not. Roy. Astron. Soc.*, vol. 404, 2010.

[70] H. Trac, P. Bode, and J. P. Ostriker, "Templates for the sunyaev-zel'dovich angular power spectrum," *Astrophys. J.*, vol. 727, 2011.

[71] F. de Bernardis, A. Melchiorri, L. Verde, and R. Jimenez, "The cosmic neutrino background and the age of the universe," *JCAP*, vol. 0803, 2008.

[72] A. e. Vikhlinin, "Chandra cluster cosmology project iii: Cosmological parameter constraints," *Astrophys. J.*, vol. 692, 2009.

[73] A. X. Gonzalez-Morales, R. Poltis, B. D. Sherwin, and L. Verde, "Are priors responsible for cosmology favoring additional neutrino species?," *arXiv:1106.5052 [astro-ph.CO]*.

[74] Y. Akrami, P. Scott, J. Edsjo, J. Conrad, and L. Bergstrom, "A profile likelihood analysis of the constrained mssm with genetic algorithms," *JHEP*, vol. 1004, 2010.

[75] F. Feroz, K. Cranmer, M. Hobson, R. Ruiz de Austri, and R. Trotta, "Challenges of profile likelihood evaluation in multi-dimensional susy scans," *JHEP*, vol. 1106, 2011.

[76] S. Hannestad, "Neutrino masses and the number of neutrino species from wmap and 2dfgrs," *JCAP*, vol. 0305, 2003.

[77] V. Barger, J. P. Kneller, H. S. Lee, D. Marfatia, and G. Steigman, "Effective number of neutrinos and baryon asymmetry from bbn and wmap," *Phys. Lett. B*, vol. 566, 2003.

[78] P. Crotty, J. Lesgourgues, and S. Pastor, "Measuring the cosmological background of relativistic particles with wmap," *Phys. Rev. D*, vol. 67, 2003.

[79] J. Hamann, "Evidence for extra radiation? profile likelihood versus bayesian posterior," *JCAP*, vol. 1203, 2012.

[80] P. Collaboration] *arXiv:astro-ph/0604069.*

[81] F. R. e. T. C. C. Bouchet, "Core (cosmic origins explorer) a white paper," *arXiv:1102.2181 [astro-ph.CO].*

[82] A. Kosowsky and M. S. Turner, "Cbr anisotropy and the running of the scalar spectral index," *Phys. Rev.D*, vol. 52, 1995.

[83] S. Hannestad, S. H. Hansen, F. L. Villante, and A. J. S. Hamilton, "Constraints on inflation from cmb and lyman alpha forest," *Astropart. Phys.*, vol. 17, 2002.

[84] T. S. K. Ichikawa and T. Takahashi, "Probing the effective number of neutrino species with cosmic microwave background," *Phys. Rev.D*, vol. 78.

[85] M. Chevallier and D. Polarski, "Accelerating universes with scaling dark matter," *Int. J. Mod. Phys. D*, vol. 10, 2001.

[86] E. V. Linder, "Exploring the expansion history of the universe," *Phys. Rev. Lett.*, vol. 90, 2003.

[87] A. Albrecht, G. Bernstein, R. Cahn, W. L. Freedman, J. Hewitt, W. Hu, J. Huth, and M. e. Kamionkowski, "Report of the dark energy task force," *[astro-ph/0609591].*

[88] E. V. Linder, "The paths of quintessence," *Phys. Rev. D*, vol. 73, 2006.

[89] E. V. Linder, "Probing gravitation, dark energy, and acceleration," *Phys. Rev.D*, vol. 70, 2004.

[90] W. J. e. S. C. Percival, "Baryon acoustic oscillations in the sloan digital sky survey data release 7 galaxy sample," *Mon. Not. Roy. Astron. Soc.*, vol. 401, 2010.

[91] G. A. Tammman, A. Sandage, and B. Reindl *Astron. AstroPhys. Rev.*, vol. 15, 2008.

[92] G. Chen and B. Ratra, "Constraints on scalar-field dark energy from galaxy cluster gas mass fraction versus redshift," *Astrophys. J.*, vol. 612, 2004.

[93] L. Samushia, G. Chen, and B. Ratra, "Galaxy cluster gas mass fraction and hubble parameter versus redshift constraints on dark energy," *arXiv:0706.1963 [astro-ph].*

[94] L. Samushia and B. Ratra, "Constraints on dark energy from galaxy cluster gas mass fraction versus redshift data," *Astrophys. J.*, vol. 680, 2008.

[95] J. R. Gott, M. S. Vogeley, S. Podariu, and B. Ratra, "Median statistics, h(0), and the accelerating universe," *Astrophys. J.*, vol. 549, 2001.

[96] M. e. Kowalski, "Improved cosmological constraints from new, old and combined supernova datasets," *Astrophys. J.*, vol. 686, 2008.

[97] A. Barreira and P. P. Avelino, "Chi-square versus median statistics in snia data analysis," *Phys. Rev.*, vol. 84, 2011.

[98] S. Podariu, T. Souradeep, J. R. Gott, B. Ratra, and M. S. Vogeley, "Binned cosmic microwave background anisotropy power spectra: Peak location," *Astrophys. J.*, vol. 559, 2001.

[99] G. Chen and B. Ratra, "Median statistics and the mass density of the universe," *Publ. Astron. Soc. Pac.*, vol. 115, 2003.

[100] G. Chen, J. R. Gott, and B. Ratra, "Non-gaussian error distribution of hubble constant measurements," *Publ. Astron. Soc. Pac.*, vol. 115, 2003.

[101] G. Chen and B. Ratra, "Median statistics and the hubble constant," *Publ. Astron. Soc. Pac.*, vol. 123, 2011.

[102] B. Ratra, "Joining conditions for cosmological perturbations at an equation of state transition," *Phys. Rev.D*, vol. 43, 1991.

[103] S. Podariu and B. Ratra, "Supernovae ia constraints on a time variable cosmological 'constant'," *Astrophys. J.*, vol. 532, 2000.

[104] P. J. E. Peebles and B. Ratra, "Cosmology with a time variable cosmological constant," *Astrophys. J.*, vol. 325, 1988.

[105] B. Ratra and P. J. E. Peebles, "Cosmological consequences of a rolling homogeneous scalar field," *Phys. Rev.D*, vol. 37, 1988.

[106] A. e. Vikhlinin, "X-ray cluster cosmology," *Astrophys. J.*, vol. 692, 2009.

[107] S. Joudaki, "Constraints on neutrino mass and light degrees of freedom in extended cosmological parameter spaces," *arXiv:1202.0005 [astro-ph.CO]*.

[108] G. Mangano and P. D. Serpico, "A robust upper limit on $n_{\rm eff}$ from bbn," *Phys. Lett. B*, vol. 701, 2011.

[109] R. e. Kessler, "First-year sloan digital sky survey-ii (sdss-ii) supernova results: Hubble diagram and cosmological parameters," *Astrophys. J.Supp.*, vol. 185, 2009.

[110] S. Hannestad, "Global neutrino parameter estimation using markov chain monte carlo," *arXiv:0710.1952 [hep-ph]*, 2007.

[111] C. Giunti and C. W. Kim, *Fundamentals of Neutrino Physics and Astrophysics*.

[112] S. Bilenky, *Introduction to the physics of massive and mixed neutrinos*.

[113] Z. Xing and S. Zhou, *Neutrinos in particle physics, astronomy and cosmology*.

[114] G. L. Fogli, E. Lisi, A. Marrone, D. Montanino, A. Palazzo, and A. M. Rotunno, "Global analysis of neutrino masses, mixings and phases: entering the era of leptonic cp violation searches," *arXiv:1205.5254 [hep-ph]*.

[115] M. Archidiacono, E. Calabrese, and A. Melchiorri, "The case for dark radiation," *Phys. Rev.D*, vol. 84, 2011.

[116] E. Calabrese, M. Archidiacono, A. Melchiorri, and B. Ratra, "The impact of a new median statistics h_0 prior on the evidence for dark radiation," *arXiv:1205.6753 [astro-ph.CO]*.

[117] M. Sorel, J. M. Conrad, and M. Shaevitz, "A combined analysis of short-baseline neutrino experiments in the (3+1) and (3+2) sterile neutrino oscillation hypotheses," *Phys. Rev. D*, vol. 70, 2004.

[118] G. Karagiorgi, A. Aguilar-Arevalo, J. M. Conrad, M. H. Shaevitz, K. Whisnant, M. Sorel, and V. Barger, "Leptonic cp violation studies at miniboone in the (3+2) sterile neutrino oscillation hypothesis," *Phys. Rev. D*, vol. 75, 2007.

[119] E. Akhmedov and T. Schwetz, "Miniboone and lsnd data: non-standard neutrino interactions in a (3+1) scheme versus (3+2) oscillations," *JHEP*, vol. 1010, 2010.

[120] J. Kopp, M. Maltoni, and T. Schwetz, "Are there sterile neutrinos at the ev scale?," *arXiv:1103.4570 [hep-ph]*.

[121] C. Giunti and M. Laveder, "3+1 and 3+2 sterile neutrino fits," *Phys. Rev.D*, vol. 84, 2011.

[122] C. Giunti and M. Laveder, "Status of 3+1 neutrino mixing," *Phys. Rev. D*, vol. 84, 2011.

[123] C. Giunti and M. Laveder, "Implications of 3+1 short-baseline neutrino oscillations," *Phys. Lett. B*, vol. 706, 2011.

[124] G. Karagiorgi, M. H. Shaevitz, and J. M. Conrad, "Confronting the short-baseline oscillation anomalies with a single sterile neutrino and non-standard matter effects," *arXiv:1202.1024 [hep-ph]*.

[125] A. Donini, J. Hernandez, P. andLopez-Pavon, M. Maltoni, and T. Schwetz, "The minimal 3+2 neutrino model versus oscillation anomalies," *arXiv:1205.5230 [hep-ph]*.

[126] A. Melchiorri, O. Mena, S. Palomares-Ruiz, S. Pascoli, A. Slosar, and M. Sorel, "Sterile neutrinos in light of recent cosmological and oscillation data: A multi-flavor scheme approach," *JCAP*, vol. 0901, 2009.

[127] F. Iocco, G. Mangano, G. Miele, O. Pisanti, and P. D. Serpico, "Primordial nucleosynthesis: from precision cosmology to fundamental physics," *Phys. Rept.*, vol. 472, 2009.

[128] A. G. e. Riess, "A redetermination of the hubble constant with the hubble space telescope from a differential distance ladder," *Astrophys. J.*, vol. 699, 2009.

[129] R. e. Amanullah, "Spectra and light curves of six type ia supernovae at 0.511 $<$ z $<$ 1.12 and the union2 compilation," *Astrophys. J.*, vol. 716, 2010.

[130] E. Aver, K. A. Olive, and E. D. Skillman, "A new approach to systematic uncertainties and self-consistency in helium abundance determinations," *JCAP*, vol. 1005, 2010.

[131] Y. I. Izotov and T. X. Thuan, "The primordial abundance of 4he: evidence for non-standard big bang nucleosynthesis," *Astrophys. J.*, vol. 710, 2010.

[132] M. Pettini, B. J. Zych, M. T. Murphy, A. Lewis, and C. C. Steidel, "Deuterium abundance in the most metal-poor damped lyman alpha system: Converging on omega baryons," *arXiv:0805.0594 [astro-ph].*

[133] O. Pisanti, A. Cirillo, S. Esposito, F. Iocco, G. Mangano, G. Miele, and P. D. Serpico, "Parthenope: Public algorithm evaluating the nucleosynthesis of primordial elements," *Comput. Phys. Commun.*, vol. 178, 2008.

[134] J. Hamann, J. Lesgourgues, and G. Mangano, "Using bbn in cosmological parameter extraction from cmb: A forecast for planck," *JCAP*, vol. 0803, 2008.

[135] G. Mention, M. Fechner, T. .Lasserre, T. A. Mueller, D. Lhuillier, M. Cribier, and A. Letourneau, "The reactor antineutrino anomaly," *Phys. Rev.D*, vol. 83, 2011.

[136] A. A. e. M. C. Aguilar-Arevalo, "Unexplained excess of electron-like events from a 1-gev neutrino beam," *Phys. Rev. Lett.*, vol. 102, 2009.

[137] A. A. e. T. M. C. Aguilar-Arevalo, "Event excess in the miniboone search for $\bar{\nu}_\mu \to \bar{\nu}_e$ oscillations," *Phys. Rev. Lett.*, vol. 105, 2010.

[138] E. D. M. C. Zimmerman, "Updated search for electron antineutrino appearance at miniboone," *arXiv:1111.1375 [hep-ex].*

[139] Z. M. C. Djurcic, "Miniboone oscillation results 2011," *arXiv:1201.1519 [hep-ex].*

[140] K. N. e. Abazajian, "Light sterile neutrinos: A white paper," *arXiv:1204.5379 [hep-ph]*, 2012.

[141] T. A. Mueller, D. Lhuillier, M. Fallot, A. Letourneau, S. Cormon, M. Fechner, L. Giot, and T. e. Lasserre, "Improved predictions of reactor antineutrino spectra," *Phys. Rev.C*, vol. 83, 2011.

[142] P. Huber, "On the determination of anti-neutrino spectra from nuclear reactors," *Phys. Rev.C*, vol. 84, 2011.

[143] C. Giunti and Y. F. Li, "Matter effects in active-sterile solar neutrino oscillations," *Phys. Rev.D*, vol. 80, 2009.

[144] A. Palazzo, "Testing the very-short-baseline neutrino anomalies at the solar sector," *Phys. Rev.D*, vol. 83, 2011.

[145] A. Palazzo, "An estimate of θ_{14} independent of the reactor antineutrino flux determinations," *Phys. Rev.D*, vol. 85, 2012.

[146] F. P. e. D.-B. C. An, "Observation of electron-antineutrino disappearance at daya bay," *Phys. Rev. Lett.*, vol. 108, 2012.

[147] J. K. e. R. C. Ahn, "Observation of reactor electron antineutrino disappearance in the reno experiment," *Phys. Rev. Lett.*, vol. 108, 2012.

[148] C. Giunti *Talk presented at nuTURN2012, 8-10 May 2012, LNGS, Assergi, Italy.*

[149] S. Hannestad, I. Tamborra, and T. Tram, "Thermalisation of light sterile neutrinos in the early universe," *JCAP*, vol. 1207, 2012.

[150] A. Mirizzi, N. Saviano, G. Miele, and P. D. Serpico, "Light sterile neutrino production in the early universe with dynamical neutrino asymmetries," *arXiv:1206.1046 [hep-ph]*, 2012.

[151] M. A. Acero and J. Lesgourgues, "Cosmological constraints on a light non-thermal sterile neutrino," *Phys. Rev.D*, vol. 79, 2009.

[152] S. Dodelson, A. Melchiorri, and A. Slosar, "Is cosmology compatible with sterile neutrinos?," *Phys. Rev. Lett.*, vol. 97, 2006.

[153] R. Barbieri and A. Dolgov, "Neutrino oscillations in the early universe," *Nucl. Phys. B*, vol. 349, 1991.

[154] M. Archidiacono, E. Giusarma, A. Melchiorri, and O. Mena, "Dark radiation in extended cosmological scenarios," *arXiv:1206.0109 [astro-ph.CO].*

[155] M. C. Gonzalez-Garcia, M. Maltoni, and J. Salvado, "Robust cosmological bounds on neutrinos and their combination with oscillation results," *JHEP*, vol. 1008, 2010.

[156] A. Slosar, "Detecting neutrino mass difference with cosmology," *Phys. Rev. D*, vol. 73, 2006.

[157] G. L. e. Fogli, "Observables sensitive to absolute neutrino masses (addendum," *Phys. Rev. D*, vol. 78, 2008.

[158] F. De Bernardis, P. Serra, A. Cooray, and A. Melchiorri, "An improved limit on the neutrino mass with cmb and redshift-dependent halo bias-mass relations from sdss, deep2, and lyman-break galaxies," *Phys. Rev. D*, vol. 78, 2008.

[159] M. J. Mortonson and W. Hu *Astrophys. J.*, vol. 686, 2008.

[160] T. R. Choudhury and A. Ferrara, "Physics of cosmic reionization," *astro-ph/0603149*.

[161] R. H. e. S. C. Becker, "Evidence for reionization at z 6: Detection of a gunn-peterson trough in a z = 6.28 quasar," *Astron. J.*, vol. 122, 2001.

[162] W. Hu and M. J. White, "A cmb polarization primer," *New Astron.*, vol. 2, 1997.

[163] M. J. Mortonson and W. Hu, "Model-independent constraints on reionization from large-scale cmb polarization," *Astrophys. J.*, vol. 672, 2008.

[164] S. Pandolfi, A. Cooray, E. Giusarma, E. W. Kolb, A. Melchiorri, O. Mena, and P. Serra, "Harrison-z'eldovich primordial spectrum is consistent with observations," *Phys. Rev. D*, vol. 81, 2010.

[165] M. e. Lueker, "Measurements of secondary cosmic microwave background anisotropies with the south pole telescope," *Astrophys. J.*, vol. 719, 2010.

[166] P. A. R. e. P. C. Ade, "Planck early results: The planck mission," *arXiv:1101.2022 [astro-ph.IM]*, 2011.

[167] E. e. W. C. Komatsu, "Five-year wilkinson microwave anisotropy probe (wmap) observations: Cosmological interpretation," *Astrophys. J.Suppl.*, vol. 180, 2009.

[168] N. Sehgal, P. Bode, S. Das, C. Hernandez-Monteagudo, K. Huffenberger, Y. T. Lin, J. P. Ostriker, and H. Trac, "Simulations of the microwave sky," *Astrophys. J.*, vol. 709, 2010.

[169] C. L. Reichardt, L. Shaw, O. Zahn, K. A. Aird, B. A. Benson, L. E. Bleem, J. E. Carlstrom, and C. L. e. Chang, "A measurement of secondary cosmic microwave background anisotropies with two years of south pole telescope observations," *Astrophys. J.*, vol. 755, 2012.

[170] L. D. Shaw, D. Nagai, S. Bhattacharya, and E. T. Lau, "Impact of cluster physics on the sunyaev-zel'dovich power spectrum," *Astrophys. J.*, vol. 725, 2010.

[171] M. Tegmark and G. Efstathiou, "A method for subtracting foregrounds from multi-frequency cmb sky maps," *MNRAS*, vol. 281.

[172] T. L. et al. *MNRAS*, vol. 297, 1998.

[173] G. e. a. De Zotti *A&A*, vol. 431, 2005.

[174] N. e. a. Aghanim *Rept. Prog. Phys.*, vol. 71, 2008.

[175] M. e. Millea, "Modeling extragalactic foregrounds and secondaries for unbiased estimation of cosmological parameters from primary cmb anisotropy," *arXiv:1102.5195 [astro-ph.CO]*.

[176] F. Atrio-Barandela and J. P. Mücket *ApJ*, vol. 515, 1999.

[177] K. E. and K. T. *ApJ*, vol. 526, 1999.

[178] A. Cooray, "Large scale pressure fluctuations and sunyaev-zel'dovich effect," *PRD*, vol. 62, 2000.

[179] J. e. a. Bond *ApJ*, vol. 626, 2005.

[180] A. Cooray, W. Hu, and M. Tegmark *ApJ*, vol. 540, 2000.

[181] E. e. a. Shirokoff, "Improved constraints on cosmic microwave background secondary anisotropies from the complete 2008 south pole telescope data," *arXiv:1012.4788 [astro-ph.CO]*.

[182] A. e. a. Amblard *Nature*, vol. 470, 2011.

[183] P. e. a. P. C. Ade, "Planck early results: The power spectrum of cosmic infrared background anisotropies," *arXiv:1101.2028 [astro-ph.CO]*.

[184] S. e. a. Oliver *in preparation*, 2010.

[185] G. e. a. Pilbratt *A&A*, vol. 518, 2010.

[186] D. e. a. Hanson *GRG*, vol. 42, 2010.

[187] R. e. a. Gispert *Lecture Notes in Physics*, vol. 548/2000, 2000.

[188] P. e. a. Serra *PRD*, vol. 78, 2008.

[189] N. Battaglia, J. R. Bond, C. Pfrommer, J. L. Sievers, and D. Sijacki, "Simulations of the sunyaev-zel'dovich power spectrum with agn feedback," *arXiv:1003.4256*, 2010.

[190] N. e. a. Hall *ApJ*, vol. 718, 2010.

[191] S. Galli, M. Martinelli, A. Melchiorri, L. Pagano, B. D. Sherwin, and D. N. Spergel, "Constraining fundamental physics with future cmb experiments," *Phys. Rev.*, vol. D82 , 2010.

[192] M. Shimon, N. J. Miller, C. T. Kishimoto, C. J. Smith, G. M. Fuller, and B. G. Keating, "Using big bang nucleosynthesis to extend cmb probes of neutrino physics," *JCAP*, vol. 1005 , 2010.

[193] A. e. a. Cooray, "The herschel-spire legacy survey (hsls): the scientific goals of a shallow and wide submillimeter imaging survey with spire," *arXiv.org:1007.3519*, 2010.

List of refereed publications

- "CMB Neutrino Mass Bounds and Reionization", M. Archidiacono, A. Cooray, A. Melchiorri, S. Pandolfi, Journal-ref: Phys.Rev.D82:087302, (2010);
- "Constraints on massive sterile neutrino species from current and future cosmological data", E. Giusarma, M. Corsi, M. Archidiacono, R. de Putter, A. Melchiorri, O. Mena, S. Pandolfi, Journal-ref: Phys.Rev.D83:115023, (2011);
- "The impact of Reionization modelling on CMB Neutrino Mass Bounds", M. Archidiacono, A. Melchiorri, S. Pandolfi, Journal-ref: Nuclear Physics B (Proc. Suppl.) 217 (2011) 65–67;
- "Amplitudes of thermal and kinetic Sunyaev-Zel'dovich signal from small scales CMB anisotropies", M. Archidiacono, F. de Bernardis, A. Cooray, A. Amblard, P. Serra, A. Melchiorri, Journal-ref: Phys. Rev. D 85, 043015, (2012);
- "The Case for Dark Radiation", M. Archidiacono, E. Calabrese, A. Melchiorri, Journal-ref: Physical Review D 84, 123008, (2012);
- "The Impact of Assuming Flatness in the Determination of Neutrino Properties from Cosmological Data", A. Smith, M. Archidiacono, A. Cooray, F. De Bernardis, A. Melchiorri, J. Smidt, Journal-ref: Physical Review D 85, 123521, (2012);
- "Sterile neutrino models and non minimal cosmologies", E. Giusarma, M. Archidiacono, R. de Putter, A. Melchiorri, O. Mena, Journal-ref: Phys. Rev. D 85, 083522, (2012);
- "The fine structure constant and the CMB Damping Scale", E. Menegoni, M. Archidiacono, E. Calabrese, S. Galli, C. J. A. P. Martins, A. Melchiorri, Journal-ref: Phys. Rev. D 85, 107301, (2012);
- "The impact of a new median statistic H_0 prior on the evidence for dark radiation", E. Calabrese, M. Archidiacono, A. Melchiorri, B. Ratra, Journal-ref: Phys. Rev. D 86, 043520, (2012);
- "Dark Radiation in extended cosmological scenarios", M. Archidiacono, E. Giusarma, A. Melchiorri, O. Mena, Journal-ref: Phys. Rev. D 86, 043509, (2012);

- "Testing 3+1 and 3+2 neutrino mass models with cosmology and short baseline experiments", M. Archidiacono, N. Fornengo, C. Giunti, A. Melchiorri, Journal-ref: Phys. Rev. D 86, 065028, (2012).